Computational Investigation of the Structure, Dynamics, and Functions of Glyceraldehyde-3-Phosphate Dehydrogenase (GAPDH) Relevant to Its Reactions with Nitric Oxide Donors

Vinodbhai Parmar

A Thesis
In the Department
of
Chemistry and Biochemistry

Presented in Partial Fulfillment of the Requirements
For the Degree of
Doctor of Philosophy (Chemistry) at
Concordia University
Montreal, Quebec, Canada

July 2018

CONCORDIA UNIVERSITY
School of Graduate Studies

This is to certify that the thesis prepared

By: Vinodbhai Parmar

Entitled: Computational Investigation of the Structure, Dynamics, and Functions of Glyceraldehyde-3-Phosphate Dehydrogenase (GAPDH) Relevant to Its Reactions with Nitric Oxide Donors

and submitted in partial fulfillment of the requirements for the degree of

Doctor of Philosophy (Chemistry)

complies with the regulations of the University and meets the accepted standards with respect to originality and quality.

Signed by the final examining committee:

____________________________ Chair
Dr. W. Brake

____________________________ External Examiner
Dr. J. Gauld

____________________________ External to Program
Dr. L. Kalman

____________________________ Examiner
Dr. G. Lamoureux

____________________________ Examiner
Dr. P. Pawelek

____________________________ Supervisor
Dr. A. English

____________________________ Supervisor
Dr. G. Peslherbe

Approved by ____
Dr. P. Pawelek, Graduate Program Director

August 14, 2018 ____
Dr. A. Roy, Dean, Faculty of Arts and Science

Abstract

Computational Investigation of the Structure, Dynamics, and Functions of Glyceraldehyde-3-Phosphate Dehydrogenase (GAPDH) Relevant to Its Reactions with Nitric Oxide Donors

Vinodbhai Parmar, Ph.D.
Concordia University, 2018

Glyceraldehyde-3-phosphate dehydrogenase (GAPDH), a well-known glycolytic enzyme, exhibits *moonlighting* functions, including catalysis of glyceryl trinitrate (GTN) to release vasoactive nitrite (NO_2^-) or nitric oxide (NO). GTN catalysis generates a thionitrate (E-Cys-NO_2) intermediate at the catalytic thiol of GAPDH. Thus, we investigated decomposition of CH_3SNO_2, a model compound for E-Cys-NO_2, using state-of-the-art quantum mechanics techniques. We showed that the well-studied homolysis pathway, which releases NO, is energetically unfavorable. Instead, hydrolysis and thiolysis pathways that release NO_2^- are energetically favorable. The release of NO_2^- upon the attack of anionic nucleophiles (e.g. OH^- or CH_3S^-) along the S–N bond is barrierless which could explain the instability of thionitrates in aqueous solutions. We also looked at the effect of protonation on the stability of the S–N bond of CH_3SNO_2 to mimic the effect of proton donation from the protein. We found that O- and S-protonation stabilize and destabilize the S–N bond, respectively. We evaluated the electronic structures of the protonated isoforms of CH_3SNO_2 to elucidate the observed stability/instability of the S–N bond. Further investigation of nitrite release by hydrolysis of E-Cys-NO_2 in the active site of GAPDH using quantum mechanics / molecular mechanics (QM/MM) techniques revealed similar activation barriers as shown by the QM methods.

Each subunit of the GAPDH homotetramer binds the cofactor nicotinamide adenine dinucleotide (NAD^+). The tetramer binds NAD^+ with negative cooperativity. We carried out normal mode analysis and molecular dynamics (MD) simulations of GAPDH-NAD^+ to probe the

mechanism of negative cooperativity and define the subunit interactions that contribute to this phenomenon. We compared the dynamics of GAPDH-NAD$^+$, GAPDH-NADH, and apo-GAPDH and observed concerted motions between subunits of GAPDH-NAD$^+$ and GAPDH-NADH. These motions are lost in apo-GAPDH, indicating that NAD$^+$ binding induces these dominant and functionally relevant motions of GAPDH. We also indicated the changes in the NAD binding-site residues and active-site residues that are observed in the crystal structure of apo- vs. holo-GAPDH.

Many *moonlighting* functions of GAPDH depend on its oligomeric state. MD simulations are thus carried out for the three oligomeric states, tetramer, dimer or monomer. Our study shows that the dimer and monomer are less stable than the tetramer and functionally important motions are centered on the NBDs in tetramer and dimer, but they are centered on the S-loop in the monomer. The importance of the dynamics of the S-loop are highlighted. This disordered loop in the dimer and particularly monomer could promote binding of the GAPDH dimer and monomer with multiple protein partners to affect different functions.

We modeled GAPDH and the seven in absentia homolog 1 (Siah1) protein-protein interactions. By investigating complex formation between the different oligomeric states of each protein, we show that the GAPDH monomer binds more tightly to Siah1 than the GAPDH tetramer. Thus, GAPDH monomer could stabilize Siah1 and the complex could be translocated to the nucleus to initiate apoptosis.

Overall, our study provides molecular-level insights into novel functions of GAPDH. We have highlighted the importance of the dynamics of its various structural domains, which contribute to the different functions of GAPDH.

Acknowledgment

First and foremost, I would like to thank my supervisors, Dr. Ann M English and Dr. Gilles H Peslherbe, for their guidance and support. I also would like to thank my committee members, Dr. Guillaume Lamoureux and Dr. Peter Pawelek, for their evaluation and advice on my project work.

I am grateful to current and past members of the Centre for Research in Molecular Modeling (CERMM) team and to Dr. English's group for fruitful conversations about our research.

I want to acknowledge the financial support that I received in the form of graduate awards from Concordia University, PROTEO, and the NSERC CREATE Training Program in Bionanomachines. I also want to acknowledge the generous allocations of computational resources from Calcul Québec and the Natural Sciences and Engineering Research Council of Canada for funding.

I am very grateful to my caring parents and my brothers for their love and support at every step of my life.

At last, I would like to thank my dear wife for her unconditional love, encouragement, support, and patience.

Contribution of Authors

The work presented in this thesis was performed by Vinod Parmar and supervised by Dr. Ann M English and Dr. Gilles H Peslherbe. Philippe Archambault performed the QTAIM and AIMALL calculations and wrote the results in Chapter 3. I would like to thank Dr. Guillaume Lamoureux for providing the initial input files for QM/MM calculations that led to the work presented in Chapter 7. The thesis was edited by Dr. Ann English and Dr. Gilles Peslherbe.

Table of Contents

List of Figures

List of Tables

Chapter 1. Introduction

1.1. Preamble

Glyceraldehyde-3-phosphate dehydrogenase (GAPDH), a well-known glycolytic enzyme, catalyzes the reversible oxidation and phosphorylation of glyceraldehyde-3-phosphate to 1,3-biphosphoglycerate in presence of the cofactor NAD^+ and inorganic phosphate. GAPDH, a homotetramer, is composed of four 37-kDa subunits, referred to as subunit-O, -P, -Q and -R. Each subunit is composed of two subdomains, namely a NAD-binding domain (NBD; residue 1-151 and 315-335), which adopts a Rossmann fold, and the glyceraldehyde-3-phosphate catalytic domain (CTD; residue 152-314). Each subunit of GAPDH binds one nicotinamide adenine dinucleotide (NAD^+) cofactor.[1,2]

GAPDH is ubiquitous in nature and abundant in cells. This led to investigations of its various physiological and pathological functions. GAPDH is now known as a *moonlighting* protein, a single protein's ability to exhibit alternate functions apart from its classical function.[3] For example, GAPDH exhibits acyl phosphatase [4] and esterase [5] activities, endocytosis,[6,7] RNA transport,[8,9] DNA replication,[10] DNA repair,[11,12] apoptosis[13,14] and many other physiological functions.[3,15] GAPDH also is implicated in pathological conditions like cancer,[16,17] Alzheimer's,[18,19] Parkinson's,[20,21] and Huntington's diseases.[22,23]

These multifold physiological and pathological functions of GAPDH may require its post-translation modification, oligomerization, protein-protein interactions, binding of cofactors, or exposure of intrinsically disordered subdomains.[2,3,15,24] Various proteins like Huntington protein,[25] the androgen receptor,[26] ataxin,[26] β-amyloid precursor protein,[27] seven in absentia homolog 1 (Siah1),[14] GOSPEL,[28] transferrin[29] are known to interact with GAPDH. GAPDH is also known to interact with RNA[30,31] and single-stranded DNA.[32] These protein-protein or protein-nucleic acid interactions give rise to different functions. Apart from its interactions with protein partners, many post-translational modifications (PTMs) such as S-nitrosation, S-thiolation, sulphonation, and phosphorylation are known to occur in GAPDH. These PTMs could change GAPDH's function by altering its conformation and/or oligomeric states, which could trigger a change in cellular localization and/or interaction with other protein partners, and alter its reactivity.[3,33]

GAPDH also is a target for the drug design to combat protozoan parasites like *Leishmania mexicana*,[34–37] *Trypanosoma cruzi*,[37–39] *Trypanosoma brucei*,[36,40] and *Plasmodium falciparum*.[41,42] These parasites rely on glycolysis for survival in a human host, thus selective inhibition of the parasitic GAPDH is proposed as an effective strategy to cure diseases caused by such parasites. Its multifold functions and involvement in disease makes GAPDH one of the most studied enzymes over the last decade.[2,43]

1.1.1. GAPDH's role in nitric oxide biochemistry

GAPDH is a known target for nitric oxide (NO), NO donors and reactive oxygen species (ROS).[44,45] We observed that stimulation of isolated human erythrocytes by glyceryl trinitrate (GTN), a prodrug, leads to a rapid increase in ATP, [46] a well-known vasodilator.[47] We further demonstrated that GAPDH interacts with GTN and releases nitrite (NO_2^-) and 1,2-GDN as major products.[48] We found an increase in the rate of GAPDH-catalyzed NO_2^- release from GTN upon addition of NAD^+. These observations implicate GAPDH in the formation of NO_2^- during GTN biotransformation. Many other enzymes are implicated in GTN biotransformation, including cytochrome P-450,[49] xanthine oxidase,[50] glutathione S-transferase,[51] and mitochondrial aldehyde dehydrogenase (ALDH2).[52]

The underlying mechanisms of GTN biotransformation are not very well understood. It produces NO_2^- and/or NO to rapidly trigger vasodilation.[53] However, the extent of NO_2^- or NO release from GTN remains the subject of much debate, as does the relative contribution of these two metabolites to the vasodilatory effect of GTN. In addition, the reaction mechanism involved in the enzymatic bioactivation of GTN has been debated for a long time. According to a recent review,[54] there seems to be a consensus that GTN interacts with small-molecule thiols or active-site thiols in proteins to form an enzyme thionitrate (E-Cys-NO_2) complex.

An E-Cys-NO_2 intermediate is observed in the crystal structure of an ALDH2 triple mutant variant following reaction with GTN.[55] The three mutations, C301S, C303S and E268Q, are in the vicinity of the catalytic cysteine, Cys302. A +46 amu mass adduct of the GTN-treated triple variant of ALDH2 was observed by mass spectrometry, which was attributed to the E-Cys-NO_2 formation at Cys302. Thus, we speculate that E-Cys-NO_2 is formed upon GTN binding to the catalytic Cys152 of GAPDH. However, the mechanism of E-Cys-NO_2 decomposition is not known. Several pathways for the decomposition of E-Cys-NO_2 are proposed based on computational and experimental studies of small-molecule thionitrates ($RSNO_2$).[52,56–58] No detailed computational studies have been carried out to rigorously investigate all the proposed pathways.

Depending on the E-Cys-NO_2 decomposition pathway, the catalytic cysteine (Cys152 in GAPDH) would be chemically modified to cysteine disulfide (Cys152-S–S-Cys156), cysteine sulfenic acid (Cys152-S-OH) due to hydrolysis, or di-thiolsulfinate (Cys152-S(O)–S-Cys156) and/or di-thiolsulfonate (Cys152-S(O_2)–S-Cys156) due to homolysis. Also, these different pathways of decomposition require the involvement of different residues. Thus, understanding the pathway involved in GTN denitration will help us identify the residues that can be selectively mutated to better understand the complete mechanism of GTN denitration in GAPDH. Furthermore, E-Cys-NO_2 decomposition could affect the functions and oligomeric states of GAPDH by alteration of its active-site. Thus, a detailed understanding of the GTN denitration will shed light on the possible fate of GAPDH. Also, understanding the GTN denitration mechanism will inform the design of new NO donors that have fewer side effects and do not induce tolerance like GTN.[59,60]

Oae *et al*. synthesized small-molecule thionitrates and reported that some *t*-alkyl thionitrates were stable at room temperature.[61,62] Recent crystal structures of aromatic thionitrates indicate that they can be protected from decomposition by large cage-like structures.[63,64] The study of the decomposition of tertiary butylthionitrate (*t*-BuSNO$_2$) reveals its rapid decomposition in aqueous solution at neutral pH.[65] These reports raise questions about the stability of thinoitrates.

1.1.2. Cofactor binding to the GAPDH tetramer

GAPDH is an asymmetric homotetramer (subunit-O, -P, -Q, and -R), which is functionally and structurally a dimer of dimers.[2] Subunit-O interacts with subunit-P, -Q and -R as interaction across the P-, Q- and R-axes, respectively. The number of contacts across the axes are in the order P > R > Q. GAPDH's NBD features the well-known Rossmann fold, which is highly conserved in all dehydrogenases.[66] The mechanism of NAD$^+$ binding and subsequent changes in the conformations of the NBD were examined in the crystal structures of the apo-GAPDH (NAD$^+$-free) and holo-GAPDH (NAD$^+$-bound) of *Bacillus stearothermophilus*.[67] The adenosine and nicotinamide moieties of NAD$^+$ bind away from and close to the active-site, respectively. According to the published study, the adenosine moiety of NAD$^+$ binds first to apo-GAPDH because it does not require any conformational change. Several attractive interactions lead to the tight binding of adenosine moiety, which induces conformational changes to form the binding site for the nicotinamide moiety close to the active-site. However, this requires NAD$^+$ to move deeper into the active-site and necessitates thermal fluctuations of the enzyme and cofactor to overcome local energy barriers. These conformational changes create an H-bond between the catalytic Cys152 and His179 residues in the active-site, which enhances reactivity. The reactive thiolate form of Cys152 also stabilizes the positively charged N-atom of the nicotinamide moiety of NAD$^+$. These interactions additionally optimize the phosphate binding site.[67]

Considering that the NAD$^+$ binding-site is mostly conserved in *B. stearothermophilus* and human GAPDH,[67] structural changes induced by NAD$^+$ in the bacterial enzyme might also occur in the human enzyme. NAD$^+$ binds in the NBD of human GAPDH with negative cooperativity, where binding of one NAD$^+$ decreases the affinity of the next NAD$^+$, which causes loose binding of additional NAD$^+$ molecules.[68,69] However, the structural details of NAD$^+$ binding to GAPDH with negative cooperativity are not very well understood in the human enzyme.

NADH also binds to GAPDH with negative cooperativity but has 100-fold less binding affinity than NAD$^+$.[70] NAD$^+$ binding promotes tetramer formation,[71] but NADH binding results in conformational changes that lead to destabilization of the tetramer.[72,73] Also, NBD of GAPDH is involved in the binding of nucleic acids[9,74] and glutathione conjugates.[75,76] NAD$^+$ or NADH inhibit the binding of nucleic acid to GAPDH.[74] Thus, the effect of NAD$^+$ or NADH binding on dynamics of NBD could help understand the binding mechanism of nucleic acids to GAPDH.

1.1.3. Oligomeric states of GAPDH

GAPDH is translated as 37 kDa monomer but mainly exists as the tetramer.[2] However, PTMs could give rise to dimers or monomers.[14,77–79] It has been shown that cellular localization and oligomeric states of GAPDH lead to many of its different functions.[80,81] For example, GAPDH exhibits dehydrogenase activity in the cytoplasm as the tetramer. Some literature reports indicate that the tetramer is the only active form of GAPDH,[71] but a few reports suggest that the dimer is also active.[82,83] The tetramer dissociates into monomers at extreme pH or in the presence of chemical denaturants such as guanidine or urea.[72,84,85] The monomers and dimers of GAPDH are implicated in the aggregation that contributes to neurodegenerative diseases such as Alzheimer's disease.[86] GAPDH monomer is found in cells that are undergoing apoptosis,[14] and monomeric nuclear GAPDH is implicated in DNA repair.[10,87]

Such literature reports raise various questions about GAPDH's structure and function. What are the structural differences between the GAPDH oligomers? How do the different oligomeric states possess different functions? There is no detailed understanding of the mechanism of GAPDH oligomerization/deoligomerization. Understanding the GAPDH oligomerization process and identifying the amino acids that contribute to the different oligomeric states will provide insight into the important physiological and pathological phenomena, including apoptosis and neurodegenerative diseases involving GAPDH.

Cofactor removal from GAPDH (apo-GAPDH) increases internal solvation, which signals the instability of apo-GAPDH. Thus, examining the effects of cofactor binding or removal on tetramer GAPDH would reveal the importance of the cofactor in the formation of GAPDH tetramer.

Ionic interactions between the positively charged NAD^+ cofactor and the negatively charged thiolate of the catalytic Cys152, with a pK_a of 6.03,[88] contribute to the stability of tetrameric GAPDH. Hence, modification of Cys152 can decrease the stability of the tetramer, giving rise to monomers, dimers and other denatured GAPDH products [89,90] that affect glycolytic function.[91] Elucidating precisely how these electrostatic interactions influence the stability of each oligomeric state is critical to understanding GAPDH's diverse functions. It is important to establish how changes in the active-site control the formation of different oligomers. For example, what regions of GAPDH are the most flexible, and what interactions are involved in the stabilization of the dimer or tetramer compared to the monomer?

1.2. Objectives and outline

The goal of this thesis is to gain molecular and structural insights into GAPDH's role in NO biochemistry and other functions. To understand GAPDH's involvement in GTN bioactivation at the molecular level, we investigated pathways proposed for decomposition of E-Cys-NO_2, the intermediate formed upon GTN reaction with GAPDH. We show that GTN turnover is doubled in presence of NAD^+,[48] thus we carried out molecular dynamics (MD) simulations of GAPDH-NAD^+ and GAPDH-NADH to investigate effects of the cofactor on the dynamics of the active-site. We compare the dynamics of holo- and apo-GAPDH to identify cofactor-induced dynamic changes. The removal of NAD^+ from the tetramer promote monomer formation, so we examined the dynamics of the GAPDH tetramer, dimer, and monomer. These oligomeric states could play important roles in the moonlighting functions of GAPDH. The role of GAPDH in one moonlighting function, apoptosis, is investigated to understand complex formation between GAPDH and Siah1.

In Chapter 2 of this thesis, we use CH_3SNO_2 as a model compound for E-Cys-NO_2 to investigate its decomposition with state-of-the-art quantum mechanics (QM) calculations. We investigated all the proposed pathways [52,56–58] for thionitrate decomposition using CCSD(T)//MP2/aug-cc-pVTZ model chemistry [92–96] in the gas phase and solvent effects were included implicitly with the Polarized Continuum Model (PCM).[97,98] We specifically investigated E-Cys-NO_2 decomposition by reaction with the anionic nucleophiles, OH^- and CH_3S^-, which represent activated water molecules and activated thiols, respectively. Geometries and the activation barriers for CH_3SNO_2 decomposition are compared with CH_3SNO as a model S-nitrosothiol because S-nitrosothiols are well-known NO donors. We also carried out benchmark calculations for CH_3SNO_2 decomposition with density functional theory (DFT) methods such as

BLYP and B3LYP and a different basis sets, which are relatively fast, to find the best model chemistry to use in quantum mechanics / molecular mechanics (QM/MM) calculations of E-Cys-NO_2 decomposition.

In Chapter 3 of this thesis, we investigate the effect of protonation on the stability and electronic structure of CH_3SNO_2. We used CCSD(T)//MP2/aug-cc-pVTZ model chemistry to investigate the geometry and decomposition of the protonated isomers of CH_3SNO_2 and the electronic structures of the isomers were evaluated using natural bond orbital (NBO), and natural resonance theory (NRT), as well as AIMALL and QTAIM analysis. The results are compared with those for CH_3SNO_2 to explain the increase/decrease in the stability of the protonated isomers.

In Chapter 4 of this thesis, cofactor-dependent structural dynamics of GAPDH are investigated. We carried out molecular dynamics (MD) simulations of GAPDH tetramer with bound NAD^+ or NADH (GAPDH-NAD^+ or GAPDH-NADH) and apo-GAPDH. We used the CHARMM27 force-field and NAMD2.9 [99] to carry out the MD simulations. Multivariate statistical analysis, principal component analysis (PCA) [100,101] and cross-correlation analysis (CCA) was used to evaluate the large MD simulations data. Further, normal mode analysis (NMA) [102–104] was carried out using the crystal structure of human GAPDH (PDB 1U8F) [105] to investigate the global motions of GAPDH and compared with the MD simulations trajectories.

In Chapter 5, we investigate the dynamics of the three oligomeric states of GAPDH, the tetramer, dimer and monomer, to understand the conformational changes induced by oligomerization or deoligomerization of the tetramer. We carried out these simulations in presence of NAD^+ and evaluated subdomain and subunit dynamics of the oligomeric states. We also compare the dynamics from MD simulations with the global dynamics obtained from NMA of the crystal structures.

In Chapter 6, we investigated the binding of GAPDH with Siah1 using molecular docking. The study evaluates complex formation between the oligomeric states of GAPDH and Siah1. Molecular docking was carried out using web servers and possible docking poses were predicted for the tetramer, dimer and monomer of GAPDH with the Siah1 dimer and monomer.

In Chapter 7, QM/MM calculations were performed to investigate the activation barrier for E-Cys-NO_2 decomposition by hydrolysis at the active-site of GAPDH. The active-site residues within 4 Å of catalytic Cys152, including His179 and Glu317, were treated in the QM part using BLYP/TZV2P-GTH, while the remaining residues of the protein and the solvent molecules were treated by MM using CHARMM force field.[106] We used the CP2K program [107] for the QM/MM calculations.

Chapter 2. Barrierless nitrite release from thionitrates exposed on modeling CH_3SNO_2 decomposition: Relevance in nitroglycerin bioactivation

2.1. Abstract

Organic thionitrates ($RSNO_2$) release vasoactive nitrite and nitric oxide and are key intermediates in the biotransformation of organic nitrates like glyceryl trinitrate (GTN). However, mechanisms of NO_2^- and NO release from $RSNO_2$ are controversial. To address this, we performed a comprehensive high-level quantum chemistry investigation of $RSNO_2$ decomposition using CH_3SNO_2 as a model compound. We find prohibitively high activation enthalpy ($\Delta H^{\ddagger}_{calc}$) for S–N bond homolysis (> 40 kcal/mol) or CH_3SNO_2 concerted rearrangement (> 50 kcal/mol) although the $CH_3S(O)NO$ and CH_3SONO products of these reactions undergo facile homolysis to release NO ($\Delta H^{\ddagger}_{calc} \sim 6$ kcal/mol). Gas-phase hydrolysis of CH_3SNO_2 by three water molecules to release NO_2^- is substantially more favorable ($\Delta H^{\ddagger}_{calc} \sim 21$ kcal/mol). The most favorable pathways, however, involve an attack by OH^- or CH_3S^- perpendicular to the S–N bond ($\Delta H^{\ddagger}_{calc} \sim 17$ kcal/mol) or barrierless attack ($\Delta H^{\ddagger}_{calc} \sim 0$ kcal/mol) along the S–N bond to release NO_2^-. Reactions with the anionic nucleophiles model attack by an activated water or a neighboring cysteinate on an enzyme-bound $RSNO_2$ (E–Cys–NO_2), the intermediate implicated in GTN enzymatic bioactivation. In sum, our calculations predict biologically viable pathways for $RSNO_2$ decomposition with NO_2^- release but not with NO release.

2.2. Introduction

Organic nitrates are used in the treatment of heart diseases,[53] cancer pain management,[108] osteoporosis,[109] neuropathic pain[110] and as NO-NSAIDs (nitric oxide-donating nonsteroidal anti-inflammatory drugs).[111] Nitroglycerin (or glyceryl trinitrate; GTN) has been widely used as a vasodilator for over 130 years. GTN acts as a prodrug and undergoes biotransformation to release nitrite (NO_2^-) and/or nitric oxide (NO) to rapidly trigger vasodilation.[53] The extent of NO_2^- or NO release from GTN remains the subject of much debate as does the relative contribution of these two metabolites to the vasodilatory effect of GTN. Thatcher *et al.*[112] reviewed evidence for NO or NO_2^- release from GTN and discussed the reactions of organic nitrates with thiols. They suggested mechanisms for NO generation in these reactions, including the formation of an organic thionitrate intermediate, which was proposed over 30 years ago by Yeates *et al.*[113] GTN decomposition by various enzymes with catalytic Cys residues, including mitochondrial aldehyde dehydrogenase (ALDH2) and glyceraldehyde-3-phosphate dehydrogenase (GAPDH), gives NO_2^- plus 1,2- or 1,3-glyceryl dinitrate (GDN) as products.[48,52,114] For example, we reported that in the presence of dithiothreitol (DTT) to regenerate the thiol form of its catalytic Cys, GAPDH catalyzes the release of NO_2^- and 1,2-GDN from GTN.[48] Based on the observed products, a consensus emerges that an enzyme bound thionitrate (E–Cys–NO_2) is an intermediate in organic nitrate decomposition by cysteine nitrate reductases such as GAPDH.[54]

From their synthesis of various low-molecular-weight aromatic and aliphatic thionitrates ($RSNO_2$), Oae *et al.* reported that only *t*-alkyl thionitrates are stable at room temperature.[61,62] However, the crystal structure of an aromatic $RSNO_2$ was recently reported[115] and the E-Cys-NO_2 group also was observed in the crystal structure of an ALDH2 variant.[55] These findings suggest that $RSNO_2$ are viable intermediates in nitrate biotransformation.

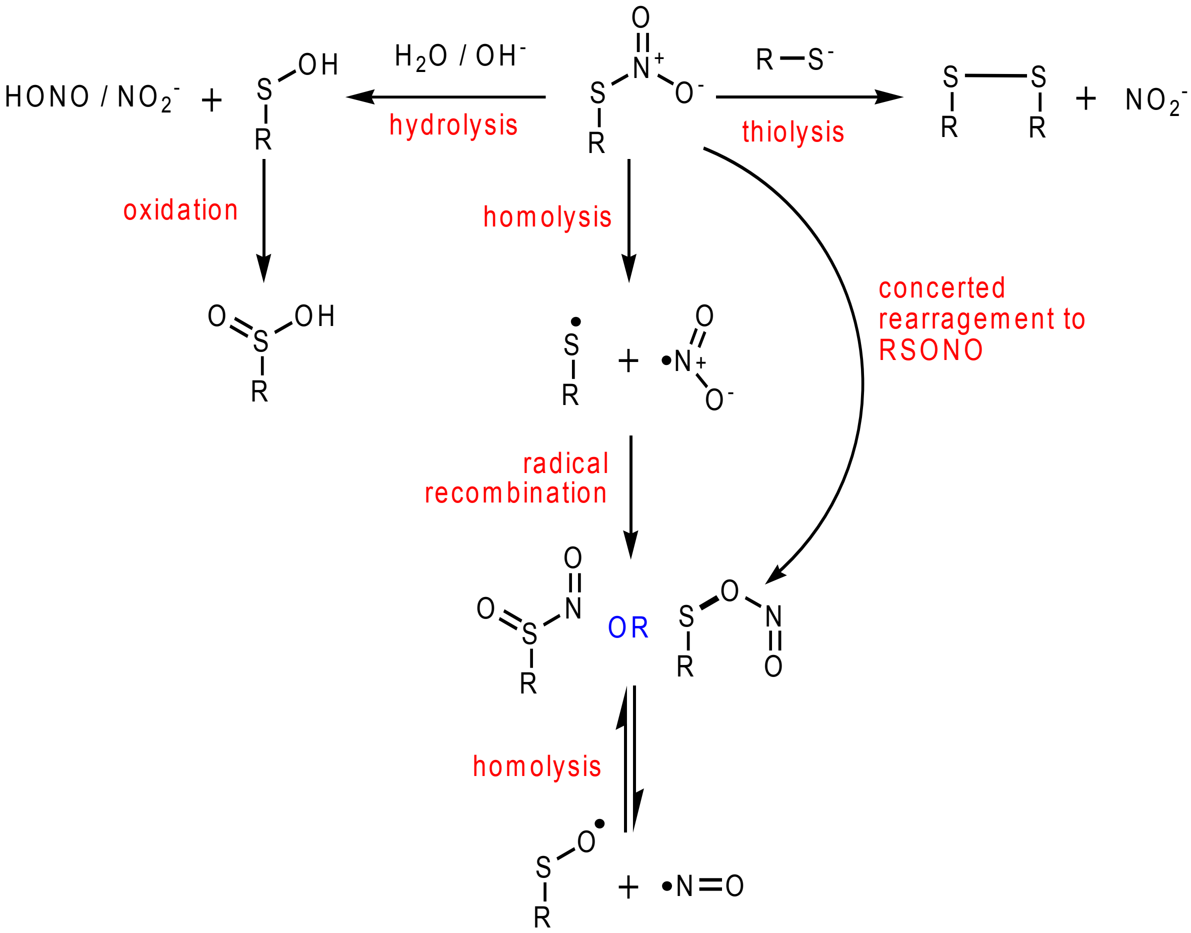

Figure 2.1: Proposed pathways for thionitrate ($RSNO_2$) decomposition to NO_2^- and $^{\bullet}NO$.[52,56–58,113,116] **Hydrolysis** by H_2O or OH^- (activated water) as well as **thiolysis** by R–S⁻ (small-molecule thiolate or a protein-based cysteinate) release NO_2^-. S–N bond **homolysis** in $RSNO_2$ produces highly reactive radicals that recombine to give RSONO (sulfenyl nitrite) or RS(O)NO (sulfinyl nitrite) and O–N or S–N bond homolysis, respectively, release NO. Alternatively, **concerted rearrangement** of $RSNO_2$ could generate RSONO. In this work, we examine these pathways for R = CH_3.

Several mechanisms for $RSNO_2$ decomposition have been proposed,[52,56–58,113,116] including homolysis, hydrolysis, and thiolysis (Figure 2.1). For instance, homolysis of the S–N bond is implicated in the rapid decomposition of *t*-butylthionitrate ($RSNO_2$; R= *t*-Bu) to RS(O)SR, $RS(O_2)SR$ and NO.[65] The mechanism of $HSNO_2$ and CH_3SNO_2 decomposition also was investigated with quantum chemistry calculations. The MP4SDQ//6-31G*//MP2/6-31G* activation free energy barrier ($\Delta G^{\ddagger}_{calc}$) for the rearrangement of $HSNO_2$ to HSONO is 55.3

kcal/mol,[56] while the MP2/6-311+G** activation enthalpy barrier ($\Delta H^{\ddagger}_{\mathrm{calc}}$) for homolytic cleavage of CH_3SNO_2 to $CH_3S^{\bullet}$ + $^{\bullet}NO_2$ is reported to be 33.3 kcal/mol.[112] Another computational investigation of CH_3SNO_2 decomposition with ROCCSD(T)//HF/6-311+G* yielded similar results for the homolysis and rearrangement pathways.[117] Thus, the reported computational studies suggest that $RSNO_2$ decomposition via homolysis is not favorable.

Although NO release from $RSNO_2$ has been the focus of theoretical work to date, various experimental reports suggest that NO_2^- is the main product formed upon the decomposition of organic nitrates by protein-based thiols as seen in the catalysis of GTN decomposition by ALDH2[52,58] and GAPDH.[48] A study on the hydrolysis in an alkaline solution of an aromatic thionitrate within a bowl-shaped steric protection group (Bpq-SNO_2) produced a stable sulfenic acid,[64] consistent with the release of NO_2^- (Figure 2.1). Also, the reaction of glutathione (GSH) with peroxynitrite ($ONOO^-$) is reported to give $GSNO_2$, which forms NO_2^- and GSSG on further reaction with GSH, pointing to thiolysis as a viable pathway for $RSNO_2$ decomposition.[118] Interestingly, the $GSNO_2H^+$ ion is found to be stable to fragmentation in ESI/MS/MS experiments,[118] which suggests that some $RSNO_2$ might be more stable than assumed.[56,113]

In order to rigorously examine the proposed mechanisms of NO and NO_2^- release from $RSNO_2$ and to address the confounding issue of $RSNO_2$ stability, here we report a comprehensive quantum chemical investigation of CH_3SNO_2 decomposition to NO_2^- or NO via homolysis, hydrolysis, and thiolysis (Figure 2.1). We also consider the reaction of CH_3SNO_2 with OH^- to approximate a water activated by H-bonding in the active-site of an enzyme such as GAPDH, whereas the attack on CH_3SNO_2 by CH_3S^- serves to model thiolysis by an activated Cys residue, which likely occurs in ALDH2. Throughout, we contrast CH_3SNO_2 and CH_3SNO decomposition since S-nitrosothiols are well-characterized NO donors.

2.3. Computational Methods

Molecular geometries of the reactants, products and transition states (TS) were optimized with second-order Møller-Plesset perturbation theory (MP2)[92,119] and the aug-cc-pVTZ augmented correlation-consistent basis set.[94] Vibrational analysis was performed to confirm the nature of the stationary points (energy minima, TS) and to estimate thermodynamic properties under the rigid rotor-harmonic oscillator approximation,[120] while Intrinsic Reaction Coordinate (IRC)[121,122] calculations were performed to unambiguously connect the TS to reactants and products. Hartree-Fock wavefunction stability tests were performed for all intermediates and transition states and confirmed the absence of open-shell character. Electronic energies were further refined at the Coupled Cluster with Single, Double and perturbative linearized Triple excitations [CCSD(T)] level of theory.[95,96] Calculations were carried out within the restricted wavefunction formalism, except in the case of (open–shell) radicals where the unrestricted formalism was employed (spin contamination was checked for and found to be insignificant). Solvent effects were included implicitly with the Polarized Continuum Model (PCM)[97,98] using dielectric constants of 4, 30 and 78.4 to represent diethyl ether, methanol, and water as solvents. The Gaussian09[123] program was used for all calculations.

2.4. Results

2.4.1. Model compound selection

$HSNO_2$, CH_3SNO_2, and *t*-$BuSNO_2$ were considered as model compounds for Cys–NO_2, which itself is deemed representative of the thionitrate intermediate in an enzyme (E–Cys–NO_2) such as GAPDH and ALDH2. The calculated geometries of $HSNO_2$, CH_3SNO_2, *t*-$BuSNO_2$, and Cys–NO_2 are shown in Figure 2.2 while selected geometric parameters and charge distributions are collected in Table 2.1. The geometries of all four compounds exhibit similar S–N bond lengths (1.776-1.785 Å), which are in good agreement with the observed S–N bond lengths (1.780-1.790 Å) in the recently published crystal structures of bowl-shaped aromatic thionitrates.[115,124] However, the H–S–N angle of $HSNO_2$ (92.79 °) is 6−12 ° smaller than the R–S–N angle in $RSNO_2$ (98.87-105.15 °), which is close to the angle (100.47-107.9 °) observed in the Bpq-SNO_2 crystal structures.[115,124] Also, the partial charge of sulfur is significantly less positive in $HSNO_2$ (0.247) than in $RSNO_2$ (0.432 − 0.470). Furthermore, we observed in the gas phase that $HSNO_2$ easily transfers a proton from sulfur to a nearby nucleophile (data not shown), which is not possible for $RSNO_2$. Hence, based on geometry, charge distribution and reactivity, $HSNO_2$ is not a good model for the larger $RSNO_2$. CH_3SNO_2, *t*-BuSNO_2, and Cys–NO_2 exhibit similar structural properties, so we selected CH_3SNO_2 as the smallest model compound to investigate the stability and decomposition of $RSNO_2$, including E–Cys–NO_2.

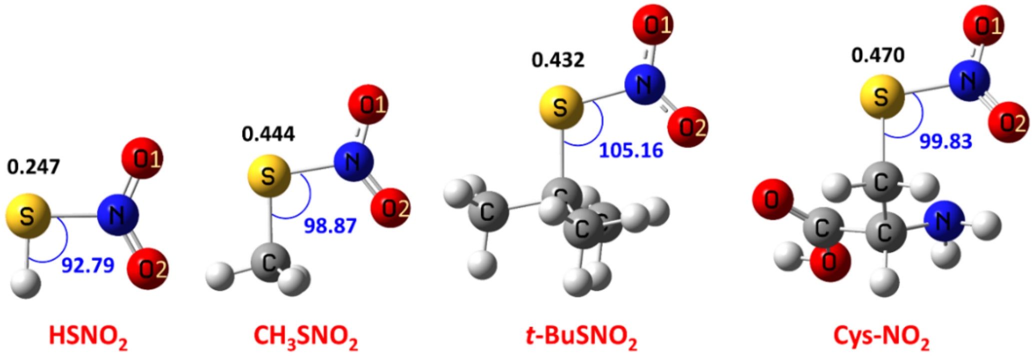

Figure 2.2: $HSNO_2$, CH_3SNO_2, t-BuSNO_2, and Cys–NO_2 gas-phase molecular geometries optimized with MP2/aug-cc-pVTZ. The H/R–S–N angle (degrees, °) and the partial charge on the sulfur atom are indicated. Note that in each structure the H/C–S–NO_2 atoms are in the same plane and the barrier for rotation around the S–N bond is ~8 kcal/mol (see text). In the plane of the molecule, nucleophiles can attack the sulfur atom along the S–N bond or perpendicular to this bond either *trans* (top attack) or *cis* (bottom attack) to the R-group. Attack perpendicular to the molecular plane is not favored due to electrostatic repulsion with the sulfur lone pairs (Figure S2.1). O1 and O2 refer to oxygen atoms *trans* and *cis* to R-group, respectively.

The C–S–NO_2 atoms of CH_3SNO_2 in Figure 2.2 are in the same plane, which also has been observed in the crystal structures of bowl-shaped aromatic thionitrates.[63,115,124] The barrier for rotation around the S–N bond is calculated to be 8 kcal/mol, which restricts rotation of the nitro group out of the plane. Also, the electrostatic potential map for CH_3SNO_2 (Supporting Information Figure S2.1) reveals that nucleophilic attack on the sulfur atom occurs in the C–S–NO_2 plane to minimize electrostatic repulsion between the nucleophile and the sulfur lone pairs perpendicular to this plane.

Table 2.1. Geometric parameters and charge distribution for $RSNO_2$[a]

RSNO2	Bond lengths (Å)			Angle (°)	Atomic partial charges			
	S–N	N–O1b	N–O2b	H/C–S–N	S	N	O1 b	O2 b
HSNO2	1.785	1.222	1.220	92.79	0.247	0.497	-0.429	-0.433
CH3SNO2	1.776	1.225	1.223	98.87	0.444	0.482	-0.438	-0.448
t-BuSNO2	1.776	1.226	1.224	105.15	0.432	0.487	-0.439	-0.458
Cys–NO2	1.779	1.225	1.224	99.83	0.470	0.490	-0.433	-0.470

[a] Geometries are optimized with MP2/aug-cc-pVTZ in the gas phase and partial charges calculated with the Natural Bond Orbital (NBO) module as implemented in Gaussian09.

[b] See Figure 2.2 for the definition of O1 and O2.

2.4.2. Decomposition of CH_3SNO_2 by homolysis

The two pathways investigated for CH_3SNO_2 decomposition by homolysis are shown in Figure 2.1. Direct homolytic cleavage of the CH_3SNO_2 S–N bond gives the highly reactive nitrogen dioxide ($^•NO_2$) and thiyl ($CH_3S^•$) radicals, which would recombine to form sulfenyl (CH_3SONO) or sulfinyl ($CH_3S(O)NO$) nitrite. Homolytic cleavage of the (S)O–N bond in CH_3SONO or the S–N bond in $CH_3S(O)NO$ would then generate the nitric oxide ($^•NO$) and sulfenyl ($CH_3SO^•$) radicals. Alternatively, CH_3SNO_2 may rearrange to CH_3SONO via a concerted mechanism.[56] The profile for these reactions is shown in Figure 2.3 along with selected molecular geometries. The calculated S–N bond length in CH_3SNO_2 (1.776 Å) matches the experimental value of 1.780–1.790 Å observed for aromatic $RSNO_2$ by X-ray crystallography,[115,124] and $\Delta H^{\ddagger}_{calc}$ for CH_3SNO_2 homolytic cleavage to $^{\bullet}NO_2$ and $CH_3S^{\bullet}$ is 42.6 kcal/mol in the gas phase. The concerted rearrangement of CH_3SNO_2 to CH_3SONO is less favorable, with $\Delta H^{\ddagger}_{calc} = 51.7$ kcal/mol. Our transition state (TS1) and reaction profile for this rearrangement are consistent with previously published reports.[56,117] We performed further energy refinement with CCSD(T)/aug-cc-pVQZ//MP2/aug-cc-pVTZ but the activation barriers for S–N bond homolysis or rearrangement to CH_3SONO (Supporting Information Table S2.1) change by only ~1 kcal/mol upon extension of the basis set to quadruple zeta quality. Hence, energy refinement is carried out with a triple zeta basis set hereafter for the sake of computational efficiency.

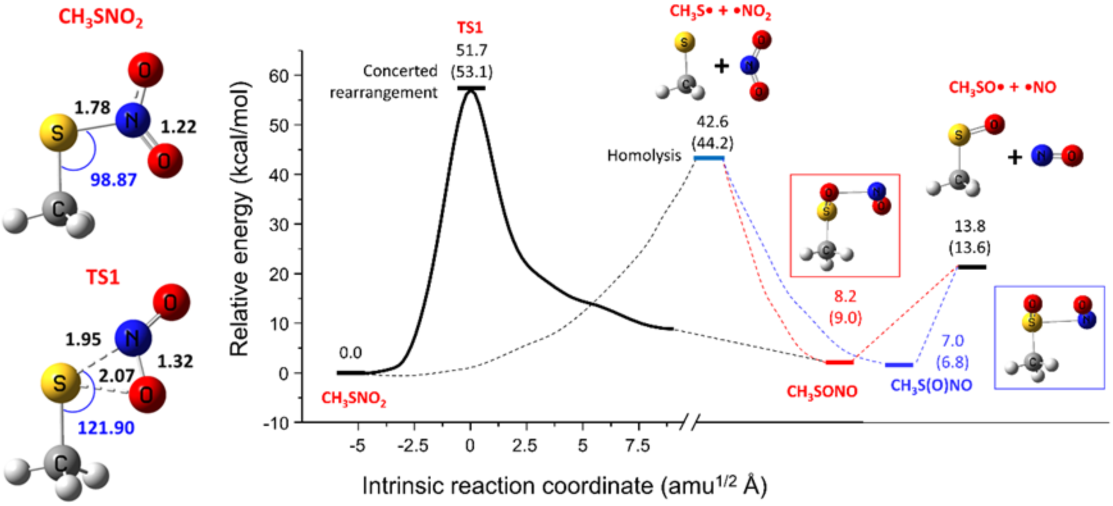

Figure 2.3. Modeling CH_3SNO_2 homolysis and its rearrangement to CH_3SONO and $CH_3S(O)NO$. Geometries are optimized with MP2/aug-cc-pVTZ in the gas phase. The vertical axis represents MP2/aug-cc-pVTZ relative energies with respect to the reactants. Indicated on the graph are the ΔH_{calc} (or $\Delta H^{\ddagger}_{calc}$ for TS) values calculated with CCSD(T)//MP2/aug-cc-pVTZ in the gas phase and the ΔH_{calc} that further include solvent effects with PCM-water are in parentheses. Energies/enthalpies in kcal/mol, distances in Å and angles in degrees (°).

The most stable conformations of CH_3SONO and $CH_3S(O)NO$ lie 7–8 kcal/mol higher in enthalpy than their CH_3SNO_2 precursor. Their weak elongated (S)O–N (2.10 Å) and S–N (2.43 Å) bonds can undergo homolytic cleavage to release $CH_3SO^\bullet$ and $^\bullet NO$ with a modest $\Delta H^\ddagger_{calc} = 6$ kcal/mol. Note that the $CH_3SO^\bullet + {}^\bullet NO$ products lie 13.8 kcal/mol higher in enthalpy than the CH_3SNO_2 reactant, indicating that $^\bullet NO$ release is endothermic but significantly less so than direct $^\bullet NO_2$ release (42.6 kcal/mol) from CH_3SNO_2.

Table 2.2. Activation barriers ($\Delta H^\ddagger_{calc}$; kcal/mol) of CH_3SNO_2 decomposition by S–N bond homolysis, hydrolysis, reaction with OH^- and CH_3S^-

	CCSD(T)//MP2/aug-cc-pVTZ[a]		CCSD(T)//MP2/aug-cc-pVTZ(PCM-water)[b]		
	Homolysis	Hydrolysis (3 H_2O top)	Reaction with OH^- (top)	Reaction with OH^- (bottom)	Reaction with CH_3S^- (top)
Gas phase	42.6	20.9	~ 0[c]	~ 0[c]	~ 0[c]
PCM Ɛ=4	43.6	20.7	9.0	22.3	12.9
PCM Ɛ=30	44.2	20.6	16.1	28.4	17.0
PCM Ɛ=78.4	44.2	20.6	16.7	28.9	17.3

[a] Gas-phase molecular geometries are used to calculate $\Delta H^\ddagger_{calc}$ values for homolysis (Figure 2.3) and hydrolysis (Figure 2.4a,b and Figure 2.5). Solvent effects are included using PCM with dielectric constants (ε) corresponding to diethyl ether (4), methanol (30) and water (78.4).

[b] Molecular geometries for reactions with OH^- (Figure 2.6a,b) and CH_3S^- (Figure 2.7) are calculated in PCM-water.

[d] $\Delta H^\ddagger_{calc} \sim 0$ for the reaction of CH_3SNO_2 with OH^- and CH_3S^- because the ions are unstable in the gas phase.

The ΔH_{calc} values of the reactants, intermediates, and products with the inclusion of implicit solvent are reported in Figure 2.3 for PCM-water and those evaluated with varying dielectric constants are collected in Table 2.2. The ΔH_{calc} values change by < 1 kcal/mol when solvent effects are considered and $\Delta H^\ddagger_{calc}$ for direct S–N bond homolytic cleavage or rearrangement to CH_3SONO or $CH_3S(O)NO$ increases by ~1.5 kcal/mol. Thus, solvent effects are negligible despite the large increase in the dipole moment of CH_3SNO_2 from 4.44 D in the gas phase to 5.61 D in PCM-water since a similar trend is observed for all chemical species (Supporting Information Table S2.2). In summary, NO release from CH_3SNO_2 via homolysis is unfavorable since it requires steps with prohibitory high activation barriers in the gas phase and in solvent.

2.4.3. Decomposition of CH_3SNO_2 by hydrolysis

The products of CH_3SNO_2 hydrolysis are HONO and CH_3SOH (Figure 2.1). The calculated profiles for the reaction of CH_3SNO_2 with a single water molecule are displayed in Figure 2.4a,b along with selected molecular geometries, while activation barriers are collected in Table 2.3. Water can attack the sulfur atom from the top of the C–S–NO_2 plane (Figure 2.2) to give TS2-t (Figure 2.4a) or from the bottom of this plane to give TS2-b (Figure 2.4b). Both pathways are characterized by pre- and post-reaction complexes lying 1−5 kcal/mol lower in enthalpy than the reactants and products. Both TS2-t and TS2-b exhibit an elongated S–N bond (2.32 and 2.12 Å), a relatively short S–O(water) separation (1.96 and 2.03 Å), and an elongated water O–H bond, consistent with their role as precursors to the CH_3SOH and HONO products. The reaction is endothermic by ~8 kcal/mol and $\Delta H^{\ddagger}_{\mathrm{calc}}$ is large, 50.0 and 45.2 kcal/mol for the top and bottom attack, respectively. As observed for homolysis, the inclusion of implicit solvent effects has a negligible impact on the $\Delta H^{\ddagger}_{\mathrm{calc}}$ values (Table 2.3).

Hydrolysis and water-mediated reactions often involve proton shuttle between multiple water molecules. Thus, the inclusion of additional explicit water molecules can significantly alter a reaction profile by forming stabilizing hydrogen bonds,[125–130] so CH_3SNO_2 hydrolysis also was investigated with two to four water molecules. Interestingly, two water molecules form a ring with CH_3SNO_2 in top attack (TS3-t, Figure 2.5, Figure S2.2a,b) but, due to steric constraints enforced by the methyl group, the second water acts as a spectator in bottom attack (TS3-b, Figure S2.2b). Similarly, due to steric constraints imposed by the methyl group, the reaction of CH_3SNO_2 with three and four water molecules occur from the top of the C–S–NO_2 plane only. TS geometries with one to three water molecules are all consistent with the formation of CH_3SOH and HONO as reaction products (Figure 2.4a,b and Figure 2.5) but $\Delta H^{\ddagger}_{calc}$ drops by 16 kcal/mol on going from two (37.2 kcal/mol) to three water molecules (20.9 kcal/mol, Table 2.3). A slight increase occurs when a fourth water (estimated $\Delta H^{\ddagger}_{calc}$ of 22 kcal/mol, Supporting Information Table S2.3) is introduced, indicating that three water molecules provide optimum ring strain and hence the lowest activation barrier.

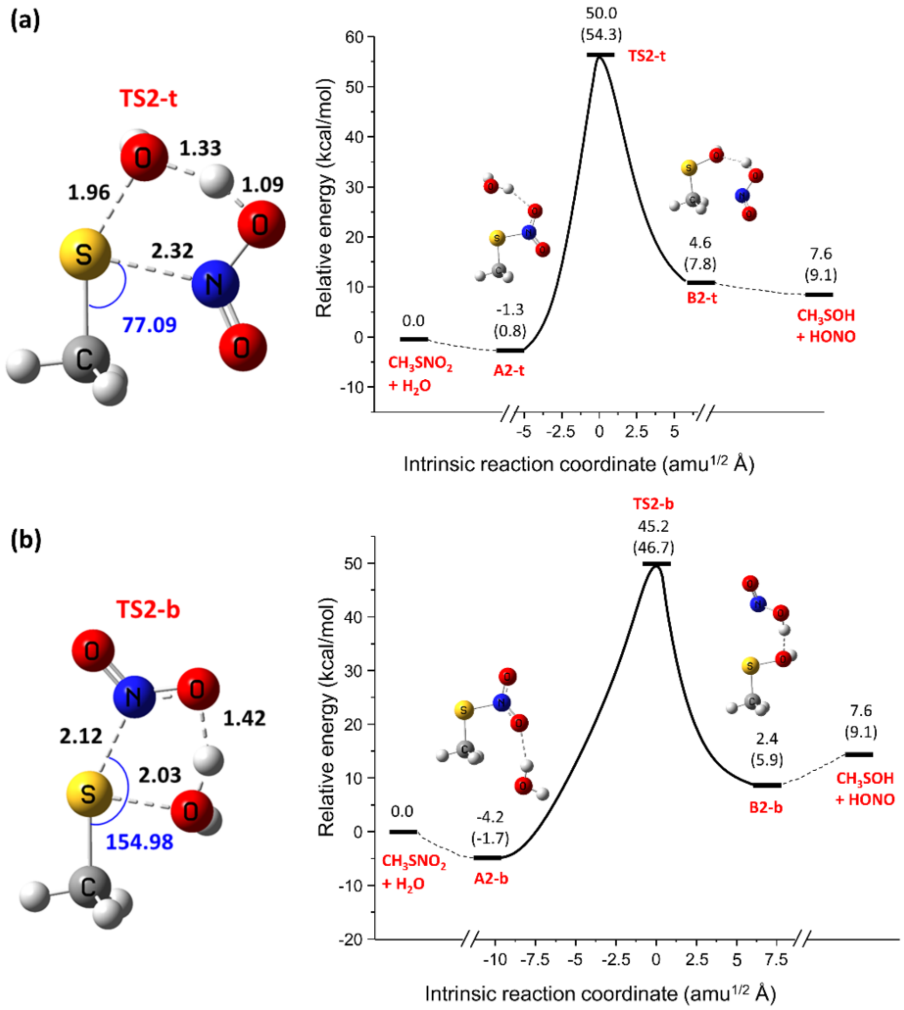

Figure 2.4: Modeling CH_3SNO_2 hydrolysis by one water molecule. Water attack from the (a) top and (b) bottom of the C–S–NO_2 plane of CH_3SNO_2. See captions to Figure 2.2 and Figure 2.3 for details.

Table 2.3. Activation barriers ($\Delta H^{\ddagger}_{calc}$, kcal/mol) for CH_3SNO_2 hydrolysis [a]

	1 H_2O top	1 H_2O bottom	2 H_2O top	2 H_2O bottom	3 H_2O top
Gas phase	50.0	45.2	37.2	39.9	20.9
PCM Ɛ=4	52.8	46.3	38.4	42.4	20.7
PCM Ɛ=30	54.1	46.7	38.9	43.3	20.6
PCM Ɛ=78.4	54.3	46.7	38.9	43.4	20.6

[a] $\Delta H^{\ddagger}_{calc}$ calculated with CCSD(T)//MP2/aug-cc-pVTZ for gas-phase geometries. Solvent effects are included with the PCM model and dielectric constants (ε) for diethyl ether (4) methanol (30) and water (78.4).

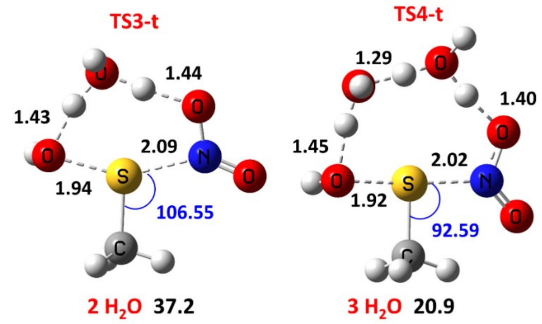

Figure 2.5: Transition state in modeling CH_3SNO_2 hydrolysis by two and three water molecules. Water attack from the top of the C–S–NO_2 plane. See captions to Figure 2.2 and Figure 2.3 for details. The $\Delta H^{\ddagger}_{calc}$ values (kcal/mol) indicated under each transition state structure are calculated with CCSD(T)//MP2/aug-cc-pVTZ in the gas phase.

2.4.4. Decomposition of CH_3SNO_2 by reaction with OH^-

As mentioned above, water can be activated for the nucleophilic attack in enzyme active-sites by hydrogen-bond donation to neighboring residues. Thus, to mimic hydrolysis with a highly activated water, we examined the OH^-/CH_3SNO_2 reaction. Due to the questionable relevance of the results from gas-phase calculations for anionic species (Figure S2.3a), the reaction profiles for OH^- attack from the top and bottom of the C–S–NO_2 plane are characterized in PCM-water (Figure 2.6a,b). OH^- attack from the top (Figure 2.6a) or bottom (Figure 2.6b) of the C–S–NO_2 plane is highly exothermic (ΔH_{calc} = -25.4 kcal/mol), but not as much as in the gas phase. Attack from the bottom (TS5-b) or top (TS5-t) of the C–S–NO_2 plane gives a transition state with an elongated S–

N bond and a nascent S–O bond that is a precursor for CH_3SOH and NO_2^- formation (Figure 2.6a,b). However, the barrier for attack from the top ($\Delta H^{\ddagger}_{calc}$ = 16.7 kcal/mol) is remarkably lower than that from the bottom ($\Delta H^{\ddagger}_{calc}$ = 28.9 kcal/mol; Figure 2.6a,b and Table 2.2), which we attribute in part to distortion of the C–S–N angle. Relative to the CH_3SNO_2 reactant (Figure 2.2), the C–S–N angle is compressed by only 20 ° in TS5-t but expanded by 37 ° in TS5-b. Additionally, TS5-t has a stabilizing OH–ONO bond which is absent in TS5-b. Since OH^- attack from the top is 4 kcal/mol more favorable than hydrolysis with three water molecules (Table 2.2), $RSNO_2$ is predicted to be less stable with increasing pH or in an enzyme's active-site close to an activated water molecule.

Attempts to locate a TS for the attack of OH^- along the S–N bond with an $O_{(OH-)}$--- S–N angle of ~180 ° were unsuccessful. Thus, we calculated the potential energy curve (PEC) by scanning the distance between $O_{(OH-)}$---S, while relaxing the geometry. The relaxed PEC reveals barrierless attack along the S–N bond (Figure 2.6c), which explains why we failed to locate a TS. The O(OH^-)---S distances are 1.6, 2.3 and 3.8 Å in A5-l, B5-l and C5-l complexes, respectively. The NBO charges of these structures show a charge transfer from OH^- (-0.984 to -0.433) to NO_2^- (-0.483 to -0.986) going from C5-l to A5-l (Table S4). NBO analysis reveals an NBO interaction between a lone pair of O_{OH}^- and σ*(S–N) with stabilization energy of 50 kcal/mol for structure B5-l (Table S2.5 and Figure S2.4), which destabilizes the S–N bond. This NBO interaction is absent in A5-l and C5-l. Thus, the charge transfer from OH^- to NO_2^- with S–N bond breaking favored due to strong interactions between a lone pair of OH^- and sulfur makes the attack of OH^- along the S–N bond barrierless. Also, the electrostatic surface shows a positive charge (σ-hole) on the sulfur atom in CH_3SNO_2, which favors a barrierless attack of anionic nucleophile along the S–N bond (Figure S2.1).

The barrierless attack of OH^- along the S–N bond was further confirmed by QM simulation of CH_3SNO_2 and OH^- complex. We started QM simulation with $O_{(OH^-)}$---S distance of 3.8 Å and relaxed geometry of the complex by following the negative energy gradient using our own code, which uses Gaussian09 for geometry optimization (Figure S2.5). The calculation was carried out using MP2/6-311+G(d,p)(PCM-water) and further energies were corrected for selected geometries with CCSD(T)/aug-cc-pVTZ(PCM-water) (Figure S2.5a). It reveals similar reaction coordinates as seen with relaxed PEC (Figure S2.5b-d vs Figure 2.6c).

2.4.5. Decomposition of CH_3SNO_2 by reaction with CH_3S^-

Protein-based thiols, particularly those involved in enzyme catalysis, are frequently in an activated thiolate form.[131–133] Accordingly, the reaction of CH_3SNO_2 with CH_3S^- was investigated (Figure 2.1). Because this reaction also involves anionic species, the gas-phase profile reveals a highly exothermic reaction (ΔH_{calc} -29.5 kcal/mol) along with the pronounced stability of the pre- and post-reaction complexes and no activation barrier (Figure S2.3b). Therefore, we also characterized the CH_3S^-/CH_3SNO_2 reaction profile and stationary points with PCM-water (Figure 2.7). S–N bond elongation and partial disulfide bond formation characterize TS6-t as a precursor of the products, CH_3SSCH_3 and NO_2^-. Notably, $\Delta H^{\ddagger}_{\text{calc}}$ in PCM-water for attack from the top of the C–S–NO_2 plane by CH_3S^- and OH^- are very similar (~17 kcal/mol; Table 2.2). Although CH_3S^- is a stronger nucleophile than OH^-, presumably TS5-t is stabilized by the H-bond interaction between OH^- and the ONO moiety (Figure 2.6a). As seen for OH^-, attack of CH_3S^- along the S–N with an S---S-N angle of ~180 ° is barrierless (Figure 2.7b). The $S_{(CH_3S^-)}$---S distances are 2.0, 2.8 and 3.5 Å in structures A6-l, B6-l and C6-l, respectively. As similar to OH^-, this barrierless attack also involves a charge transfer from CH_3S^- (-0.975 to -0.018) to NO_2^- (-0.493 to -0.990) going from C6-l to A6-l (Table S6). The NBO interaction between a lone pair of $S_{CH_3S^-}$ and σ*(S–N) has stabilization energy of 42 kcal/mol for structure B6-l, which favors the barrierless attack (Figure S2.6).

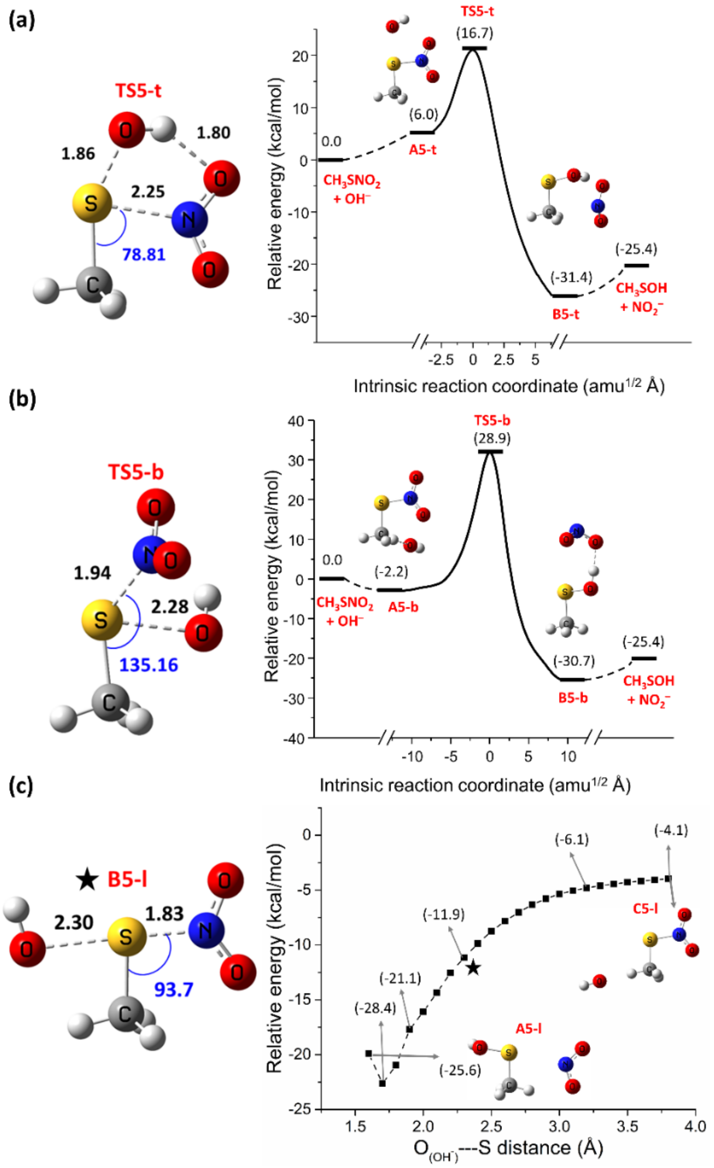

Figure 2.6: Modeling the reaction of CH$_3$SNO$_2$ with OH$^-$ where the nucleophile attacks from the (a) top or (b) bottom of the C–S–NO$_2$ plane and (c) along the S–N bond (see Figure 2.2). Panels (a,b) show IRCs, whereas panel (c) shows the relaxed potential energy curve (PEC) calculated for the O$_{(OH^-)}$---S distance scan. Geometries are optimized with MP2/aug-cc-pVTZ(PCM-water). The vertical axis represents MP2/aug-cc-pVTZ(PCM-water) relative energies with respect to the reactants. Indicated on the graph are the ΔH_{calc} (or $\Delta H^{\ddagger}_{\text{calc}}$ for TS) values calculated with CCSD(T)// MP2/aug-cc-pVTZ(PCM-water). Energies/enthalpies in kcal/mol, distances in Å and angles in degrees (°).

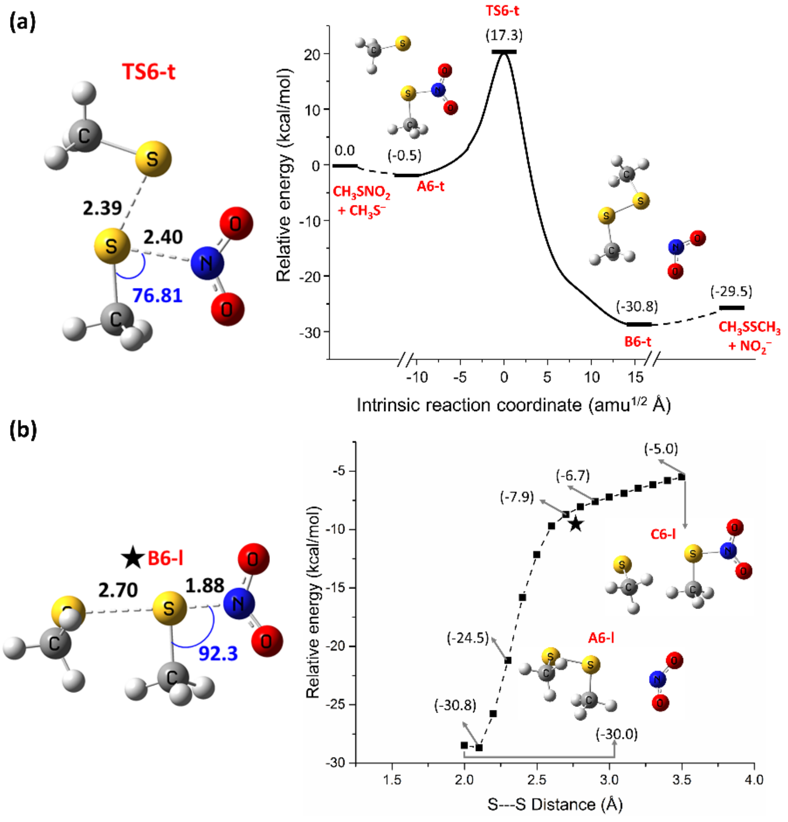

Figure 2.7: Modeling the reaction of CH_3SNO_2 with CH_3S^- where the nucleophile attacks from (a) top of the C–S–NO_2 plane (b) along the S–N bond. Note that panel (a) shows the IRC whereas panel (b) shows the relaxed PEC calculated for the S---S distance scan. See captions to Figure 2.2 and Figure 2.6 for details.

2.5. Discussion

2.5.1. S–N bond homolysis and concerted rearrangement in $RSNO_2$

Homolytic cleavage of the S–N bond in CH_3SNO_2 is unfavorable ($\Delta H^{\ddagger}_{\text{calc}}$ = 42.6 kcal/mol). The previously reported MP2/6-311+G** $\Delta H^{\ddagger}_{\text{calc}}$ values (33.3 kcal/mol)[112] and ROCCSD(T)//HF/6-311+G* (38.3 kcal/mol)[117] underestimate the stability of the S–N bond in CH_3SNO_2 as higher-level model chemistries predict higher activation enthalpies. The present gas-phase CCSD(T)//MP2/aug-cc-pVTZ calculations provide one of the best estimates of this barrier, which increases only slightly ($\Delta H^{\ddagger}_{\text{calc}}$ = 43.9 kcal/mol, Supporting Information Table S2.1) upon extension of the basis set to quadruple zeta quality. Hence the prohibitive computational cost of such calculations is not warranted. Notably, our $\Delta H^{\ddagger}_{\mathrm{calc}}$ for S–N bond homolysis in CH_3SNO_2 is 10 kcal/mol higher than that calculated with CCSD(T)-F12/CBS for the corresponding nitrosothiol, CH_3SNO ($\Delta H^{\ddagger}_{\mathrm{calc}}$ = 32.4 kcal/mol).[134] Also, an experimental $\Delta H^{\ddagger}$ of ~ 25 kcal/mol has been reported for S–N homolysis in *t*-BuSNO,[135] suggesting that RSNO are considerably more labile than $RSNO_2$, but a comprehensive experimental examination of their relative stabilities is lacking.

As reported previously,[56] the barrier for concerted rearrangement of CH_3SNO_2 ($\Delta H^{\ddagger}_{\mathrm{calc}}$ = 51.7 kcal/mol, Figure 2.3 and Supporting Information Table S2.1) is too high to be of biological significance. Hence, given the high barrier for CH_3SNO_2 homolysis, the biological relevance of CH_3SONO and $CH_3S(O)NO$ formation (Figure 2.1) also is questionable. Nonetheless, our ΔH_{calc} for the CH_3SONO intermediate (8.2 kcal/mol, Figure 2.3 and Supporting Information Table S2.1) is comparable to the MP2/6-311+G** value (7.5 kcal/mol).[112] CH_3SONO and $CH_3S(O)NO$ were previously found to be isoenergetic,[112] and we find a difference of ≤1.5 kcal/mol in their ΔH_{calc} values. For homolysis of the O–N or S–N bond to release $^{\bullet}NO$ and $CH_3S^{\bullet}$ (Figure 2.1), the reported MP2/6-311+G** $\Delta H^{\ddagger}_{\mathrm{calc}}$ is ~13 kcal/mol,[112] while we estimate $\Delta H^{\ddagger}_{\mathrm{calc}}$ ~ 6 kcal/mol (Figure 2.3), suggesting that NO release is energetically more favorable than previously reported. Thus, the high barriers for their formation combined with their low stability would explain why RSONO and RS(O)NO have not been isolated during $RSNO_2$ decomposition.[65,118] Overall, the high $\Delta H^{\ddagger}_{\mathrm{calc}}$ for homolysis and rearrangement suggest that $RSNO_2$ are stable at room temperature as reported for *t*-$BuSNO_2$. This compound decomposes only above 100° to give the disulfide (RSSR) and thiol-sulfonate ($RS(O_2)SR$).[61]

2.5.2. Hydrolysis and thiolysis of $RSNO_2$

$\Delta H^{\ddagger}_{calc}$ for gas-phase CH_3SNO_2 hydrolysis by one water (45.2 kcal/mol, Figure 2.4b) is ~3 kcal/mol higher than that for S–N bond homolysis (42.6 kcal/mol, Figure 2.3). However, adding three water molecules lowers the barrier to ~21 kcal/mol (Figure 2.5 and Table 2.3), making hydrolysis considerably more favorable than homolysis, and more in keeping with the experimentally observed half-life of ~10 min for *t*-$BuSNO_2$ in aqueous solution at neutral pH,[65] and alkaline hydrolysis of sterically protected Bpq-SNO_2 to the sulfenic acid within 10 min.[64] Examining the structures in Figures 2.4a,b and Figure 2.5, we notice that the transition states with one and two water molecules are highly strained with large deviations in the S–N bond length (0.5 and 0.6 Å) and C–S–N angle (-21 and +16 °) from the CH_3SNO_2 reactant (Figure 2.3), which would explain the high activation barriers. In contrast, the S–N bond and C–S–N angle in the transition state structures with 3 water molecules (Figure 2.5) deviate much less from their values in the CH_3SNO_2 reactant. Thus, reduced strain and reorganization significantly lower the $\Delta H^{\ddagger}_{calc}$ for hydrolysis (Table 2.3).

Notably, $\Delta H^{\ddagger}_{calc}$ (45 kcal/mol) for hydrolysis of the corresponding S-nitrosothiol, CH_3SNO, to HNO and CH_3SOH by two water molecules is ~8 kcal/mol [127] higher than that for CH_3SNO_2 hydrolysis (37 kcal/mol). Thus, the proposed sulfhydryl pathway for NO generation involving $RSNO_2$ reduction to RSNO[113,136] would be energetically more favorable if RSNO undergoes homolysis but not hydrolysis. Also, the experimentally observed depression of NO release from $GSNO_2$ in the presence of GSH[118] confirms that thiolysis competes with homolysis.

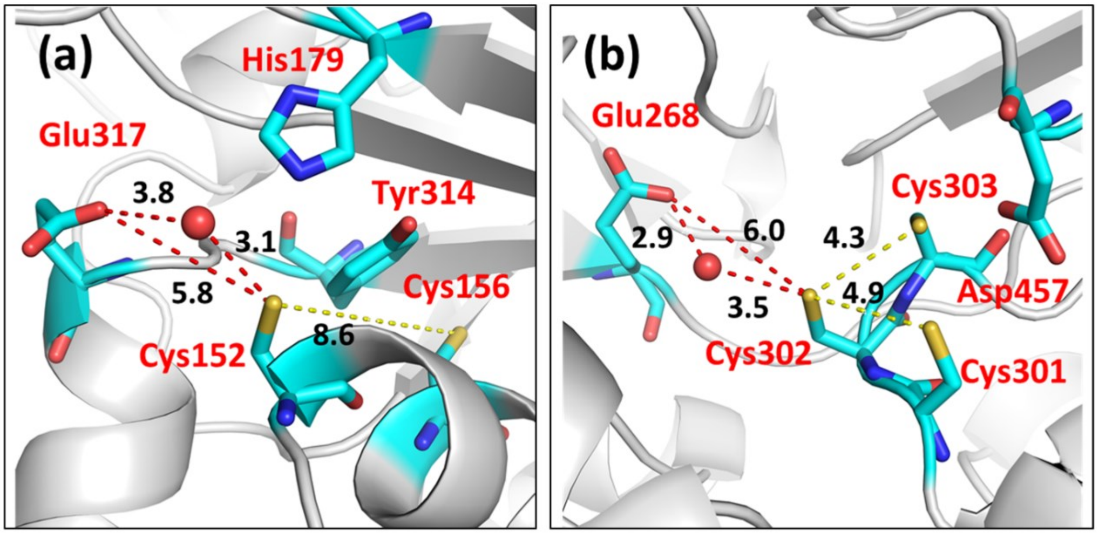

Figure 2.8: Active-site of GAPDH and ALDH2. (a) Catalytic Cys152 is converted to Cys–NO_2 on the reaction of GAPDH with GTN.[48] Glu317 is positioned to activate a water molecule for nucleophilic attack on Cys–NO_2 but Cys156 is too far away to attack Cys152. (b) Catalytic Cys302 is converted to Cys–NO_2 on the reaction of ALDH2 with GTN.[55] Either Cys301 or Cys303 is positioned to attack Cys–NO_2 and Glu268 also activates a water molecule for possible hydrolysis. Distances (black font) in Å.

The barrier is lowered further by top attack of OH^- or CH_3S^- on CH_3SNO_2 ($\Delta H^{\ddagger}_{\text{calc}}$ ~17 kcal/mol, Table 2.2). However, when the nucleophile attacks along the S–N bond, the activation energy dramatically decreases to 0 kcal/mol (Figure 2.6c and Figure 2.7b). Favorable electrostatic interaction between the nucleophile and the σ-hole on the CH_3SNO_2 sulfur atom gives rise to this somewhat unexpected barrierless pathway. Notably, the rapid decomposition of Bpq-SNO_2 in alkaline solution and its stability in aqueous acetic acid [64] corroborate barrierless hydrolysis by OH^- but not H_2O. The sulfenic acid produced on $RSNO_2$ hydrolysis is unstable and may undergo further reaction depending on the experimental conditions.[137]

2.5.3. Decomposition of E–Cys–NO_2 in GAPDH and ALDH2

NO_2^- release from E–Cys–NO_2 in GAPDH is likely catalyzed by a water molecule activated by conserved Glu317 at ~6 Å from the catalytic Cys152 (Figure 2.8a). Hence, based on our calculations, the barrier for NO_2^- release from E–Cys–NO_2 should fall within 0-21 kcal/mol depending on the extent of activation of the water molecule as well as its line of attack on the sulfur atom. The efficacy of GTN turnover by the Glu317Gln variant of GAPDH, which remains to be investigated, should indicate the importance of water activation.

The active-site of ALDH2 possesses three potential nucleophiles, Cys301, Cys303 and a water molecule activated by Glu268 (Figure 2.8b). ALDH2 variants with these residues singly, doubly or triply mutated exhibit significant loss of GTN denitrating activity,[58] indicating that all three residues are somehow involved in catalyzing NO_2^- release from GTN.

Both GAPDH and ALDH2 catalytically denitrate GTN in the presence of a reducing substrate (e.g., dithiothreitol). This will reduce the sulfenic acid or disulfide formed on nucleophilic attack on E–Cys–NO_2 (Figure 2.1) back to the thiol. Since ALDH2 turns over GTN (38 nmol min^{-1} mg^{-1})[138] 10-fold faster than GAPDH (2.6 nmol min^{-1} mg^{-1})[48] and our calculations uncover a barrierless pathway for NO_2^- release (Figure 2.6c and Figure 2.7b), we speculate that E–Cys–NO_2 formation may be rate limiting in the enzymes.

Rearrangement of E–Cys–NO_2 to sulfenyl nitrate with subsequent NO release (Figure 2.1) also has been proposed for ALDH2.[58] However, given the high barrier we find here for CH_3SNO_2 rearrangement ($\Delta H^{\ddagger}_{calc}$ ~52 kcal/mol, Figure 2.3), any ALDH2-catalyzed NO release, which is a minor pathway of GTN decomposition,[58] likely occurs via some undefined mechanism that remains to be unveiled by further investigation.

2.5.4. Benchmarking DFT for future QM/MM calculations.

The present quantum chemistry calculations provide insight into the $RSNO_2$ reactivity in the gas phase and in solvent. Since the protein environment at the active-site influences the activation barrier for E–Cys–NO_2 decomposition, quantum mechanics / molecular mechanics (QM/MM) calculations are underway to include neighboring residues in GAPDH (Figure 2.8a). To that effect, we compared the performance of computationally efficient density-functional theory in reproducing the geometry of CH_3SNO_2 calculated with MP2/aug-cc-pVTZ (Table 2.4). The S–N bond lengths calculated with B3LYP/6-311+G(d,p) and BLYP/6-311+G(2df,2pd) are close to its MP2/aug-cc-pVTZ counterpart but a smaller basis set tends to predict slightly longer S–N bonds. Comparison of the activation barriers for S–N bond homolysis, hydrolysis, reaction with OH^- and CH_3S^- with CCSD(T)//MP2/aug-cc-pVTZ values as reference data indicates that B3LYP/6-311+G(d,p) and BLYP/6-311+G(2df,2pd) reproduce acceptable activation barriers for these reaction pathways (Table 2.5). Thus, as the hybrid B3LYP model is computationally more intensive than BLYP, we consider BLYP/6-311+G(2df,2pd) to be the best compromise in terms of reliability and computational cost for further QM/MM investigations with large QM zones centered on the active-site and including relevant nearby residues.

Table 2.4. Selected gas-phase geometric parameters for CH_3SNO_2 calculated with different model chemistries

Model chemistry	Bond lengths (Å)			Angle (°)
	S–N	N–O1[a]	N–O2[a]	C–S–N
MP2/aug-cc-pVTZ	1.776	1.225	1.223	98.87
BLYP/6-311+G(2df,2pd)	1.860	1.229	1.229	100.1
BLYP/6-31+G(d,p)	1.877	1.238	1.239	99.75
B3LYP/6-311+G(d,p)	1.831	1.214	1.213	99.58

[a] See Figure 2.2 for the definition of O1 and O2.

Table 2.5. Activation barrier ($\Delta H^{\ddagger}_{calc}$, kcal/mol) for CH_3SNO_2 decomposition by homolysis, hydrolysis, reaction with OH^- and CH_3S^- calculated with different model chemistries

	Homolysis[a]	Hydrolysis by 3 H_2O (top)[a,b]	Attack by OH^- from top[b,c] or along S–N bond [c,d]	Attack by CH_3S^- from top [b,c]
CCSD(T)//MP2/aug-cc-pVTZ	42.6	20.9	16.7 (0)[d]	17.3
BLYP/6-311G+(2df,2pd)	35.0	18.2	13.5	12.5
BLYP/6-31+G(d,p)	33.9	14.9	12.3	11.4
B3LYP/6-311+G(d,p)	32.7	20.8	17.2 (0)[d]	17.4

[a] Activation barriers calculated in the gas phase.

[b] Attack from the top of the C-S-NO_2 plane (see caption to Figure 2.2).

[c] Activation barriers calculated in PCM-water.

[d] Attack along S–N bond is barrierless (0 kcal/mol)

2.6. Conclusions

CH_3SNO_2 is the smallest model compound representative of larger $RSNO_2$ such as protein-bound E–Cys–NO_2. From our investigations using high-level quantum chemistry calculations, we find that direct CH_3SNO_2 homolysis or its concerted rearrangement have prohibitively high barriers ($\Delta H^{\ddagger}_{calc}$ ~ 43 and 52 and kcal/mol, respectively, Figure 2.3). Hence, while facile S–O bond homolysis in CH_3SONO or S–N bond homolysis in $CH_3S(O)NO$ yield NO ($\Delta H^{\ddagger}_{calc}$ ~ 6 kcal/mol), the formation of these intermediates from CH_3SNO_2 is highly unfavorable. Therefore, NO release from $RSNO_2$ by mechanisms proposed in the literature (Figure 2.1)[52,56–58,113,116] is highly unlikely.

In contrast, hydrolysis or thiolysis of CH_3SNO_2 to release NO_2^- can be barrierless on attack by OH^- or CH_3S^-. This explains the aqueous instability of Bpq-SNO_2 at high but not low pH [64] and the experimental half-life (~10 min) of *t*-BuSNO_2 in neutral aqueous solution.[65] In sum, our findings from high-level quantum chemistry calculations are consistent with the low aqueous stability of thionitrates observed experimentally.

Decomposition of an enzyme-bound thionitrate, E-Cys-NO_2, may be close to barrierless if an activated water molecule and/or an activated cysteine is suitably positioned to attack the thionitrate sulfur atom. Thus, we speculate that the rate-limiting step in the catalysis of GTN denitration by GAPDH and ALDH2 is E-Cys-NO_2 formation. Our high-level quantum chemistry calculations will serve as a benchmark for QM/MM investigations of NO_2^- release from this intermediate, which will provide critical information on the biotransformation of GTN and other organic nitrates.

2.7. Supporting Information

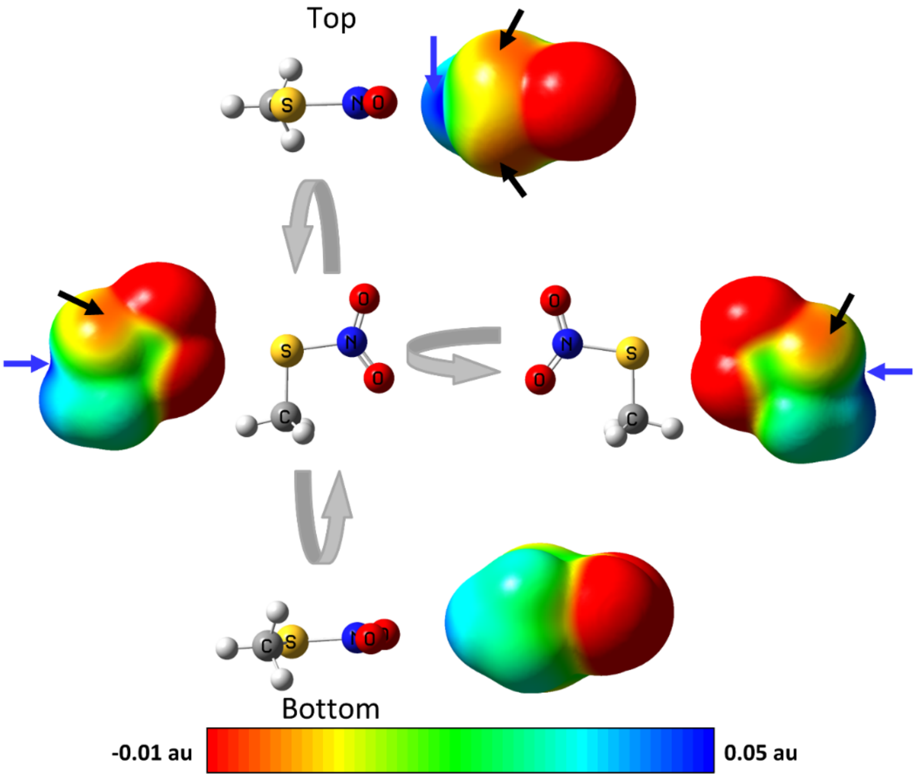

Figure S2.1: Electrostatic potential map of CH_3SNO_2 calculated with MP2/aug-cc-pVTZ. The grey arrows indicate rotation of the structure by 90° to give the top and bottom representations or by 180 ° to show the two orientations with the C–S–NO_2 plane in the page. The sulfur lone pairs (short black arrows) force nucleophilic attack in the C–S–NO_2 plane rather than perpendicular to this plane while the σ-hole on the sulfur atom (short blue arrow) favors attack by ionic nucleophiles along the S–N bond (Figure 2.6c and 2.7b of the main text). The electrostatic potential range is selected to highlight the lone pairs on sulfur.

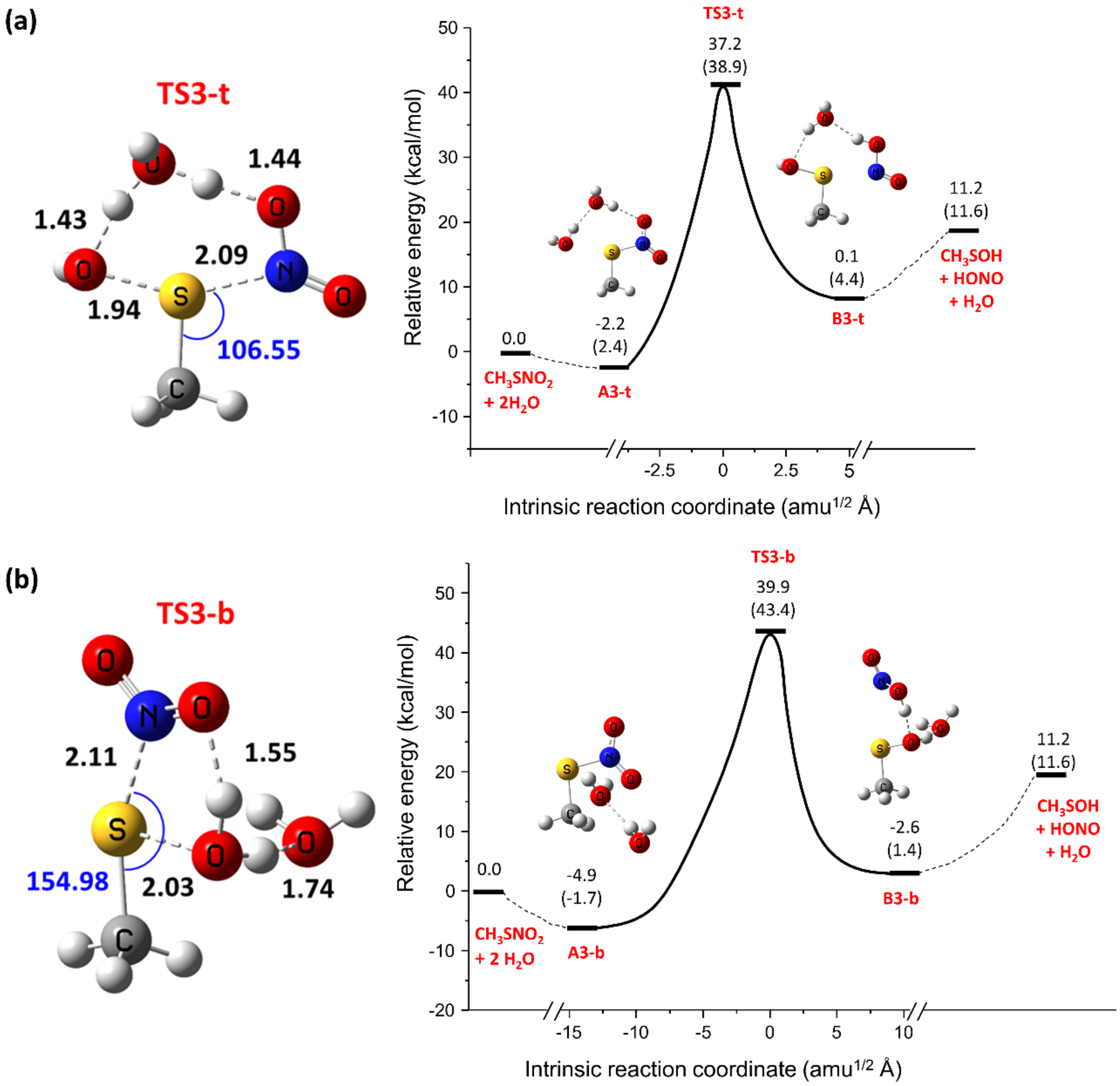

Figure S2.2: Modeling CH_3SNO_2 hydrolysis by two water molecules. Water attack from the (a) top and (b) bottom of the C–S–NO_2 plane of CH_3SNO_2 See captions to Figure 2.2 and Figure 2.3 of the main text for details.

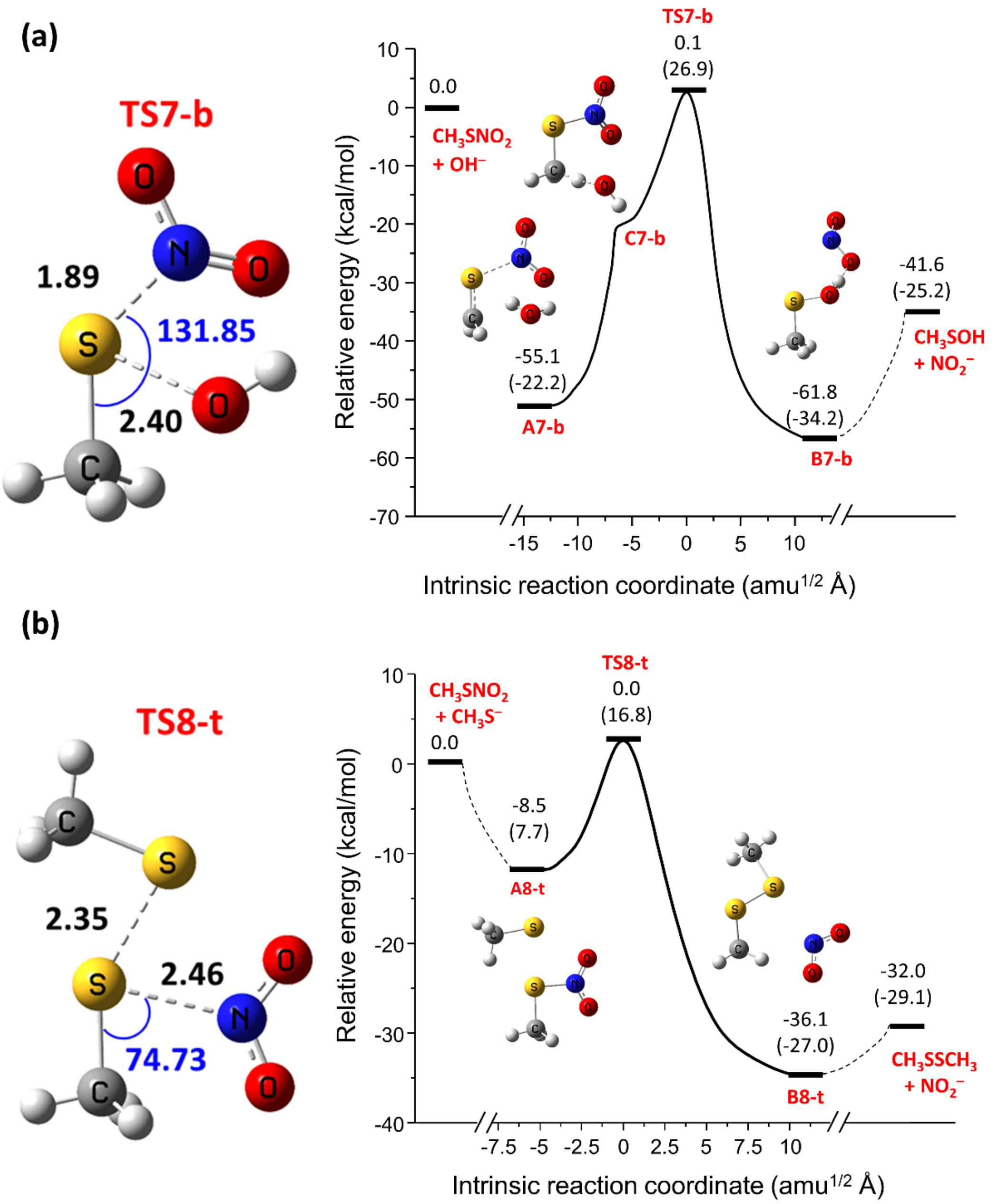

Figure S2.3: Modeling the gas-phase reaction of CH_3SNO_2 with OH^- and CH_3S^-. (a) The OH^- nucleophile attacks from the bottom* and (b) the CH_3S^- nucleophile attacks from the top.** See captions to Figure 2.2 and Figure 2.3 of the main text for details.

[*] The reaction profile for OH^- attack from the bottom of the C–S–NO_2 plane is shown along with selected molecular geometries. Panel (a) shows that this reaction is highly exothermic in the gas phase (ΔH_{calc} = -41.6 kcal/mol) and the pre- and post-reaction complexes separated by the transition state are dramatically

more stable in the gas-phase than in PCM-water (Figure 2.6b). A methyl hydrogen has been transferred to OH^- in pre-reaction complex A7-b, which is connected to TS7-b via a second intermediate complex (C7-b) where OH^- is now bound to a methyl hydrogen. OH^- has shifted to the sulfur atom in TS7-b, which promotes cleavage of the S–N bond to give the NO_2^- – CH_3SOH ion-molecule post-reaction complex, B7-b. While the gas-phase OH^-/CH_3SNO_2 reaction has a negligible $\Delta H^{\ddagger}_{calc}$ relative to the reactants (Table 2.2), the large $\Delta H^{\ddagger}_{calc}$ of 55.1 kcal/mol from the stable pre-reaction complex renders it unfavorable. The inclusion of implicit solvent shifts the entire reaction profile by ~20 kcal/mol, essentially the difference in the solvation free energy ($\Delta G_{solv,calc}$) of OH^- (–80.5 kcal/mol) and NO_2^- (–64.4 kcal/mol) in PCM-water (Table S2.7).

[**] Similar to the OH^-/CH_3SNO_2 reaction, the CH_3S^-/CH_3SNO_2 reaction in panel (b) also involves ionic species. Thus, the gas-phase profile reveals a highly exothermic reaction (ΔH_{calc} -29.5 kcal/mol) along with the pronounced stability of the pre- and post-reaction complexes and no activation barrier (ΔH_{calc} ~0 kcal/mol).

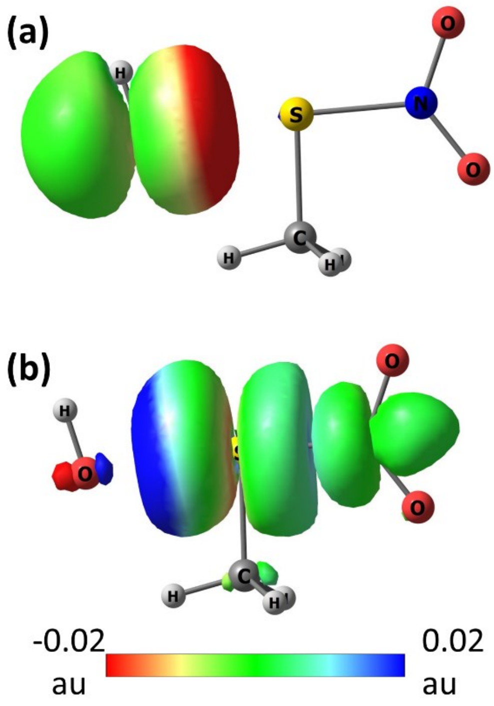

Figure S2.4: NBO interactions showing (a) donor orbital ($n(O_{OH^-})$) and (b) acceptor orbital (σ*(S–N)) of structure B5-l. $n(O_{OH^-})$ → σ*(S–N) NBO interaction with stabilization energy of 50 kcal/mol, which is absent in complexes A5-l and C5-l. Chemcraft was used to visualize the orbitals and NBO module was used for the calculations as implemented in Gaussian09.

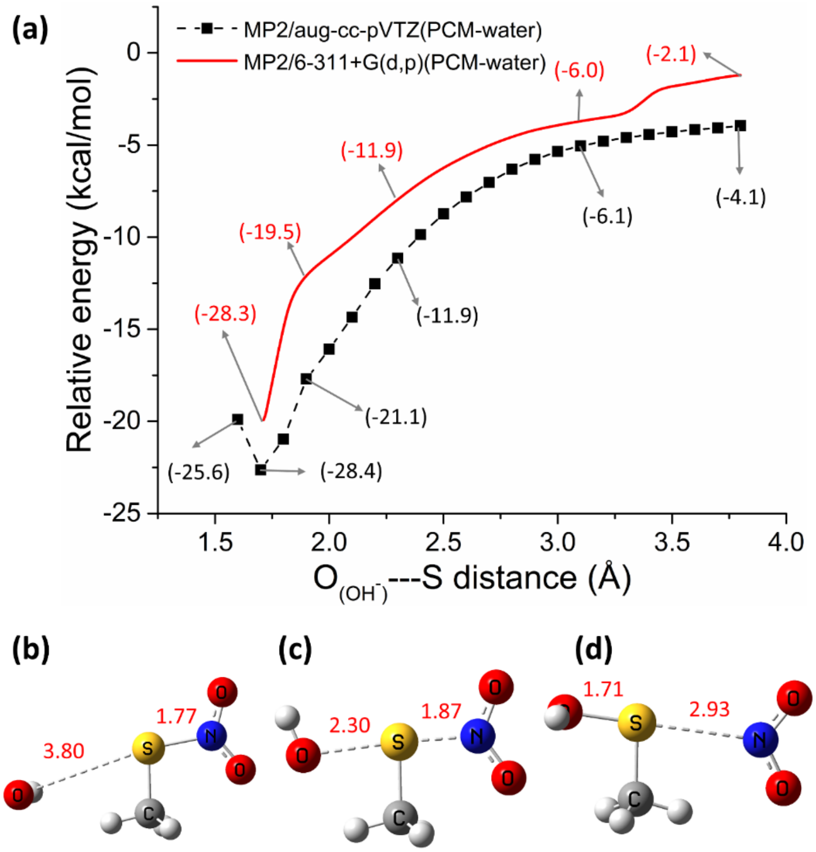

Figure S2.5: Reaction profile for the attack of OH^- along the S–N bond. (a) Potential energy curve calculated for OH^- attack along the S–N bond calculated with MP2/6-311+G(d,)(PCM-water) (red line) and selected constrained O(OH^-)---S distance with MP2/aug-cc-pVTZ(PCM-water) (black line). Indicated on the graph are ΔH_{calc} values calculated with CCSD(T)/aug-cc-pVTZ//MP2/6-311+G(d,p)(PCM-water) (red) and CCSD(T)//MP2/aug-cc-pVTZ(PCM-water) (black). The reaction profile shows the barrierless attack of OH^- along the S–N bond. The structures (b-d) represent the geometry of reaction coordinates with O(OH^-)---S distance (Å) of (b) 3.80 (c) 2.30 and (d) 1.71 calculated with MP2/6-311+G(d,p)(PCM-water).

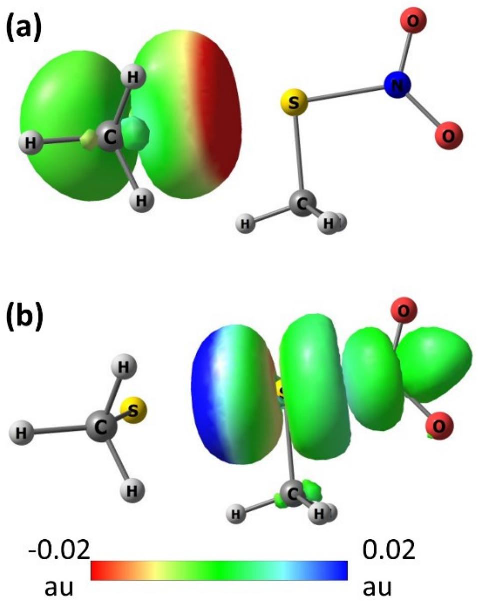

Figure S2.6: NBO interactions showing (a) donor orbital ($n(S_{CH_3S}^{-})$) and (b) acceptor orbital (σ*(S–N)) of structure B6-l. $n(S_{CH_3S}^{-}) \rightarrow \sigma^*(S\text{–}N)$ NBO interaction with stabilization energy of 42 kcal/mol, which is absent in complexes A6-l and C6-l. See caption to Figure S2.4.

Table S2.1. Relative enthalpies (ΔH_{calc} or $\Delta H^{\ddagger}_{calc}$ kcal/mol) for CH_3SNO_2 homolysis and concerted rearrangement [a]

	CH_3SNO_2	CH_3S• + •NO_2	TS1	CH_3SONO	$CH_3S(O)NO$	CH_3SO• + •NO
Gas phase[b]	0	42.6	51.7	8.2	7.0	13.8
PCM $\varepsilon=4$[c]	0	43.6	52.6	8.7	7.0	13.7
PCM $\varepsilon=30$[c]	0	44.2	53.0	9.0	6.8	13.6
PCM $\varepsilon=78.4$[c]	0	44.2	53.1	9.0	6.8	13.6
Gas phase[d]	0	43.9	52.0	8.0	6.8	12.4

[a] See Figure 2.3 of the main text for the reaction profile for CH_3SNO_2 homolysis and rearrangement to CH_3SONO and CH3S(O)NO. Geometries are optimized with MP2/aug-cc-pVTZ in the gas phase. The ΔH_{calc} (or $\Delta H^{\ddagger}_{calc}$ for TS) values are calculated with CCSD(T)//MP2/aug-cc-pVTZ except where indicated.

[b] ΔH_{calc} /$\Delta H^{\ddagger}_{calc}$ in the gas phase.

[c] ΔH_{calc} /$\Delta H^{\ddagger}_{calc}$ for the gas-phase optimized geometries in PCM solvent with dielectric constants (ε) for diethyl ether (4), methanol (30) and water (78.4).

[d] ΔH_{calc} /$\Delta H^{\ddagger}_{calc}$ calculated with CCSD(T)/aug-cc-pVQZ//MP2/aug-cc-pVTZ in the gas phase.

Table S2.2. Dipole moments (D) of all reactants, products, and complexes

Chemical species	Figure[a]	Gas phase[b]	PCM ε=4[c]	PCM ε=30[c]	PCM ε=78.4[c]
CH_3SNO_2	2.3	4.44	5.21	5.57	5.61
CH_3SONO	2.3	2.87	3.56	3.98	4.00
$CH_3S(O)NO$	2.3	3.55	4.28	4.67	4.96
$CH_3S\bullet$	2.3	1.73	2.04	2.19	2.21
$NO_2\bullet$	2.3	0.66	0.74	0.79	0.79
H_2O	2.4	1.99	2.18	2.27	2.28
HONO	2.4	2.30	2.60	2.74	2.76
CH_3SOH	2.4	2.15	2.51	2.71	2.73
$2H_2O$	2.5	2.65	2.81	2.87	2.88
OH^-	2.6	1.50	1.77	1.90	1.91
NO_2^-	2.6	0.67	0.78	0.85	0.85
CH_3S^-	2.7	3.53	4.38	4.82	4.87
CH_3SSCH_3	2.7	2.25	2.74	3.00	3.03
CH_3SNO_2–H_2O top TS2-t	2.2a	3.07	3.55	3.79	3.82
CH_3SNO_2–H_2O bottom TS2-b	2.2b	6.28	7.43	7.94	8.00
CH_3SNO_2–$2H_2O$ top TS3-t	2.5	4.95	5.81	6.20	6.24
CH_3SNO_2–$2H_2O$ bottom TS3-b	S2.2b	6.02	6.97	7.38	7.42
CH_3SNO_2–OH^- top TS5-t	2.6a	4.32	4.32	4.76	4.80
CH_3SNO_2–OH^- bottom TS5-b	2.6b	4.45	5.65	6.21	6.27
CH_3SNO_2–CH_3S^- top TS6-t	2.7	5.66	7.13	7.81	7.88
CH_3SNO_2–OH^- bottom TS7-b	S2.3a	4.47	5.54	6.07	6.13
CH_3SNO_2–CH_3S^- top TS8-t	S2.3b	5.90	7.30	7.96	8.04

[a] Figure in the main text that displays the structure of the chemical species.

[b] Dipole moments calculated with CCSD(T)//MP2/aug-cc-pVTZ in the gas phase.

[c] Dipole moments calculated with CCSD(T)//MP2/aug-cc-pVTZ for gas-phase geometries with solvent effects included using the PCM model with the dielectric constants (ε) of diethyl ether (4), methanol (30), and water (78.4).

Table S2.3. MP2/6-311+G** activation barriers ($\Delta H^{\ddagger}_{\mathrm{calc}}$, kcal/mol) for CH_3SNO_2 hydrolysis [a]

	1 H_2O top	1 H_2O bottom	2 H_2O top	2 H_2O bottom	3 H_2O top	4 H_2O top
Gas phase	56.6	51.3	45.7	46.0	26.7	28.0
PCM Ɛ=4	59.7	52.5	46.2	48.2	26.4	26.9
PCM Ɛ=30	60.9	52.9	46.3	49.0	26.3	26.6
PCM Ɛ=78.4	61.0	52.9	46.3	49.1	26.3	26.6

[a] $\Delta H^{\ddagger}_{\mathrm{calc}}$ calculated with MP2/6-311+G** for gas-phase geometries (less than 8% deviation in bond lengths compared to MP2/aug-cc-pVTZ). Solvent effects are included with the PCM model and the dielectric constants (ε) of diethyl ether (4), methanol (30), and water (78.4). The MP2/6-311+G** barriers overestimate their CCSD(T)//MP2/aug-cc-pVTZ counterparts by 6-7 kcal/mol; i.e., by 12, 16 and 20% for hydrolysis by 1, 2 and 3 water molecules, respectively. The CCSD(T)//MP2/aug-cc-pVTZ barriers for hydrolysis by 4 water molecules are thus estimated as 21-22 kcal/mol by scaling the MP2/6-311+G** data by 20%.

Table S2.4. Charge distribution in the CH_3SNO_2---OH^- complexes.[a]

	A5-l [b]	B5-l [b]	C5-l [b]
-S	0.522	0.503	0.472
-NO_2^-	-0.986	-0.610	-0.483
-CH_3	-0.099	-0.037	-0.005
-OH^-	-0.433	-0.857	-0.984

[a] The structures A5-l, B5-l, and C5-l are from the PEC calculated with MP2/aug-cc-pVTZ(PCM-water). The charges are calculated with the Natural Bond Orbital (NBO) module as implemented in Gaussian09.

[b] The $O_{(OH^-)}$---S distances are 1.6, 2.3 and 3.8 Å in A5-l, B5-l and C5-l structures, respectively. See Figure 2.6c for the structures.

Table S2.5. NBO interactions in the CH_3SNO_2, and CH_3SNO_2---OH^- complexes [a]

NBO interactions	CH_3SNO_2-----OH^-			CH_3SNO_2
	A5-l [b]	B5-l [b]	C5-l [b]	
***n*(O$_{OH^-}$) → σ*(S–N)**	-	**50**	-	-
n(O1) → σ*(S–N)	-	14	20	24
n(O2) → σ*(S–N)	-	18	25	29
n(O2) → σ*(N–O1)	-	-	-	28
n(O2) → σ*(N–O1)	192	28	29	-
n(O2) → π*(N–O1)	23	-	-	261
n(S) → π*(N–O1)	-	-	-	30
n(O1) → σ*(N–O2)	24	29	29	29
n(S) → σ*(N–O2)	-	06	05	04
n(O1) → π*(N–O2)	-	230	244	-
n(S) → π*(N–O2)	-	31	40	-
n(O$_{OH^-}$) → σ*(C–H)	-	-	10	-
n(O$_{OH^-}$) → σ*(S–C)	06	-	-	-
n(N) → σ*(S–O$_{OH^-}$)	05	-	-	-

[a] NBO interactions calculated using geometries optimized with MP2/aug-cc-pVTZ. We report the stabilization energies, $E^{(2)}$, of the NBO donor orbital → acceptor orbital pair with > 5 kcal/mol.

[b] The $O_{(OH^-)}$---S distances are 1.6, 2.3 and 3.8 Å in the A5-l, B5-l and C5-l structures, respectively. See Figure 2.6c for the structures.

Table S2.6. Charge distribution on CH_3SNO_2---CH_3S^- complexes [a]

	A6-l [b]	B6-l [b]	C6-l [b]
-S	0.054	0.402	0.488
-NO_2^-	-0.990	-0.593	-0.493
-CH_3	-0.047	-0.039	-0.020
- CH_3S^-	-0.018	-0.770	-0.975

[a] The structures A6-l, B6-l, and C6-l are from the PEC calculated with MP2/aug-cc-pVTZ(PCM-water) (Figure 2.7b). The charges are calculated with the NBO module as implemented in Gaussian09.

[b] The $S_{(CH_3S^-)}$---S distances are 2.1, 2.8 and 3.5 Å in A6-l, B6-l and C6-l structures, respectively. See Figure 2.7b.

Table S2.7. Solvation free energy ($\Delta G_{\mathrm{solv,calc}}$, kcal/mol) for CH_3SNO_2 homolysis, hydrolysis, and thiolysis[a]

Homolysis

	CH_3SNO_2	$CH_3S\bullet$	$\bullet NO_2$	TS1	CH_3SONO	$CH_3S(O)NO$	$CH_3SO\bullet$	$\bullet NO$
PCM Ɛ=4	-2.5	-1.1	-0.4	-1.6	-2.0	-2.6	-2.5	-0.2
PCM Ɛ=30	-3.7	-1.6	-0.6	-2.3	-2.9	-3.9	-3.6	-0.2
PCM Ɛ=78.4	-3.9	-1.7	-0.6	-2.4	-3.0	-4.0	-3.8	-0.2

Hydrolysis

	H_2O	2 H2O	CH_3SOH	HONO	TS2-t	TS2-b	TS3-t	TS3-b
PCM Ɛ=4	-2.7	-4.8	-2.3	-1.9	-2.3	-4.1	-6.1	-4.8
PCM Ɛ=30	-3.9	-6.8	-3.4	-2.8	-3.5	-6.2	-8.8	-7.0
PCM Ɛ=78.4	-4.0	-7.0	-3.6	-2.9	-3.6	-6.4	-9.1	-7.3

Reaction with OH^-

	OH^-	NO_2^-	TS4-b	TS5-t	TS5-b
PCM Ɛ=4	-60.5	-48.8	-42.4	-40.2	-41.9
PCM Ɛ=30	-78.8	-63.1	-56.2	-51.7	-54.4
PCM Ɛ=78.4	-80.5	-64.4	-57.6	-52.7	-55.5

Reaction with CH_3S^-

	CH_3S^-	CH_3SSCH_3	TS6-t	TS7-t
PCM Ɛ=4	-48.9	-1.5	-38.5	-38.9
PCM Ɛ=30	-64.7	-2.3	-51.1	-50.7
PCM Ɛ=78.4	-65.8	-2.4	-52.3	-51.8

[a] Calculated with CCSD(T)//MP2/aug-cc-pVTZ using the PCM model with the dielectric constants (ε) for diethyl ether (4), methanol (30), and water (78.4).

Chapter 3. Effects of Protonation on the Electronic Structure and Reactivity of Thionitrates: A Computational Investigation of CH_3SNO_2

3.1. Abstract

Thionitrates ($RSNO_2$), active intermediates in nitrate biochemistry, are shown to be stable in the presence of an acidic environment. Thus, we investigated the effect of protonation on the electronic structure and reactivity of CH_3SNO_2 as a model thionitrate. We show that the complex electronic structure of CH_3SNO_2 calculated with natural resonance theory (NRT) can be explained by three resonance structures with characteristics with a single S–N bond, a double S=N bond and S^----N^+ ionic structure. The contribution of the resonance structure with double S=N bond character (3 %) increases upon O-protonation (13 %), whereas the S^----N^+ structure (6 %) increases upon S-protonation (42 %). This explains the altered S–N bond stability of to homolysis (~ 43 kcal/mol) upon O-protonation (~ 90 kcal/mol) and S-protonation (~ 30 kcal/mol). Also, our study shows that O-protonation is more favorable, which stabilizes $RSNO_2$ them in an acidic environment.

3.2. Introduction

The interest in understanding the reactivity and stability of thionitrates ($RSNO_2$) spiked recently after they were proposed as active intermediates in organic nitrate decomposition.[54,113] Crystal structures of small aromatic thionitrates [63,64,115,124] and cysteine thionitrate (E-Cys-NO_2) in the triple variant of mitochondrial aldehyde-dehydrogenase (ALDH2) [55] indicate that $RSNO_2$ are stable. However, tert-butyl thionitrate (*t*-BuSNO_2) readily decomposes in neutral aqueous solution.[65] Hydrolysis in aqueous alkaline solution of the bowl-shaped aromatic thionitrate, Bpq-SNO_2, produces the sulfenic acid in 10 min at room temperature, whereas the reaction does not proceed even after 4 h with aqueous acetic acid in $CDCl_3$, or with aqueous tetrahydrofuran at room temperature.[64] Additionally, protonated glutathione thionitrate ($GSNO_2$) is resistant to decomposition at a collision energy of 25 eV in the electrospray ionization source of a mass spectrometer.[118] These reports suggest that the stability and reactivity of thionitrates change in different environments.

Protonation and deprotonation are fundamental steps in many chemical and biochemical reactions. Especially, the microenvironment provided by acidic or basic residues within a protein's active-site can change the pKa to protonate or deprotonate another residue. Moreover, the reactivity and stability of reaction intermediates are influenced by protonation or deprotonation. For example, the reactivity of E-Cys152-NO_2 in the active-site of glyceraldehyde-3-phosphate dehydrogenase (GAPDH) [48] could be altered if neighbouring His179 becomes protonated (See Chapter 2, Figure 2.8). Thus, studying the effects of protonation on $RSNO_2$ reactivity could provide insight into the stability of $RSNO_2$ in an acidic environment. The gas-phase proton affinity (PA), represented as a negative enthalpy change upon protonation, is used to express the ability of a molecule to accept a proton. *Ab initio* calculations are often used to predict gas-phase proton affinities due to difficulties in experimental measurement.[139–141]

The energetics of $RSNO_2$ decomposition pathways (Figure 2.1) indicate a very high activation barrier for homolysis,[65,112,117] but small activation barriers for hydrolysis and thiolysis are predicted by our computational study (Chapter 2). The reactivity of $RSNO_2$ are reported in various computational [56,112,117] and experimental [61,65,115,142] studies. However, there are no reports on the electronic structure of $RSNO_2$. Thus, we investigated their resonance structures using CH_3SNO_2 as a model compound. The effect of CH_3SNO_2 protonation on its resonance description is evaluated to reveal how an acidic environment might alter its reactivity. We further looked at the homolysis and hydrolysis of protonated isomers of CH_3SNO_2 to predict the changes in $RSNO_2$ decomposition at low pH.

3.3. Computational Methods

Molecular geometries of the reactants, products and transition states (TS) were optimized using second-order Møller-Plesset perturbation theory (MP2) [92,93,119,143,144] and the aug-cc-pVTZ augmented correlation-consistent basis set. [94] Vibrational analyses were performed to confirm the nature of the stationary points (energy minima, TS) and to estimate thermodynamic properties under the rigid rotor-harmonic oscillator approximation, [120] while Intrinsic Reaction Coordinate (IRC) [121,122] calculations were performed to unambiguously connect the TS to reactants and products. Electronic energies were further refined at the Coupled Cluster with Single, Double and perturbative linearized Triple excitations [CCSD(T)] [95,96] level of theory. Solvent effects were included implicitly with the Polarized Continuum Model (PCM) [97,98] and dielectric constants of 4, 30 and 78, representative of diethylether, methanol and water as solvents. The Gaussian09 [123] program was used for all calculations. Natural bond orbital (NBO) [145] and natural resonance theory

(NRT) [146–148] analyses were carried out using the NBO 5.0 program. [149,150] Wavefunctions for the optimized reactants, products, and TS were obtained using the MP2/aug-cc-pVTZ method. Bonding interactions were determined from computed electron densities, ρ(r), using the AIMAll program [151] within the Quantum Theory of Atoms in Molecules (QTAIM). [152,153] Atomic charges were determined using the NBO approach and AIMAll as implemented in Gaussian09.

3.4. Results

Our previous investigations into $HSNO_2$, CH_3SNO_2, *t*-$BuSNO_2$ and Cys-NO_2 indicate that sulfur is significantly less positive in $HSNO_2$ compared to $RSNO_2$ (R= Methyl, *tert*-Butyl, and Cysteine). Additionally, the H–S–N angle is 6-12 ° smaller than the R–S–N angle. Thus, CH_3SNO_2 is a minimal model compound to represent E-Cys-NO_2 (See Chapter 2).

There are three protonation sites in CH_3SNO_2, the two oxygen atoms ($CH_3SNO_2H^+$-1, $CH_3SNO_2H^+$-2) and the sulfur atom ($CH_3S(H)NO_2^+$) (Figure 3.1). The C-S-NO_2 atoms are in the same plane in CH_3SNO_2 (Figure 2.2) and its three-protonated forms. The H-atom in the O-protonated isomer is also in the same plane, whereas it is out of the plane in the S-protonated isomer. We have shown in Chapter 2, that the S–N, N–O1 and N–O2 bond lengths (Table 3.1) of CH_3SNO_2 calculated with MP2/aug-cc-pVTZ are in good agreement with the recently published crystal structure of bowl-shaped aromatic thionitrates. [64,124] O-protonation shortens the S–N bond to 1.676 Å ($CH_3SNO_2H^+$-1) and 1.678 Å ($CH_3SNO_2H^+$-2), which is close to the S=N bond length of ~1.5 Å,[154] whereas S-protonation lengthens the S–N bond to 2.298 Å. The lengthening of the S–N bond is consistent with the calculated NBO charges in $CH_3S(H)NO_2^+$ (Table 3.1), where the CH_3SH moiety has +0.7 charge, whereas NO_2 moiety has +0.3. Thus, it might partially behave as a CH_3SH^+ and NO_2. The charges on the sulfur atom become more positive in the O-protonated isomers (+0.690 and +0.678 in $CH_3SNO_2H^+$-1 and $CH_3SNO_2H^+$-2, respectively), whereas it does not change significantly upon S-protonation (Table 3.1). The changes in S–N bond length and charges on the sulfur and nitrogen atoms point towards different reactivities for the protonated isomers compared to CH_3SNO_2. The calculated proton affinities (PA) indicate that O2 ($CH_3SNO_2H^+$-2; PA=180.6 kcal/mol) possess the highest PA than $CH_3SNO_2H^+$-1 and $CH_3S(H)NO_2^+$ (Figure 3.1).

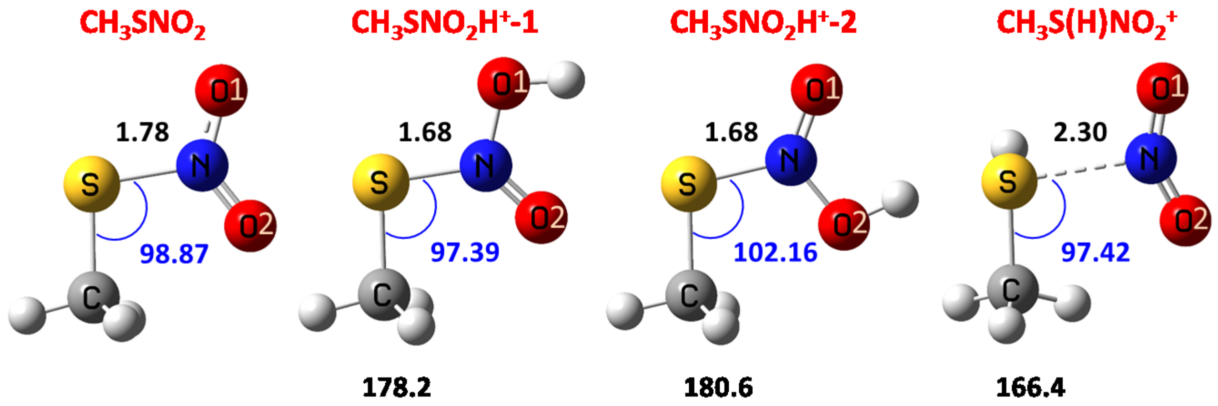

Figure 3.1. Geometries of CH_3SNO_2 and its protonated isomers. Optimized geometries for protonation of oxygen (O1) *trans* to the carbon atom ($CH_3SNO_2H^+$-1), oxygen (O2) *cis* to the carbon atom ($CH_3SNO_2H^+$-2) and sulfur ($CH_3S(H)NO_2^+$) are shown. Geometries were optimized with MP2/aug-cc-pVTZ in the gas phase. The proton affinities (PA; kcal/mol) calculated with CCSD(T)//MP2/aug-cc-pVTZ are reported under each protonated isomer.

Table 3.1. Geometric parameters and charge distribution for CH_3SNO_2 and its protonated isomers [a]

	Bond lengths (Å)			Angle (°)	Atomic partial charges			
	S–N	N–O1[b]	N–O2[b]	C–S–N	S	N	O1[b]	O2[b]
CH_3SNO_2	1.776	1.225	1.223	98.87	0.444	0.482	-0.438	-0.448
$CH_3SNO_2H^+$-1	1.676	1.339	1.206	97.39	0.690	0.407	-0.447	-0.234
$CH_3SNO_2H^+$-2	1.678	1.206	1.341	102.16	0.678	0.408	-0.216	-0.461
$CH_3S(H)NO_2^+$	2.298	1.175	1.176	97.42	0.491	0.743	-0.207	-0.233

[a] Geometries are optimized with MP2/aug-cc-pVTZ in the gas phase and partial charges calculated with the Natural Bond Orbital (NBO) module as implemented in Gaussian09.

[b] See Figure 3.1 for the definition of O1 and O2.

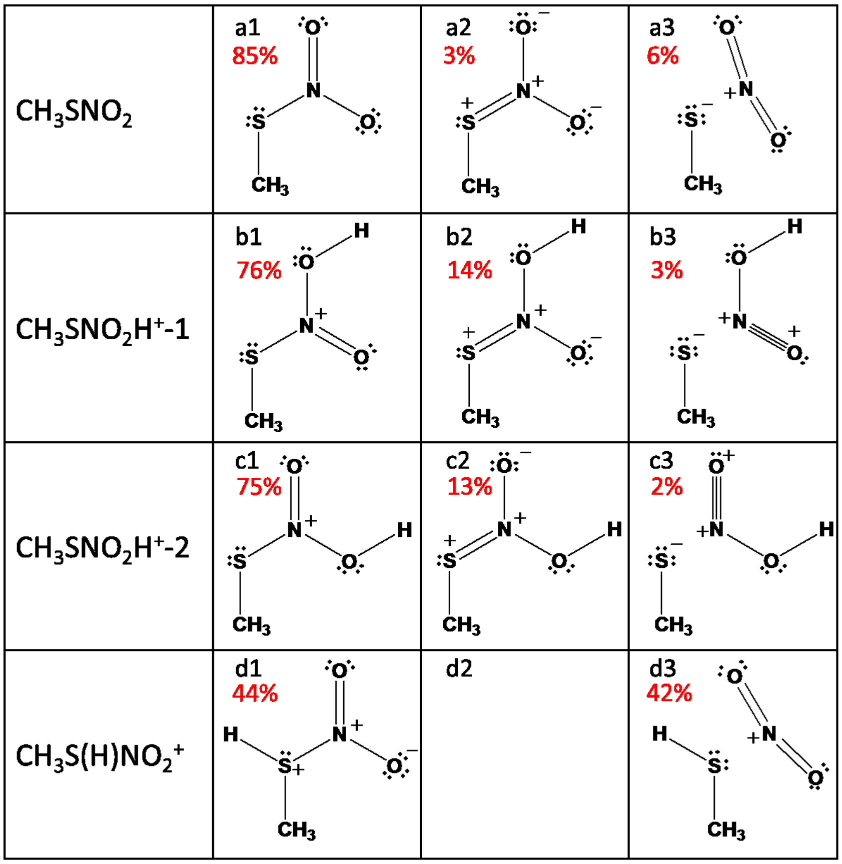

Figure 3.2. Resonance structures of CH_3SNO_2, $CH_3SNO_2H^+$-1, $CH_3SNO_2H^+$-2 and $CH_3S(H)NO_2^+$ calculated using NBO and NRT analyses with their associated resonance weights in percent. See Figure S3.2 for all resonance structures.

The most stable conformers of the O- and S-protonated isomers have the C–S–NO_2 atoms in the same plane as CH_3SNO_2. The activation barrier for rotation around the S–N bond of CH_3SNO_2 is 8 kcal/mol (See Chapter 2), which is smaller than the barrier for S–N bond rotation (≥ 10 kcal/mol) in RSNOs.[155] However, it is 13 and 10 kcal/mol for $CH_3SNO_2H^+$-1 and $CH_3SNO_2H^+$-2, respectively (Structure TN3 in Figure S3.1a). The less stable conformers of the O-protonated isomers are 4 (TN1) and 7 (TN2) kcal/mol higher in enthalpy than their respective stable conformers. The rotation barrier of 10 kcal/mol for the S–N bond of TN1 is expected due to S–N bond strengthening upon O-protonation. The high rotation barrier for the O-protonated isomers can force nucleophilic attack on the stable conformers but not in TN3. In contrast, the S-protonated isomer has a very small rotation barrier due to it weak S–N bond. Thus, nucleophilic attack could occur in either conformation shown in Figure S3.1b.

The S–N bond length changes significantly upon O- or S-protonation, influencing the resonance between the S–N, N–O1 and N–O2 bonds. NRT analysis of CH_3SNO_2 reveals three major resonance structures (a1, a2 and a3; Figure 3.2) based on the nature of the S–N bond. Resonance structure a1 (85% resonance weight) has a single S–N bond, a2 (3% resonance weight) with a double S=N bond and a3 (6% resonance weight) with no S----N bond. Structure a1 is a combination of a1-1 and a1-2 resonance structures (Figure S3.2) with a resonance weight of 43% and 42%. The resonance structures a1-1 and a1-2 arise from the NBO interaction between the lone pair of atom O2 to the π-antibonding orbital of N–O1 ($n_{O2}\rightarrow\pi^*_{NO1}$ interaction), giving rise to a strong stabilization of 261 kcal/mol that weakens N=O1 (Figure S3.2 and Table 3.2) and promotes N=O2 formation. In contrast, a2 (S=N, 3% resonance weight) arises from the $n_S\rightarrow\pi^*_{NO1}$ interactions with a stabilization energy of 30 kcal/mol. Similarly, $n_{O1}\rightarrow\sigma^*_{SN}$ (24 kcal/mol) and $n_{O2}\rightarrow\sigma^*_{SN}$ (29 kcal/mol) interactions weaken the S–N bond by contributing to a3 (S----N bond, 6% resonance weight) formation.

CH_3SNO_2 O-protonation to $CH_3SNO_2H^+$-1 and $CH_3SNO_2H^+$-2 leads to decreased resonance weight for the S–N bond structures with resonance weights of 76% (b1) and 75% (c1) (Figure 3.2), respectively from 85% in CH_3SNO_2. As expected, the resonance weight of the S=N bond increases to 14% (b2) and 13% (c2) due to strong stabilization of the $n_S\rightarrow\pi^*_{NO2}$ (90 kcal/mol, $CH_3SNO_2H^+$-1) and $n_S\rightarrow\pi^*_{NO1}$ interaction (86 kcal/mol, $CH_3SNO_2H^+$-2) compared to the CH_3SNO_2 (30 kcal/mol for $n_S\rightarrow\pi^*_{NO1}$) (Table 3.2). The increased resonance contribution of the S=N bond agrees well with the shorter S–N bond length in $CH_3SNO_2H^+$-1 and $CH_3SNO_2H^+$-2 compared to CH_3SNO_2 (Figure 3.1). In contrast, the S=N resonance contribution is 69% upon O-protonation to

CH_3SNOH^+ compared to 13% for CH_3SNO.[156] The decreased resonance weight of b3 and c3 to 3% compared to a3 (6%, CH_3SNO_2) is due to loss of the n_{O1}→σ*$_{SN}$ and n_{O1}→σ*$_{SN}$ interactions, respectively.

Table 3.2. Stabilization energies (kcal/mol) for NBO interactions in CH_3SNO_2, $CH_3SNO_2H^+$-1, $CH_3SNO_2H^+$-2, and $CH_3S(H)NO_2^+$ [a]

NBO interactions		CH_3SNO_2	$CH_3SNO_2H^+$-1	$CH_3SNO_2H^+$-2	$CH_3S(H)NO_2^+$
n(O1)	→ σ*(S–N)	24	-	21	126
n(O2)	→ σ*(S–N)	29	23	-	135
n(O2)	→ σ*(N–O1)	28	40	09	23
σ(S–N)	→ σ*(N–O1)	02	01	-	05
n(O2)	→ π*(N–O1)	261	-	57	281
n(S)	→ π*(N–O1)	30	-	86	-
n(O1)	→ σ*(N–O2)	29	10	42	24
n(S)	→ σ*(N–O2)	04	08	06	-
σ(S–N)	→ σ*(N–O2)	01	-	01	05
n(O1)	→ π*(N–O2)	-	58	-	-
n(S)	→ π*(N–O2)	-	90	-	-

[a] NBO interactions are calculated by NRT analysis on geometries optimized with MP2/aug-cc-pVTZ.

The resonance structure with a S–N bond (d1) decreases to 44% in $CH_3S(H)NO_2^+$ from 85% (a1) in CH_3SNO_2. Whereas, the resonance structure with no S----N bond (d3) increases to 42% from 6% (a3) in CH_3SNO_2 due to strong stabilization of NBO interactions like n_{O1}→σ*$_{SN}$ (126 kcal/mol) and n_{O2}→σ*$_{SN}$ (135 kcal/mol). Similarly, the resonance contribution for S----N increases for $CH_3S(H)NO^+$ (51%) compared to CH_3SNO (10%).[156] The dramatic increase in the resonance weight of d3 and a lack of resonance structures with S=N bond are consistent with the large S–N bond length in $CH_3S(H)NO_2^+$.

An analysis of the topology of the electron density of CH_3SNO_2 and its protonated isomers (Figure S3.3) supports the NBO findings. While the calculated QTAIM charges vary from the

NBO charges, they maintain a similar trend (Table 3.1 and Table 3.3). Upon O-protonation, the partial positive charge on the sulfur atom increases (i.e., this atom becomes more positive) by +0.430 and +0.423 for $CH_3SNO_2H^+$-1 and $CH_3SNO_2H^+$-2, respectively, with no significant changes observed upon S-protonation (Table S3.1).

Table 3.3. Electronic properties including electron density ($\rho_{S\text{-}N}$, e·Å^{-3}), bond ellipticity ($\varepsilon_{S\text{-}N}$), atomic partial charges (q, au) at the S-N bond critical point of CH_3SNO_2 and its protonated isomers [a, b]

	Electronic properties			
	$\rho_{S\text{-}N}$ [c]	$\varepsilon_{S\text{-}N}$ [d]	qS	qN
CH_3SNO_2	1.238	0.471	0.372	0.418
$CH_3SNO_2H^+$-1	1.357	0.955	0.802	0.181
$CH_3SNO_2H^+$-2	1.345	1.000	0.795	0.185
$CH_3S(H)NO_2^+$	0.480	0.111	0.346	0.753

[a] See Figure 3.1 for structures.

[b] Values are calculated with MP2/aug-cc-pVTZ using QTAIM.

[c] Electron density at the SN bond critical point ($\rho_{S\text{-}N}$).

[d] Bond ellipticity at the S–N bond ($\varepsilon_{S\text{-}N}$).

Table 3.4. Activation barriers (kcal/mol) for homolysis and hydrolysis of the protonated isomers of CH_3SNO_2 [a]

	Homolytic cleavage of S–N bond			Hydrolysis of $CH_3SNO_2H^+$-2
	$CH_3SNO_2H^+$-1	$CH_3SNO_2H^+$-2	$CH_3S(H)NO_2^+$	
Gas phase	91.1	88.7	29.6	29.9
PCM Ɛ=4	73.1	71.1	24.3	–
PCM Ɛ=30	69.7	67.8	23.1	–
PCM Ɛ=78.4	69.3	67.4	23.0	38.3, 38.7[b]
Gas phase	**92.5**[c]	**90.1**[c]	**29.8**[c]	**–**

[a] Activation barriers calculated with CCSD(T)//MP2/aug-cc-pVTZ (except where indicated) for the gas-phase geometries and solvent effects are included with PCM model and dielectric constants (ε) listed.

[b] Activation barrier calculated with CCSD(T)//MP/aug-cc-pVTZ(PCM-water).

[c] Activation barriers calculated with CCSD(T)/aug-cc-pVQZ//MP2/aug-cc-pVTZ in the gas phase.

As previously indicated, S-protonation weakens the S–N bond. This can be confirmed through electron density (ρ) as there is a known power law relationship between ρ and bond length.

Therefore, ρ provides a measure of the bond strength.[157,158] As expected, the short S–N bond upon O-protonation (Table 3.1) results in an increase in electron density at the S-N bond critical point ($\rho_{S\text{-}N}$) of 0.119 e·Å^{-3} and 0.107 e·Å^{-3} for $CH_3SNO_2H^+$-1 and $CH_3SNO_2H^+$-2, respectively. In contrast, the longer S–N bond upon S-protonation yields a lower $\rho_{S\text{-}N}$ of 0.480 e·Å^{-3} (Table S3.2). As later discussed, S-protonation sees a lowering of the activation energy for S–N cleavage (Table 3.4), which can be represented in a lowering of $\rho_{S\text{-}N}$.

Further electronic details can be obtained by examining the Hessian of ρ. The ellipticity at the bond critical point (ε_{BCP}), as denoted through the following equation $\varepsilon_{BCP} = [\lambda_1/\lambda_2 - 1]$, provides a measure of the accumulation of ρ in a given plane where λ_1 and λ_2 represent the negative curvature along the interatomic surface,[152] which indicates whether bonding has σ– or π–character (single or double bond). As such, it provides valuable insight into validating the π-character found from the NBO calculations and resonance weights from the NRT results. $\varepsilon_{S\text{-}N}$ values close to zero indicate a more cylindrical bond (single or triple bond character) and values close to one indicate a more elliptical bond (double bond character). CH_3SNO_2, with a large S-N single bond resonance contribution (85%), has a $\varepsilon_{S\text{-}N}$ of 0.471 (Table 3.3 and Table S3.2) which still captures the small S=N double bond resonance (as $\varepsilon_{S\text{-}N}$ is not 0). Upon O-protonation, $\varepsilon_{S\text{-}N}$ increases to 0.955 and 1.000 ($CH_3SNO_2H^+$-1 and -2, respectively) which is in line with the increase in the weighted resonance of S=N (Figure 3.2), although to varying degrees. Upon S-protonation, the double S=N bond resonance is lost and a significant decrease in bond ellipticity is observed ($\varepsilon_{S\text{-}N}$: 0.111).

Homolytic S–N bond cleavage of $CH_3SNO_2H^+$-1 and $CH_3SNO_2H^+$-2 to give CH_3S• and •$HONO^+$ has an activation barrier ($\Delta H^{\ddagger}_{calc}$) of 91.1 and 88.7 kcal/mol in the gas phase, respectively (Table 3.4). Further refinement of energies with quadruple zeta basis sets (aug-cc-pVQZ) changes $\Delta H^{\ddagger}_{calc}$ by only ~1 kcal/mol, indicating that the energies are converged in the triple zeta basis sets.

The $\Delta H^{‡}_{\text{calc}}$ values change significantly upon the implicit inclusion of solvent effects. In fact, the $\Delta H^{‡}_{\text{calc}}$ values decrease dramatically upon an increase in solvent polarity. This could be due to the stabilization of the ionic forms of the reactants, since we have shown for CH_3SNO_2 (Chapter 2). In Chapter 2, we have also observed that the inclusion of solvent effects with the gas-phase optimized geometries provides energetics close to those obtained with PCM-water optimized geometries (Figure 2.6, 2.7, and S2.3) . The gas-phase $\Delta H^{‡}_{\text{calc}}$ value for S–N bond homolytic cleavage in $CH_3S(H)NO_2^+$ to CH_3SH^{+}• and •NO_2 is 29.6 kcal/mol. The inclusion of solvent effects similarly affects the S-N bond homolytic cleavage in the $CH_3SNO_2H^+$ isomers. Overall, CH_3SNO_2 O- and S-protonation increases and decrease the activation barrier for S–N bond homolysis, respectively, which correlates well with the S–N bond length in the protonated isomers.

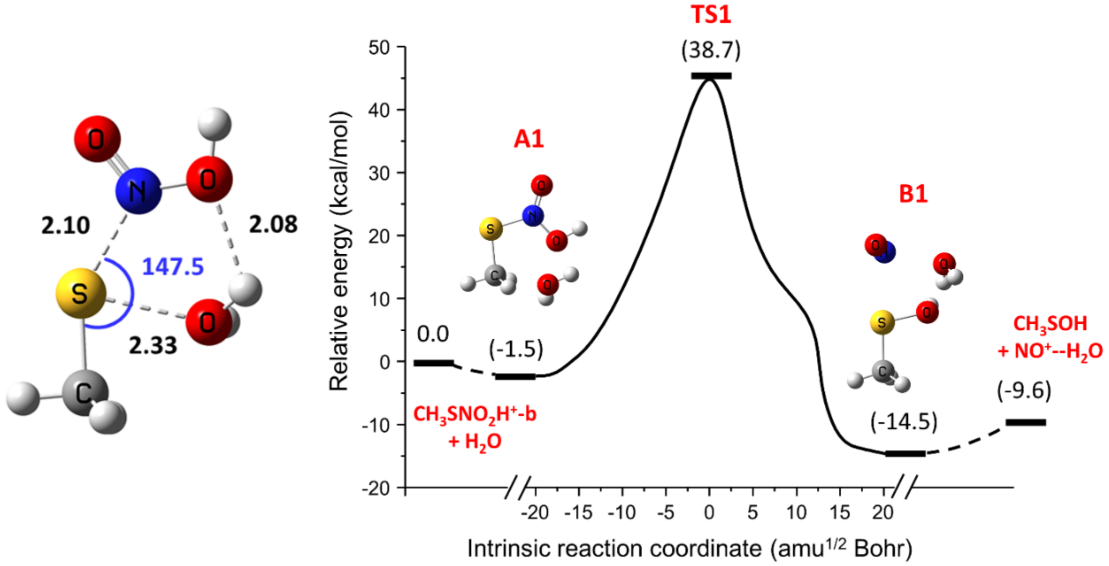

Figure 3.3. Reaction profile for hydrolysis of $CH_3SNO_2H^+$-2. Geometries were optimized with MP2/aug-cc-pVTZ(PCM-water). The relative enthalpies reported at each stationary point are calculated with CCSD(T)//MP2/aug-cc-pVTZ(PCM-water). Energies in kcal/mol, distances in Å and angles in degrees (°).

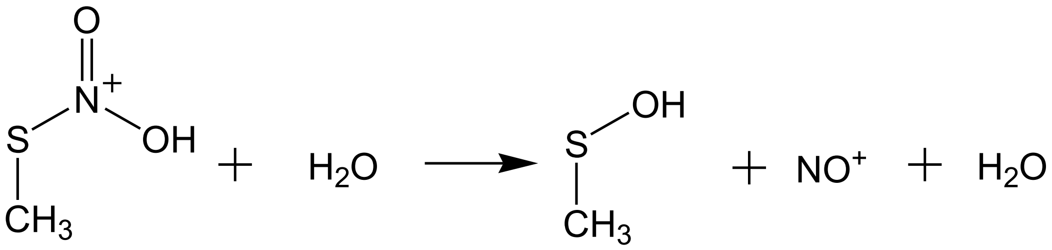

Scheme 1. Hydrolysis of $CH_3SNO_2H^+$-2.

The $\Delta H^{‡}_{calc}$ for heterolytic cleavage of $CH_3S(H)NO_2^+$ to $CH_3SH + NO_2^+$ is 29.4 kcal/mol in the gas phase and 12.3 kcal/mol with implicit inclusion of solvent using PCM-water due to better solvent stabilization of NO_2^+ compared to $CH_3S(H)NO_2^+$ ($\Delta G_{solv,calc}$ = -71.6 vs. -57.0 kcal/mol). Thus, heterolytic cleavage of $CH_3S(H)NO_2^+$ is energetically more favorable compared to homolytic cleavage. The $\Delta H^{‡}_{calc}$ for heterolytic cleavage of $CH_3S(H)NO_2^+$ to $CH_3SH^{2+} + NO_2^-$ is >100 kcal/mol, rendering it to be highly unfavorable.

Scheme 1 represents the pathway for hydrolysis of $CH_3SNO_2H^+$-2. The reaction profile in the gas-phase indicates that the TS is not connected to the correct reactants and products due to the ionic reactant (OH^-) (data not shown). A similar trend is observed in our previous study of thionitrate decomposition (Chapter 2, Figure S2.3). Thus, we calculated the reaction profile with the implicit inclusion of solvent effects using PCM-water. The reaction profile for the bottom attack of water on the sulfur atom (TS1) is characterized by pre- and post-reaction complexes, which are 1-5 kcal/mol more stable than the reactants and products, respectively. The TS1 exhibits an elongated S–N bond (2.10 Å) as well as initialization of S–O(water) bond formation (2.33 Å) (Figure 3.3), indicative of the precursor for the formation of the desired products ($CH_3SOH + NO^+$-H_2O). The reaction is exothermic by ~10 kcal/mol and $\Delta H^{‡}_{calc}$ is large at 38.7 kcal/mol (Figure 3.3 & Table 3.2). Overall, hydrolysis of $CH_3SNO_2H^+$-2 is energetically unfavorable with one water molecule but additional water molecules could lower the activation barrier as shown in Chapter 2 for CH_3SNO_2.

3.5. Discussion

O-protonation of CH_3SNO_2 at O2 ($CH_3SNO_2H^+$, 180.6 kcal/mol) leads to a strong S–N bond. The O2 atom of CH_3SNO_2 possesses the highest PA, which is slightly smaller than the PA of the O-atom of CH_3SNO (185.8 kcal/mol). By contrast, the S-protonation weakens the S–N bond and the S-atom has the highest PA in CH_3SNO (186.1 kcal/mol) [127] and the smallest in CH_3SNO_2 (166.4 kcal/mol). This properties correlate well with the observed the increase in CH_3SNO[127] decomposition and the increased stability of CH_3SNO_2 [64] in acidic aqueous environments.

We are interested in the decomposition of Cys-NO_2 formed at the catalytic Cys152 of GAPDH. Active-site His179 is protonated in glycolytically active form of GAPDH. Neutral histidine has a higher PA (~238 kcal/mol)[159] than the O-atom of CH_3SNO_2. Thus, E-Cys152-NO_2 in the GAPDH active-site might not extract a proton from His179. However, steric constraints in the active-site could force interaction between Cys152-NO_2 and protonated His179, which could stabilize/destabilize the thionitrate depending on whether the interaction occurs at the Cys152-NO_2 S or O atoms. We have proposed that the slow turnover of glyceryl trinitrate (GTN) by GAPDH (2.6 nmol min^{-1} mg^{-1}) [48] compared to ALDH2 (38 nmol min^{-1} mg^{-1}) [160] to be the lack of additional cysteine residues (Cys301 and Cys303 in ALDH2) to catalyze E-Cys-NO_2 (Cys152-NO_2 in GAPDH, Cys302-NO_2 in ALDH2). Although both proteins contain a glutamic residue (Glu317 in GAPDH, Glu268 in ALDH2) to catalyze E-Cys-NO_2 hydrolysis (Figure 2.8). Our current study reveals that protonated His179 may stabilize E-Cys-NO_2 in the GAPDH active-site and slowdown GTN decomposition by GAPDH.

The increased contribution of resonance structures with S=N (structures b2 and c2, Figure 3.2) to 13 % upon O-protonation (Figure 3.2) leads to a strong S–N bond, which increases $\Delta H^{\ddagger}_{\mathrm{calc}}$ for homolytic cleavage in both $CH_3SNO_2H^+$-1 and $CH_3SNO_2H^+$-2 (~90 kcal/mol, Table 3.2) compared to CH_3SNO_2 (~44 kcal/mol) (Chapter 2). This could explain the reported high stability of $GSNO_2$ in ESI–MS if $GSNO_2H^+$ forms in the ESI [118] since $CH_3S(H)NO_2^+$ does not have a resonance structure with S=N and the contribution to resonance structure with no S-N bond increases significantly (42% resonance weight). Thus, the S–N bond is elongated and enthalpy of homolytic cleavage is very small (~29 kcal/mol, Table 3.2).

Hydrolysis of $CH_3SNO_2H^+$-2 by one water molecule has a $\Delta H^{\ddagger}_{\mathrm{calc}}$ (38.7 kcal/mol) that is 10 kcal/mol smaller than the hydrolysis of CH_3SNO_2 by one water molecule ($\Delta H^{\ddagger}_{\mathrm{calc}}$ ~47 kcal/mol). The decrease in $\Delta H^{\ddagger}_{\mathrm{calc}}$ for $CH_3SNO_2H^+$-2 hydrolysis is due to the increase in S=N resonance contribution, which makes the S atom more positive (Table 3.1) and favors nucleophilic attack on this atom. Nonetheless, $\Delta H^{\ddagger}_{\mathrm{calc}}$ (38.7 kcal/mol) remains high but the addition of more water molecules might decrease this barrier as seen for hydrolysis of CH_3SNO_2 (Table 2.3). The resonance structure d1 with a single S–N bond contributes to the positive charge on the N atom of $CH_3S(H)NO_2^+$, which could favor the nucleophilic attacks at N atom in $CH_3S(H)NO_2^+$ compared to CH_3SNO_2. Also, protonation favors nucleophilic attack at S atom due to increase in positive chare at this atom.

3.6. Conclusions

We conclude that thionitrates ($RSNO_2$) can be represented by three major resonance structures. These resonance structures predict and rationalize $RSNO_2$ reactivity in different chemical environments. O–protonation of CH_3SNO_2 to $CH_3SNO_2H^+$ increases the stability of S–N bond, whereas S–protonation to $CH_3S(H)NO_2^+$ decreases its stability. Additionally, O-protonation and

S-protonation increase the positive charge of the S and N atoms, respectively, leading to increased reactivity towards nucleophiles.

3.7. Supporting Information

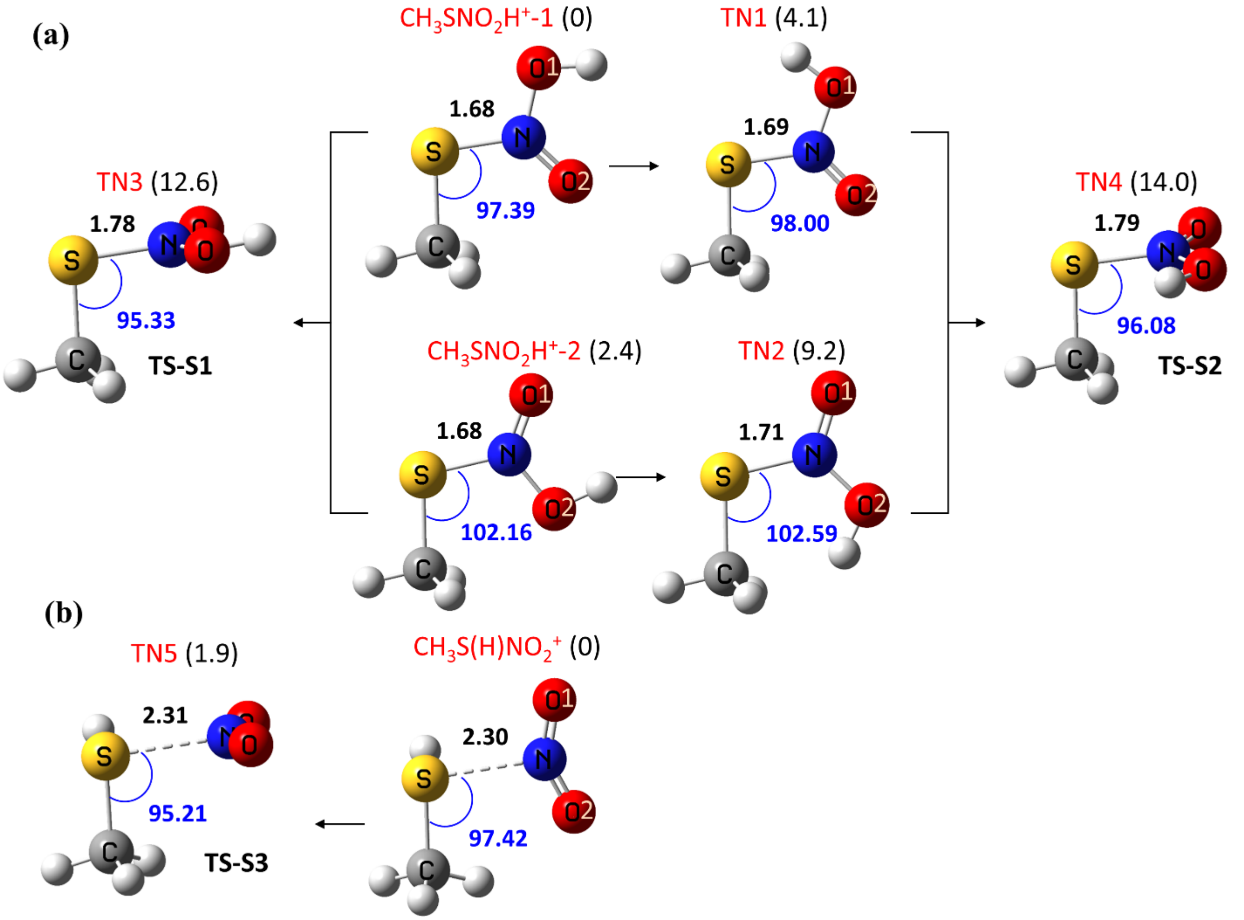

Figure S3.1. Geometries of conformers of (a) O- and (b) S-protonated CH_3SNO_2. See captions to Figure 3.1 of the main text for details. The values in parentheses represent ΔH_{calc} ($\Delta H^{\ddagger}_{calc}$ for TS) in kcal/mol calculated with CCSD(T)//MP2/aug-cc-pVTZ. All structures are minima except indicated as TS.

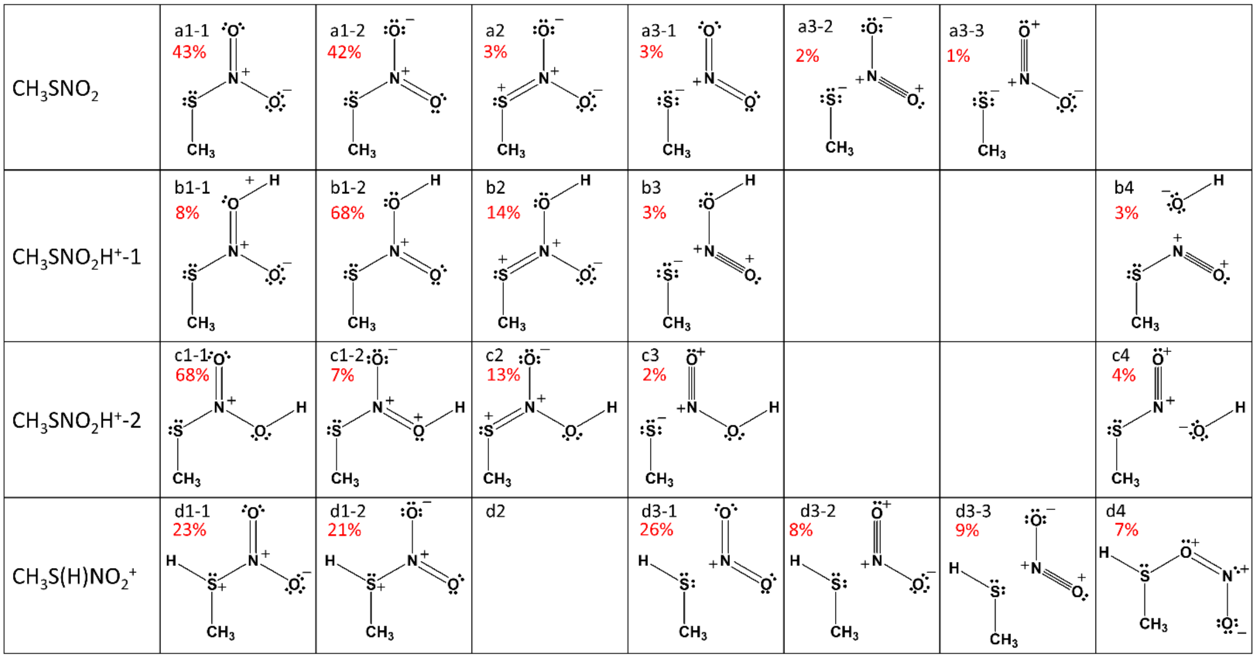

Figure S3.2. Resonance structures of CH_3SNO_2, $CH_3SNO_2H^+$-1, $CH_3SNO_2H^+$-2 and $CH_3S(H)NO_2^+$ with their associated resonance weights in percent. The resonance structures are calculated using NBO and NRT analyses.

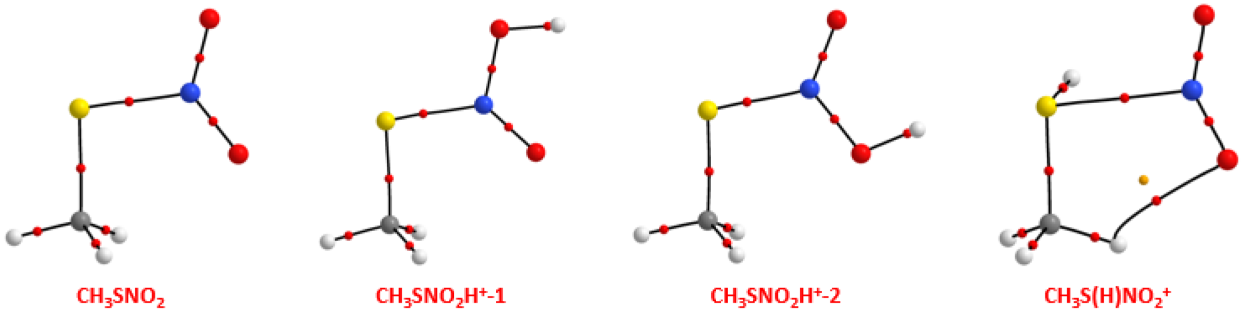

Figure S3.3. Molecular graphs of CH_3SNO_2, $CH_3SNO_2H^+$-1, $CH_3SNO_2H^+$-2 and $CH_3S(H)NO_2^+$. The molecular graphs are calculated using AIMAll from MP2/aug-cc-pVTZ optimized geometries. Atoms are represented by large spheres: carbon (grey), hydrogen (white), oxygen (red) and nitrogen (blue). Bond critical points are indicated by small red spheres, and ring critical points by small yellow spheres.

Table S3.1. QTAIM Atomic partial charges in model systems [a, b]

	Atomic partial charges			
	qS	qN	qO1[c]	qO2[c]
CH_3SNO_2	0.372	0.418	-0.432	-0.440
$CH_3SNO_2H^+$-1	0.802	0.181	-0.643	-0.293
TN1	0.694	0.232	-0.626	-0.256
$CH_3SNO_2H^+$-2	0.795	0.185	-0.277	-0.655
TN2	0.733	0.258	-0.236	-0.627
TN3	0.521	0.405	-0.235	-0.613
$CH_3S(H)NO_2^+$	0.346	0.753	-0.186	-0.203
TN5	0.329	0.761	-0.184	-0.194

[a] See Figure 3.1 and S3.1 for structures. [b] Values calculated with MP2/aug-cc-pVTZ using QTAIM.

[c] See Figure 3.1 for the definition of O1 and O2.

Table S3.2. Electronic properties (electron density [ρ_{BCP}, e·Å^{-3}], bond ellipticity [ε_{BCP}]) at the bond critical point of selected bonds in model systems [a, b]

	Bonding	Electronic properties	
		ρ_{BCP} [c]	ε_{BCP} [c]
CH_3SNO_2	S-N	1.238	0.471
$CH_3SNO_2H^+$-1	S-N	1.357	0.955
	O1-H	2.271	
	N-O1	2.554	
TN1	S-N	1.321	0.968
	O1-H	2.308	
	N-O1	2.544	
$CH_3SNO_2H^+$-2	S-N	1.345	0.999
	O2-H	2.264	
	N-O2	2.534	
TN2	S-N	1.295	1.064
	O2-H	2.330	
	N-O2	2.557	
TN3	S-N	1.097	0.564
	O-H	2.245	
	N-O	2.706	
$CH_3S(H)NO_2^+$	S-N	0.480	0.111
TN5	S-N	0.472	0.074

[a] See Figure 3.1 and S3.1 for structures.

[b] Values are calculated with MP2/aug-cc-pVTZ using QTAIM.

[c] ρ_{BCP} and ε_{BCP} values for the bond defined in the second column.

Chapter 4. NAD Cofactor Binding Alters the Dynamics of Human Glyceraldehyde-3-Phosphate Dehydrogenase (GAPDH) as Revealed by Multivariate Statistical Analysis and Molecular Dynamics Simulations

4.1. Abstract

Glyceraldehyde-3-phosphate dehydrogenase (GAPDH) is a well-known homotetrameric glycolytic enzyme. Each GAPDH subunit binds a nicotinamide adenine dinucleotide (NAD) cofactor. The cofactor in the oxidized (NAD^+) and reduced form (NADH) exhibits different binding affinity but binds with negative cooperativity. Removal of cofactor has been shown to affect the structure of the tetramer. Thus, we carried out molecular dynamics simulations of three forms of the tetramer GAPDH with NAD^+ (GAPDH-NAD^+) or NADH (GAPDH-NADH) and apo-GAPDH to investigate the effect of cofactor on tetramer dynamics. We show that the NAD-binding domains (NBDs) are more flexible and the adenine binding groove is open in apo-GAPDH compared to GAPDH-NAD^+ and GAPDH-NADH. Principal component analysis (PCA) of MD trajectories and normal mode analysis (NMA) of the crystal structure of GAPDH reveal an asymmetry in tetramer due to motions of the NBDs interacting across the R-axis, which is influenced by the S-loop. We show that interaction across the R-axis is important for negative cooperativity and explains how NAD^+ binds with negative cooperativity to GAPDH. We also show that GAPDH tetramer behaves as a dimer of OP and QR dimers. We also show that the reactivity of the catalytic Cys152 is influenced by NAD^+ binding. Overall, our findings shed light on the complex characteristics of the structural dynamics of GAPDH.

4.2. Introduction

Mammalian glyceraldehyde-3-phosphate dehydrogenase (GAPDH) is a homotetrameric enzyme composed of four 37-kDa subunits, O, P, Q, and R. Each subunit has a nicotinamide adenine dinucleotide (NAD) binding domain (NBD; residues 1-151 and 315-335) and a catalytic domain (CTD; residues 152-314) (Figure 4.1). Binding of the oxidized cofactor, NAD^+, promotes GAPDH tetramer formation,[71] but exhibits negative cooperativity such that the binding of the first NAD^+ ($K_1 = 1.4 \times 10^{-10}$ M) is followed by progressively weaker binding for the second ($K_2 = 3.8 \times 10^{-9}$ M), third ($K_3 = 1.0 \times 10^{-7}$ M) and fourth ($K_4 = 2.8 \times 10^{-6}$ M) cofactor.[68,69] The reduced cofactor, NADH, also binds to GAPDH with negative cooperativity but it binds less tightly (i.e., $K_{1,2} < 5.0 \times 10^{-7}$; $K_3 = 2.5 \times 10^{-6}$ M and K_4 5.0×10^{-5} M) than NAD^+,[70] and destabilizes the tetramer.[72,73] However, oxidation of the catalytic cysteine residue presumably to the sulfenic/sulfinic acid weakens GAPDH's affinity for NAD^+ ($K_{1,2,3,4} = 6.4 \times 10^{-5}$ M) and cooperativity is lost.[90] In contrast, NADH ($K_3 = 3.0 \times 10^{-8}$ and $K_4 = 7.0 \times 10^{-6}$ M) has higher affinity than NAD^+ for oxidized GAPDH.[90] Changes in the affinity of oxidized vs. reduced GAPDH for NAD (NAD^+ or NADH) are associated with conformational differences in the NBD on oxidation of catalytic Cys152.[90]

Cofactor removal gives apo-GAPDH, which for the yeast protein has ~ 7 % higher volume due to increased internal solvation compared to GAPDH with bound NAD^+ (GAPDH-NAD^+). This signals instability in apo-GAPDH,[161] which as demonstrated for rabbit muscle GAPDH has increased tendency to dissociate to the monomer and undergo slow aggregation.[71] The interactions between the O:R and P:Q subunits across the R-axis (Figure 4.1a) are weakened, and the S-loops (residues 181-205), [162,163] which partly cover the active-site and cofactor binding site (Figure 4.1b,c), are disordered for the apo form of *Cryptosporidium parvum* and Group B Streptococcus protein. The NBD is rotated by 4.8 ° relative to the CTD and the residues that bind NAD^+ are more flexible in apo-GAPDH of *Palinurus versicolor* and *Bacillus stearothermophilus*.[67,164] The crystal structure of GAPDH-NAD^+ from *Kluyveromyces marxianus* (radius of gyration 33.5 Å) is more compact than its apo-GAPDH (radius of gyration 34.6 Å).[165] This is consistent with reports that NAD^+ binding promotes tetramer formation.[71]

No computational studies on human GAPDH focus on the effect of NAD^+ or NADH binding on the dynamics of its sub-domains (NBDs and CTDs). However, molecular dynamics (MD) simulations evaluated changes in tetrameric *Trypanosoma cruzi* GAPDH after adding NAD^+ to the crystal structure of apo-GAPDH.[166] NAD^+ binding switches the apo-GAPDH tetramer to a closed conformation as monitored in this study by a decrease in the angle defined by the C_α atoms (*T. cruzi* residue numbering) of Gln91 (close to the adenine moiety), Glu336 (close to the nicotinamide ring) and Ser207 (middle of the S-loop).[166] This angle defines the movement of the S-loop towards and away from the NBD. The simulations also show that the NBD is more flexible than the CTD and a single NAD^+ fluctuates away from its binding site during 50 ns without causing noticeable changes in the dynamics of this subunit.[166] It is important to note that this simulation reports a single 50 ns MD simulation, without commenting on the reproducibility of the results.

The goal of this study is to investigate for the human enzyme cofactor-dependent subunit and subdomain (NBD and CTD) dynamics of the apo-GAPDH tetramer and the tetramer with NAD^+ (GAPDH-NAD^+) and NADH (GAPDH-NADH) bound. The only MD simulations of human GAPDH-NAD^+ focused on the active-site, in particular, the oxidation sensitivity of the catalytic Cys152. This study implicated Cys156 in controlling Cys152 oxidation indirectly by stabilizing H-bond donation from Tyr314 to Thr153, which is close to Cys152.[167] Importantly, Thr153 activates H_2O_2 for an attack on Cys152. Since the oxidation sensitivity of Cys152 is critical in

GAPDH activity, we examine here how NAD binding influences the relative orientations of Cys152, Cys156, Thr153, and Tyr314. Protozoan GAPDH has been proposed as a target to treat protozoan born disease due to the selectivity of human GAPDH vs. Trypanosomatid GAPDHs.[34–36,40,168] We thus compared the dynamics of a region that provides selectivity in human GAPDH with respect to inhibition of Trypanosomatid GAPDHs.

4.2.1. Overview of GAPDH structure

The GAPDH homotetramer contains subunit-O, -P, -Q and -R, which interact across the P-, Q- and R-axes as shown in Figure 4.1a-b. It has been proposed that the GAPDH homotetramer behaves as a dimer of dimers,[31,105] where dimers OP and QR (Figure 4.1b) located across the Q-axis act as two semi-independent dimers. Note that most inter-subunit interactions occur across the P-axis, between O:P and Q:R. There are also numerous interactions across the R-axis but much less across the Q-axis.[2] Each subunit has an NBD, a CTD, and an S-loop, which is at the tetramer interface (Figure 4.1b) and covers the dehydrogenase active-site and the nicotinamide binding of the cofactor. This moiety binds close to the catalytic Cys152, which is partially solvent exposed. The deprotonated Cys152 and protonated His179 are stabilized by a strong H-bond interaction (Figure 4.1c). Cys156 on the same helix as Cys152 is buried inside the protein matrix, which hinders disulfide bond formation between these two cysteines (Figure 4.1c).

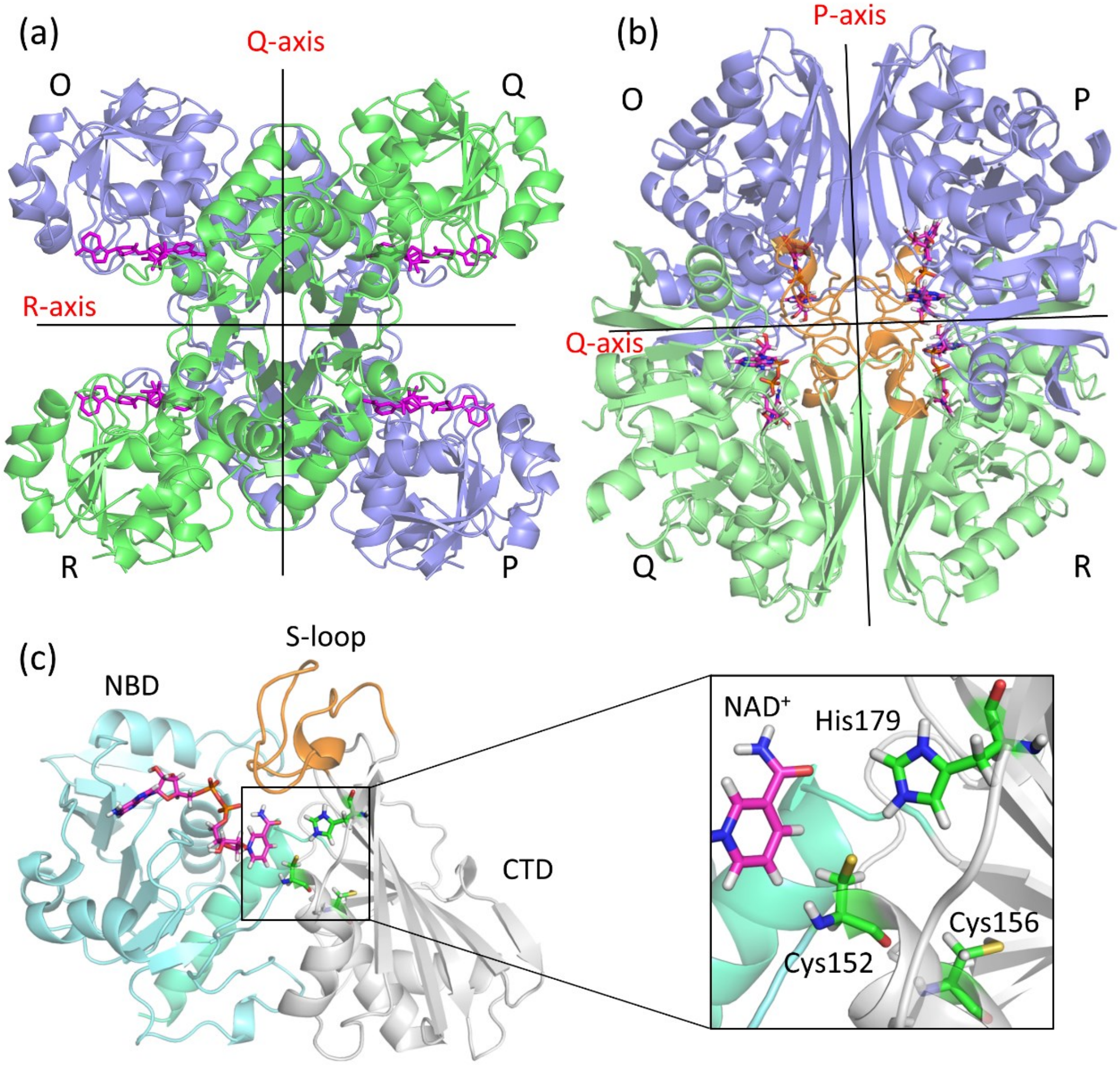

Figure 4.1. Structure of human GAPDH (PBD 1U8F). (a-b) The secondary structure of the GAPDH tetramer indicating the molecular axes defined relative to subunit-O. Subunit-P, -Q and -R interact with subunit-O across the P-, Q- and R-axis, respectively. There is a decreasing number of contacts across these axes in the order of P > R > Q. Note that the tetramer is a dimer of OP (blue) and QR (green) dimers with subunits interacting across the P-axis in each dimer. The cofactor NAD$^+$ of each subunit is shown as magenta sticks. (c) Subunit-O showing the NAD-binding domain (NBD; residues 1-151 and 315-335; cyan), catalytic domain (CTD; residues 152-314; grey) and the S-loop (residues 181-205; orange), which covers the active-site as well as the nicotinamide moiety of NAD$^+$. Inset: active-site residues Cys152, Cys156 and His179 in green sticks and the nicotinamide moiety of NAD$^+$ in magenta sticks.

4.2.2. NAD cofactor - polypeptide interactions in GAPDH

From the coordinates of human GAPDH (PDB 1U8F), we generated a 2D ligand plot using the Ligand Interaction Diagram module in Schrödinger Maestro 11.1 (Maestro, Schrödinger, LLC, New York, NY, 2017) to visualize the interactions of NAD^+ with its binding site (Figure 4.2). The NAD^+ molecule can be divided into three parts, the adenosine ribose group (away from the active-site), the phosphate groups (at the center), and nicotinamide ribose group (close to the active-site). It has been previously proposed that adenine moiety binds first to initiate the folding of the NBD and then the nicotinamide moiety binds to complete the folding of GAPDH.[2]

The adenine ring is buried in a hydrophobic pocket forming T-shaped π-π interactions with Phe37 and Phe102 on the other side of the adenine ring. The amino group of the adenosine points toward the protein matrix (Figure S4.1) and forms H-bond interaction with the backbone carbonyl of Arg80. The two hydroxyls of the adenosine ribose are directed towards the protein matrix and donate H-bonds to Asp35. The peptide N atoms of Arg13 and Ile14 donate H-bonds to the phosphate groups. The hydroxyl group of Ser122 donates a H-bond to the O atom of the ribose ring of the nicotinamide ribose.

The nicotinamide ring sits in a hydrophobic pocket but the nicotinamide ribose group is more exposed to the solvent. The nicotinamide amide points toward a polar groove and accepts an H-bond from Asn316. The cation-π interaction between N^+ of NAD and Tyr320 at a distance of 5.6 Å and its ionic interaction with the catalytic Cys152 thiolate at 5.6 Å holds the nicotinamide in place. Also, an indirect H-bond to the Glu317 via a bridged water molecule further stabilizes nicotinamide moiety at the active-site. The nicotinamide ribose ring forms an H-bond with Ser122 while its two hydroxyl groups point toward solvent. In contrast, adenine ribose ring points toward protein matrix with the hydroxyl groups forming H-bonds with Asp35. Similar to the ribose groups, the phosphate groups are partly solvent exposed and stabilized by H-bond interaction with Arg13 and Ile14. Overall, NAD$^+$ forms 11 H-bond interactions with water molecules and the NAD-binding site is partially open with solvent-exposed phosphate groups and ribose rings.

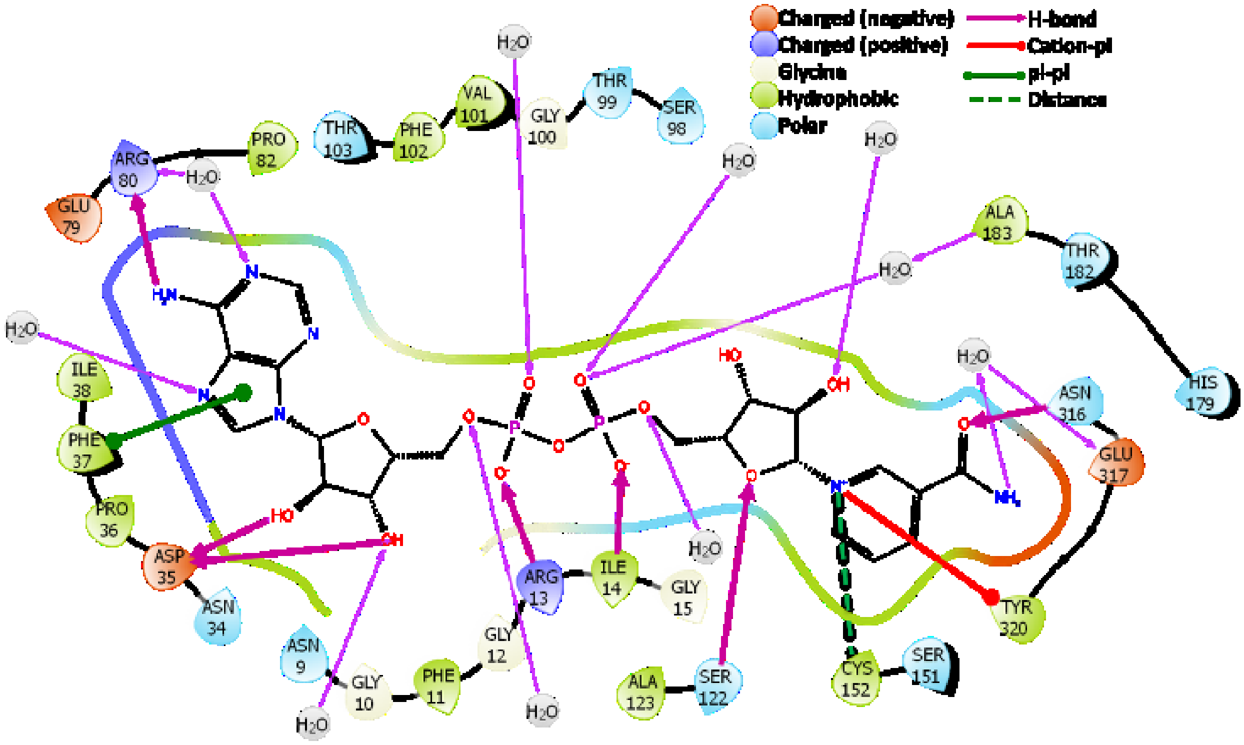

Figure 4.2. Interaction map of NAD$^+$ binding human GAPDH (PDB 1U8F). All possible interactions showing H-bond, cation-π, π-π, hydrophobic, polar interactions of NAD$^+$ with GAPDH. Thick and thin magenta lines indicate the interaction of NAD$^+$ with polypeptide (7 interactions) and water molecules (11 interactions), respectively. The distance (green dotted line) between S atom of Cys152 and positively charged N atom of NAD$^+$ is shown to highlight the ionic interaction between these two atoms. The 3D structural image of the NAD$^+$ interactions is shown in Figure S4.1 of the SI.

4.3. Computational Methods

4.3.1. Normal mode analysis (NMA) using the anisotropic network model (ANM)

NMA is an efficient method to predict large-scale motions of subdomains of a protein. NMA decomposes the global dynamics of a protein into a collection of normal modes corresponding to large motions of its subdomains. NMA was performed to visualize the backbone dynamics of NBD, CTD and the S-loop of human GAPDH. We focus on a few low frequencies/large amplitude modes that are expected to be relevant to function and remove random high-frequency modes.[169,170] We used the backbone atoms (C, Cα, N, O) and NAD$^+$ of the crystal structure of the human GAPDH tetramer (PBD 1U8F) after adding the coordinates of a fourth NAD$^+$ in subunit-O, which is in the apo-form in the crystal. [105]

NMA was performed using the ANM[102–104] of *ProDy*[171]. In ANM, the backbone atoms (i.e., nodes) within a cut-off distance of r_c are connected by elastic springs with a force constant γ and the molecular potential V(harmonic potential) is expressed as:

$$V = \frac{\gamma}{2}\sum_{j|j\neq i}^{M}(\Gamma_{ij})(R_{ij} - R_{ij}^0)^2$$

Here, M is the number of springs, $(R_{ij} - R_{ij}^0)$ the distance between nodes i and j with respect to the crystal structure, and Γ_{ij} is the element of the Kirchhoff matrix corresponding to the inter-residue contact between nodes i and j. The second derivative of V generates a 3N x 3N Hessian Matrix H, which is decomposed in 3N-6 nonzero λ_i eigenvalues and their corresponding eigenvectors μ_i.[171] The modes defined by the lowest frequencies describe functionally relevant motions of the protein and are analyzed here.[170,172]

4.3.2. Molecular dynamics (MD) simulations

All-atom MD simulations describe the motions and conformations of a system at the atomic level. MD simulations of a protein allow us to visualize the motions of residues that are sensitive to binding of a molecule (i.e. cofactor), the quaternary/tertiary structural changes, the motions of ions/water molecules and the stability of subdomains. We investigated the effect of cofactor on motions of subdomain and residues within the cofactor binding site and the active-site using MD simulations. In the crystal structure of human GAPDH (PBD 1U8F), subunit-O is in the apo form [105] so we superimposed subunit-P on subunit-O to copy the NAD^+ coordinates to the latter. We replaced NAD^+ with NADH by adding a hydride (H^-) to the positively charged N-atom of the nicotinamide moiety of each NAD^+ and apo-GAPDH was generated by removing the three NAD^+ from the crystal structure. The protonation states of the residue sidechains were assigned using PROPKA[173] and we manually deprotonated Cys152 and protonated His179 to form a strong H-bond interaction between these residues. Cys152 has pKa of 6.03 [88] in GAPDH-NAD^+ and we retained the Cys152-His179 H-bond interaction in GAPDH-NADH and apo-GAPDH.

The three forms of GAPDH were hydrated in a 10 Å-layer of TIP3P water from the protein boundary and 0.15 M Na^+ and Cl^- ions were added to represent physiological conditions. MD simulations were performed using the CHARMM27 [106,174] force field and NAMD2.9 [99] program. The system was subjected to 20,000 steps of conjugate gradient minimization and 1 ns of equilibration before production runs of 100 ns were carried out. Simulations were performed in the NPT ensemble at 300 K and 1 atm using Langevin dynamics and the time step was set to 2 fs. Five independent simulations of 100 ns (5 x 100 ns) were run for each form of GAPDH and the results were analyzed using VMD [175]. Good-Turing statistical analysis was carried out to analyze the convergence of the MD simulations trajectories.[176]

4.3.3. Principal component analysis (PCA)

Unlike NMA, the MD trajectories include nonharmonic movements of the residues and generate accessible conformational ensembles. However, the motions are highly multidimensional and include a large number of degrees of freedom. Multivariate statistical analysis such as PCA reduces the dimensionality of the data and extracts dominant motions from the MD trajectories.[177]

To carry out PCA, based on the C_α coordinates from the MD trajectories, the covariance matrix C is constructed:

$$\mathrm{C} = \langle(\mathrm{R} - \langle \mathrm{R}\rangle)(\mathrm{R} - \langle \mathrm{R}\rangle)^{\mathrm{T}}\rangle$$

R is the $3N$-dimensional configurational vector composed of instantaneous C_α coordinates of the N residues of the protein and $\langle \mathrm{R}\rangle$ is the average position over the trajectory. C is a $3N$ x $3N$ symmetric matrix that is diagonalized by orthogonal coordinate transformation T. The principal components (PCs) are derived from the eigenvalue decomposition of C:

$$\mathrm{C} = \sum_{i=1}^{3N} \sigma_i \mathrm{p}_i \mathrm{p}_i^T$$

Here p_i is the i^{th} PC (or eigenvector) and σ_i is the corresponding eigenvalue of matrix C. The PCs are ordered in descending order with respect to σ_i. The σ_i scale with the magnitude of the motion along p_i.[100,101] Thus, PC1 (p_1) and its variance σ_1 define the shape and size of the dominant motions of the C_α atoms of the protein over 5 x 100 ns MD trajectories in our analysis. Visualization of the PCA and ANM results were carried out using the Normal Mode Wizard (NMWiz)[171] of VMD.

4.4. Results

4.4.1. Convergence of the MD trajectories of GAPDH-NAD$^+$, GAPDH-NADH and apo-GAPDH

We carried out all-atom MD simulations of the three forms of GAPDH over 100 ns. Five replicates were obtained for each form of GAPDH. The convergence of each 100 ns MD simulations trajectories was evaluated using Good-Turing statistical analysis (Figure S4.2a). This approach reveals that the trajectories are converged after 50 ns. Also, the root-mean-square deviation

(RMSD) of the fluctuation of all C_α atoms from their reference crystal structure at each time point over 100 ns MD trajectories does not change significantly for each GAPDH form. Thus, the MD simulations are stable over 100 ns for the three forms of GAPDH (Figure S4.2b) so we used 100 ns MD simulations for further analysis.

Root mean square fluctuation (RMSF) of the C_α atoms from their reference crystal structure over a concatenated 5 x 100 ns MD trajectory reveals increasing subunit flexibility going from GAPDH-NAD$^+$ to GAPDH-NADH to apo-GAPDH (Figure 4.3). The atoms in the NBD and the S-loop are more flexible compared to those in the CTDs for the three forms of GAPDH. However, the subunits of GAPDH-NADH and apo-GAPDH show more variation than those of GAPDH-NAD$^+$. In contrast, the dynamics of the CTD are largely insensitive NAD$^+$ or NADH binding.

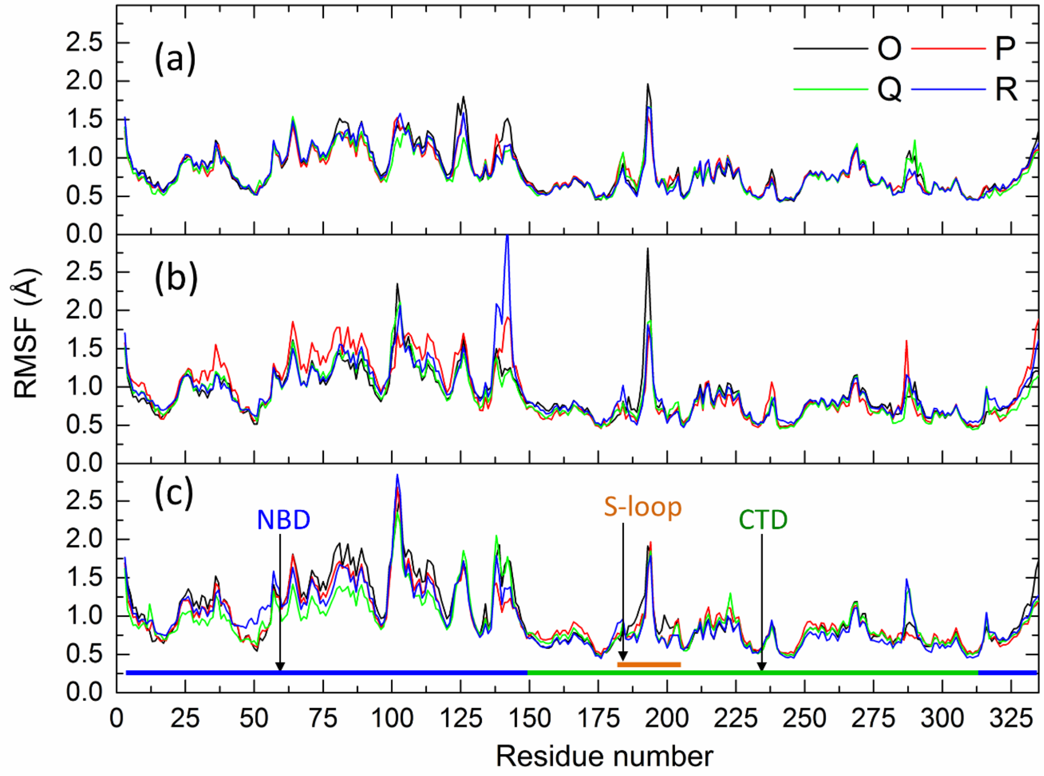

Figure 4.3. Root mean square fluctuations (RMSF) of the C_α atoms of (a) GAPDH-NAD$^+$, (b) GAPDH-NADH and (c) apo-GAPDH. RMSFs were calculated using a concatenated 5 x 100 ns MD trajectories.

4.4.2. Cross-correlation analysis (CCA) of C_α atoms of GAPDH from the MD simulations

CCA indicates whether the motions between two atoms are correlated, anticorrelated or noncorrelated. Thus, CCA shows how atoms move with respect to each other, highlighting the global motions of a protein. Correlated and anticorrelated motions reveal residues that move at the same time in the same and opposite directions, respectively. We carried out CCA using the MD trajectories and found no significant differences in the cross-correlated motions between GAPDH-NAD^+ and GAPDH-NADH (Figure 4.4a and Figure S4.3). However, the highly anticorrelated motions between subunits in GAPDH-NAD are clearly absent in apo-GAPDH (Figure 4.4b), This indicates that subunit motions in apo-GAPDH are not concerted motions and that concerted inter-subunit dynamics are lost on NAD removal.

Looking closely at the cross-correlated motions in GAPDH-NAD^+ reveals that subdomain NBD_O exhibit highly anticorrelated motions with subdomain CTD_P located across the P-axis (Figure 4.4a). Similarly, the NBD and CTD of subunits interacting across the P-axis and Q-axis show anticorrelated motions but noncorrelated motions between the NBDs of these subunits. However, there are anticorrelated motions between NBD_O and NBD_R interacting across R-axis, which indicates the NBDs move away from each other. Similar anticorrelated motions are also observed for NBD_P and NBD_Q of interacting across R-axis. The inter- and intra-subdomain motions between and within NBD and CTD of each subunit can be examined by inspection of the four squares at the diagonal. The bottom and top corner of the square at the diagonal represents the NBD and the CTD, respectively (Figure 4.4a). There are mostly noncorrelated motions between NBD and CTD (inter-subdomain) but highly correlated motions within themselves (intra-subdomain).

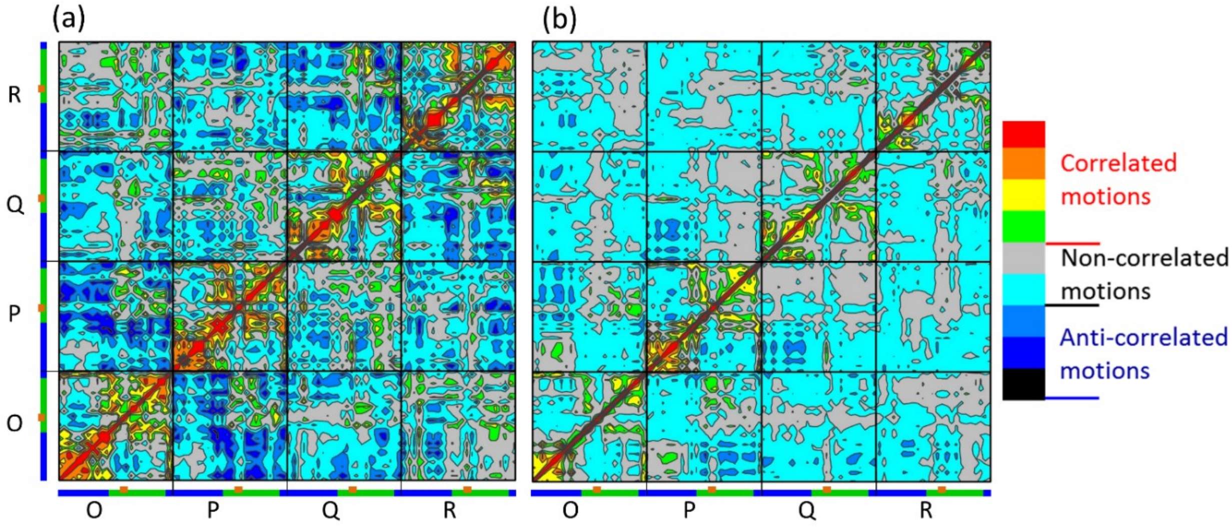

Figure 4.4. CCA of the Cα atoms of (a) GAPDH-NAD$^+$ and (b) apo-GAPDH. CCA is carried out using the C_α atoms of concatenated 5 x 100 ns MD simulations trajectories. Each square represents a subunit and the diagonals show the correlated motions of each Cα atom with itself. The blue, green and orange lines at the axes indicate NBD, CTD and S-loop of each subunit, respectively. Note that similar cross-correlated motions are seen for GAPDH-NAD$^+$ and GAPDH-NADH (See Figure S4.3).

4.4.3. CCA of the motions of NAD$^+$ and backbone atoms from the NMA of the crystal structure of GAPDH-NAD$^+$

A significant amount of information about dynamics, allostery, and mechanism can be extracted from protein crystal structures using NMA, which allows the global motions of a protein to be extracted from changes in the x-ray coordinates by applying harmonic forces.[172] However, NMA, unlike MD simulations, does not include anharmonic fluctuations and is computationally less expensive. CCA analysis based on the results of NMA will give us an overview of how large or global motions of the backbone atoms of a subunit influence the motions of another subunit. CCA of the GAPDH-NAD$^+$ crystal structure calculated from NMA (Figure S4.4a) reveals similar cross-correlated motions between subdomains (NBD and CTD) as shown by CCA of the MD simulations trajectories (Figure 4.4a). This confirms that the 5 x 100 ns MD simulations capture most of the global motions of the subunits.

Cofactor NAD^+ is essential for the dehydrogenase activity of GAPDH. Thus, we also visualized cross-correlated motions of NAD^+ with the backbone atoms of the protein (Figure S4.4 and Figure 4.5). The motions of NAD^+ are highly correlated with the backbone atoms of its own NBD and weakly correlated with its own CTD (Figure S4.4b). We note that NAD^+_O and NAD^+_R exhibit highly anticorrelated motions with NBDs interacting across the R-axis, as shown in Figure 4.5a. In contrast, NAD^+_P and NAD^+_Q bound to the less flexible NBDs show less correlated and anticorrelated motions within their own subunit and subunits interacting across the R-axis (Figure 4.5b and S4b-f). Here again, there is less cross-correlation between NBD backbone motions and NAD^+ bound in the more flexible NBDs. Additionally, motions of NBDs interacting across the P- and Q-axes are noncorrelated with motions of NAD^+ in the opposite subunits (Figure S4.4b-f).

Overall, the motions of NAD^+ are weakly correlated with the CTD of its own subunit and non-correlated with the CTDs of other subunits (Figure 4.5a,b and Figure S4.4b-f). However, exceptions are the highly anticorrelated motions of NAD^+_O with residues 153-173 and 213-229 of the CTD_P and the correlated motions with the S-$loop_Q$ and S-$loop_R$ (Figure 4.5 and Figure S4.4b-f).

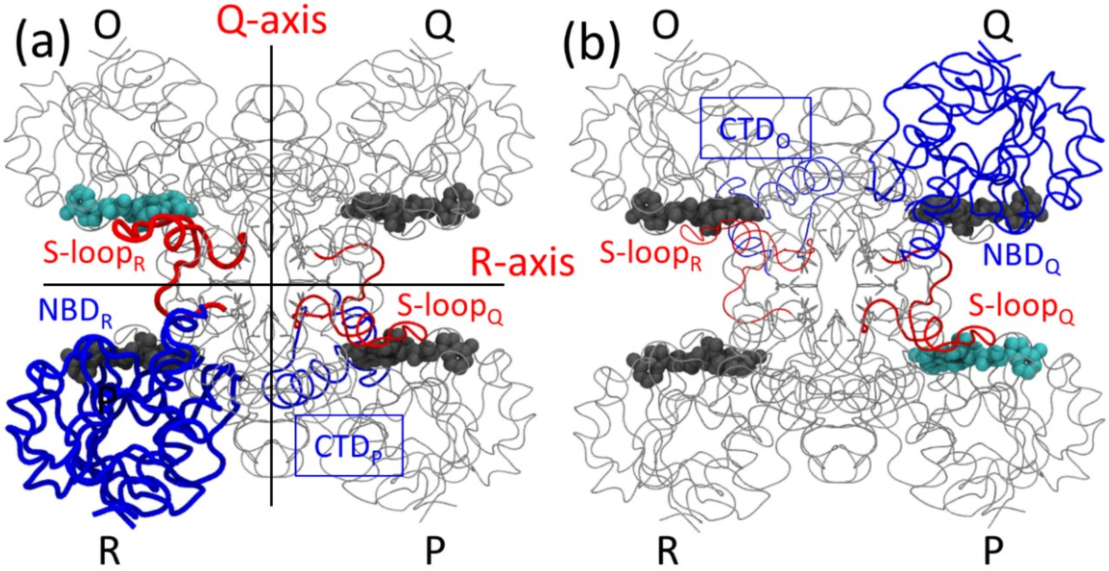

Figure 4.5. Cross-correlation analysis (CCA) of protein backbone atoms (N, C_α, C, O) with NAD^+ calculated using NMA. Correlated (red tube) and anticorrelated (blue tube) motions of (a) NAD^+_O (cyan spheres) (b) NAD^+_P (cyan spheres) with backbone atoms of other subunits. Note that we show cross-correlated motions of NAD^+ with other subunits only. NAD^+ has highly correlated motions with backbone atoms of its own subunit (i.e. NAD^+_O with backbone atoms of subunit-O, See Figure S4.4b). NAD^+_O has anticorrelated motions with NBD_R and residues 153-173 and 213-229 of CTD_P but correlated motions with backbone atoms of S-loop$_R$ and S-loop$_Q$. S-loop$_O$ and S-loop$_P$ are non-correlated with NAD^+_O and appear as thin grey lines like another backbone in the image. The cross-correlated motions of NAD^+_P, NAD^+_Q and NAD^+_R with backbone atoms of other subunits are identical to NAD^+_O but there are more motions in subunit-O and -R (thick tubes) compared to subunit-P and -Q (thin tubes) (Figure S4.4b-f). Plots of cross-correlated motions of all NAD^+ are shown in Figure S4.4b-f.

4.4.4. PCA of the MD trajectories of GAPDH-NAD$^+$, GAPDH-NADH, and apo-GAPDH

It has been shown that global protein dynamics can be described by a low number of collective degrees of freedom.[178] Thus, filtering the main modes of collective motions from local fluctuations could be used to separate functionally relevant motions from random fluctuations. PCA separates dominant persistent motion from random motion during MD trajectories. The principal components with the highest eigenvalues describe the main modes that could be functionally important.[172,177]

PCA of 5 x 100 ns concatenated MD trajectories of the three forms of GAPDH was carried out and the free energy landscape (FEL) was plotted to visualize the conformational sampling of each form. FEL is a plot of two variables derived from the MD trajectories (e.g., principal components, RMSD, radius of gyration, torsion angle, etc.) vs. the free energy. The free energy is estimated from the probability distribution of the frequency of each variable. Thus, the FEL identifies the relative population of two conformational states. The FEL calculated using PC1 and PC2 (Figure S4.5a-c) for the three forms of GAPDH reveals that conformational sampling is distributed around the crystal structure with more conformations sampled by GAPDH-NAD$^+$. We show only intrasubunit motions by superimposing the four subunits of a given form of GAPDH (Figure S4.5d-f). For example, Figure S4.5d shows the superimposition of the four subunits of GAPDH-NAD$^+$ and its conformational states are different from those in GAPDH-NADH (Figure S4.5e) and apo-GAPDH (Figure S4.5f). This highlights the variation in the subdomain motions in the three forms of GAPDH.

The first three principal components, PC1, PC2, and PC3 reveal that the major and functionally important motions are centered on the NBD as shown by. The square fluctuations indicate the mobility of each C_α atom along the respective PCs (Figure S4.6), whereas the arrows indicate the direction of motion of each C_α atom along the respective PCs (Figure S4.7). GAPDH-NAD$^+$ and GAPDH-NADH show similar directions of motions along PC1 and PC2. In fact, NBD_O and NBD_R move in opposite directions in all three forms of GAPDH (Figure S4.7). NBD_P and NBD_Q of GAPDH-NAD$^+$ and GAPDH-NADH also move in opposite direction but in the same direction in apo-GAPDH (Figure S4.7a, d, g, b, e, h).

Examining the motions along PC1 for GAPDH-NAD$^+$ reveal concerted motions of decreasing amplitude: NBD$_R$ > NBD$_O$ > NBD$_P$ ~ NBD$_Q$ (Figure 4.6a,b). NBD$_O$ and NBD$_R$ interacting across R-axis show higher fluctuation than the NBDs of the other subunits interacting across the same axis. Moreover, the direction of motion of NBDs interacting across the R-axis is opposite, indicating that the NBDs move away from each other.

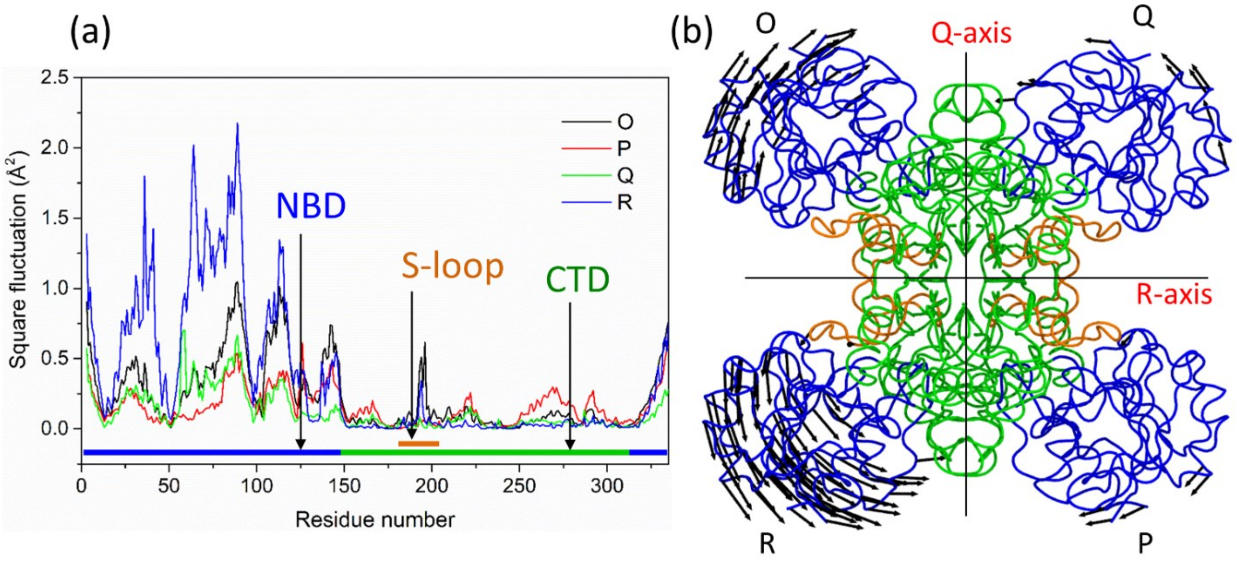

Figure 4.6. The mobility of the C_α atoms of GAPDH as revealed by PC1. (a) Square fluctuation of each C_α atom in PC1. (b) Arrows showing square fluctuations ≥ 0.5 Å^2 of C_α atoms in NBD (blue), CTD (green) and S-loop (orange). Note that the arrows reveal the concerted motion of decreasing amplitude NBD$_R$ > NBD$_O$ > NBD$_P$ ~ NBD$_Q$. The NAD$^+$ cofactors are omitted for clarity.

4.4.5. Square fluctuations of the backbone N, C_α, C and O atoms from NMA of GAPDH-NAD$^+$ crystal structure

The low-frequency normal modes calculated with NMA reveal functionally important motions of a protein similar to the principal components with the highest variance or largest eigenvalues. However, as mentioned previously, NMA is computationally less expensive than MD simulations. For the GAPDH tetramer, the amplitude of the lowest frequency mode (normal mode 1; NM1) shows that residues in the CTD and S-loop have superimposable low fluctuations. NBD_O and NBD_R of the subunits interacting across the R-axis are almost twice as flexible as the second pair of NBDs (NBD_P and NBD_Q) that interact across the same axis (Figure 4.7a). Subunits interacting across the Q-axis (NBD_O:NBD_Q and NBD_R:NBD_P) and the P-axis (NBD_O:NBD_P and NBD_Q:NBD_R) (Figure 4.1) also have one more flexible and one less flexible NBD. Note that similar behavior is revealed by PC1 of the MD trajectories of GAPDH-NAD^+ except the NBD_R is more flexible than NBD_O in PCA (Figure 4.6a vs. Figure 4.7a).

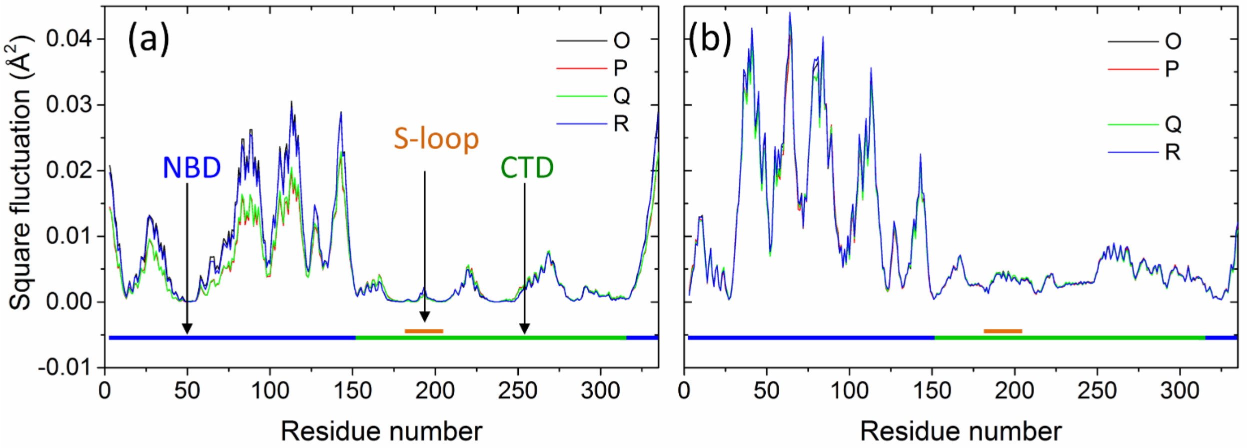

Figure 4.7. Normal mode analysis (NMA) of GAPDH-NAD^+ carried out using ANM. (a) Square fluctuation of C_α atoms of each subunit along normal mode 1 (NM1). Note that NBD_O and NBD_R exhibit higher flexibilities compared to NBD_P and NBD_Q. (b) Square fluctuations of each subunit in the OP and QR dimers extracted from the tetramer along NM1. Subunits in the OP/QR dimers relate to each other across the Q-axis.

When we break the tetramer into its dimer of dimers (OP and QR) and examine the square fluctuations of the subunits in the dimers (Figure 4.7b), we again clearly see that the NBD exhibits high flexibility compared to the CTD and the S-loop. Remarkably, the NBD has identical flexibility in all subunits and is more flexible than any NBD in the tetramer. Thus, we conclude that the asymmetry in the tetramer occurs across the R-axis. Furthermore, NBD_P and NBD_Q are stabilized in the tetramer by interaction across the R-axis.

4.4.6. PCA of the C_α and sidechain heavy atoms of residues within 4 Å of NAD^+

To look at the conformational sampling of the residues that interact with NAD^+, we performed PCA of residues within 4 Å of the cofactor. These represent the NAD binding-site residues in GAPDH-NAD^+ and the same atoms were selected in GAPDH-NADH and apo-GAPDH. Also, we aligned the four subunits on subunit-O in this analysis. We see from the PCA that the residues within 4 Å of NAD access conformations that fall mainly within one cluster in GAPDH-NAD^+ and GAPDH-NADH but two clusters in apo-GAPDH (Figure S4.8). Conformations in cluster-1 (Figure 4.8a) are close to the conformation of subunit-O in the crystal structure. However, residues in cluster-2 (Figure 4.8b) in apo-GAPDH adopt different conformations (Figure 4.8b).

The average structures of cluster-1 and cluster-2 from the FEL plots (Figure S4.8) are shown in Figure 4.8a, b. This figure confirms that apo-GAPDH accesses different conformations compared to GAPDH-NAD^+ and GAPDH-NADH. We quantified these conformational differences by calculating the dihedral angle of the Arg80 sidechain (C-C_α-C_β-C_γ) and the RMSDs of C_α and sidechain heavy atoms of Gly100-Phe102 in the three forms of GAPDH (Figure 4.8c-h). Arg80, which interacts with the adenine ring of adenosine moiety (Figure 4.2 and Figure S4.1), exhibits increasing flexibility in GAPDH-NAD^+ < GAPDH-NADH < apo-GAPDH. Note that Arg80 accesses a dihedral angle of 50-90° more frequently in apo-GAPDH. Also, residues Gly100-Phe102 accesses conformations with RMSD > 3 Å more frequently in apo-GAPDH compared to GAPDH-NAD^+ and GAPDH-NADH.

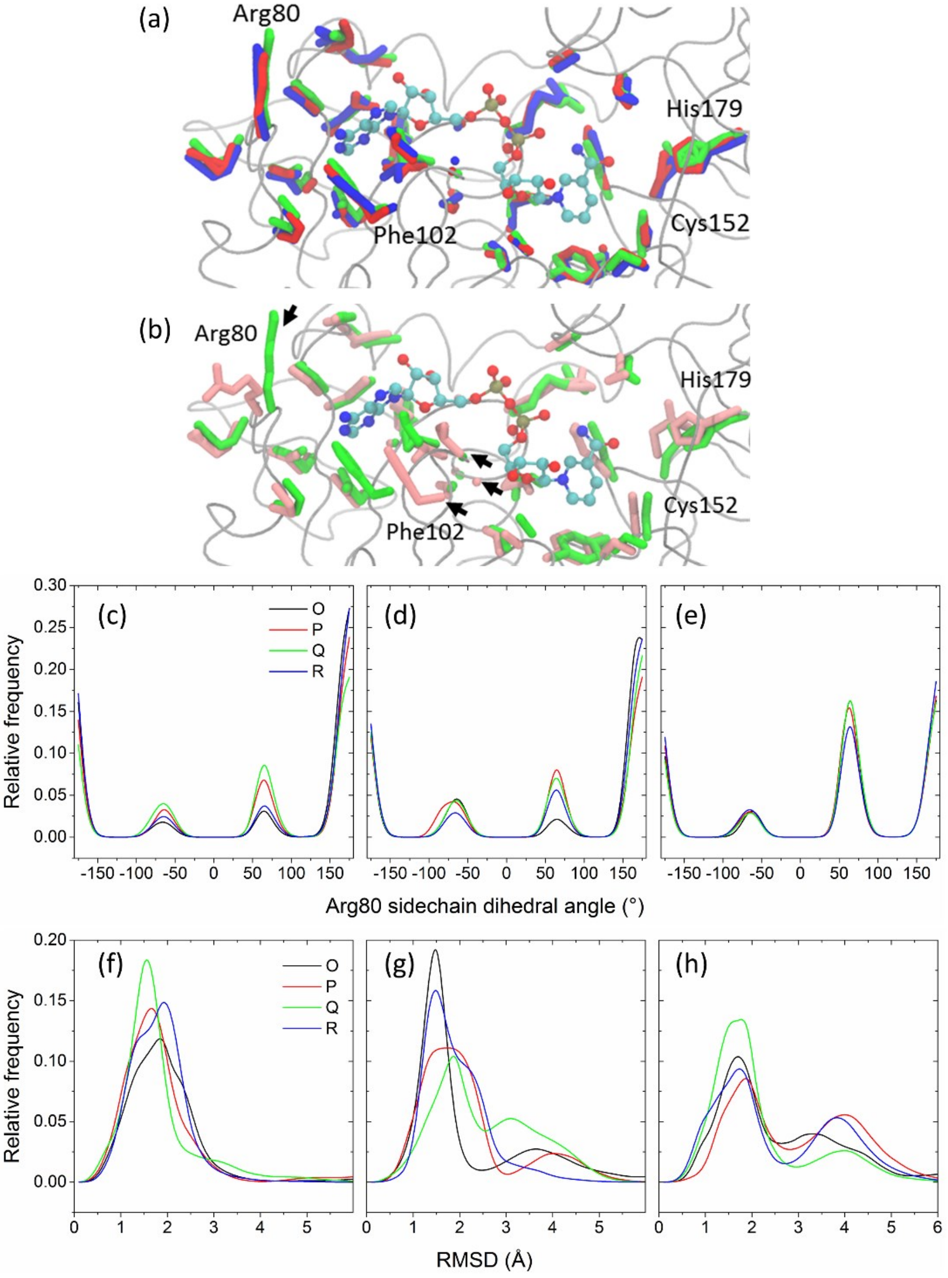

Figure 4.8. The difference in the conformations of the NAD$^+$-binding residues of GAPDH-NAD$^+$, GAPDH-NADH and apo-GAPDH. The average structure of (a) cluster-1 and (b) cluster-2 extracted from the FEL plots (see Figure S4.8) for the three forms of GAPDH. Green, red, blue and pink sticks in (a) and (b) represent the crystal structure, GAPDH-NAD$^+$, GAPDH-NADH and apo-GAPDH, respectively. (c-e) The dihedral angle of the Arg80 sidechain and (f-h) RMSDs of residues Gly100-Phe102 from the crystal structure (PDB 1U8F) in concatenated 5 x 100 ns MD trajectories for GAPDH-NAD$^+$, GAPDH-NADH and apo-GAPDH going from left to right.

4.4.7. Effect of cofactor on the Cys152 and His179 interaction

The catalytic Cys152 transfers a proton to His179 to give the active thiolate form of the GAPDH.[88] The stability of ion-pairing between deprotonated Cys152 and protonated His179 at neutral pH is important for dehydrogenase activity because this maintains Cys152 in the thiolate form.[71] Thus, we evaluated whether NAD$^+$ cofactor removal or reduction alter the stability of the ion-pairing between Cys152 and His179, and hence the dehydrogenase activity of GAPDH.

The S_γ(Cys152)–N_ε(His179) distance varies between 3.4–3.7 Å in the subunits of the crystal structure of human GAPDH (PDB 1U8F). A distance of ~3.2 Å is accessed more frequently in GAPDH-NAD$^+$ and GAPDH-NADH, whereas a distance of > 5 Å is more frequently accessed in apo-GAPDH during the MD simulations (Figure 4.9). A larger S_γ–N_ε separation also has been observed in apo-GAPDH (4.0–4.2 Å) vs. GAPDH-NAD$^+$ (3.4–3.5 Å) in the crystal structures of the Group B Streptococcus enzyme (PDB 5JYF, 5JY6). Loss of interaction between the positively charged N-atom of NAD$^+$ and the Cys152-thiolate (Figure 4.2) weakens the S_γ–N_ε interaction in GAPDH-NADH (Figure 4.9a vs. Figure 4.9b). Also, the loss of steric constraints imposed by NAD increases the flexibility of Cys152 and His179, which further weakens the S_γ–N_ε interaction in apo-GAPDH (Figure 4.9c).

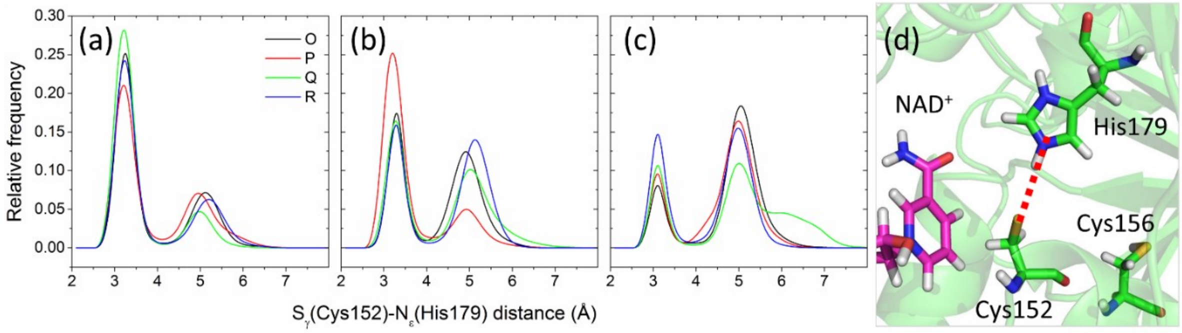

Figure 4.9. (a) The distance between S$_\gamma$(Cys152)–Nε(His179) in GAPDH-NAD$^+$, GAPDH-NADH, and apo-GAPDH. (b) The position of Cys152 and His179 in the active-site of GAPDH-NAD$^+$ (3.4 Å; red dotted line). Distance is obtained from the concatenated 5 x 100-ns MD trajectories.

4.4.8. Effect of NAD on Cys152–Cys156 separation and on Cys152 oxidation

The S$_\gamma$(Cys152)–S$_\gamma$(Cys156) separation (Figure 4.10a) during the MD simulations is examined to evaluate the possibility of disulfide bond formation. The S$_\gamma$–S$_\gamma$ distance is > 7 Å in all subunits of GAPDH-NAD$^+$, GAPDH-NADH and apo-GAPDH and the average distance is ~ 9 Å (Figure 4.10a-c). Since the S$_\gamma$–S$_\gamma$ bond length is 2.05 ± 0.11 Å,[179] disulfide formation is highly unlikely in any of the three forms of GAPDH examined here.

Cys156 is implicated in indirectly controlling the oxidation of Cys152 in GAPDH-NAD$^+$ from reported MD simulations on human GAPDH.[167] Cys156 imposes steric constraints on Tyr314 which promotes the formation of a moderately strong H-bond interaction with Thr153. This residue partakes in proton relay to H_2O_2 bound at Cys152 and facilitates its oxidation to the sulfenic acid.[167] Thus, to evaluate the effect of cofactor on the H_2O_2 sensitivity of Cys152, we looked at the changes in the H-bond interaction between Thr153-Tyr314 (Figure 4.10e-h). The O$_\gamma$(Thr153)–O$_\zeta$(Tyr314) separation is 2.7-2.8 Å in the crystal structure (PDB 1U8F) indicating a strong H-bond interaction (Figure 4.10h). The average O$_\gamma$–O$_\zeta$ distance is larger and fluctuates slightly more in GAPDH-NADH (3.17 ± 0.54 Å) and apo-GAPDH (3.14 ± 0.52 Å) vs. GAPDH-

NAD^+ (2.98 ± 0.37 Å) during the MD simulations (Figure 4.10e-g). Thus, NAD^+ binding may increase the H_2O_2 sensitivity of Cys152, which could be examined experimentally.

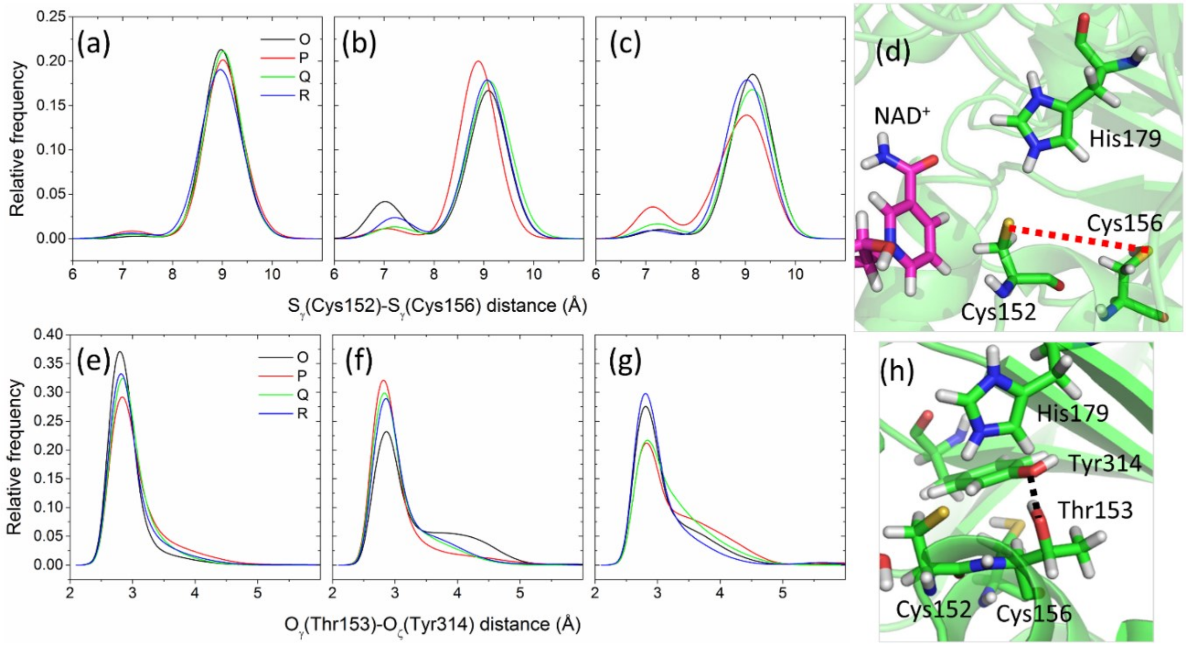

Figure 4.10. (a-c) S_γ(Cys152)–S_γ(Cys156) (e-g) O_γ(Thr153)–O_ζ(Tyr314) distances in (a,e) GAPDH-NAD^+, (b,f) GAPDH-NADH and (c,g) apo-GAPDH. Panels (d) and (h) show the positions of the residues in the active-site and dotted lines indicate the plotted distances. The distances in the graphs are obtained from the concatenated 5 x 100-ns MD trajectories.

4.4.9. Effect of cofactor on the selectivity cleft identified in GAPDH

GAPDH is a target for antiparasitic drugs against protozoan parasites like *T. cruzi* [38] or *Leishmania Mexicana.*[34] N^6-(1-naphthalenemethyl)-20-deoxy-20-(3,5-dimethoxybenzamido) adenosine (NMDBA) and its analogs are designed to selectively inhibit GAPDH in the parasite and not human GAPDH. It has been proposed that *L. Mexicana* GAPDH has an open cleft near O2' of adenine ribose ring and N-6 of adenine ring of NAD^+ that accommodates the dimethoxybenzamide and naphthalene groups of NMDBA, respectively. These clefts appear to be closed in human GAPDH.[34,105] Residues 39-41 of subunit-O and 206-208 of subunit-R in *L. Mexicana* GAPDH form the selectivity cleft that accommodates inhibitors with substitution at O2' of the adenine ribose ring, whereas substitutions at N-6 of the adenine ring are accommodated between residues 38 and 92 of subunit-O of *L. Mexicana* GAPDH. We aligned the adenine and ribose groups of NMDBA in *L. Mexicana* GAPDH with NAD^+ in human GAPDH to visualize the residues that form the selectivity clefts in human GAPDH (Figure 4.11a). The alignment reveals that residues 37-39 (subunit-O) and 191-193 (subunit-R), which also were identified by Jenkins and Tanner,[105] forms cleft near O2' of adenine ribose ring, whereas the N-6 substitution is located between Phe37 and Arg80 of subunit-O in human GAPDH. Note that the residues 37-39 and 191-193 are from the two separate subunits interacting across the R-axis (subunit-O and -R or subunit-P and -Q).

Residues Phe37, Ile38 and Pro191, which are involved in the opening and closing of the cleft (Figure 4.11a), have direct steric clashes with NMDBA. The Phe37-Pro191 (6.7−7.8 Å) and Ile38-Pro191 (7.1−7.5 Å) separations in the crystal structure of human GAPDH (PDB 1U8F) are ~2.5 Å shorter than the corresponding Met39-Val206 (9.6−10.0 Å) and Ser40-Val206 (9.8−10.1 Å) separation in the crystal structure of *L. Mexicana* GAPDH (PDB 1I32). The average Ile38-Pro191 separation (Å) in GAPDH-NAD^+ (7.34 ± 0.75), GAPDH-NADH (7.79 ± 0.71) and apo-GAPDH (7.37 ± 0.79) varies little in the three forms of GAPDH (Figure 4.11b-d) and it is short enough to create steric clashes with the inhibitor. However, distances (Å) equal or larger than those in the crystal structure of *L. Mexicana* GAPDH (> 9) between Phe37-Pro191 are accessed during MD simulations in GAPDH-NAD^+ (7.94 ± 1.40), GAPDH-NADH (8.65 ± 1.28) and apo-GAPDH (7.81 ± 1.24) (Figure S4.9a-c). The large distances arise due to the flexibility of Phe37 and may promote NMDBA binding despite the short distance between Ile38-Pro191. Thus, NMDBA affinity for human GAPDH, especially the apo-GAPDH, might not be as low as predicted by X-ray structures.

In the crystal structures, the distance between Phe37 and Arg80 are 6.7-6.8 Å in human GAPDH but ~ 3.0 Å larger in *L. Mexicana* GAPDH (9.7-9.9 Å). However, we observe a Phe37-Arg80 distance of 8-9 Å in GAPDH -NAD$^+$ (8.57 ± 1.48), GAPDH-NADH (8.40 ± 1.46) and apo-GAPDH (9.08 ± 1.72) (Figure S4.9d-f). Thus, the MD simulations indicate that the selectivity cleft is open in all three forms of GAPDH. Hence, substitutions at N-6 of adenine are unlikely to be as selective as predicted by the crystal structures.

4.5. Discussion

4.5.1. GAPDH tetramer behaves as a dimer of dimers

Square fluctuations along NM1 calculated using NMA of the backbone atoms reveal that NBD_O and NDB_R, which are related across the R-axis are more flexible than NBD_P and NBD_Q interacting across the same axis (Figure 4.7a). Thus, one NBD is more flexible than the other in the OP and QR dimers. Presumably, NAD$^+$ binds more tightly to the more rigid NBDs, which is supported by experiment where rabbit muscle GAPDH was found to have two moles of tight bound NAD$^+$ and two moles of loosely bound NAD$^+$.[83] Additionally, a crystal structure of mixed-holo Group B Streptococcus GAPDH was reported (PDB 5JYE) with NAD$^+$ occupying NBD_O and NBD_R only.[163] Moreover, maleylation of active of swine muscle apo-GAPDH decreases the ability of the enzyme to rebind all four NAD$^+$ molecules. Only two NAD$^+$ molecules are capable of re-binding to the inactive enzyme.[83] These findings support that tetramer behaves as a dimer of dimers because only one NAD$^+$ is bound per dimer. However, the loss in differential mobility if the NBDs in the tetramer in OP or QR dimer (Figure 4.7a,b) indicates that the OP and QR behave as two semi-independent dimers. These results are consistent with a model of tetrameric GAPDH that is composed of two symmetrical dimers that are positioned asymmetrically.[83]

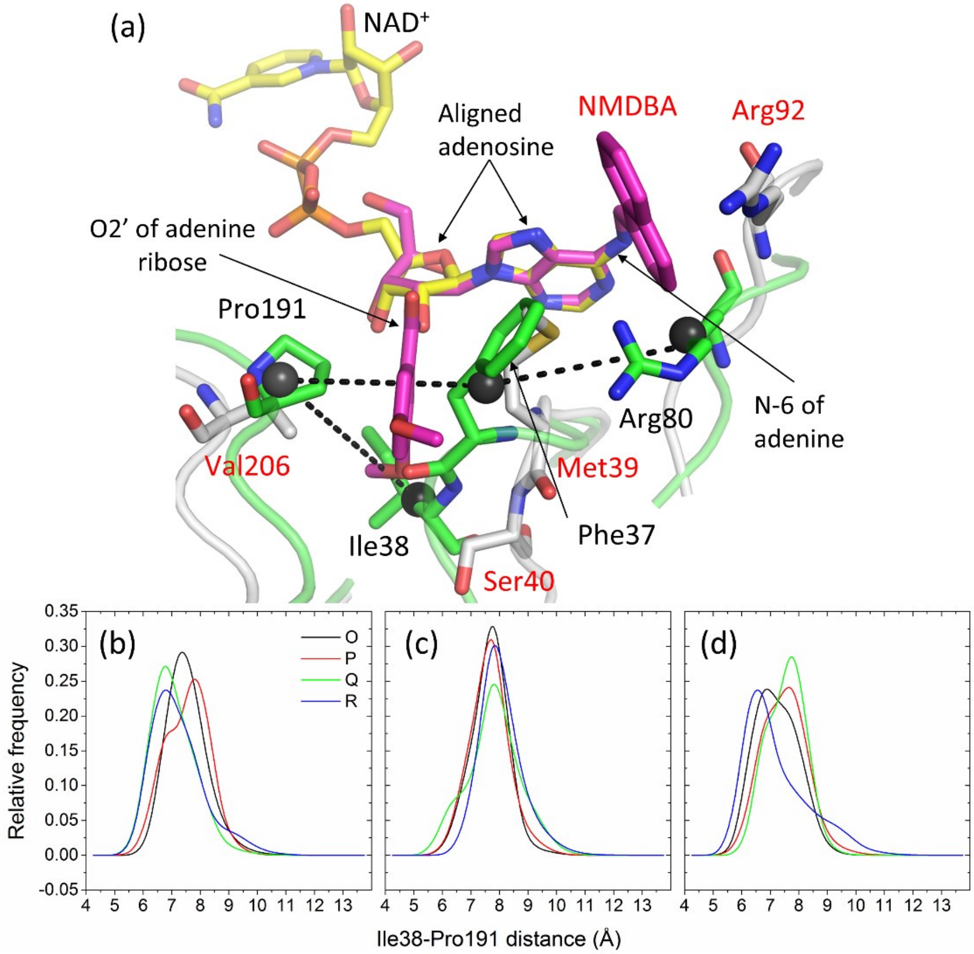

Figure 4.11. Dynamics of the selectivity cleft in the three forms of GAPDH. (a) Residues that form the selectivity cleft in human GAPDH (PDB 1U8F; green) and *L. Mexicana* GAPDH (PDB 1I32; cyan) are shown after aligning the adenine moiety of NAD$^+$ (yellow) and those of the inhibitor, NMDBA (magenta). Adenosine analogs like NMDBA with substitution at O2' of adenine ribose and N-6 of adenine are designed to selectively inhibit *L. Mexicana* GAPDH. Phe37, Ile38 and Pro191 form a closed cavity in human GAPDH that lead to steric clashes with the O2' substituent of NBDBA. Distribution of distance (shown by dashed lines) between the center of mass of residues Ile38 and Pro191 (shown by black spheres) of subunits interacting across the R-axis (O:R or P:Q) from the concatenated 5 x 100-ns MD trajectories for subunits of (b) GAPDH-NAD$^+$ (c) GAPDH-NADH and (d) apo-GAPDH.

4.5.2. Effect of cofactor binding on the motions of the NBD and CTD subdomains of GAPDH

Figure 4.3 shows that the flexibility of the NBD decreases as apo-GAPDH > GAPDH-NADH > GAPDH-NAD$^+$. Flexible NBDs are also seen in the crystal structure of *P. versicolor* and *B. stearothermophilus* apo-GAPDH, NAD$^+$-binding residues are more compact in the cofactor-bound vs. apo-enzyme.[67,164] Our MD simulations show that cofactor binding makes NBDs more compact (Figure 4.3).

CCA of MD trajectories reveals anticorrelated motions between the NBDs of the subunits interacting across the R-axis in GAPDH-NAD$^+$ and GAPDH-NADH but not in apo-GAPDH (Figure 4.4 and Figure S4.3). The presence of noncorrelated motions in apo-GAPDH indicates that its subunit motions are not concerted even though the NBDs are more flexible as seen from the calculated RMSF (Figure 4.3). Thus, cofactor binding induces concerted motions between the NBDs (Figure 4.4). The anticorrelated motions between the NBDs interacting across the R-axis are further confirmed by dominant opposite motions of the NBDs in PC1 and PC2 of GAPDH-NAD$^+$ and GAPDH-NADH (Figure S4.7a,b,d,e).

Conformational sampling visualized by FEL calculated with PC1 and PC2 of the three forms of GAPDH (Figure S4.5b) shows that all three forms access different conformations. PCA and CCA clearly suggest that the conformational differences arise from the variable fluctuation of NBDs in each GAPDH form. Motions are centered on NBDs in the three forms of GAPDH and concerted motions between NBDs are induced by NAD$^+$.

4.5.3. Effect of cofactor binding on the cofactor binding site and the active-site:

The NAD-binding residues are affected upon removal of cofactor as shown in Figure 4.8. However, the changes are not apparent from the RMSFs (Figure 4.3); thus, we use PCA to distinguish molecular-level fluctuations of the NAD-binding residues. We find that the NAD-binding residues in apo-GAPDH attain a specific subset of conformation as shown by cluster-2 of FEL (Figure S4.8 and Figure 4.8). In all four subunits of apo-GAPDH, cluster-2 represents an open conformation for residues Gly100-Phe102 and the sidechain of Arg80 (Figure 4.8). These residues form a binding groove for the adenine moiety of NAD (Figure 4.2). So, the conformation of these residues indicates that an adenine binding groove is an open form in apo-GAPDH. It has been previously proposed that adenine binding initiates the folding of the NBD then the nicotinamide moiety binds to complete the folding of GAPDH.[2] Also, large positively charged and flexible sidechain of Arg80 in apo-GAPDH could initiate the interaction between the GAPDH polypeptide and NAD^+, leading to binding of adenosine moiety in the groove close to Arg80.

Apo-GAPDH has no stable S_γ(Cys152)-N_ε(His179) interaction compared to GAPDH-NADH and GAPDH-NAD^+ (Figure 4.9). The weak interaction between Cys152 and His179 should affect the formation of the Cys152 thiolate and decrease the reactivity of the catalytic Cys152. Thus, we hypothesize that nucleophilic attack on Cys152 of GAPDH is favored in presence of NAD^+. In terms of H_2O_2 sensitivity of Cys152,[167] we show that removal of cofactor has little effect on the H-bond interaction between Thr152-Tyr314 (Figure 4.10d-f), nevertheless, a decrease in Cys152 thiolate population would render apo-GAPDH less sensitive as compared to GAPDH-NAD^+.

4.5.4. The R-axis is important for negative cooperativity

CCA of the NMA (Figure S4.4) and MD data (Figure 4.4a) reveal anticorrelated motion between NBDs interacting across R-axis and noncorrelated motions between NBDs interacting across P- and Q-axes (Figure 4.4, Figure 4.5 and Figure S4.4). Additionally, NAD^+ shows highly anticorrelated with NBD and correlated motions with the S-loop of the subunits related across R-axis, respectively (Figure S4.4b-f and Figure 4.5). NAD^+ also has weak correlated and anticorrelated motions with CTD and the S-loop of the subunit related across the P- and Q-axes, respectively. The strong cross-correlated motions across the R-axis could explain the binding of NAD^+ to GAPDH with negative cooperativity. For example, NAD^+_O binds first and forces S-loop$_R$ to move opposite to NBD$_R$ since NAD^+_O has correlated motions with S-loop$_R$ but anticorrelated motions with NBD$_R$ (Figure 4.5 and Figure S4.4). This opens NBD$_R$ so NAD^+_R does not bind as tightly as NAD^+_O. Additionally, NAD^+_O shows weakly correlated motion with S-loop$_Q$, which will influence the binding of NAD^+_P because S-loop$_Q$ interacts with NAD^+_P (Figure 4.5 and Figure S4.4c-f). Thus, binding of NAD^+_O weakens the binding of NAD^+_R and NAD^+_P, allowing NAD^+_Q to bind second, but this in turn strongly affects the binding of NAD^+_P so NAD^+_R binds third and NAD^+_P binds last. In essence, each time NAD^+ binds, the NBD across the R-axis becomes more flexible, which decreases its NAD^+ affinity and gives rise to negative cooperativity in NAD^+ binding to human GAPDH.

4.5.5. Selectivity cleft in human GAPDH

The selectivity cleft close to O2' of the adenosine ribose ring might be open because the slightly large distance between Phe37-Pro191 (Figure S4.9d-f) is accessed, although the distance Ile38-Pro191 is short during MD simulation (Figure 4.11). This suggests that trypanosomatid GAPDH may be selectively inhibited by O2' substituted inhibitors. However, the cleft near N-6 adenine ring is open during MD simulations of the three forms of GAPDH, rendering N-6 substituted inhibitors to be as selective as O2' substituted inhibitors.

4.6. Conclusions

Our study shows that cofactor binding affects the motions of NBDs since NAD^+ binding makes the NBD of its own subunit more rigid. Cofactor removal could influence the reactivity of Cys152 by decreasing thiolate formation. However, disulfide formation is not possible between Cys152 and Cys156, irrespective of cofactor binding. We also predict that the oxidation sensitivity of Cys152 does not change on cofactor binding due to change in the active-site of GAPDH but the reactivity it may be affected by the increasing the thiolate formation at Cys152 on NAD^+ binding.

Our study shows that cofactor binding induces concerted motions between NBDs interacting across the R-axis. This highlights the importance of interaction across the R-axis in the asymmetry of GAPDH tetramer. Our study also shows how the tetramer behaves as a dimer of OP and QR dimers and not of other dimer pairs. Overall, our study provides insights into the complex dynamics of GAPDH structure and how they impact its asymmetry.

4.7. Supporting Information

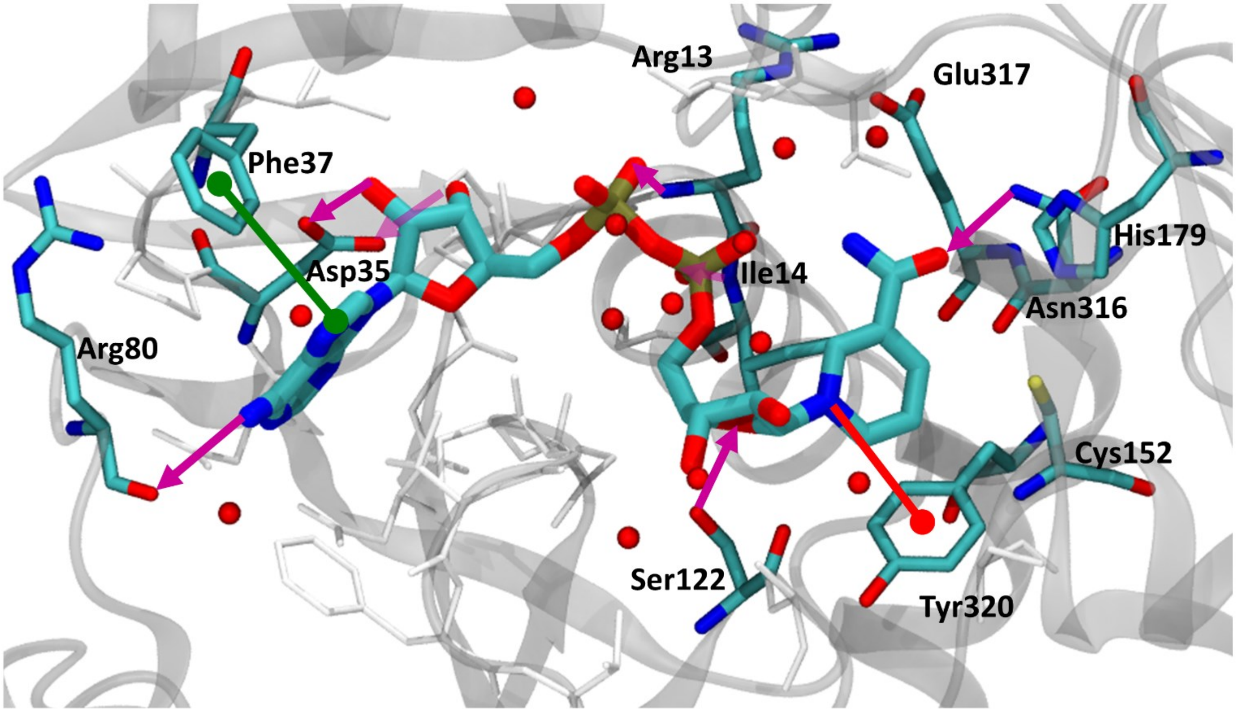

Figure S4.1. All possible interactions of NAD^+ with human GAPDH (PDB 1U8F). The residues interacting with NAD^+, discussed in the main text based on the 2D interaction map (Figure 4.2), are shown in the licorice representation. The rest of the structure is shown in cartoon representation and the red spheres represent water molecules found in the crystal structure. The image was generated using VMD.

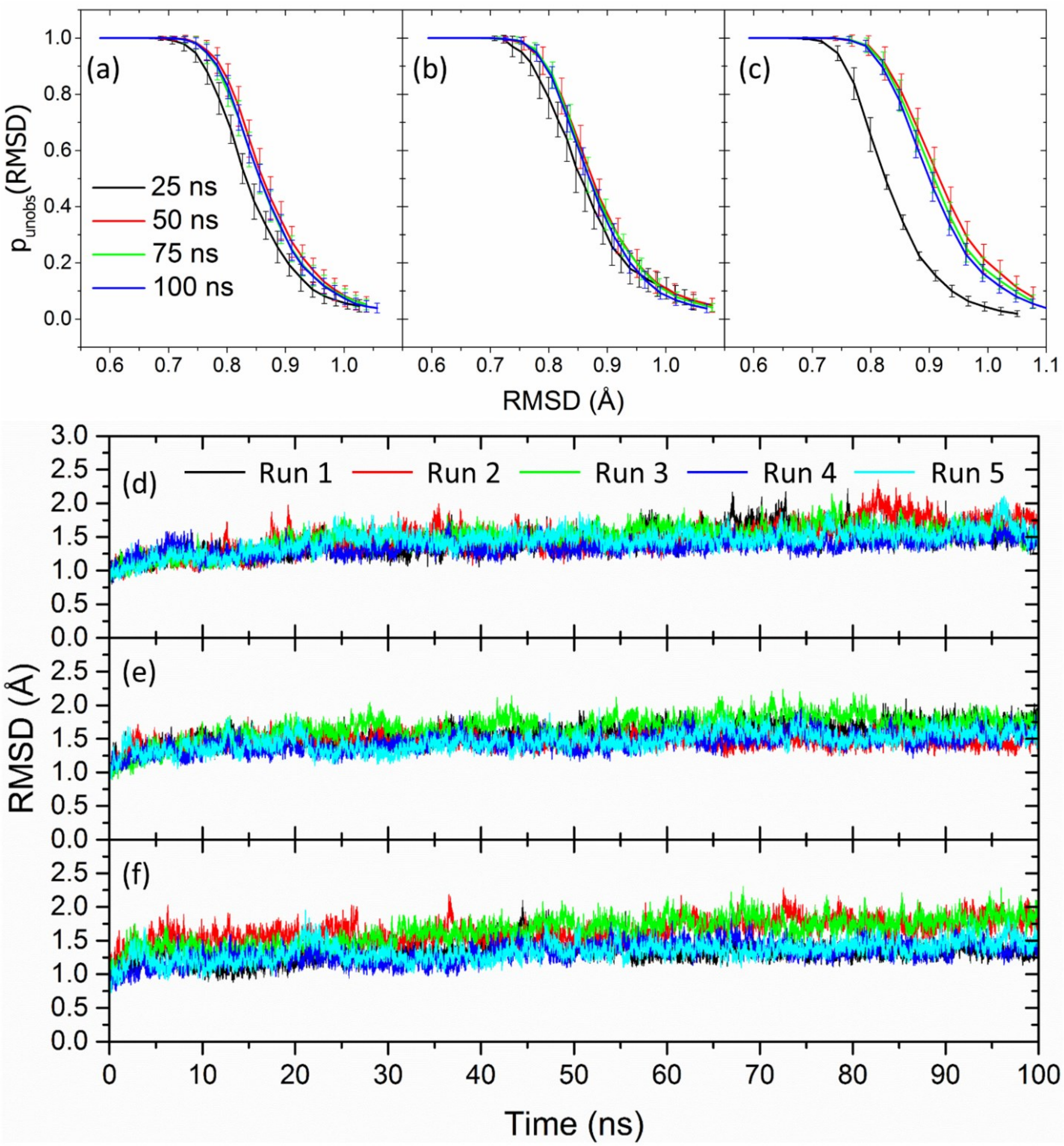

Figure S4.2. Convergence of the MD trajectories. (a-c) Good-Turing statistical analysis of convergence. The 5 x 100-ns MD trajectories were separated into 5 x 25, 5 x 50, 5 x 75, and 5 x 100 ns trajectories. The separated trajectories were used for Good-Turing statistical analysis. The overlapping curves for the 5 x 50, 5 x 75 and 5 x 100 ns trajectories indicate that the root-mean-square deviations (RMSD) are converged. (d-f) RMSD from crystal structure geometry calculated for each of the five 100 ns trajectories for the three forms of GAPDH.

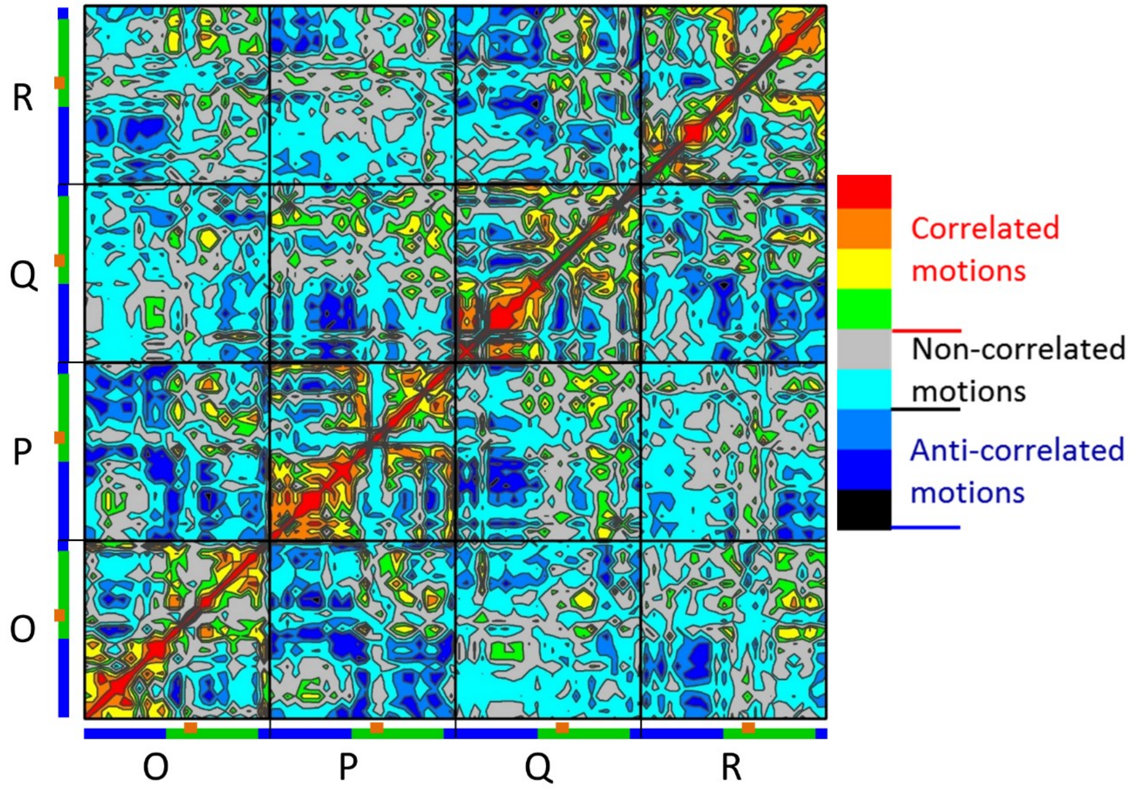

Figure S4.3. Cross-correlation analysis (CCA) calculated using C_α atoms of GAPDH-NADH from MD simulations trajectories. CCA is carried out using C_α atoms of concatenated 5 x 100 ns MD simulations trajectories. Each square represents a subunit and the diagonal show the correlated motions of each C_α atom with itself.

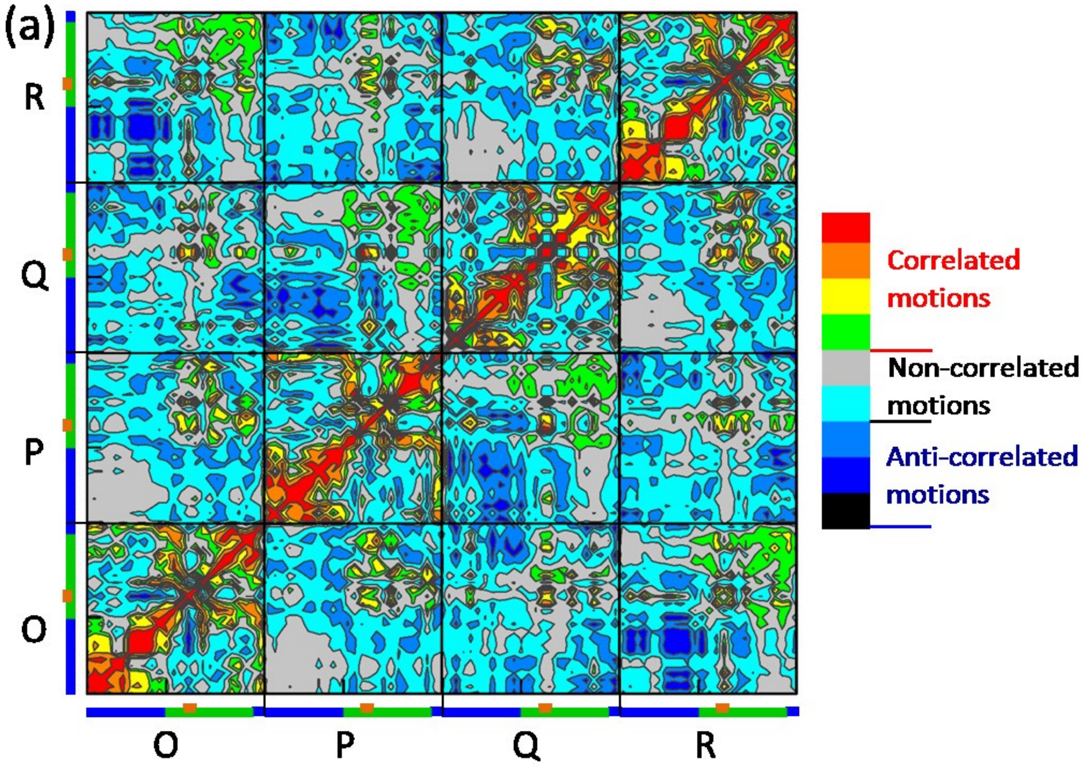
(a)
R
Q
P
O
O
P
Q
R
Correlated motions
Non-correlated motions
Anti-correlated motions

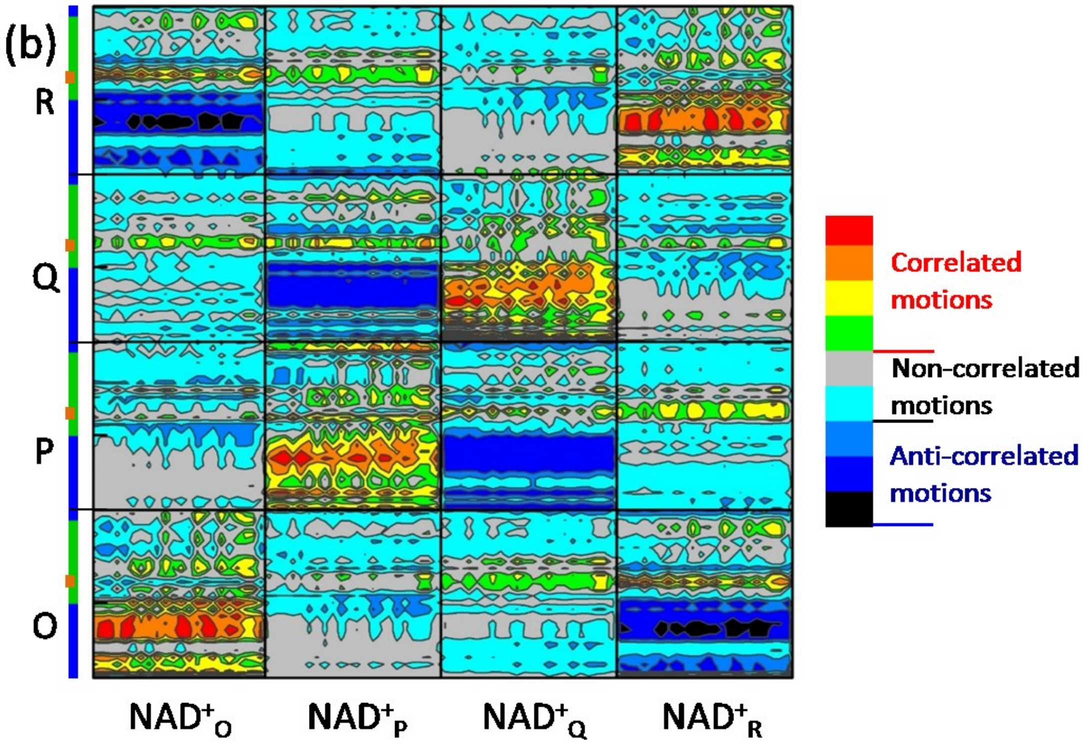
(b)
R
Q
P
O
NAD+O
NAD+P
NAD+Q
NAD+R
Correlated motions
Non-correlated motions
Anti-correlated motions

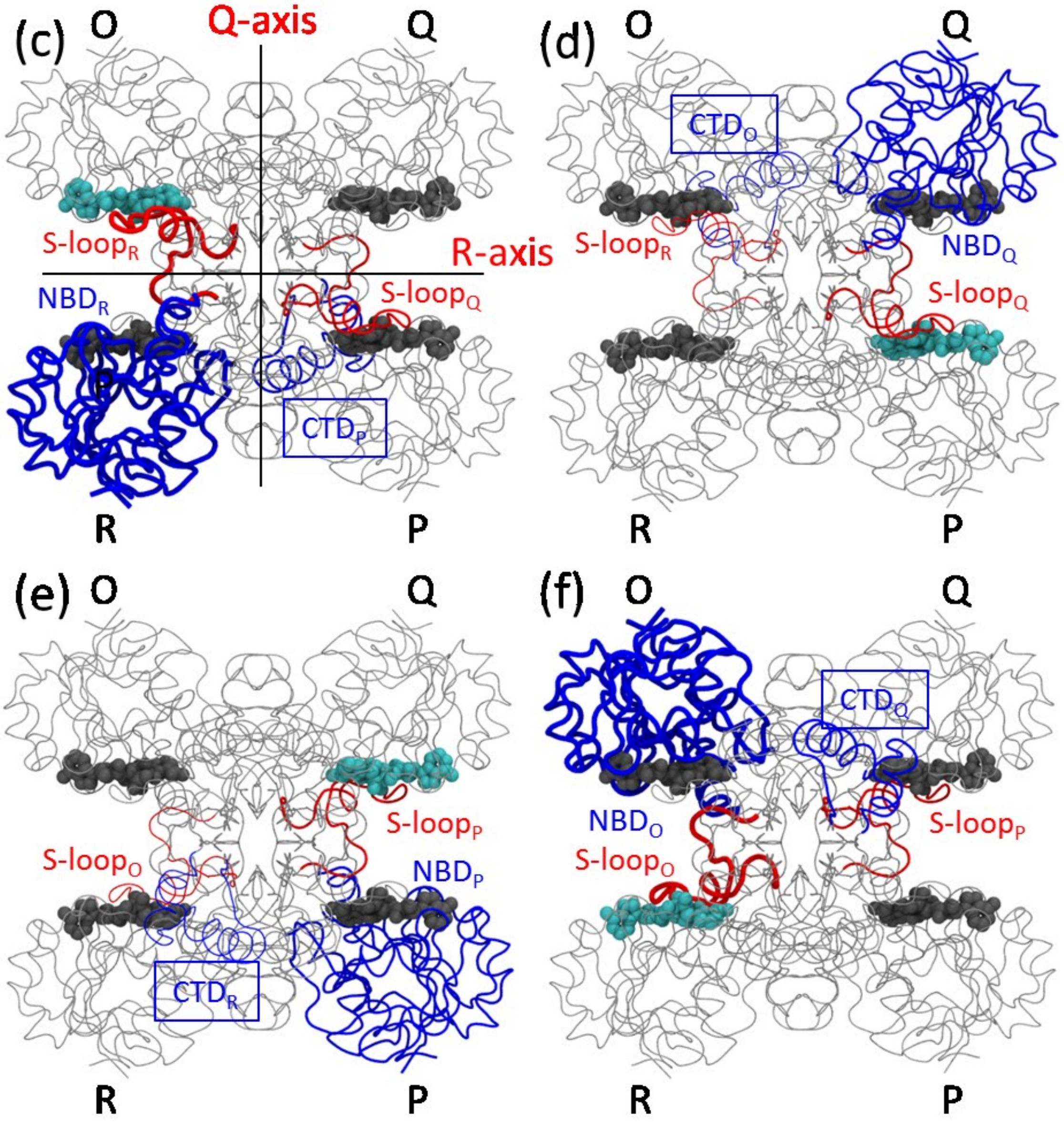

Figure S4.4. CCA of protein backbone atoms (N, C_α, C, O) and NAD^+ calculated using NMA. (a) Plot showing cross-correlated motions of subunits with each other. Each square represents cross-correlated motions of a subunit with itself and other subunits. (b) Plot showing cross-correlated motions of protein backbone atoms with NAD^+. Each square represents cross-correlated motions of a NAD^+ with backbone atoms of a subunit. There are mostly correlated motions between the protein backbone and NAD^+ atoms of the same subunit as seen in the four squares at the diagonal. Note that the blue, green and orange lines at the axes indicate NBD, CTD, and S-loop of each subunit, respectively. (c-f) Correlated (orange) and anticorrelated (blue) motions of residues with respect to given NAD^+ (cyan). See captions to Figure 4.5 of the main text for details.

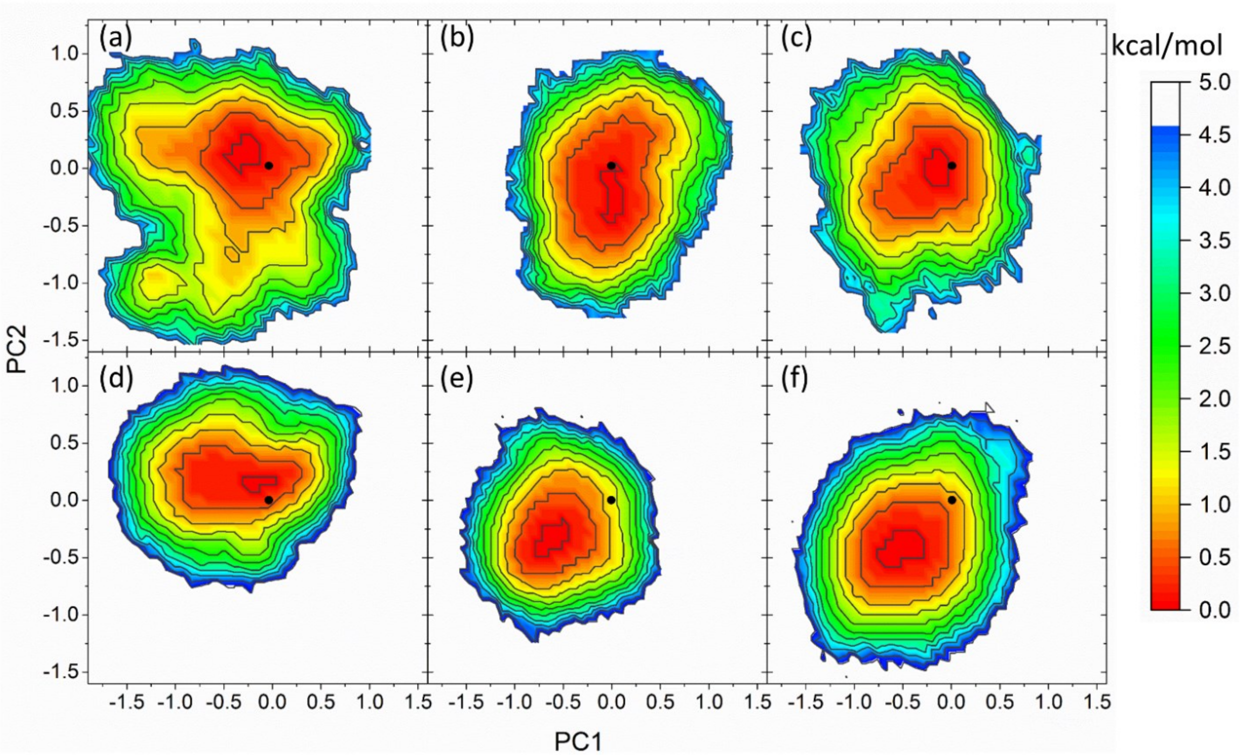

Figure S4.5. Free energy landscape (FEL) plotted using a projection of C_α atoms along PC2 and PC1. PCA was carried out using (a-c) C_α atoms of tetramer and (d-f) C_α atoms of all four superimposed subunits for (a,d) GAPDH-NAD$^+$, (b,e) GAPDH-NADH and (c,f) apo-GAPDH. We used concatenated 5 x 100 ns MD simulations trajectories for PCA. The black dot represents the conformations of the crystal structure of the tetramer in panels (a-c) and the conformations of the crystal structure of subunit-O in panels (d-f). The unit for free energy is kcal/mol.

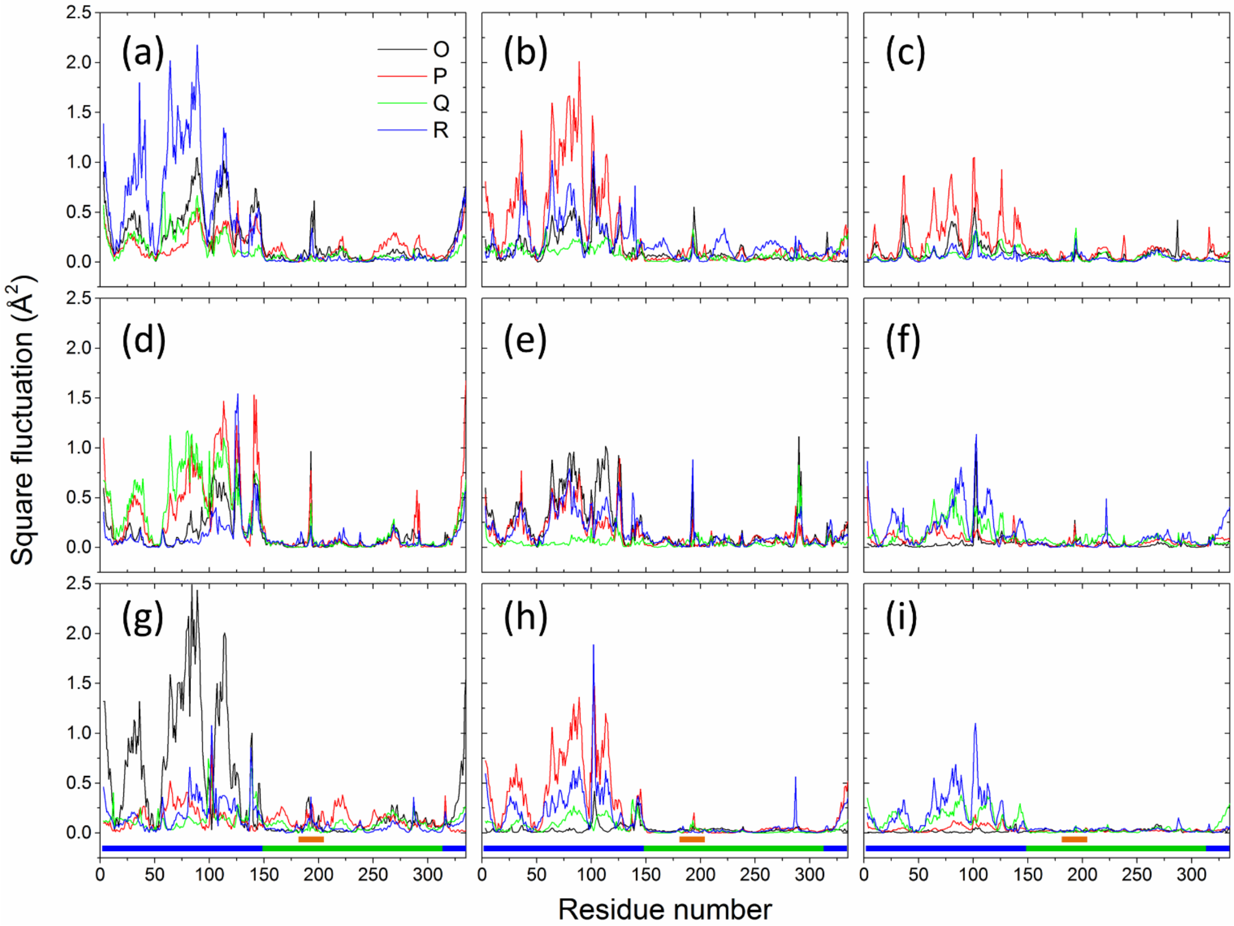

Figure S4.6. The mobility of the C$_\alpha$ atoms of three forms of GAPDH as revealed by PCA. Square fluctuation of each C$_\alpha$ atom of (a-c) GAPDH-NAD$^+$, (d-f) GAPDH-NADH and (g-i) apo-GAPDH in (a, d, g) PC1, (b, f, h) PC2, and (c, g, i) PC3.

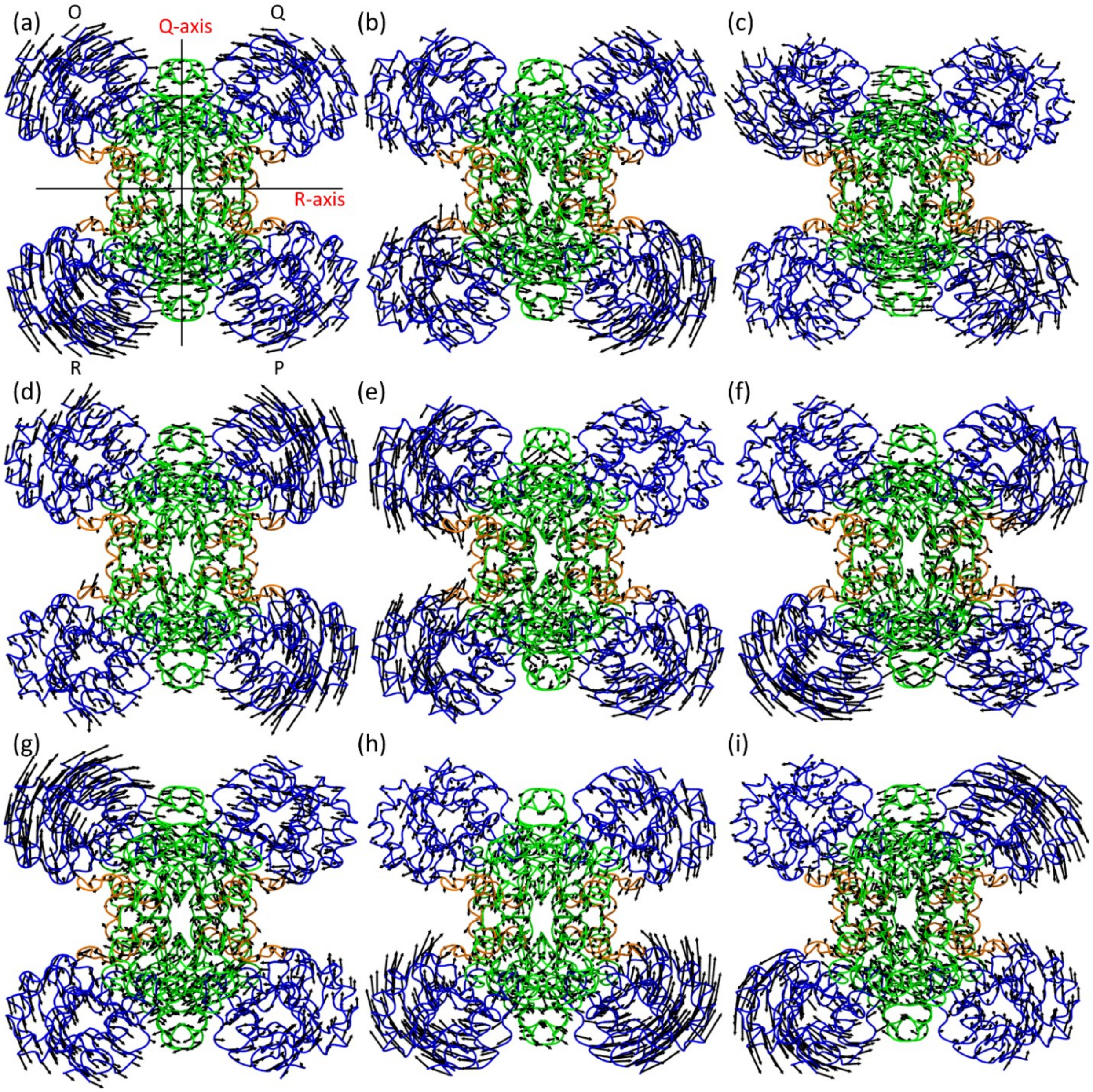

Figure S4.7. Directions of dominant motions of the C_α atoms of the three forms of GAPDH as revealed by PCA. Arrows showing square fluctuation of each C_α atom of (a-c) GAPDH-NAD$^+$, (d-f) GAPDH-NADH and (g-i) apo-GAPDH in (a, d, g) PC1, (b, f, h) PC2, and (c, g, i) PC3. The NBD (blue) , CTD (green), and S-loop (orange) of each subunit are shown in tube representation, respectively.

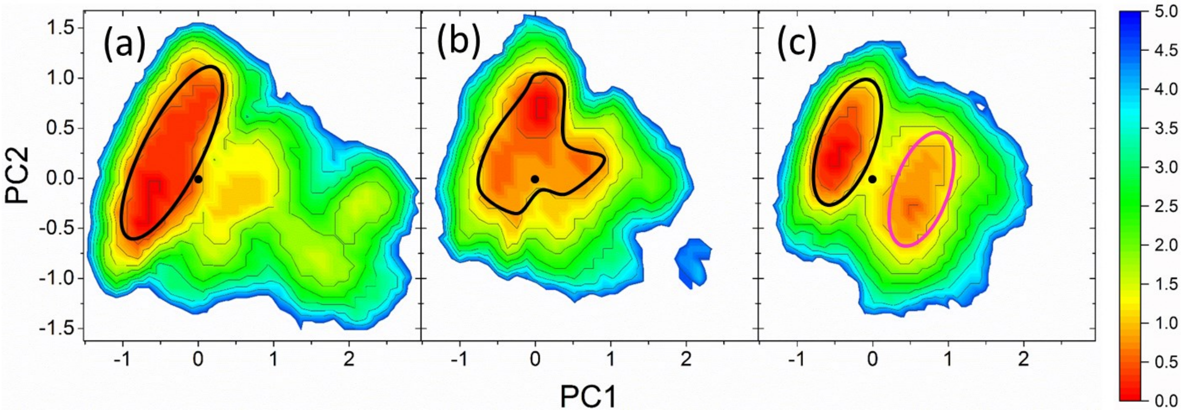

Figure S4.8. FEL plotted using a projection of the NAD-binding residues along PC2 vs PC1. PCA of the C_α and sidechain heavy atoms of residues within 4 Å of NAD^+ of the four subunits of (a) GAPDH-NAD^+ (b) GAPDH-NADH and (c) apo-GAPDH aligned on each other. Data from concatenated 5 x 100 ns MD trajectories were used for the analysis. The black dot represents the conformations of C_α and sidechain heavy atoms of residues within 4 Å of NAD^+ in the subunit-O of the crystal structure (PDB 1U8F). Cluster-1 and cluster-2 are highlighted by black and magenta circles, respectively. The unit for free energy is kcal/mol.

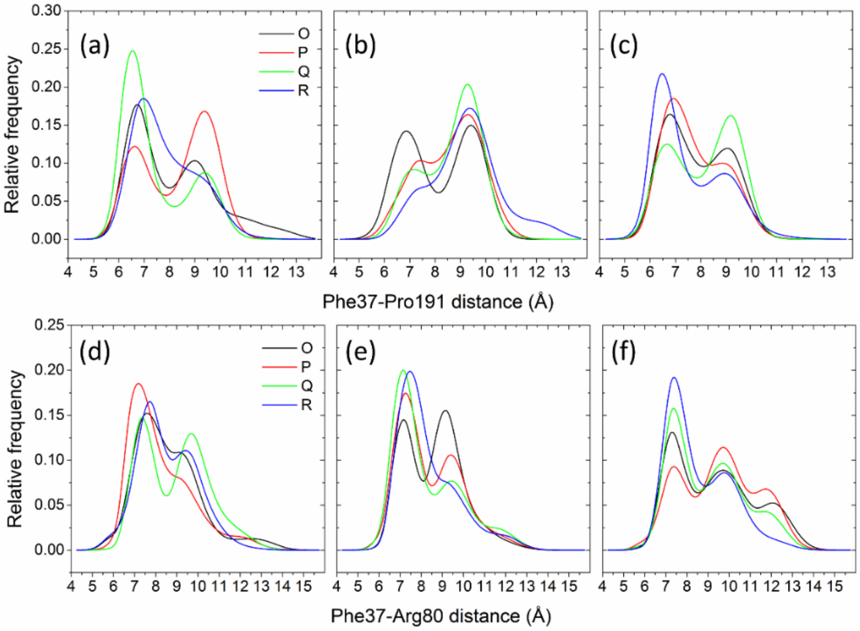

Figure S4.9. Change in size of the selectivity cleft in human GAPDH with the cofactor. (a) Distribution of distance between center of mass of residues (a-c) Phe37 and Arg80 of subunits interacting across R-axis (O:R or P:Q) (d-f) Phe37 and Arg80 of the same subunit calculated from 5 x 100 ns MD trajectories for each subunit of (a,d) GAPDH-NAD^+ (b,e) GAPDH-NADH and (c,f) apo-GAPDH. See Figure 4.11 of the main text for the positions of these residues.

Chapter 5. Dynamics of Glyceraldehyde-3-Phosphate Dehydrogenase (GAPDH): Variations upon Deoligomerization of Tetramer to Dimer or Monomer

5.1. Abstract

Glyceraldehyde-3-phosphate dehydrogenase (GAPDH) exhibits various moonlighting functions depending on its oligomeric states, tetramer, dimer and monomer. However, no report has evaluated the relation of functional diversity with the structure and dynamics of these oligomeric states. The GAPDH homotetramer has identical subunits, so functional diversity could arise due to alteration in subunit or subdomain dynamics upon deoligomerization from the tetramer to dimer or monomer. The global motions calculated using normal mode analysis (NMA) of the crystal structure of the human GAPDH show that the tetramer behaves as a dimer of dimers. This is evident from the varied dynamics of the NAD-binding domain (NBD) in the tetramer. The catalytic domain (CTD), which is at the center of the tetramer, becomes highly dynamic depending on the dimer pairs (OP/OQ/OR) examined which reveals dimer-OP and dimer-QR are the most stable dimer pairs. The highly dynamic nature of the S-loop, which moves away from NBD in the monomer, is also revealed by NMA. Variation in subunit and subdomain dynamics in the three oligomeric states was confirmed by molecular dynamics (MD) simulations and multivariate statistical analysis, including principal component analysis (PCA) and cross-correlation analysis (CCA). For example, PCA confirms that the major dominant motions are centered on the NBD in the tetramer and dimer whereas S-loop motions are dominant in the monomer. The NBD of all four subunits of the tetramer have varying displacements, which we correlate with NAD^+ binding with negative cooperativity to GAPDH. CCA reveals that highly anticorrelated motions between subdomains in the QR dimer are absent in tetramer, showing that the tetramer is more stable than the dimer. The highly correlated motions within the CTD of the tetramer and dimer are lost in the monomer, confirming that deoligomerization disrupts the CTD, which may lead to loss of activity. Notably, the high flexibility of the S-loop revealed by NMA and PCA indicates that this loop

behaves as an intrinsically disordered domain that may promote binding of the monomer to many of GAPDH's multitude of protein partners in the cell. Overall, our study shows that dissociation of tetramer to the dimer or monomer alters inter- and intradomain dynamics in addition to subunit dynamics. These distinct essential dynamics of the oligomeric states likely dictate their functions and stabilities.

5.2. Introduction

Glyceraldehyde-3-phosphate dehydrogenase (GAPDH), a well-known glycolytic enzyme, exhibits remarkable moonlighting functions. For example, it has been implicated in physiological functions as diverse as cell signaling, gene regulation, and apoptosis as well as in the pathologies of diabetes, neurodegeneration, and malaria.[1,3,15,43] Additionally, GAPDH's role in nitric oxide biochemistry has been demonstrated by our group and others.[48,180,181] For example, we showed that GAPDH catalyzes nitrite generation from glyceryl trinitrate.[48]

GAPDH is translated as a 37 kDa monomer but mainly exists as a tetramer.[2] The tetramer of GAPDH is composed of four identical subunits, labeled O, P, Q and R (Figure 5.1a). Each subunit has a nicotinamide adenine dinucleotide (NAD) binding domain (NBD; residues 1-151 and 315-335) and a catalytic domain (CTD; residues 152-314) (Figure 5.1a). However, various post-translational modifications give rise to dimer and monomer.[14,77–79] GAPDH's function is determined by its oligomeric state. For example, the monomer [182,183] and dimer [77] exhibits no dehydrogenase activity. Only the monomer and dimer are implicated in GAPDH aggregation, which is associated with neurodegenerative diseases.[19,86] In the cell, the tetramer and monomer are found mainly in the cytoplasm [33] and nucleus,[19] respectively, but little is known about the cellular localization of dimer. Non-native forms of GAPDH, which are implicated in apoptosis, are also found in the nucleus, but the oligomeric status of the non-native forms is obscure.[184]

Evidently, cellular localization will dictate some functions of GAPDH since glycolytic activity is confined to the cytosol and the involvement of the monomer in DNA repair [87] will occur in the nucleus. The post-translational modification of GAPDH regulates localization and oligomerization that in turn determines the multifold functions of GAPDH. However, GAPDH is a homotetramer with the identical structure for each subunit so the different functions should arise from changes in conformations or dynamics of the oligomeric states. However, no studies have compared the dynamics of the different oligomeric states of GAPDH.

Various double mutations transform the *Bacillus stearothermophilus* GAPDH tetramer to dimers like dimer-OP and dimer-OR, that exhibit different cooperativity compared to the tetramer.[77,185] For example, dimer-OP [77,185] binds NAD^+ with positive cooperativity as oppose to the negative cooperativity seen for the tetramer,[68,69] whereas dimer-OR shows no cooperativity for the binding of NAD^+.[77,185] Also, the rabbit muscle GAPDH tetramer was converted to dimers by incubation with RNA[90] but no similar studies have been reported on human GAPDH. The conformational changes upon deoligomerization of the tetramer to the dimer can be seen from the crystal structure of dimeric *Kluyveromyces marxianus* GAPDH which reveals a very high B-factor for the S-loop (residues 181-205). This loop partly covers the active-site and the cofactor binding site (Figure S5.1), indicating that tetramer to dimer dissociation destabilizes the S-loop.[165] However, there are no other human GAPDH crystal structures of the dimer or monomer mostly due to the instability of these oligomeric states. The T227K mutation in rat GAPDH produced a wide range of molecular weights from 37–148 kDa with the highest amount eluted in gel filtration at 37 kDa, corresponding to the monomer.[186] It was also shown that thermal aggregation involves stages of reversible dissociation of the enzyme tetramer into oligomeric forms of lesser size, like the dimer or monomer.[187] Thus, human GAPDH could be partially stable as a dimer or monomer oligomeric state in addition to tetramer form.

Overview of GAPDH structure: As we discussed in Chapter 4, the GAPDH homotetramer has most inter-subunit interactions across P-axis, between O:P and Q:R. GAPDH homotetramer behaves as a dimer of dimers (OP and QR dimers) located across Q-axis (Figure 5.1a). [31,105] Note that the two dimers are located across Q-axis and each dimer consists of two subunits interacting across P-axis. We use subunits-QR as dimer and subunit-P as a monomer for MD simulation (Figure 5.1b,c). The important structural regions, the NBD, the CTD and the S-loop of each subunit are shown in Figure S5.1. Note that the NBDs are located at the periphery of the tetramer and the CTDs are at the center of the tetramer. The nicotinamide moiety of NAD$^+$ binds close to the catalytic Cys152, which is partially solvent exposed. GAPDH active-site contains the catalytic Cys152 (deprotonated or cysteine thiolate form) and His179 (protonated form) at neutral pH,[88] which are essential for dehydrogenase activity.[71] Deprotonated Cys152 and protonated His179 are stabilized by a strong H-bond interaction (Figure S5.1). Cys156 on the same helix as Cys152 is buried inside the protein matrix, which hinders the disulfide bond formation between them (Figure S5.1).

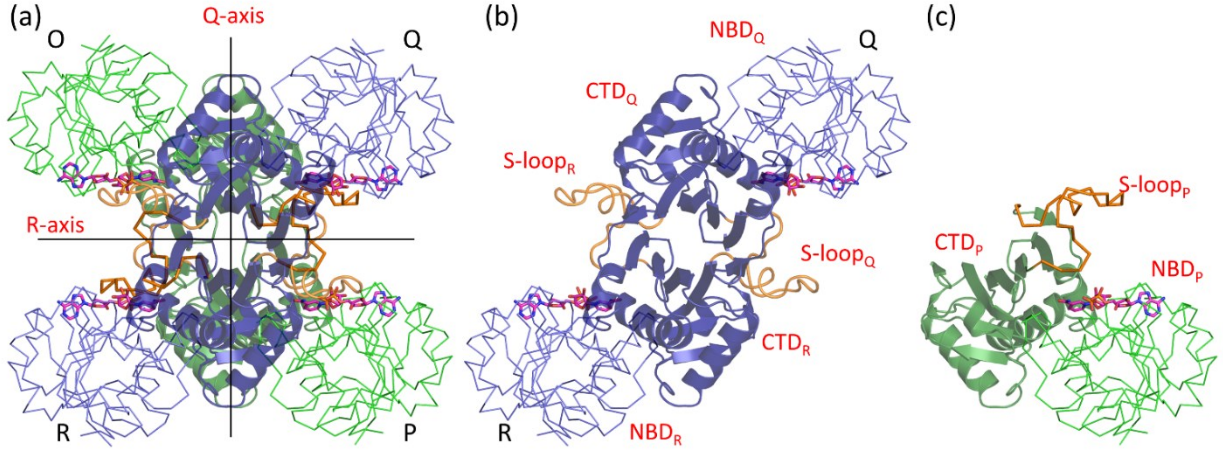

Figure 5.1. Location of subdomains of human GAPDH structure (PBD 1U8F). (a) The secondary structure of the GAPDH tetramer. Note that the tetramer is a dimer of OP (blue) and QR (green) dimers with subunits interacting across P-axis as a dimer. Thus, we used dimer-QR for MD simulation as shown in panel (b). Panel (c) shows the monomer GAPDH (subunit-P). The cofactor NAD$^+$ is shown as magenta sticks. NAD-binding domain (NBD; residues 1-151 & 315-335) are shown in ribbon with NBD$_O$ and NBD$_P$ in green color, whereas NBD$_Q$ and NBD$_R$ in blue color. Catalytic domain (CTD; residues 152-314) are shown in cartoon representation with CTD$_O$ and CTD$_P$ in green color whereas, CTD$_Q$ and CTD$_R$ in blue color. The S-loop (residues 181-205), which covers the active-site and the nicotinamide moiety of NAD$^+$, are shown

in orange color with S-loop$_O$ and S-loop$_P$ in ribbon format, whereas S-loop$_Q$ and S-loop$_R$ in the tube. See Figure S5.1 for the location of active-site residues.

Studies on the dynamics of the human GAPDH tetramer have looked at effects of Cys156 modification by persulfide (-SSH),[188] Met46 oxidation,[189] H_2O_2 sensitivity of Cys152 [167] (Section 4.4.10). However, there are no reported attempts to correlate conformational change to with the function of GAPDH upon deoligomerization of tetramer to dimer or monomer. In the present study, we describe the changes in the dynamics of subunit and subdomains upon deoligomerization. The variable dynamics could change the reactivity of each oligomeric state and could allow GAPDH to interact with different protein partners to drive the functional diversity of GAPDH.

5.3. Computational Methods

5.3.1. Normal mode analysis (NMA) using anisotropic network model (ANM):

The large-scale motions of subdomains of a protein can be extracted into a collection of normal modes using NMA.[169,170] Thus, we performed NMA using the anisotropic network model (ANM)[102–104] of *ProDy*[171] and analyzed the low-frequency normal modes to extract the functionally relevant motions of GAPDH.[170,172] See section 4.3.1 for details. We used the backbone atoms (C, Cα, N, O) and NAD$^+$ of the crystal structure of the human GAPDH tetramer (PBD 1U8F) after adding coordinates of fourth NAD$^+$ in subunit-O [105] as a tetramer for NMA. We used the edited tetramer structure to extract two subunits for dimer (dimer-OP, -QR, -OQ, -PR, _OR, -PQ) and one subunit for monomer (monomer-O, -P, -Q, -R) to carry out the NMA.

5.3.2. Molecular dynamics simulations:

We prepared crystal structure of human GAPDH (PBD 1U8F) [105] as described in section 4.3.2 for MD simulations of a tetramer. We extracted subunit-Q and -R as dimer and subunit-P as a monomer from the tetramer structure. These three structures were further used to generate systems for MD simulations.

The tetramer, dimer (dimer-QR) and monomer (monomer-P) were hydrated in a 10 Å-layer of TIP3P water from the protein boundary and 0.15 M Na^+ and Cl^- ions were added to represent physiological conditions. MD simulations were performed using the CHARMM27[106,174] force field and the NAMD2.9[99] software. The system was subjected to 20,000 steps of conjugate gradient minimization and 1 ns of equilibration before production runs of 100 ns were carried out. We also performed a 300 ns production run for the three oligomeric forms of GAPDH, tetramer, dimer, and monomer. Simulations were performed in the NPT ensemble at 300 K and 1 atm using Langevin dynamics and the time step was set to 2 fs. Seven independent simulations of 100 ns (7 x 100 ns) were run for each form of GAPDH and the results were analyzed using VMD [175] and *ProDy*[171]. Good-Turing statistical analysis was carried out to analyze the convergence of the MD trajectories.[176]

5.3.3. Principal component analysis (PCA):

MD trajectories include nonharmonic residues motions and generate accessible conformational ensembles. However, the motions are highly multidimensional and include a large number of degrees of freedom. Multivariate statistical analysis such as PCA reduces the dimensionality of the data and allows us to extract the dominant motions from the large data sets that comprise the MD trajectories.[100,101,177]

To carry out PCA, we selected three sets of atoms (1) all C_α atoms, (2) the C_α atoms and the heavy atoms of the sidechains of the S-loop, and (3) the C_α atoms and the heavy atoms of the sidechains of residues within 4 Å of NAD^+ (NAD-binding residues) from the 7 x 100 ns MD trajectories of the tetramer, dimer and monomer to carry out PCA. PCA and ANM results were visualized using the Normal Mode Wizard (NMWiz)[171] of VMD.

The variation in a conformational sampling of the three oligomeric forms of GAPDH is evaluated by calculating the free energy landscape (FEL). PC1 and PC2 calculated by PCA of the concatenated 7 x 100 ns MD trajectories are plotted vs. free energy for the three oligomeric forms.

5.4. Results

5.4.1. Square fluctuations of the backbone atoms N, C_α, C, and O calculated by NMA

NMA allows extraction of the global motions of a protein by applying harmonic forces to the x-ray crystal structure (See Chapter 4).[172] Square fluctuations of the C_α atoms along the lowest frequency normal mode (NM1) are high for residues 25-35, 60-95 and 107-120 of NBD_O and NBD_R compared to NBD_P and NBD_Q (Figure 5.2a,b). The differences in the square fluctuation of the NBDs are lost, when we extracted dimer-OP and -QR, and NBDs become more flexible (Figure 5.2c,d). This reveals the characteristics of tetramer to behaves as a dimer of dimers (See Chapter 4). Also, NM1 is centered on the NBD in the tetramer and dimer, which reveals the importance of NBD motions in these oligomeric states. Extraction of subunit as monomer-O, -P, -Q and -R dramatically increases the square fluctuation of their S-loop (Figure 5.2e,f). Thus, the functionally important motions switch to the S-loop in the monomer from the NBD in the tetramer and dimer.

We also extracted dimer-OQ, -PR, -OR and -PQ from the tetramer. The square fluctuations of the NBD and CTD for these dimers are 3-4 fold higher than those of dimer-OP and -QR (Figure

5.2c,d, and Figure S5.2), revealing the loss of stabilizing interaction across the R-axis. Dimer-OP and -QR also were found to be stable in *Bacillus stearothermophilus* GAPDH.[77] Additionally, their identical square fluctuations indicate that dimer-OP and -QR exhibit similar dynamics and the similar square fluctuation are seen for other dimer pairs related across P- (dimer-OQ and -PR) and Q-axis (dimer-OR and -PQ) (Figure S5.2).

NBD_Q and NBD_R move in the opposite direction to NBD_O and NBD_P, respectively in tetramer (Figure 5.2a,b). However, the motions of the NBD_Q and NBD_R change in such a way that they move away from their respective CTDs in the dimer (Figure 5.2c,d) indicating the dimer's instability. The NBD and the S-loop move opposite to each other in the monomer and there is an opening of the S-loop in the monomer (Figure 5.2e,f). Notably, the S-loop is not as dynamic in dimer or tetramer.

NMA reveals that dimer-OP and -QR are most stable dimers and exhibit identical dynamics (Figure 5.2c). Thus, MD simulations of dimer-QR are used to evaluate the dynamics of both dimer-OP and -QR. In case of monomer, all four subunits have identical normal modes, so the monomer dynamics are examined for subunit-P. We also looked at the cross-correlated motions between subunits and subdomains of tetramer, dimer, and monomer calculated from NMA (Figure S5.3). The detailed results are discussed and compared with CCA from MD trajectories in section 5.4.4.

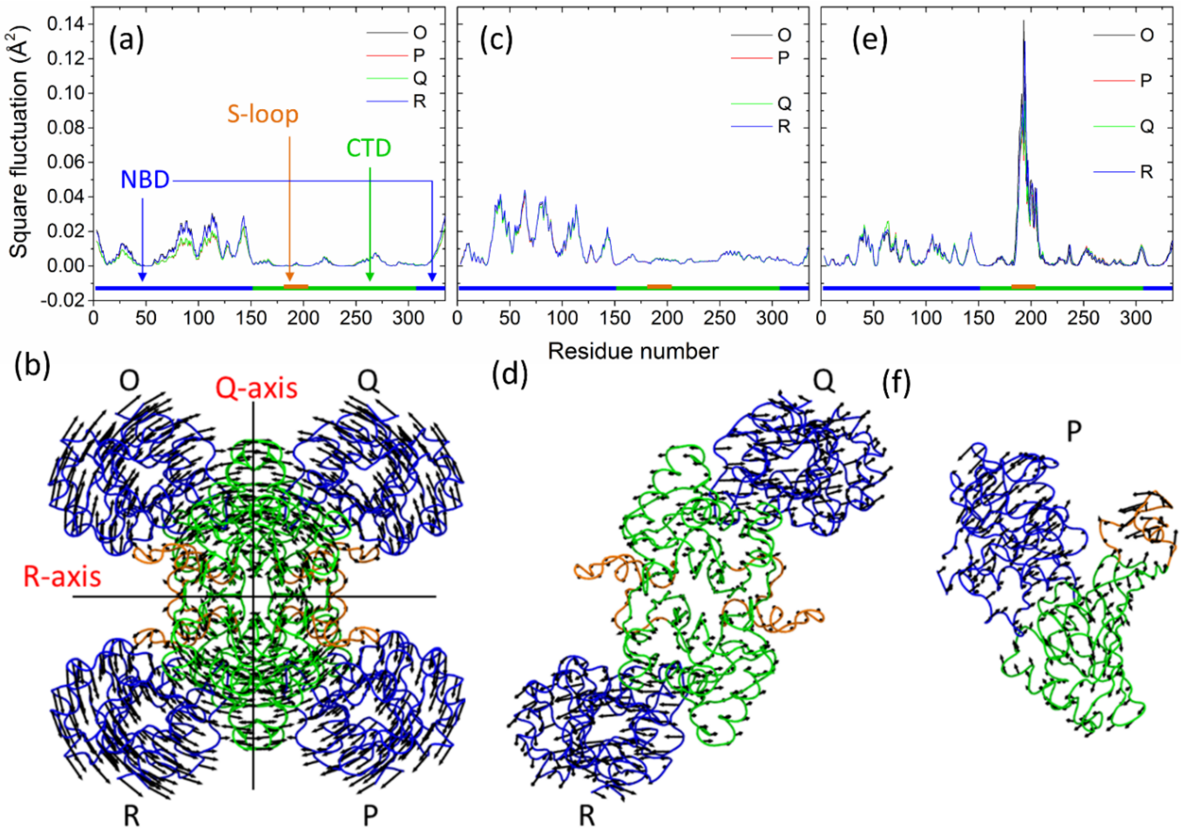

Figure 5.2: Normal mode analysis (NMA) of the tetramer, dimer, and monomer performed using ANM. Square fluctuation and the direction of C_α atoms of the (a, b) tetramer, (c, d) dimer-OP and -QR, and (e, f) monomer-O, -P, -Q, -R along normal mode 1 (NM1). NMA was carried on the crystal structure of the human GAPDH tetramer (PDB 1U8F), and the dimers and monomers extracted from it. Note that the monomer is in the pose shown in Figure S5.1 but NAD$^+$ is omitted for clarity.

5.4.2. Convergence of the MD trajectories of the tetramer, dimer, and monomer

We carried out seven replicate 100-ns (7 x 100 ns) all-atom MD simulations of the tetramer, dimer, and monomer of the human GAPDH. The convergence of the 100-ns MD trajectories was evaluated using the Good-Turing statistical analysis (Figure S5.4a). This approach reveals that 100-ns MD trajectories are converged because the probability of the unobserved RMSDs from the already sampled RMSDs remains unchanged between 100- and 300-ns MD trajectories for the three oligomeric states (Figure S5.4a-c). Also, the average RMSD of the C_α atoms of tetramer

(1.50 ± 0.24 Å; Figure S5.4d), dimer (1.80 ± 0.36 Å; Figure S5.4e) and monomer (2.32 ± 0.50 Å; Figure S5.4f) is stable for each 100 ns trajectory with minute differences between trajectories. Thus, we used the 100-ns MD trajectories for further analysis.

5.4.3. Flexibilities in the NBD and CTD subdomains calculated from MD simulations

Root-mean-square fluctuation (RMSF) of each C_α atom in the concatenated 7 x 100 ns MD trajectories is used to quantify the subdomain flexibilities of the three oligomeric states (Figure 5.3b). All the regions of the tetramer exhibit low RMSF values (< 2 Å; Figure 5.3a). Similarly, the dimer and monomer have low RMSF values for most subunit regions, except the S-loop. The S-loop is more flexible in the dimer (2-5 Å; Figure 5.3b) and highly flexible in the monomer (2-10 Å; Figure 5.3c). The RMSF values confirm high flexibility of the S-loop in monomer shown by NMA (Figure 5.2e).

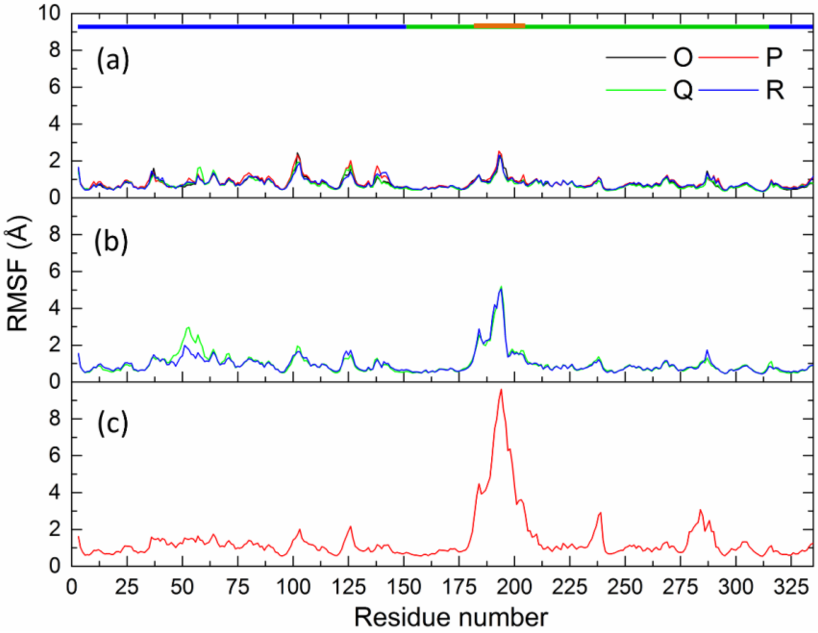

Figure 5.3: Root-mean-square fluctuation (RMSF) of the C_α atoms of the (a) tetramer, (b) dimer and (c) monomer. We analyzed concatenated 7 x 100 ns MD trajectories to calculate the RMSF from the crystal structure geometry. Note that RMSF is significantly larger for the S-loop in monomer vs. dimer and tetramer.

5.4.4. Correlated motions changes upon deoligomerization

We compared the cross-correlated motions of subunit-O with -P (Figure 5.4a) and subunit-Q with -R (Figure 5.4b) of the tetramer with those of the dimer (Figure 5.4c). Each square in Figure 5.4 represents a subunit of the tetramer or dimer with identical information on both sides of the diagonal. There are highly anticorrelated motions between the NBD and CTD of the subunits in the tetramer interacting across the P-axis, NBD_O and CTD_P, NBD_P and CTD_O, NBD_Q and CTD_R, NBD_R and CTD_Q (Figure 5.4a,b). However, there are noncorrelated motions between the NBDs of the subunits interacting across P-axis, NBD_O and NBD_P, NBD_Q and NBD_R (Figure 5.4a,b). These noncorrelated motions convert to anticorrelated motions in the dimer (Figure 5.4c). We also observe that there are highly correlated motions between CTD_Q and CTD_R in the dimer, which are anticorrelated in the tetramer. We previously showed that there are highly anticorrelated motions between the NBDs of subunits interacting across R-axis, e.g., NBD_O and NBD_R in the tetramer (Section 4.4.4).

We also examined intra-subunit cross-correlated motion, which highlights the motions within a subdomain or between subdomains, of a single subunit of the tetramer (Figure 5.4d), and compared with a subunit of the dimer (Figure 5.4e) and monomer (Figure 5.4f). There are highly correlated motions within the NBD and CTD in the tetramer and dimer. However, the noncorrelated motions between the subdomains in tetramer change to highly anticorrelated motions in the dimer (Figure 5.4d,e), signifies that the subdomains move in opposite directions in the dimer. The monomer exhibits the cross-correlated motions that differ significantly from those of the tetramer and dimer. In particular, the S-loop shows highly anticorrelated motion with all other residues, indicating that it moves opposite to the rest of the subunit (Figure 5.4f). Also, the monomer has highly correlated motions within NBD but not within CTD.

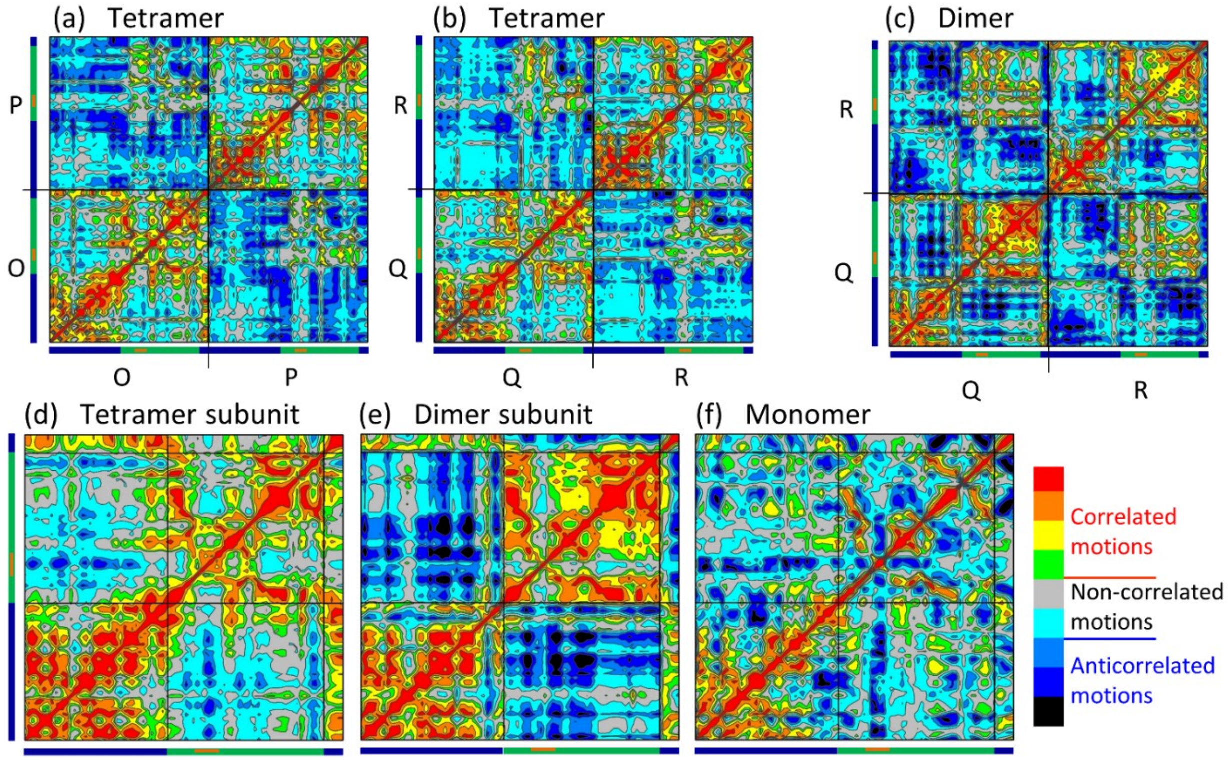

Figure 5.4: CCA carried out for C_α atoms of tetramer, dimer, and monomer using the concatenated 7 x 100 ns MD trajectories of the three oligomeric states. Inter-subunit cross-correlated motions of (a) subunit-O and subunit-P, (b) subunit-Q and subunit-R of the tetramer and (c) the dimer. The intra-subunit cross-correlated motions of (d) a tetramer subunit, (e) a dimer subunit, and (f) the monomer. Each square represents a subunit in panels (a-c) and a subdomain in panels (d-f). The blue, green and orange lines on the axes indicate NBD, CTD, and S-loop of each subunit, respectively. Note that the diagonals show the correlated motions of each C_α atom with itself.

To visualize the global motions of the three oligomeric states, we calculated cross-correlated motions using ANM and backbone atoms of the crystal structures the tetramer, and dimer and monomer extracted from it (Figure S5.3). The ANM cross-correlated motions are similar to the those from MD trajectories of the three oligomeric states (Figure 5.4a-f vs Figure S5.4a-f). However, the dominant S-loop anticorrelated motions eclipse the other anticorrelated motions during the MD simulation (Figure 5.4f vs Figure S5.4f). The similar cross-correlated motions generated by ANM and from the MD trajectories indicate that ANM captures the similar global motion of the oligomeric states without computational intensive MD simulations.

5.4.5. Varied conformational sampling of subdomains

PCA is used to separate functionally relevant motions from local fluctuation in the MD trajectories.[172,177,178] PCA of the 7 x 100 ns concatenated MD trajectories were performed and the free energy landscapes (FEL) based on principal component 1 (PC1) and PC2 allow us to visualize the conformational sampling of the three oligomeric states. The projection of the C_α atoms of each subunit on PC1 and PC2 indicates that the tetramer and dimer sample different conformations from the monomer, which exhibits the largest conformational space (Figure S5.5).

We projected the motions of the C_α atoms on PC1 to visualize their dominant displacements. The square fluctuations of all C_α atoms of the tetramer indicate the varied displacement of the NBDs between subunits (Figure 5.5a). This could reflect the binding of NAD^+ with negative cooperativity to GAPDH because flexible NBDs bind NAD^+ less tightly than rigid NBDs. Additionally, the direction represented as black arrows in the structures indicate that NBD_O and NBD_R move opposite to each other as do NBD_P and NBD_Q (Figure 5.5a). These motions highlight the importance of interactions across the R-axis. Most of the dynamics are centered on the NBDs, which move away from each other and from their respective CTDs in the dimer (Figure 5.5b). The S-loop is the most dynamical region of the monomer and its residues have the highest square fluctuation compared to all other residues. Also, the direction of motion indicates the opening of the S-loop in the monomer (Figure 5.5c).

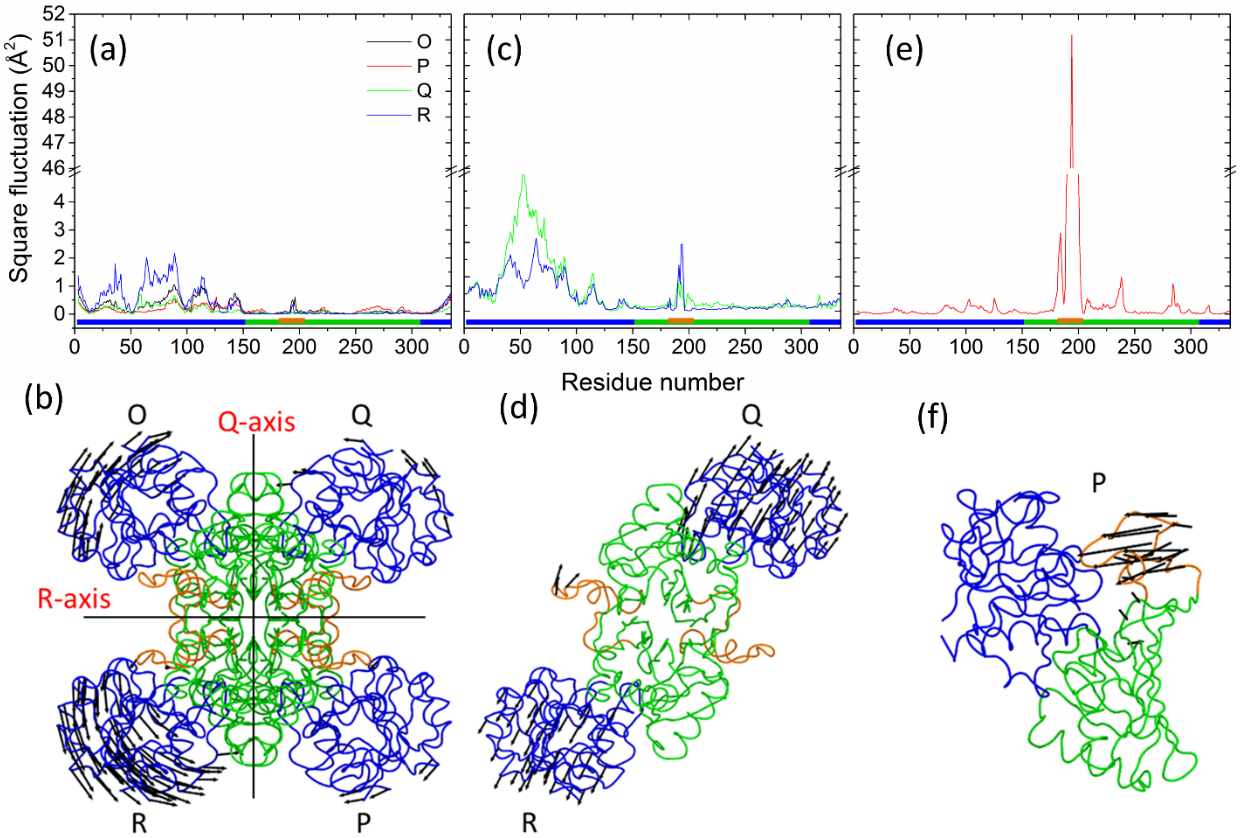

Figure 5.5: Square fluctuations of the tetramer, dimer, and monomer along PC1. PCA analysis was carried out using the 7 x 100 ns concatenated MD trajectories. Regions at the periphery in the tetramer and dimer structures correspond to the NBDs, whereas the CTDs are at the center. The arrows indicate the motions of C_α atoms with the square fluctuation of > 0.5 Å^2 in the tetramer and > 1 Å^2 in the dimer and monomer. The color blue, green and orange in structure represent the NBD, CTD, and S-loop, respectively. Note that the monomer is in the pose shown in Figure S5.1.

5.4.6. PCA of the S-loop

The FEL calculated using the C_α atoms of the S-loop projected along PC1 and PC2 reveals the limited conformational space close to the crystal structure in the four subunits of tetramer (Figure 5.6a-d). In the dimer, the S-loop accesses larger conformational space with two populations. In the monomer, the S-loop accesses the largest conformational space with multiple minima.

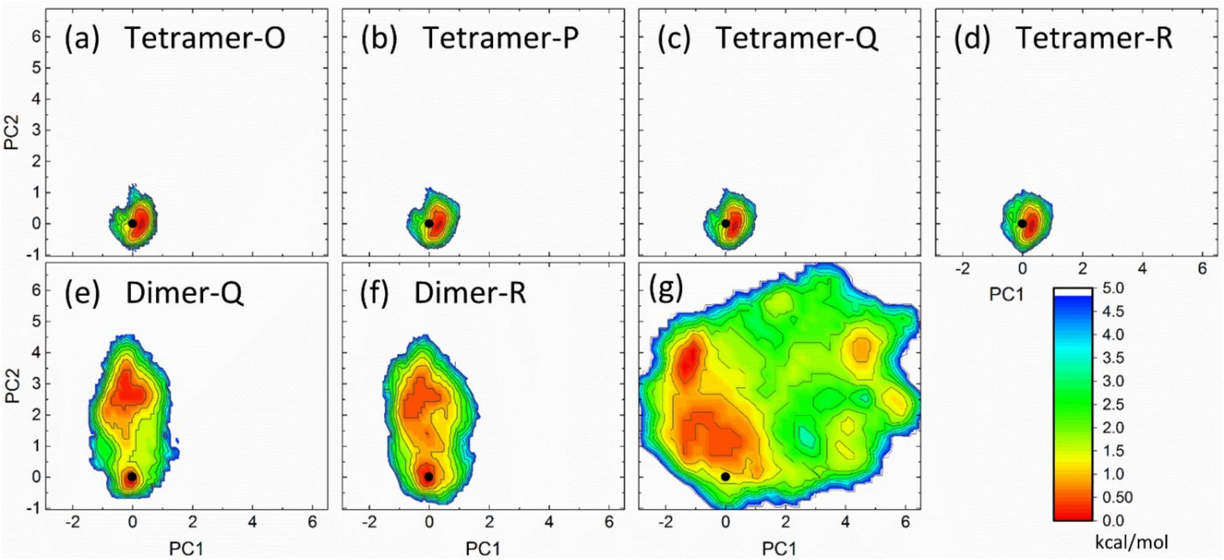

Figure 5.6: Free energy landscape (FEL) plotted using the projection of the C_α atoms of the S-loop of the tetramer, dimer, and monomer. PCA was carried out using the concatenated 7 x 100 ns MD trajectories of the S-loop of (a-d) the tetramer subunits, (e, f) the dimer subunits and (g) the monomer. The black dot in each panel indicates the crystal structure geometry of subunit-O of the tetramer. The unit for free energy is kcal/mol.

Since the S-loop accesses different conformational clusters in the monomer, we carried out 200-, 300- and 500-ns longer MD simulations to see if the S-loop attains a stable conformation as determined by PCA. The FEL show the three minima in the 7 x 100 ns MD simulations trajectories (Figure 5.7a), cluster-1, which has an S-loop conformation close to the crystal structure, cluster-2 with a closed S-loop conformation and cluster-3 with an open S-loop conformation. Cluster-1 and cluster-2 are accessed in the longer MD simulations of 200, 300 and 500-ns (Figure 5.7b-d). Cluster-2 is more populated in longer MD simulation compared to 100 ns MD simulations.

The closed S-loop conformations in cluster-2 arise due to NAD^+ movement. The nicotinamide moiety moves away from its binding site (away from Cys152) but, the less constrained S-loop interacts with the nicotinamide moiety and restricts NAD^+ from leaving its binding site in the monomer. This suggests that monomer is catalytically inactive because the nicotinamide moiety binds far from Cys152. However, the interaction of the nicotinamide moiety with the S-loop, as seen in cluster-2, could facilitate cofactor binding and in turn promote monomer to tetramer folding. The opening of the S-loop in cluster-3 could expose the active-site residues including catalytic Cys152 to the solvent, which could affect the reactivity of the monomer. However, we do not see this conformation accessed in longer MD simulations.

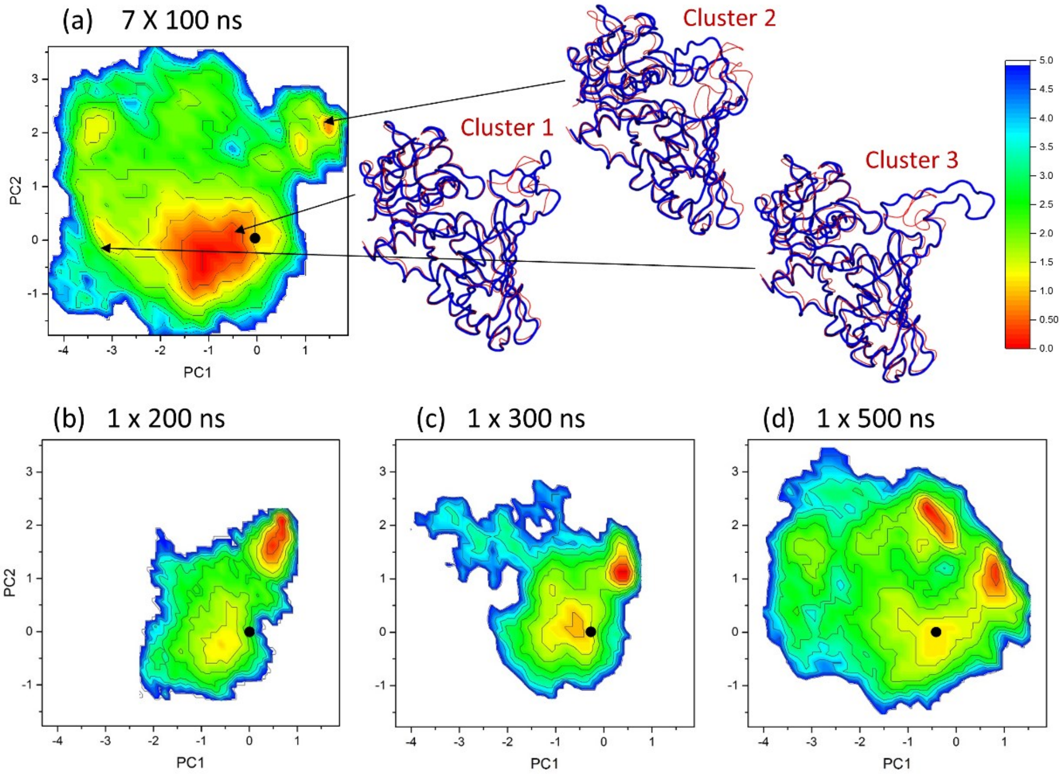

Figure 5.7: FEL plotted using the projection of all C_α atoms along PC2 vs PC1 calculated with all C_α atoms from 7 x 100 ns, 1 x 200 ns, 1 x 300 ns and 1 x 500 ns MD trajectories of the monomer. The black dot in each FEL plot indicates the conformation of subunit-O in the crystal structure. Structural images in red and blue tube indicate crystal structure and the average structure of the cluster, respectively. The unit for free energy is kcal/mol.

5.4.7. PCA of the NAD-binding residues

To evaluate the changes in the dynamics of the NAD binding residues, we carried out PCA of selected residues around 4 Å of NAD^+ (Figure S5.6). The significant differences in the conformational space of the NAD-binding residues in the subunits of the tetramer indicate the dynamical asymmetry in NAD-binding (Figure S5.6a-d). There are two major clusters in the four subunits of the tetramer, and their intensity varies between the subunits. The two clusters differ in the sidechain orientation of Phe37, one cluster has a Phe37 dihedral angle of 74° between the C-C_α-C_β-C_γ atoms and the other cluster has a dihedral angle of 173° (Figure 5.8a,b, and Figure 5.5a-b). Phe37 forms a T-shaped π-π interaction with the adenine group of NAD^+. This interaction is lost in cluster-2, which lead to weak binding of adenine moiety. These two clusters also are seen in the dimer subunits and monomer (Figure S5.6e-g), but the conformational space accessed varies significantly from the tetramer. Furthermore, these conformational variations are not dominant and cannot be separated based on cluster analysis.

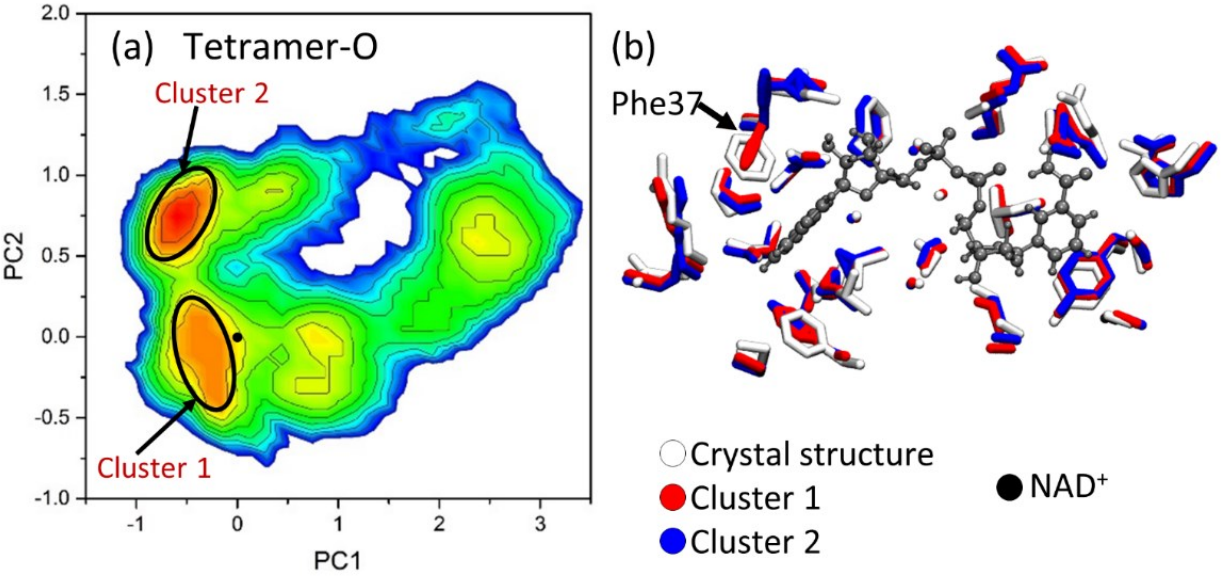

Figure 5.8: Free energy landscape (FEL) plotted using the projection of the C_α atoms and heavy atoms of the sidechains of residues within 4 Å of NAD^+ (NAD-biding residues) of subunit-O of the tetramer. (a) PCA was carried out using the concatenated 7 x 100 ns MD trajectories. (b) Average structure of the NAD-binding residues from cluster-1 and -2 are compared with the crystal structure of subunit-O of the tetramer. The unit for free energy is kcal/mol.

5.4.8. Variable stability of the Cys152 and His179 interaction

The interaction between catalytic Cys152 and His179 is important for dehydrogenase activity.[2,88] The distance between S_γ(Cys152) and Nε(His179) in the crystal structure of human GAPDH (PDB 1U8F) is between 3.4–3.7 Å in all four subunits of the tetramer. There are two populations of distances accessed in the tetramer and dimer. The first population has the S_γ(Cys152)–Nε(His179) distance of ~ 3.3 Å and the second population has the distance of ~ 5 Å (Figure 5.9). However, the monomer accesses only one population of the distance of ~ 3.1 Å (Figure 5.9) suggesting the H-bond interaction between Cys152 and His179 is strongest in the monomer compared to the dimer and tetramer.

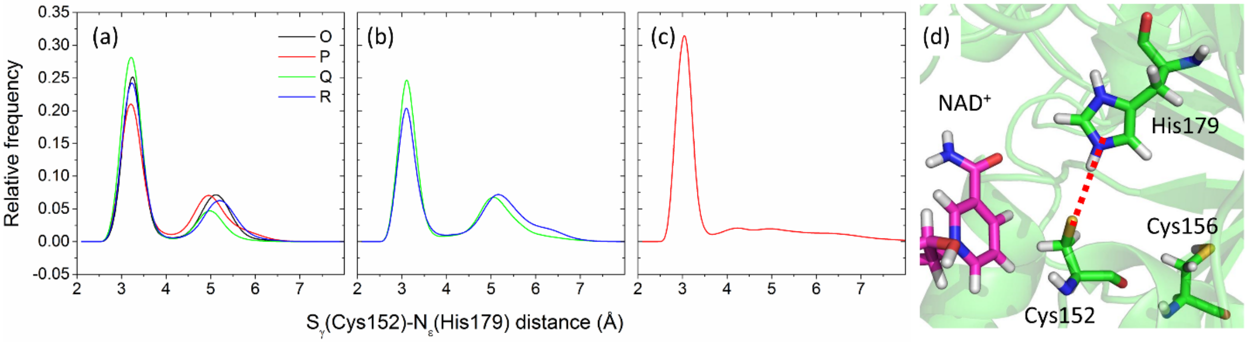

Figure 5.9: The S_γ(Cys152)–Nε(His179) separation in the tetramer, dimer, and monomer. Relative frequency of the distance is determined from the concatenated 7 x 100 ns MD trajectories of the (a) tetramer, (b) dimer, and (c) monomer. (d) The position of Cys152 and His179 in the active-site of the crystal structure of subunit-O GAPDH tetramer (PDB 1U8F). The measured distance is shown as a red dotted line.

5.4.9. NAD$^+$ binding to the three oligomeric states of GAPDH

NAD$^+$ moves away from its binding site in the tetramer during the MD simulations. Thus, the RMSF of selected atoms of NAD$^+$, shown as spheres, are calculated to quantify its motions (Figure 5.10). Atoms AO4' and AN9, O3, plus NO4' and NN1 represent the adenosine, pyrophosphate, and nicotinamide groups of NAD$^+$, respectively. NAD$^+$ fluctuates away from its binding site in one or two subunits of the tetramer in each run, which could be attributed to the negative cooperativity of NAD$^+$ binding to the tetramer. Note, NAD^+_P moves out of its binding site in run-5 (> 28 Å RMSF). The negative cooperativity of the tetramer is also observed in different crystal structures of GAPDH e.g. PDB 1U8F [105], 1J0X [190], 1ML3 [191]. In the dimer, part of NAD$^+$ moves away from its binding site in all trajectories but the cofactor does not completely leave its binding site as seen for the tetramer. NAD$^+$ remains in its binding site, except in run-5, suggesting a higher affinity for NAD$^+$ in the monomer.

The fluctuations of NAD$^+$ do not affect the global dynamics of the subunits in the tetramer because there is no difference in the RMSD (Figure S5.4) and RMSF (Figure 5.3) values between subunits that have large and small fluctuations in NAD$^+$.

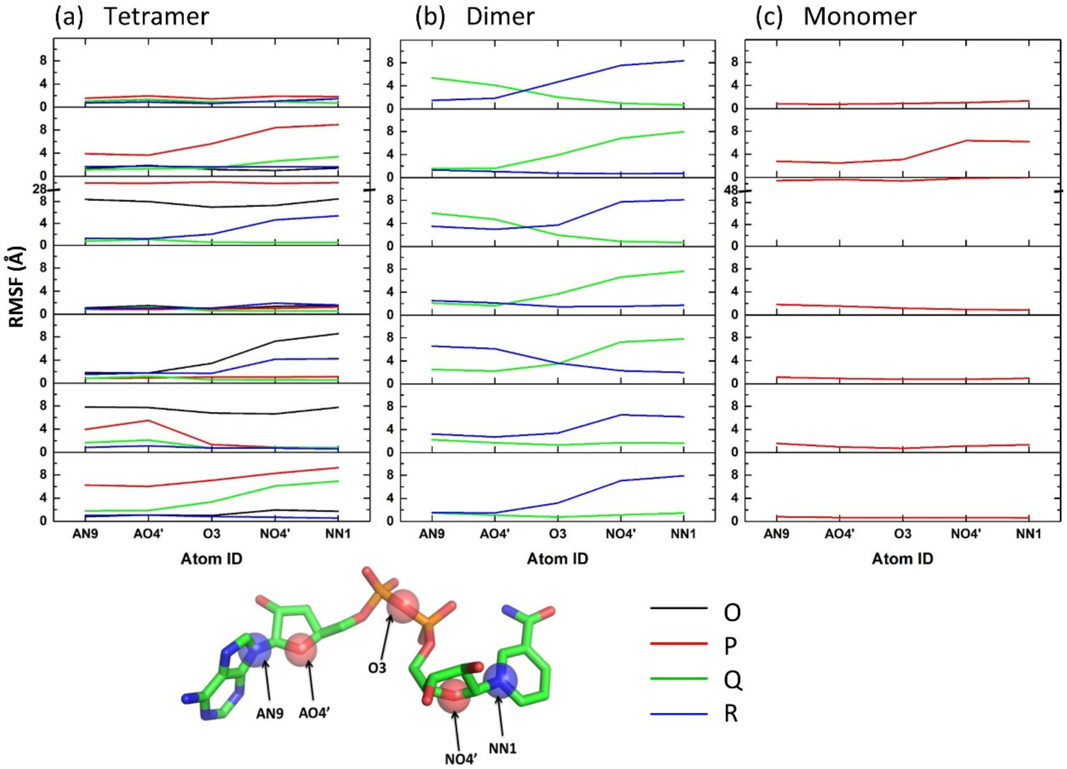

Figure 5.10: RMSF of selected atoms of NAD$^+$ in the tetramer, dimer, and monomer. RMSF is calculated for the selected atoms, shown as spheres, to quantify NAD$^+$ motion during individual 100-ns MD trajectories (run 1 to 7, bottom to top) for the tetramer, dimer, and monomer. Each graph represents a single trajectory and each line in the graph represents the RMSF of the selected NAD$^+$ atoms from each subunit as follows: AO4' and AN9 (adenosine), O3 (phosphate), and NO4' and NN1 (nicotinamide).

Similar significant fluctuations of the nicotinamide moiety of NAD^+ were also observed in MD simulations of *Trypanosoma cruzi* GAPDH-NAD^+ in the tetramer form.[166] MD simulations of the transition of *T. cruzi* apo- to holo-GAPDH shows that the angle between the C_α atoms of Arg80-Glu317-Ser192 (residue number according to human GAPDH) decreases due to binding of NAD^+.[166] The large angle between C_α atoms of these three residues in apo- compared to holo-GAPDH indicates an open form of NAD binding site in *T. cruzi* apo-GAPDH.[166] We compared the angle between these residues (56-59 ° in crystal structure of the human GAPDH) with the movement of NAD^+ measured by the distance between Cys152 and the positively charged nitrogen of NAD^+ [S_γ(Cys152)–N^+(NAD^+); 5.5-5.6 Å in human GAPDH crystal structure] (Figure S5.7). The angle does not change with the increase in the distance indicates that fluctuation of NAD^+ does not immediately affect the opening or closing of the NAD^+ binding site in the GAPDH tetramer.

5.4.10. GAPDH tetramer asymmetry and negative cooperativity

It has been shown that the Cys152 is close to His179 in two subunits (one subunit from each stable dimer) and near the nicotinamide of NAD^+ in the other two subunits of lobster GAPDH.[192] This phenomenon is associated with the asymmetry in the GAPDH tetramer and indirectly represents NAD^+ binding with the negative cooperativity to GAPDH tetramer. Thus, we compared the S_γ(Cys152)-N_ε(His179) and S_γ(Cys152)–N^+(NAD^+) distances in 9 runs of 100 ns of tetramer GAPDH (Table 5.1). Cys152 is close to His179 in one subunit and away in the other subunit of the OP or QR stable dimers of tetramer 11/18 times. This agrees with the observation of Rossmann and coworkers [192] that the distance S_γ(Cys152)-N_ε(His179) is smaller in one subunit of each stable dimer and reflects the asymmetry of the tetramer. Overall, Cys152 is close to His179 and away from the nicotinamide of NAD$^+$ for 19/36 times suggesting Cys152 interaction with His179 could influence the negative cooperativity to NAD$^+$ binding.

Table 5.1 Variation in S_γ(Cys152)-$N\varepsilon$(His179) and S_γ(Cys152)–N^+(NAD$^+$) distances in the human GAPDH tetramer [a]

Run	**Distance**	**Subunit-O**	**Subunit-P**	**Subunit-Q**	**Subunit-R**
1	CH	9	89	4	99
	CN	100	22	52	100
2	CH	28	13	54	86
	CN	5	100	100	100
3	CH	24	96	100	38
	CN	68	99	100	69
4	CH	43	71	96	90
	CN	100	99	100	99
5	CH	12	68	100	100
	CN	37	67	100	2
6	CH	48	55	16	18
	CN	100	69	80	99
7	CH	100	41	85	18
	CN	100	96	100	100
8	CH	22	97	76	98
	CN	16	100	50	38
9	CH	26	31	98	90
	CN	100	26	100	52

[a] The CH and CN denote S_γ(Cys152)-$N\varepsilon$(His179) and S_γ(Cys152)–N^+(NAD$^+$) distances. The distances are monitored for each 100-ns trajectory of GAPDH tetramer. The number represents the time (ns) when the CH or CN distance increases to ≥ 5 or ≥ 8 Å, respectively. Black, green and red texts represent stable, moderately stable and unstable interactions, respectively.

5.5. Discussion

5.5.1. Changes in the dominant motions upon deoligomerization of the GAPDH tetramer to dimer and monomer

NMA (Figure 5.2) and PCA (Figure 5.5) reveal that the dominant motions are centered on the NBD in tetramer and dimer. However, the high square fluctuations of the NBD and its motion in the direction opposite to the CTD of the same subunit reveal that dimer is less stable compared to tetramer. Also, the increase in anticorrelated motions (Figure 5.4a-c) between the NBD and CTD of the same subunit reveals destabilization of the interaction between the NBD and CTD subdomains in the dimer. Thus, deoligomerization of tetramer to dimer changes subdomain motions within a subunit.

NMA reveals that the S-loop is more flexible, not the NBD, in the monomer. The MD simulations further confirm that the major motions are centered on the S-loop, as shown by the 4-fold higher RMSFs (Figure 5.3c) and 25-fold higher square fluctuation along PC1 (Figure 5.5c,f) of the S-loop compared to other residues in the monomer. This signifies the importance of S-loop dynamics in the monomer and the NBD dynamics the in dimer and tetramer. Although the monomer retains highly correlated motions within the NBD, these are lost within the CTD (Figure 5.4f) revealing its destabilization. However, NMA reveals instability in both NBD and CTD subdomains of the monomer (Figure S5.3f). Thus, the loss of highly correlated motions within subdomains reveals the monomer is less stable compared to the tetramer and dimer. The instability of the monomer is also represented by the highly anticorrelated motions of the S-loop with all other residues. Since the S-loop and NBD move opposite to each other, this allows the S-loop to attain the open/closed conformation as shown by FEL (Figure 5.7a).

5.5.2. Importance of S-loop flexibility in the function of the GAPDH monomer and dimer

NMA of the crystal structure and MD simulations reveal that the S-loop is highly flexible in the monomer. The S-loop also is more dynamic in the dimer compared to the tetramer, but less dynamic in the monomer. S-loop flexibility is observed in the crystal structure of apo-GAPDH from *K. marxianus* (PDB: 2I5P), which is proposed to be a transition structure from the tetramer to the dimer with very high B-factor for residues 183-202 (part of the S-loop) and does not have bound NAD^+.[165] Also, dimeric *B. stearothermophilus* GAPDH has less affinity for NAD^+ compared to its tetramer.[77] Thus, the large movement of the S-loop during MD simulations of the dimer and monomer could be a pathway for the dissociation of the GAPDH tetramer to the dimer and to the monomer. The dissociation of the tetramer is highly likely to occur because of the simultaneous process of removal of NAD^+ from its binding site and increased flexibility in the S-loop.

Moreover, the inactivity of the dimer (equivalent to the dimer-QR) in *B. stearothermophilus* GAPDH[77] can be explained by its flexible S-loops, which expose the active-site to the solvent and inactivate the dimer. Additionally, disulfide bond formation between catalytic Cys152 residue to form the aggregates, implicated in neurodegenerative disease,[193] could be explained by the flexible S-loop in the monomer. Because Cys152 is buried in the protein matrix in the tetramer, as it is covered by the S-loops, disulfide bond formation between the catalytic Cys152 of two subunits is impossible due to steric clashes (Figure 5.1c), as shown previously.[189] However, a highly flexible S-loop would expose Cys152 and allow disulfide bond formation in monomer or dimer. Note that the same report proposed that Cys281 (residue number according to rabbit muscle GAPDH) is involved in aggregation, but the equivalent cysteine residue is not present in human GAPDH.

The increased flexibility in the S-loop could induce binding of monomer or dimer of GAPDH to other proteins. Also, the exposure of the catalytic Cys152 could allow it to react with residues of other proteins. Thus, S-loop motions could play an important role in different functions of monomer or dimer of GAPDH.

Apart from the S-loop, residues Arg234–Asn239 and Glu278–Thr290 are more flexible than other residues of the CTD in the monomer. Interestingly, Arg234-Asn239 are part of the residues (222-240) of GAPDH implicated in binding with seven in absentia homologue (Siah1) to promote neuronal cell death after S-nitrosation of GAPDH (See Chapter 6).[14] Siah1 is assumed to bind to the GAPDH tetramer, but the large movement in this region during MD simulations of the GAPDH monomer suggests that the Arg234-Asn239 loop could play important role in GAPDH-Siah1 binding.

5.5.3. Insight into the glycolytic active-site

The weak interaction between S_γ(Cys152)-N_ε(His179) in dimer and tetramer compared to the monomer indicate that the reactivity of Cys152 may change upon deoligomerization. However, the interaction is mostly stable during MD simulations, which suggests that the charged Cys152 and His179 stabilize the active-site in the tetramer, dimer, and monomer. Residues Cys152 and Cys156 in the glycolytic active-site of GAPDH are in proximity to each other, but Cys156 is buried inside the protein matrix (Figure 5.1). Additionally, Cys156 is located in a helix, which adds additional structural constraints to keep Cys152 and Cys156 away from each other. This is evident from the S_γ(Cys152)-S_γ(Cys156) distance (>8 Å) in the tetramer, dimer, and monomer calculated during MD simulations (Figure S5.8). Thus, a disulfide bond between Cys512 and Cys156 is highly unlikely in the three oligomeric states of GAPDH.

Water molecules are readily accessible to the Cys152, but not Cys156 (Figure S5.9). This suggests that Cys152 can be readily oxidized, but Cys156 oxidation is less probable. Additionally, the oxidation sensitivity of Cys152 and Cys156 does not change upon opening of the S-loop in the monomer. Although, Cys156 might not be directly involved in the oxidation of Cys152 but could influence it by a proton relay mechanism as proposed by Peralta *et al.* (Section 4.4.10).[167] We observed a similar strong H-bond interaction between O_γ(Thr153)-O_ζ(Tyr314) in the tetramer, dimer, and monomer (Figure S5.10).

5.5.4. Cooperativity of NAD$^+$ binding to GAPDH

NAD$^+$ movement in one or two subunits only may be attributed to the negative cooperativity of NAD$^+$ binding to the tetramer. There is no change in Arg80-Glu317-Ser192 angle (Figure S5.7), indicating no changes in the size of the NAD$^+$ binding site upon NAD$^+$ movement. Also, there is no direct correlation between the movement of a specific residue and NAD$^+$. Thus, the negative cooperativity could be due to collective motions of the NBDs in the tetramer as shown by PCA (Figure 5.5).

The flexible S-loop in its closed conformation stabilizes the interaction of NAD binding residues with nicotinamide of NAD$^+$ (cluster-2) in the monomer (Figure 5.7). Similarly, the flexible S-loop could stabilize interaction with NAD$^+$, making up for the loss of affinity for NAD$^+$ upon solvent exposure of the adenosine binding site in the dimer. This explains the positive cooperativity found in the dimer of *B. stearothermophilus* GAPDH, where the first NAD$^+$ (K_1 = 5.20 ± 0.43 μM) binds less tightly than the second NAD$^+$ (K_2 = 1.51 ± 0.16 μM).[77]

5.6. Conclusions

Our study highlights the alterations in the dominant motions of the subdomains upon deoligomerization of the GAPDH tetramer to the dimer or monomer. Specifically, we show that NBD motions are dominant in the tetramer and dimer. NBD and CTD of the same subunit move in opposite direction to each other in the dimer. Also, the dominant motions are centered on the S-loop in monomer. The highly flexible S-loop in the monomer and in the dimer to lesser extent suggests that the monomer and dimer favor binding with other protein partners to stabilize the disordered S-loop. Interactions of monomer or dimer of GAPDH with other protein partners could lead to different functions other than glycolysis.

We show that the dimer and monomer are less stable compared to the GAPDH tetramer. Deoligomerization of the tetramer to the dimer leads to increased anticorrelated motions between NBD and CTD of the same subunit. Further deoligomerization to monomer leads to anticorrelated motions within both the NBD and CTD. Lower stability is also evident from the more flexible S-loop in dimeric and monomeric GAPDH.

NAD^+ binding is very dynamic as shown by its fluctuations during MD simulations of the tetramer, dimer and monomer. However, there are no significant changes in the NAD-binding residues upon deoligomerization of the tetramer to the dimer or monomer. Also, our study confirms that disulfide bond formation is highly unlikely between Cys152-Cys156 in the three oligomeric states of GAPDH but tetramer dissociation to the monomer might affect the oxidation sensitivity of GAPDH due to the increased flexibility of the active-site. In sum, our study shows that the tetramer, dimer, and monomer posses specific structural dynamics that could influence their functions.

5.7. Supporting Information

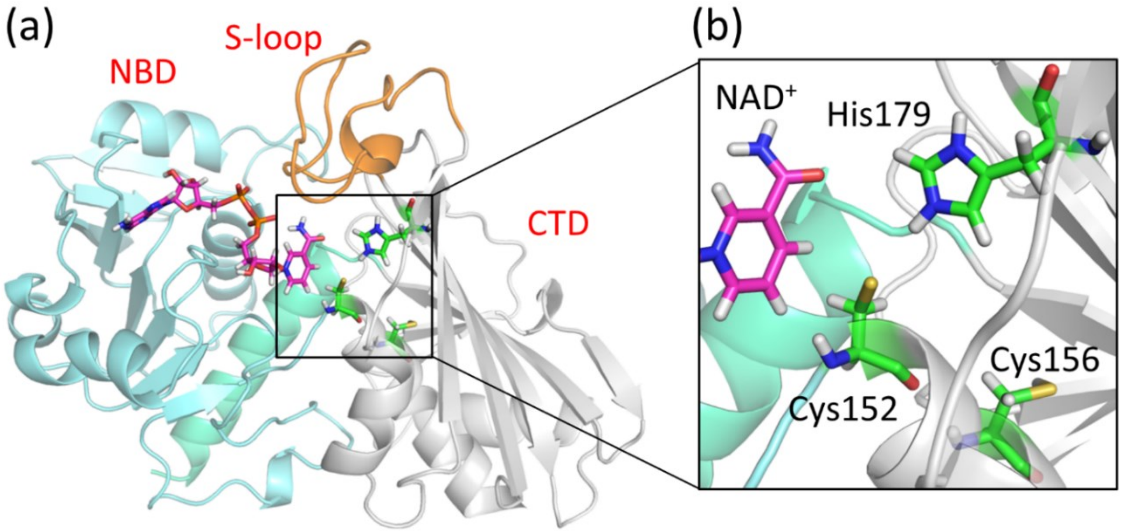

Figure S5.1: Subdomains and active-site residues in the GAPDH subunit. (a) Subdomains including the NAD-binding domain (NBD; residues 1-151 & 315-335; cyan), catalytic domain (CTD; residues 152-314; white) and S-loop (residues 181-205; orange) are shown. (b) The position of catalytic Cys152 and other active-site residues are shown as sticks. NAD$^+$ is shown in magenta colored sticks.

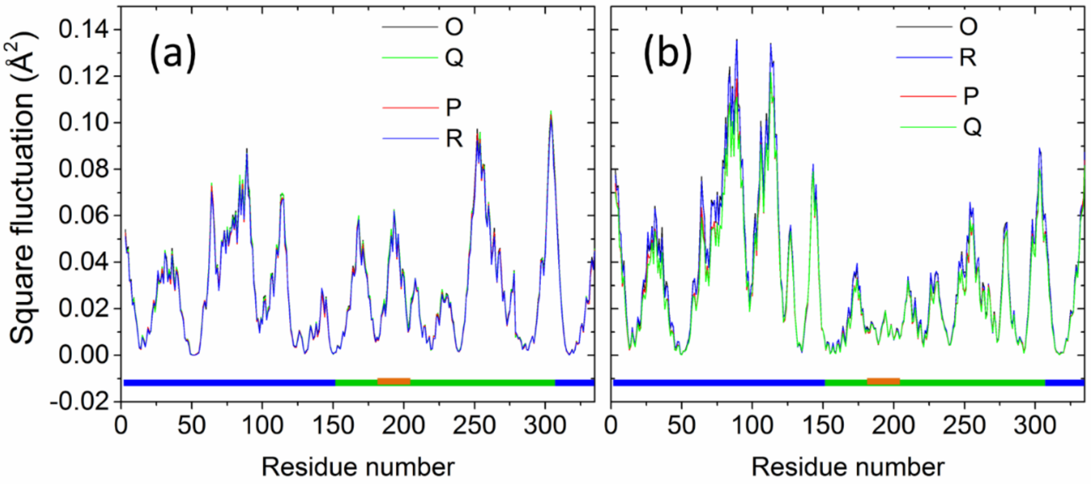

Figure S5.2: Normal mode analysis (NMA) of the dimer-OQ, -PR, -OR and -PQ carried out using ANM. Square fluctuation of the C_α atoms of (a) dimer-OQ, (b) dimer-PR (c) dimer-OR and (d) dimer-PQ along NM1. The dimers were extracted from the crystal structure geometry of GAPDH tetramer (PDB 1U8F).

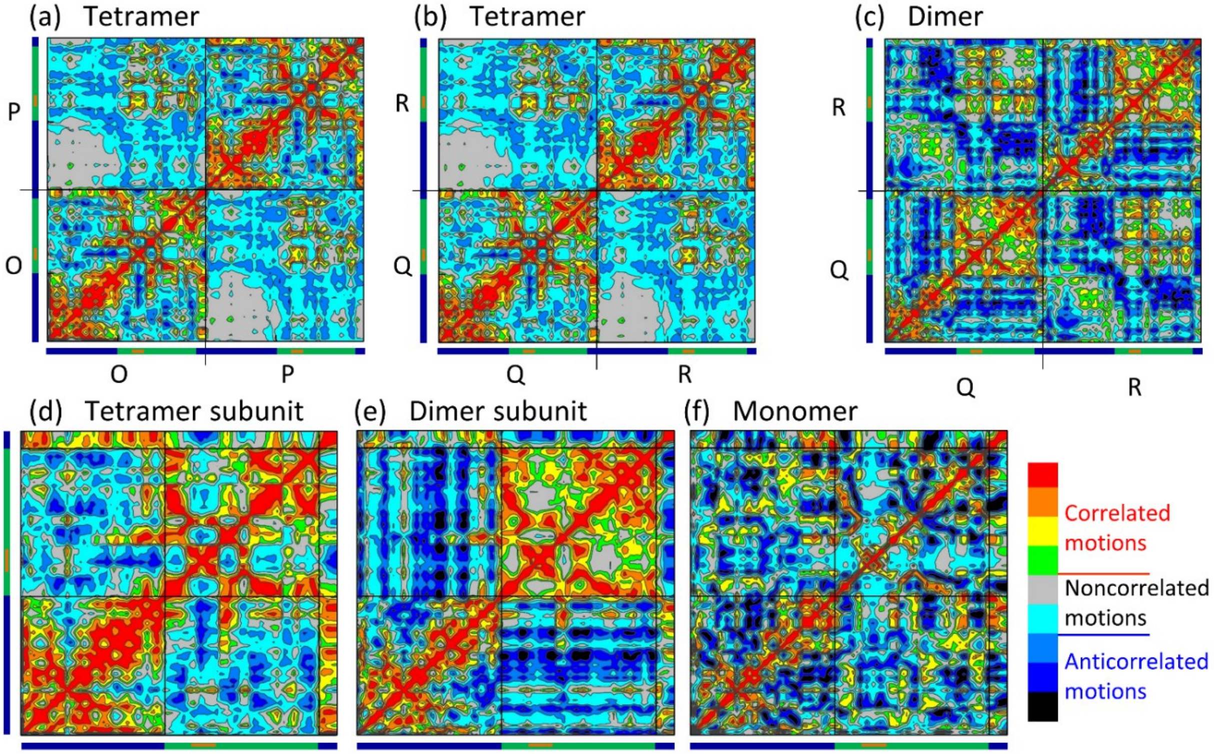

Figure S5.3: CCA carried out for C, C_α, N, and O backbone atoms of the tetramer, dimer, and monomer using ANM. We used the crystal structure of the tetramer of human GAPDH and extracted the dimer and monomer. Inter-subunit cross-correlated motions of (a) subunit-O and subunit-P of the tetramer, (b) subunit-Q and subunit-R of the tetramer are compared with (c) dimer. The intra-subunit cross-correlated motions of (d) a tetramer subunit, (e) a dimer subunit and (f) monomer are compared to highlight the motions within and between subdomains. See captions to Figure 5.4.

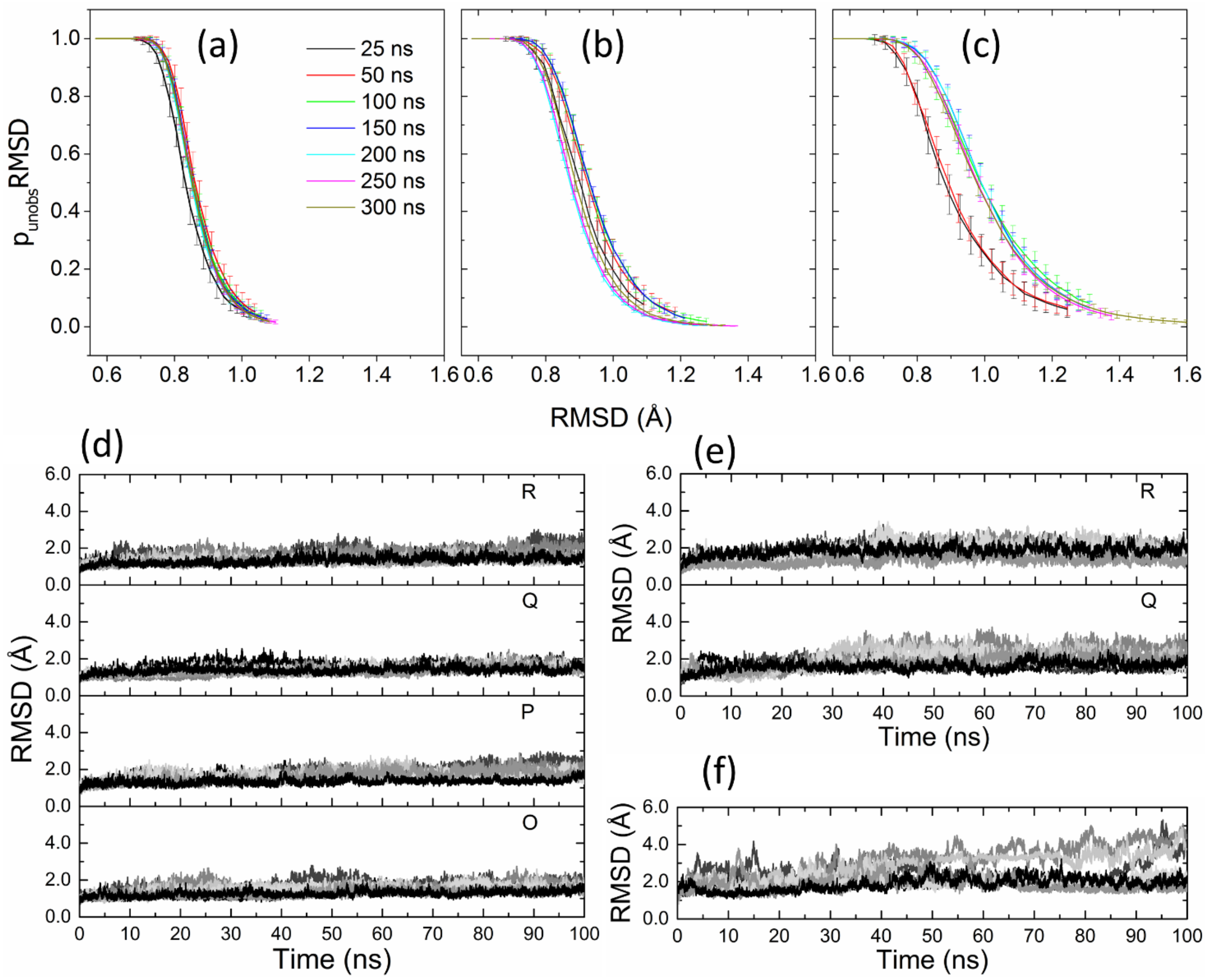

Figure S5.4: Convergence of MD simulations trajectories evaluated with Good-Turing statistical analysis and root mean square deviation (RMSD). Good-Turing statistical analysis was carried out using the C_α atoms extracted at every 20 ps for tetramer, dimer, and monomer from a 300 ns trajectory. No change in the shape of the curve going from 100- to 300-ns trajectory indicates that 100-ns trajectories are converged. RMSD was calculated for the 7 x 100 ns MD trajectories for the three oligomeric states. RMSD does not change over 100 ns, except monomer, which has the highly dynamic S-loop.

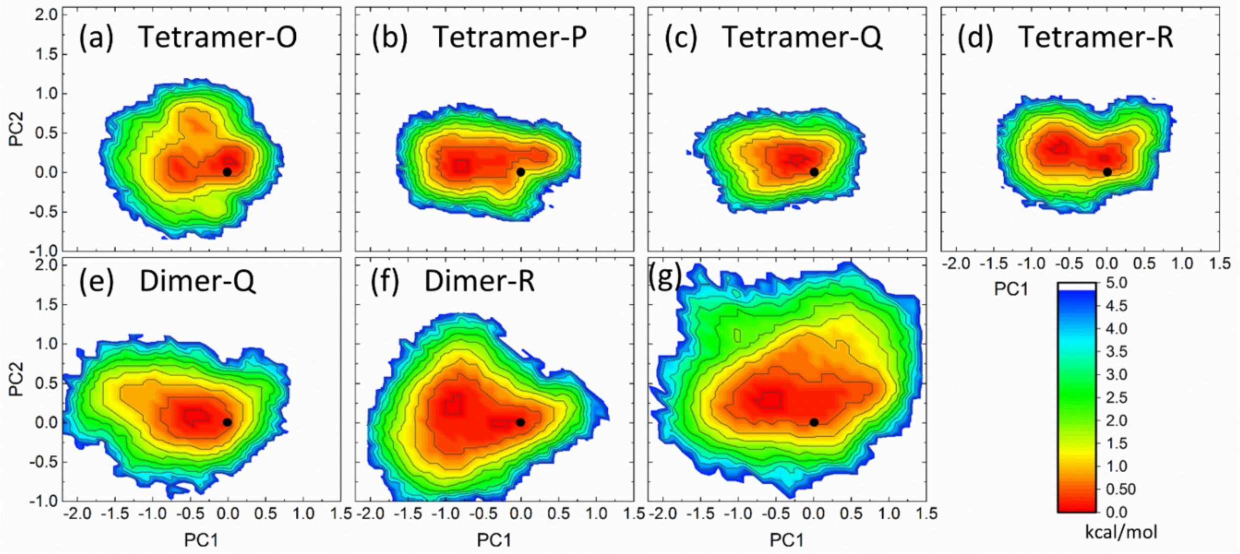

Figure S5.5: Free energy landscape (FEL) plotted using a projection of the C_α atoms along PC1 and PC2. PCA was carried out using the concatenated 7 x 100 ns MD trajectories of (a-d) tetramer subunits, (e,f) dimer subunits and (g) monomer. The black dot in each panel indicates crystal structure geometry of subunit-O of the tetramer. The unit for free energy is kcal/mol.

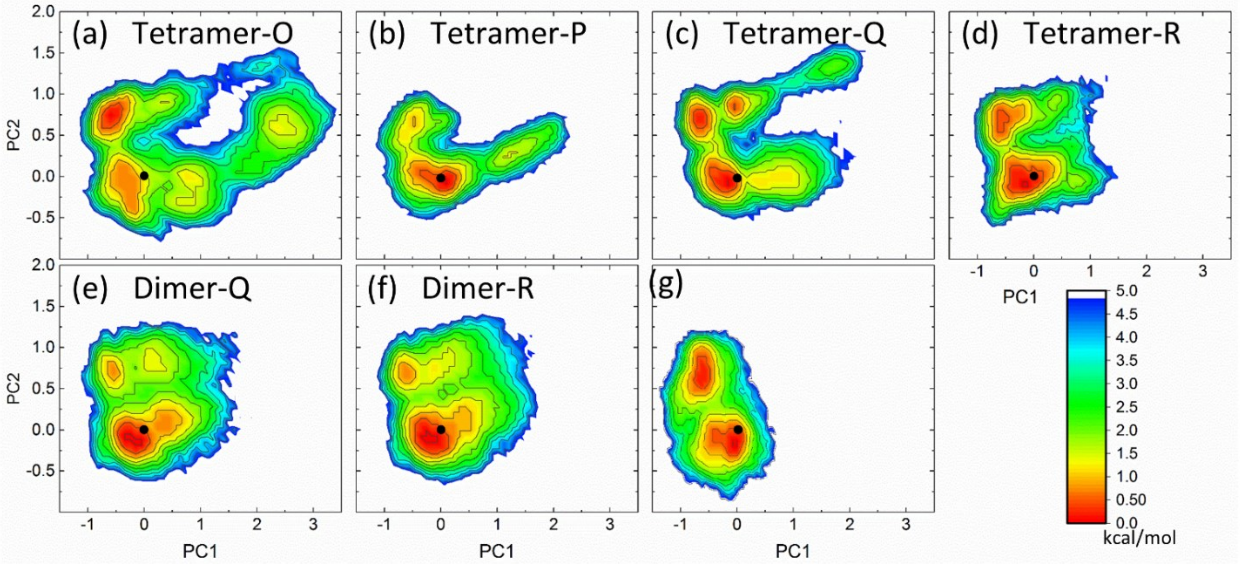

Figure S5.6: FEL plotted using a projection of C_α atoms and heavy atoms of sidechains of residues around 4 Å of NAD^+ (NAD binding site residues). PCA was carried out using the concatenated 7 x 100 ns MD trajectories of (a-d) tetramer subunits, (e, f) dimer subunits and (g) monomer. The black dot in each panel indicates crystal structure geometry of subunit-O of the tetramer. The unit for free energy is kcal/mol.

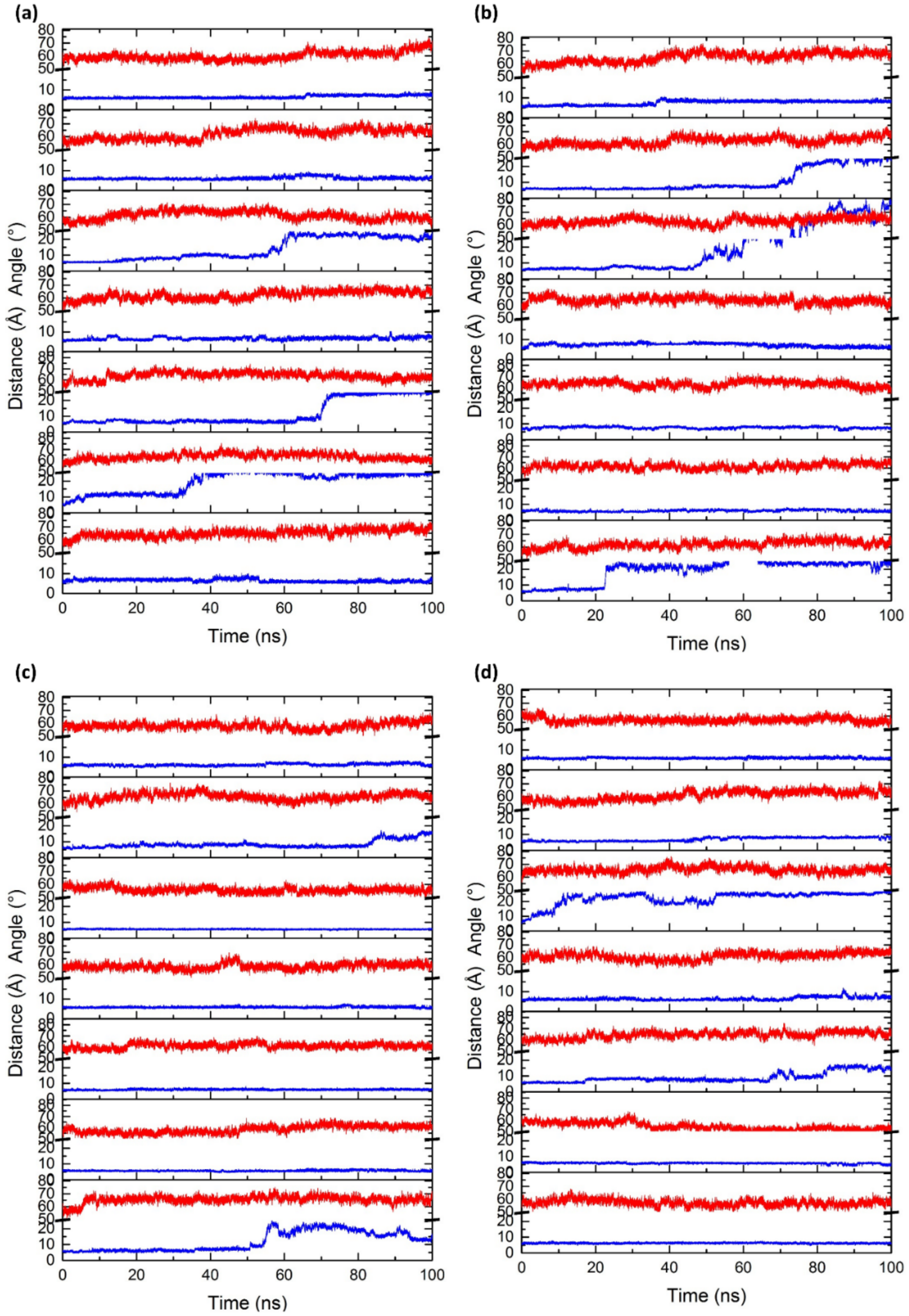

Figure S5.7: Flexibility of NAD binding site with respect to NAD$^+$ fluctuation. Comparison between Arg80-Glu317-Ser192 (red line) angle and S_γ(Cys152)–N^+(NAD$^+$) distance (SN distance; blue line) of (a) subunit-O (b) subunit-P (c) subunit-Q (d) subunit-R of tetramer in 7 individual 100 ns MD trajectories (run 1 to 7, bottom to top).

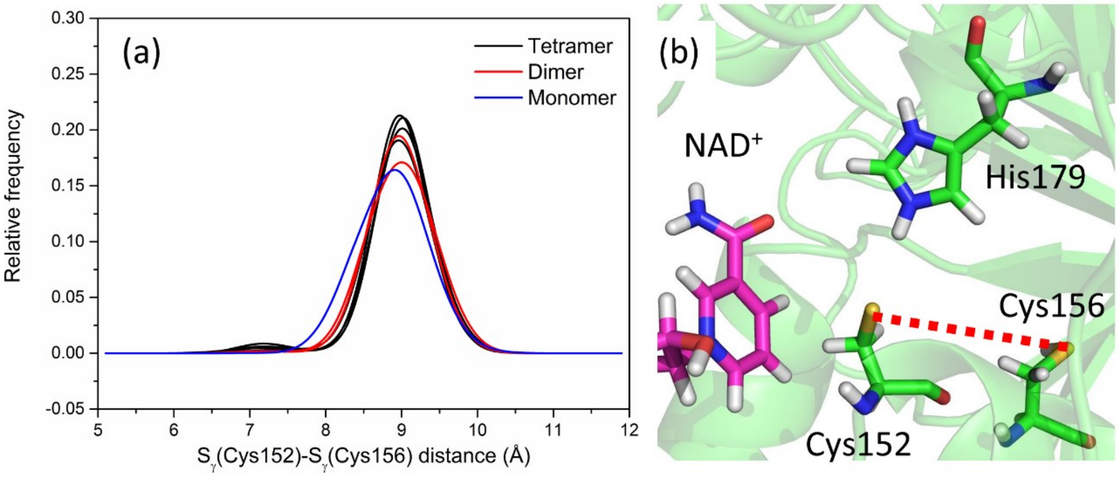

Figure S5.8: The distance between S_γ(Cys152)– S_γ(Cys156) in the tetramer, dimer, and monomer. (a) Relative frequency of the distance is calculated using concatenated 7 x 100 ns MD simulations trajectories. (b) The position of Cys152 and Cys156 in the active-site of subunit-O of the crystal structure of human GAPDH. The distance is shown as a red dotted line.

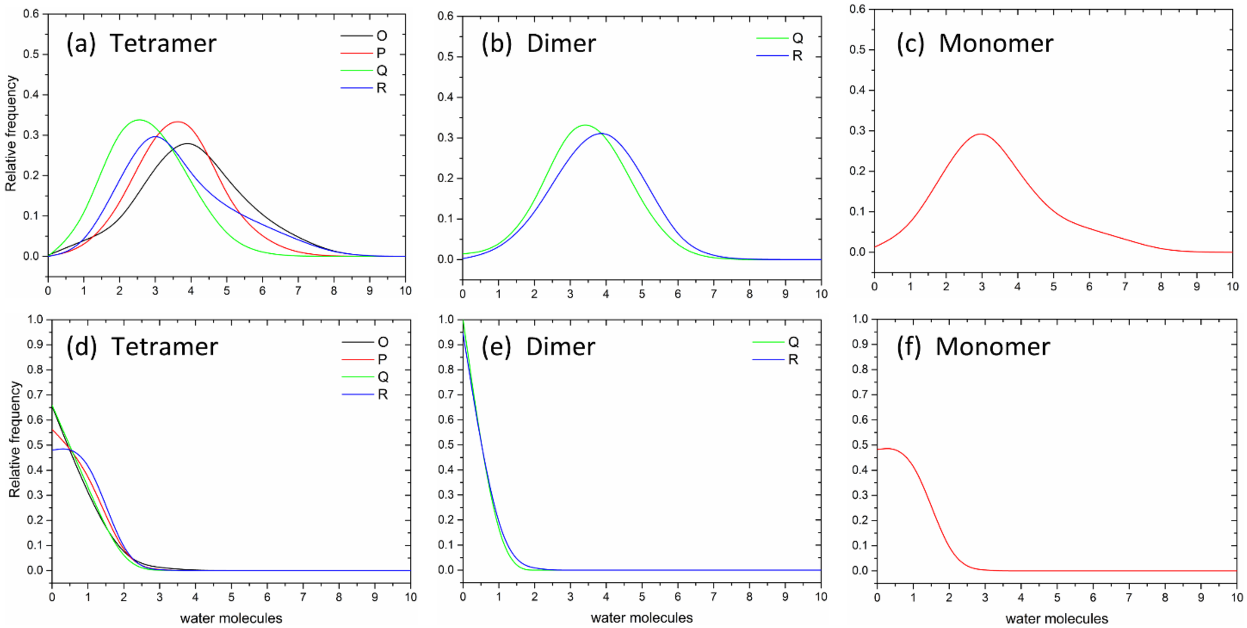

Figure S5.9: Number of water molecules near Cys152 and Cys156. Relative frequency of a number of water molecules near 3 Å of (a-c) Cys152 and (d-f) Cys156 calculated using the concatenated 7 x 100-ns trajectories for (a, d) tetramer, (b, e) dimer and (c, f) monomer.

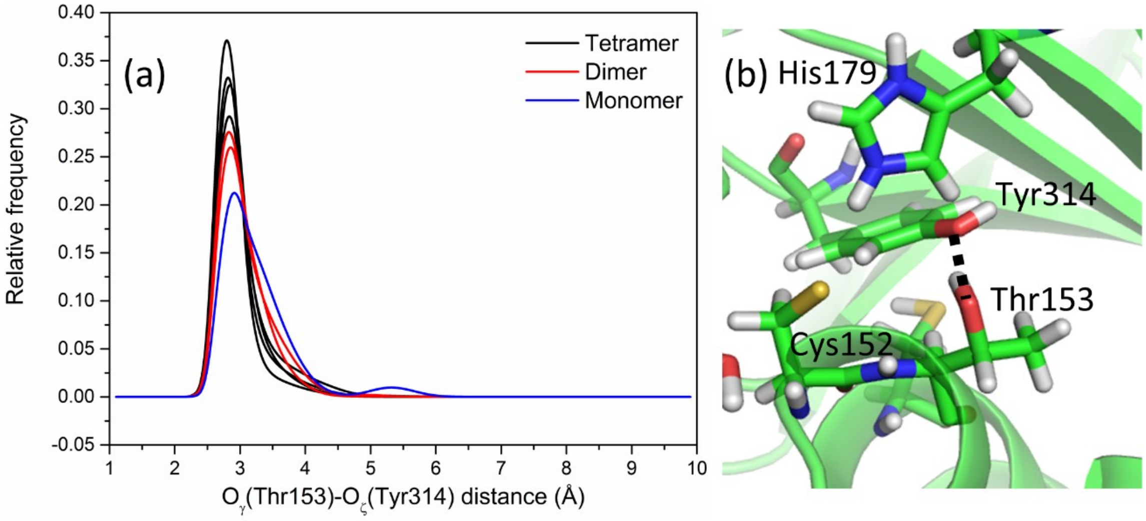

Figure S5.10: The distance between O_γ(Thr153)-O_ζ(Tyr314) in the tetramer, dimer, and monomer. (a) Relative frequency of the distance is from the concatenated 7 x 100 ns trajectories of the tetramer, dimer, and monomer. (b) The position of Cys152 and Cys156 in the active-site of subunit-O of the crystal structure of human GAPDH. The measured distance is shown as a black dotted line.

Chapter 6. Computational Modeling of Glyceraldehyde-3-Phosphate Dehydrogenase – Seven-In-Absentia Homolog 1 (Gapdh-Siah1) Complex

6.1. Abstract

The role of glyceraldehyde-3-phosphate dehydrogenase (GAPDH) in apoptosis is associated with complexation and stabilization of seven-in-absentia homolog 1 (Siah1). Upon GAPDH S-nitrosation the complex, formed between S-nitrosylated GAPDH and Siah1, is translocated to the nucleus, which initiates a cascade of events to trigger apoptosis. It is proposed that the GAPDH tetramer forms a complex with four Siah1 dimers to give ~400 kDa complex. However, our docking analysis of the GAPDH tetramer and monomer with the Siah1 dimer and monomer indicates stronger complex formation between the GAPDH monomer and Siah1 dimer (~110 kDa complex) or monomer (~80 kDa complex), compared to that between the GAPDH tetramer and Siah1 dimer. Complex formation with the GAPDH monomer stabilizes the S-loop and promotes complexation.

6.2. Introduction

Glyceraldehyde-3-phosphate dehydrogenase (GAPDH) is implicated in apoptosis. This is a mechanism of cell death, which in neurons contributes to neurodegenerative diseases.[1,15,24,194,195] However, the mechanism of GAPDH's accumulation in the nucleus during apoptosis was poorly understood until recently because the enzyme does not have a nuclear localization signal (NLS). Nuclear translocation of GAPDH is associated with S-nitrosation of its catalytic Cys152, which leads to its binding to the unstable seven-in-absentia homolog 1 (Siah1),[14,181] an E3 ubiquitin ligase that has a NLS. It was shown that binding to S-nitrosated GAPDH stabilizes Siah1 in cells. The complex is translocated into the nucleus by the NLS on Siah1 and Siah1 facilitates degradation of nuclear targets to promote apoptosis.[14] A further study by the same group reported that GAPDH is acetylated at Lys160 by the acyltransferase P300/cAMP response element-binding protein (P300/CBP) in the nucleus to increase cytotoxicity.[196] GOSPEL (GAPDH's competitor Of Siah Protein Enhances Life) was found to compete with Siah1 for complex formation with GAPDH to retain GAPDH in the cytoplasm and decrease cytotoxicity of the GAPDH-Siah1 complex.[28]

The question arises as to how a small post-translational modification such as S-nitrosation initiates complex formation between GAPDH and Siah1. What structural changes occur in GAPDH on S-nitrosation? What are the molecular level interactions between Siah1 and GAPDH? It is proposed that the GAPDH tetramer binds to Siah1 but, monomeric GAPDH is found in the nucleus.[87] Also, nitric oxide-induced S-nitrosation of GAPDH is proposed to alter the equilibrium between monomers, dimers, and tetramers of GAPDH.[197] Thus, we hypothesize that the GAPDH monomer is formed upon S-nitrosation, and it interacts with Siah1 to form a stable complex rather than the tetramer of GAPDH.

Human GAPDH, a homotetramer, is 150 kDa protein. Each subunit (labelled O, P, Q and R) contains a NAD-binding domain (NBD; residues 1-151, 315-335) and a catalytic domain (CTD; residues 181-205) (Figure 6.1a,b). Residues 222-240 (yellow), implicated in Siah1 binding, are located at the dimer interface of subunits interacting across the P-axis.[14] Mutation of Lys227 (yellow spheres) causes loss of Siah1 binding, indicating the importance of this GAPDH residue in complex formation.[14] The Siah1 subunit consists of an N-terminal RING (Really Interesting New Gene) domain, which is involved in its ligase function, two zinc-finger subdomains and a C-terminal substrate-binding domain (SBD; residues 90-282), which is involved in the formation of the Siah1 dimer.[198,199] All the crystal structure of Siah1 do not have resolved the structure of the RING domains. Residues 270-282 of Siah1 are involved in its binding with GAPDH. These residues are part of the SBD (residues 90-282), which is located at the dimer interface of Siah1.

Based on the information about the residues involved in GAPDH and Siah1 complex formation, a docking study was carried out to probe binding between these two proteins.[105] This study proposed that the GAPDH tetramer binds with four Siah1 dimers, making the complex of ~ 400 kDa.[105] Although, the NLS can translocate large nucleic acids of 100-200 kDa,[200,201] the large complexes of ~ 400 kDa size are not that easy to translocate. Our hypothesis is that the GAPDH monomer forms a complex with either the monomer or dimer of Siah1 to create a complex of ~ 80 or ~ 110 kDa, respectively.

We carried out docking analysis to model the complex of GAPDH and Siah1. The electrostatic surface of GAPDH and Siah1 were evaluated for the complementarity between both the GAPDH tetramer and monomer with the Siah1 dimer or monomer.

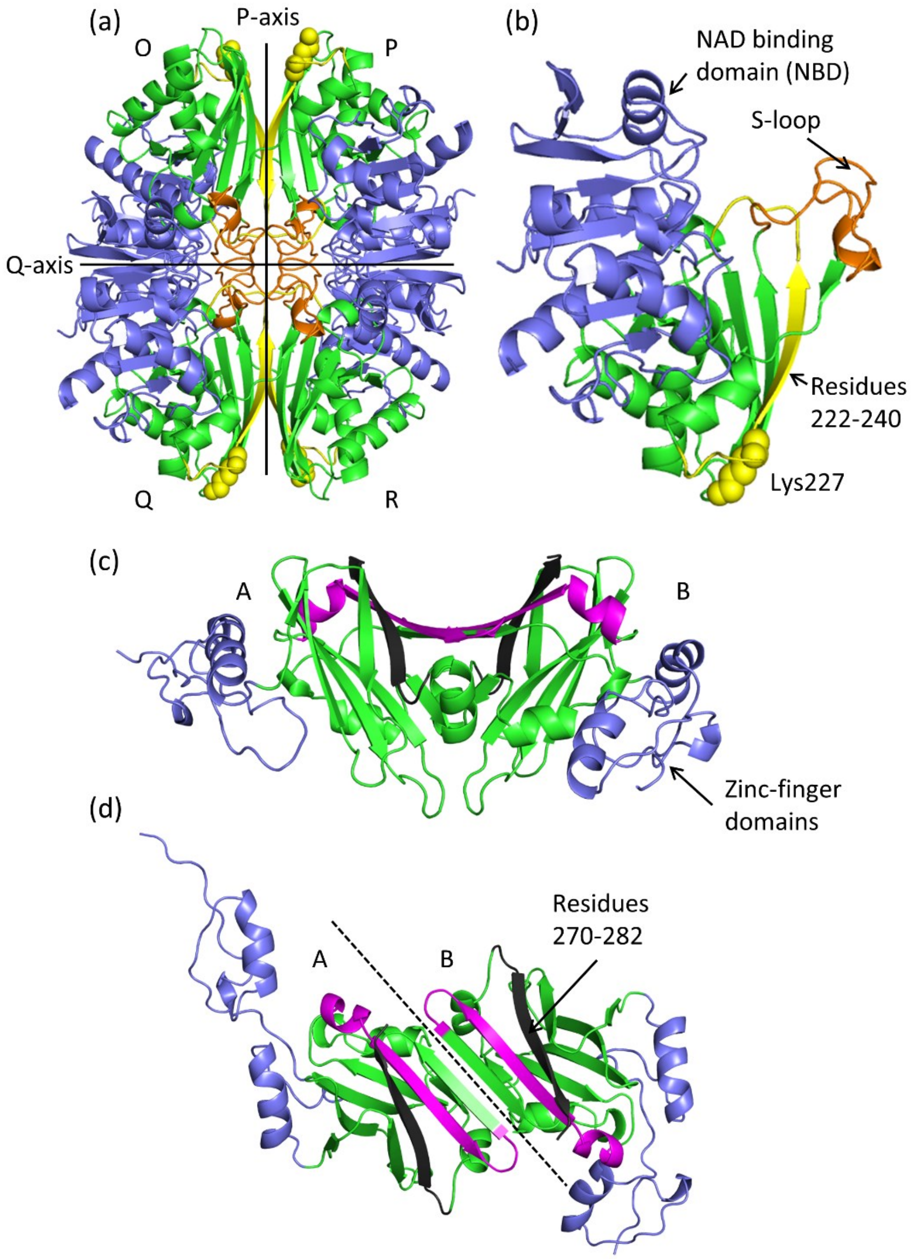

Figure 6.1. Structural features of human GAPDH (PDB 1U8F) and Siah1 (PDB 4C9Z). The secondary structure of the human GAPDH (a) homotetramer and (b) its subunit, showing the NAD binding domain (NBD, blue; residues 1-151, 315-335), the catalytic domain (CTD, green; residues 152-314) and the S-loop (orange; residues 181-205). Residues 222-240 of the CTD (yellow) are implicated in Siah1 binding and the yellow spheres are Lys227. (c,d) The secondary structure of Siah1. Residues 215-232 (magenta) correspond to nuclear localization signal (NLS) and residues 270-282 (grey) are implicated in binding to GAPDH**.** Note that NAD$^+$ is omitted from GAPDH in the panels (a, b) and Zn^{2+} from Siah1 in panels (c, d) for clarity.

6.3. Computational Methods

We used the crystal structures of human GAPDH (PDB 1U8F) and human Siah1 (PDB 4C9Z) to generate electrostatic surfaces of these proteins. The crystal structures do not have hydrogen atoms so we used the PDB2PQR server [202] to generate forcefield parameters, add hydrogen atoms, and protonate residues to optimize the hydrogen bonding networks in order to prepare the structures for calculations of the electrostatic potential surface. The distribution of electrostatic charges in the two protein structures was calculated in water with 0.15 M NaCl using Adaptive Poisson-Boltzmann Solver (APBS) software [203] and mapped onto their molecular surfaces. PyMol [204] was used to visualize the electrostatic surfaces and the secondary structure of the proteins.

A combination of webservers, PatchDock [205,206] and FireDock [207,208] was used for the docking studies. PatchDock carries out rigid-body docking by dividing the surfaces of the two proteins into small patches based on their shapes. These patches are matched and superimposed based on their surface complementarity. Complexes with steric clashes are filtered and the remaining complexes are ranked based on a shape complementarity score. PatchDock generates 1000 complexes, and the top 20 complexes were further refined and scored by FireDock. This refines the complexes by side-chain rearrangement, which were modeled based on their rotamers. The complexes were further refined by soft rigid-body rotation of the proteins and the refined complexes were ranked based on the binding score. We visualized the top 10 binding complexes based on the score and characterized the interactions between the protein partners.

6.4. Results and Discussion

6.4.1. Electrostatic surfaces of GAPDH

The electrostatic charges mapped on the GAPDH tetramer show a large positively charged surface area (blue) along the P-axis with small scattered negatively charged surface regions (red) (Figure 6.2a). The electrostatic surface close to Lys227 is mostly negatively charged (Figure 6.2b), indicating that the proposed binding site of Siah1 close to Lys227 should have a complementary positively charged surface. We also observe a narrow negatively charged cavity along the Q-axis (Figure 6.2c). A similar negatively charged cavity is observed in the crystal structure of GAPDH from other species (e.g. *P. versicolor* and *B. stearothermophilus* GAPDH, data not shown) but, the corresponding cavity is positively charged in lactate dehydrogenase and mitochondrial aldehyde dehydrogenase (ALDH2). Thus, this structural feature might be unique to GAPDH but its role in the different functions of GAPDH has not been investigated.

In contrast to the GAPDH tetramer (Figure 6.2a,b), the electrostatic surface of the GAPDH monomer shows a positively charged surface area close to Lys227 on removal of the other subunits, especially those interacting across the P-axis (Figure 6.3a,b). Also, residues 222-240 of GAPDH implicated in Siah1 binding are exposed, enabling direct interaction with Siah1. The electrostatic surface in the monomer has large positively charged surface on one side and large negatively charged on the other side of the residues 222-240.

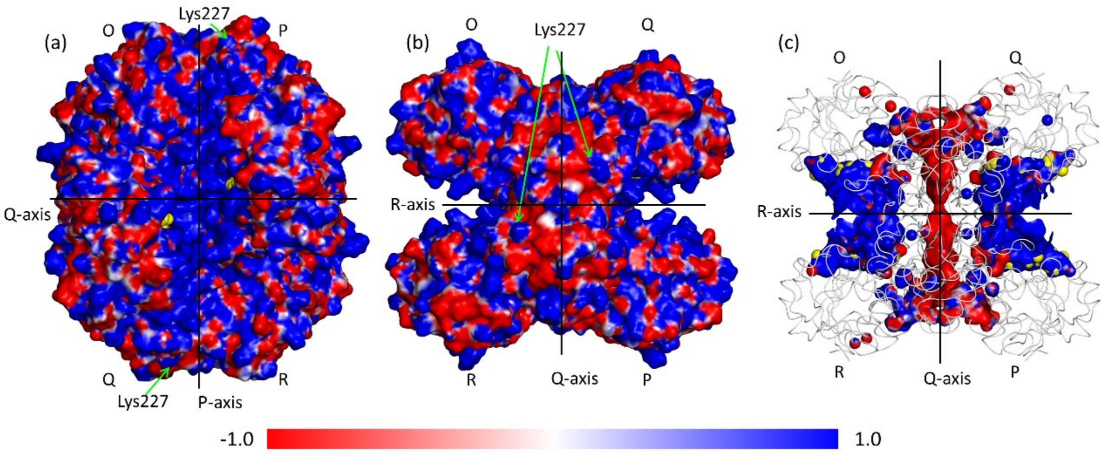

Figure 6.2. Electrostatic surface of the GAPDH tetramer. The structural pose in panel (a) is similar to that in Figure 6.1a. The tetramer is rotated in panel (b) to show the electrostatic surface close to Lys227, which is implicated in Siah1 binding. Note that residues 222-240, implicated in Siah1 binding, are mainly buried in the protein matrix between the subunits interacting across the P-axis. Panel (c) shows the electrostatic surface of cavities inside the GAPDH tetramer. The large positively charged cavities along the R-axis represent the NAD-biding sites, whereas the negatively charged cavity along the Q-axis represents a tunnel between subunits interacting across the Q-axis. The secondary structure of the protein is shown as white tubes. The contour scale for electrostatic surface is -1 kT/e (red) and +1 kT/e (blue). PyMol was used for visualization of electrostatic potential surface.

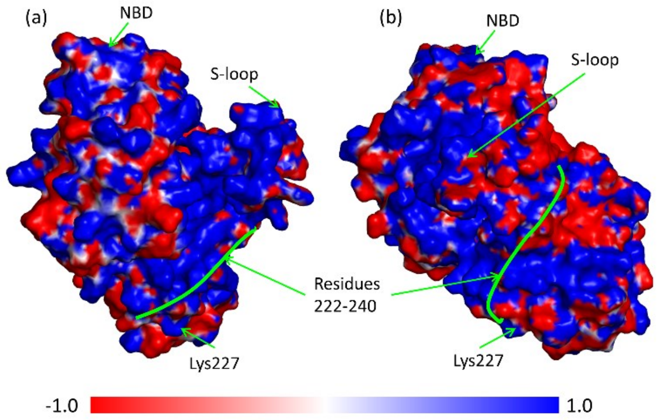

Figure 6.3. Electrostatic surface of the GAPDH monomer. The structural pose in panel (a) is similar to the one shown in Figure 6.1b. The monomer structure is rotated by 90° in panel (b) to show the electrostatic surface area close to residues 222-240, including Lys227, which are implicated in Siah1 binding. Note that residues 222-240 are exposed in the monomer. See caption to Figure 6.2 for details.

6.4.2. Electrostatic surface of the Siah1 dimer and monomer

The Siah1 dimer has a large negatively charged electrostatic surface with a small positively charged area near the zinc-finger domain (Figure 6.4a,b). The surface close to residues 270-282, implicated in GAPDH binding, are highly negatively charged (Figure 6.4b). However, the electrostatic surface area of the GAPDH tetramer near Lys227 is mostly negatively charged (Figure 6.2b) suggesting that the tetramer is unlikely to form a strong complex with the Siah1 dimer. Separation of the GAPDH subunits exposes a positively charged electrostatic surface patch near Lys227 and residues 222-240 in the GAPDH monomer (Figure 6.3). This positively charged area should favor the interaction of Siah1 with the GAPDH monomer. Siah1 is known to exist as a dimer, but the monomer also could interact with GAPDH. Thus, we looked at the electrostatic surface at the Siah1 dimer interface and find that the interface has a complementary positive and negative charged regions between to subunits. Hence, Siah1 monomer could be a better binding partner for monomer GAPDH.

6.4.3. Docking of the GAPDH tetramer with the Siah1 dimer

We carried out docking analysis with the GAPDH tetramer as a target and the Siah1 dimer as a substrate without targeted docking. The Siah1 dimer was allowed to explore interactions with all regions of the GAPDH tetramer without any constraints. However, multiple runs with different parameters did not reveal any docking pose where residues 270-282 of Siah1 bind close to Lys227 of GAPDH. Thus, we defined a binding site in GAPDH close to Lys227 and Siah1 close to residues 281-282, which are part of the residues implicated in GAPDH binding, to perform a targeted docking analysis. Only one docking pose was found , where Lys227 interacts with residue 281 and 282 (Figure 6.5a,b). The GAPDH tetramer interacts mainly with the zinc-finger domain of the Siah1 dimer (Figure 6.5a). In contrast, Jenkins and Tanner [105] reported a docking pose where

GAPDH interacts with the SBD of Siah1. They further used the symmetry of GAPDH to generate a complex of the GAPDH tetramer with four Siah1 dimers, two the dimers OP and QR of the GAPDH tetramer. However, our analysis produces no docking pose similar to the published report.[105] Furthermore, our analysis indicates that the complex formed by the GAPDH tetramer and Siah1 dimer is weak with very small interface area.

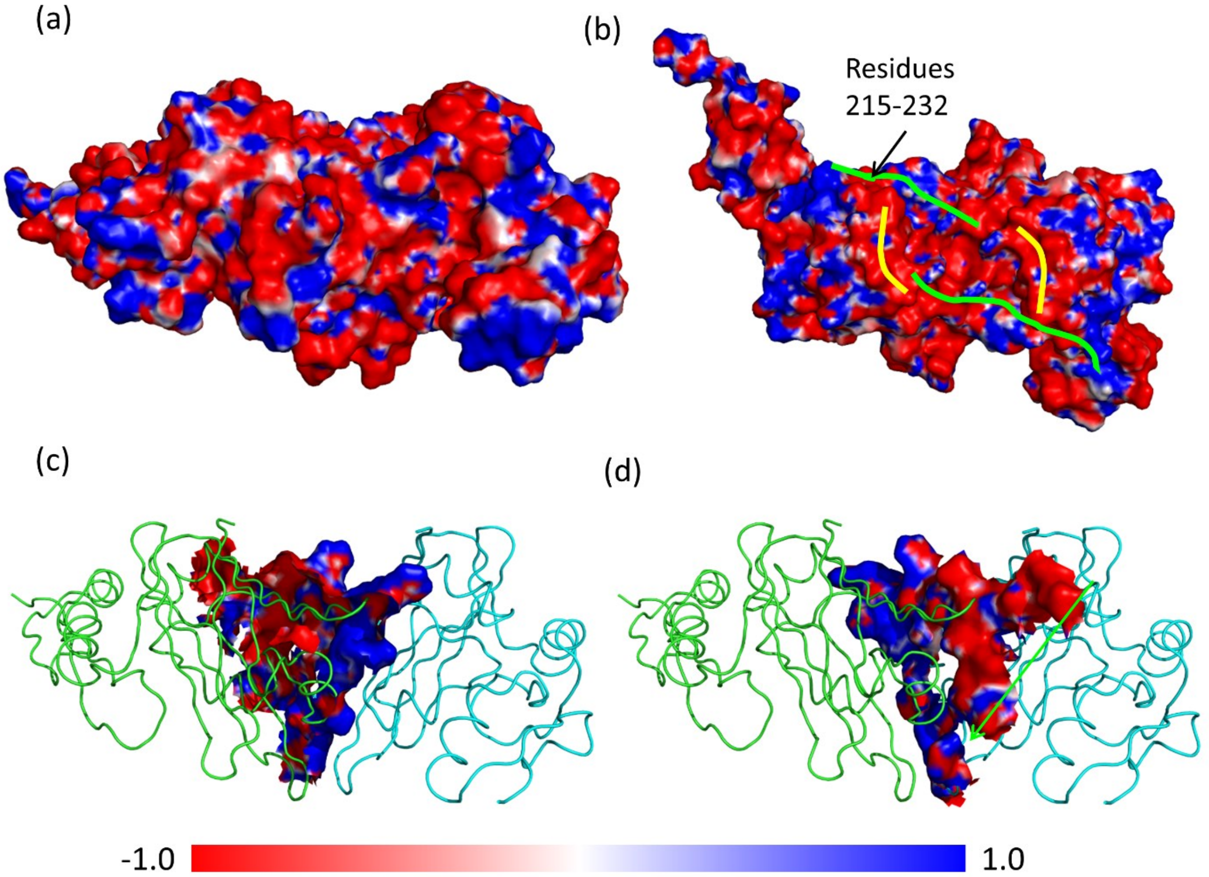

Figure 6.4. Electrostatic surface of the Siah1 dimer. The poses in panels (a) and (b) are similar to those shown in Figure 6.1c and 6.1d, respectively. The electrostatic surface of the Siah1 dimer is mostly negatively charged, so its interaction with GAPDH requires positively charged complementary regions. Residues 270-282, implicated in GAPDH binding, are in the region highlighted by the yellow lines. The green curved lines mark residues 215-232, which contains the nuclear localization signal (NLS). Panels (c) and (d) show the interacting electrostatic surface of subunit-A with subunit-B. Positive and negative region complement each other at the binding interface. Note that the structural pose in panels (c) and (d) is similar to that in panel (a). See caption to Figure 6.2 for details.

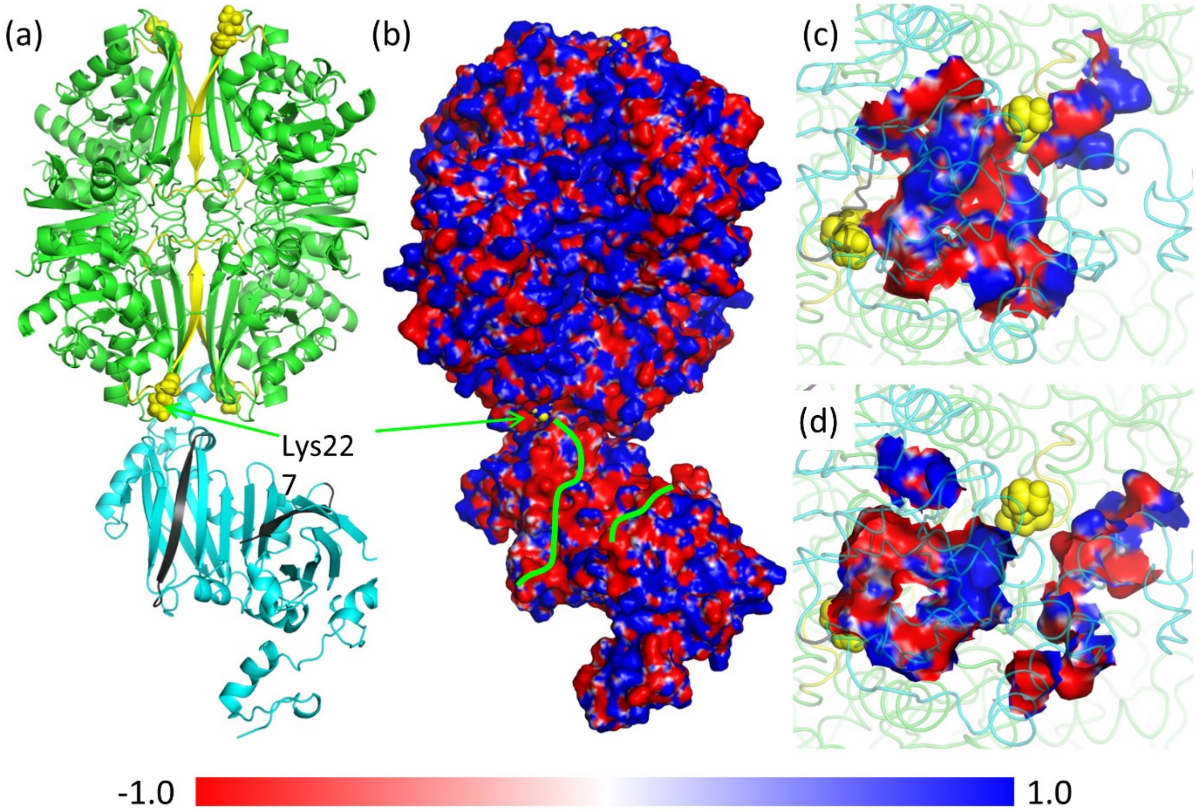

Figure 6.5. Docking analysis of the GAPDH tetramer and the Siah1 dimer. (a) The secondary structure of the docking pose of the GAPDH tetramer (green) interacting with the Siah1 dimer (cyan). Residue Lys227 (yellow sphere) of GAPDH interacting with residues 281-282 (grey) of Siah1. (b) Electrostatic surface of the GAPDH tetramer - Siah1 dimer complex from the docking analysis. The green lines on Siah1 indicate residues 270-280. The interacting electrostatic surface of (c) the GAPDH tetramer and (d) the Siah1 dimer shows little complementarity between them, which indicates weak interactions between the two proteins. Note that the structures in panels (c) and (d) are rotated to show the interacting surface, which is similar to the pose shown in Figure 6.2b. See caption to Figure 6.2 for details.

6.4.4. Docking of the GAPDH monomer with the Siah1 dimer

The docking analysis, without specifying any interacting residues, shows that among the top 10 poses, the top two poses and three others involve interactions with Lys227 of the GAPDH monomer and residues 281-282 of the Siah1 dimer (Figure 6.6). The remaining five poses do not involve the experimentally determined interacting residues. Also, these poses do not overlap so, they are not preferred binding poses. The preferred docking pose would be similar to that shown in Figure 6.6.

We refined the docking analysis by defining Lys227 of the GAPDH monomer and residues 281-282 of the Siah1 dimer as interacting regions. This analysis imposes constraints to keep the defined regions close to each other and filters out docking poses that lack interactions between the specified residues. We visualized the top ten poses and show one in Figure 6.7, which reveals that the largely positively charged electrostatic surface area of the GAPDH monomer interacts with the negatively charged electrostatic surface area of the SBD of the Siah1 dimer. These interactions represent the large electrostatic surface complementarity and strong interaction between the GAPDH monomer and the Siah1 dimer.

Note that the binding pose in Figure6.7a shows that the SBD of Siah1 is near the S-loop of GAPDH (orange, residues 181-205), which is disordered and highly dynamic in the GAPDH monomer (Section 5.4.6). Our MD simulations show that the S-loop of the GAPDH monomer moves away from its NBD and attains an open/closed conformation (Figure 5.7). Stabilization of the S-loop by the binding of the Siah1 dimer to the GAPDH monomer will further promote the formation of this complex and supports our hypothesis that GAPDH monomer complexes with Siah1.

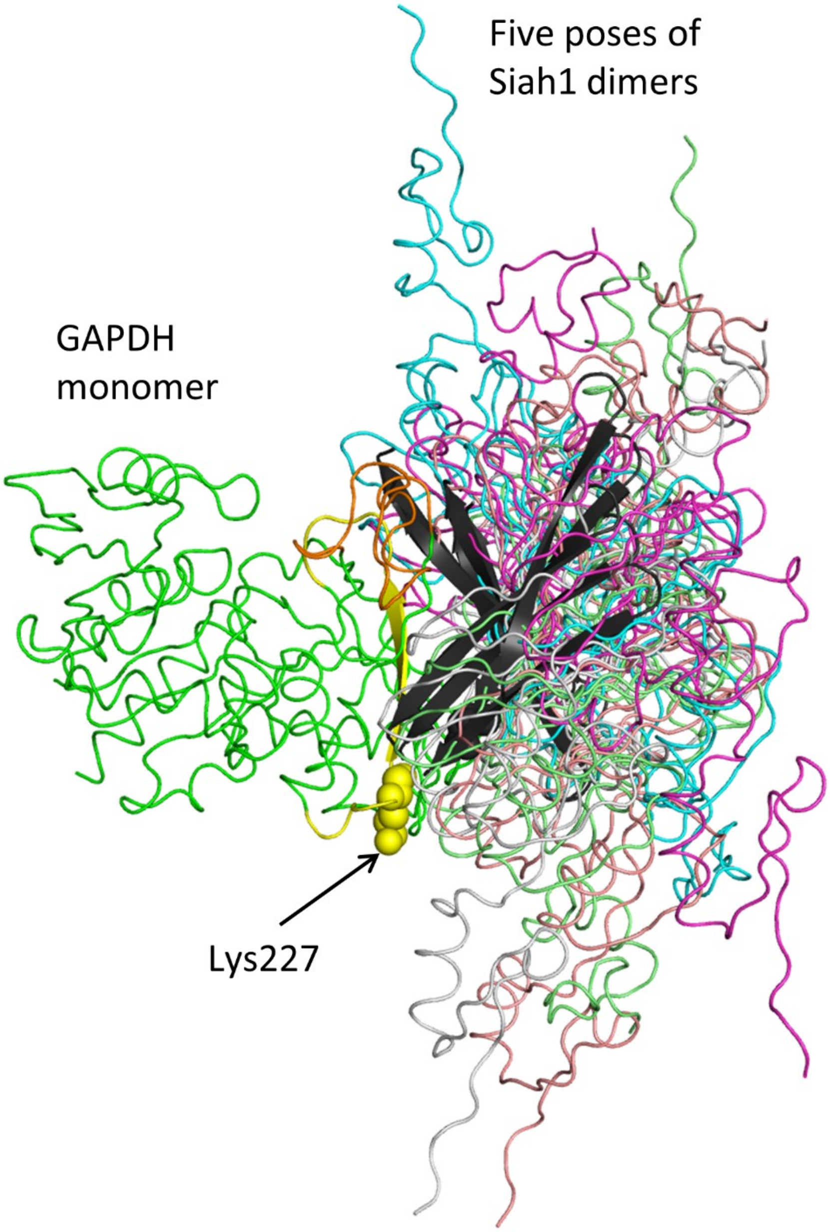

Figure 6.6. Blind docking analysis of the GAPDH monomer (green; left) and Siah1 dimer. The five poses from the top ten with interactions between residues of 222-240 of GAPDH (yellow β-sheet) and 270-282 of Siah1 (black β-sheet). The preferred binding pose for the Siah1 dimer - GAPDH monomer complex should be similar to those shown in this image.

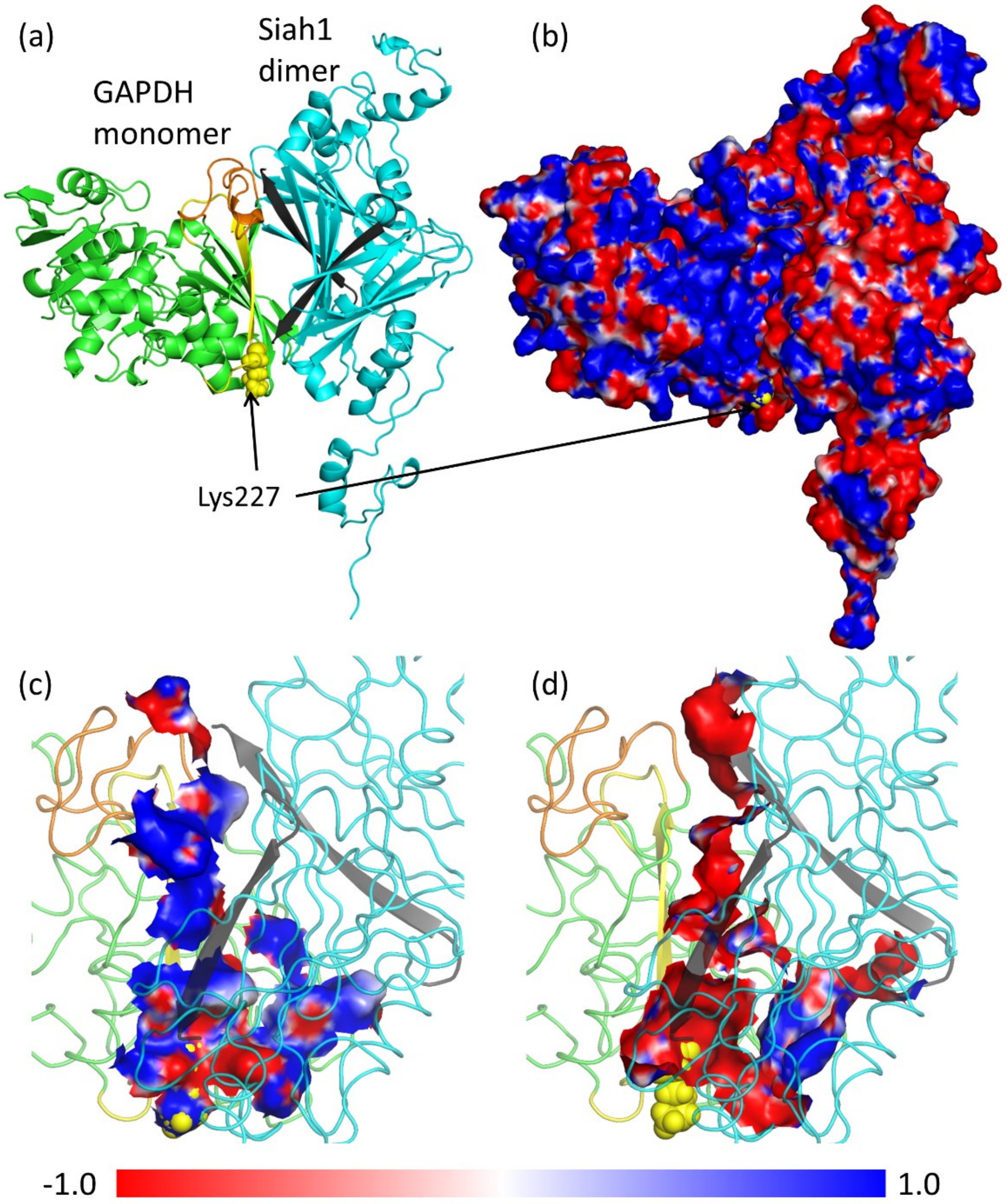

Figure 6.7. Docking analysis of the GAPDH monomer and the Siah1 dimer. (a) The secondary structure of the docking pose of the GAPDH monomer (green) interacting with the Siah1 dimer (cyan). Residue 222-240 (yellow β-sheet) and Lys227 (yellow spheres) of GAPDH are in close proximity to residues 270-282 (black β-sheets) of Siah1. (b) Electrostatic surface of the complex in the same pose. Note that mostly the SBD (residues 90-282) of Siah1 interacts with GAPDH. The interacting electrostatic surface of (c) the GAPDH monomer and (d) Siah1 dimer show the high complementarity between the interacting residues. Largely positively charged surfaces of GAPDH interact with the mostly negatively charged surface of Siah1, indicating strong interaction between the GAPDH monomer and Siah1 dimer. Note that the structures in panels (c and d) are rotated to show the interacting region. See caption to Figure 6.2 for details.

6.4.5. Docking of the GAPDH monomer with the Siah1 monomer

The results of blind docking of the GAPDH monomer with Siah1 monomer show that in four of the top ten docking poses, residue Lys227 of GAPDH and residues 281-282 of Siah1 are near each other (Figure 6.8). Thus, the preferred docking pose should be similar to Figure 6.8, where residues 222-240 of GAPDH are close to residues 270-282 of Siah1.

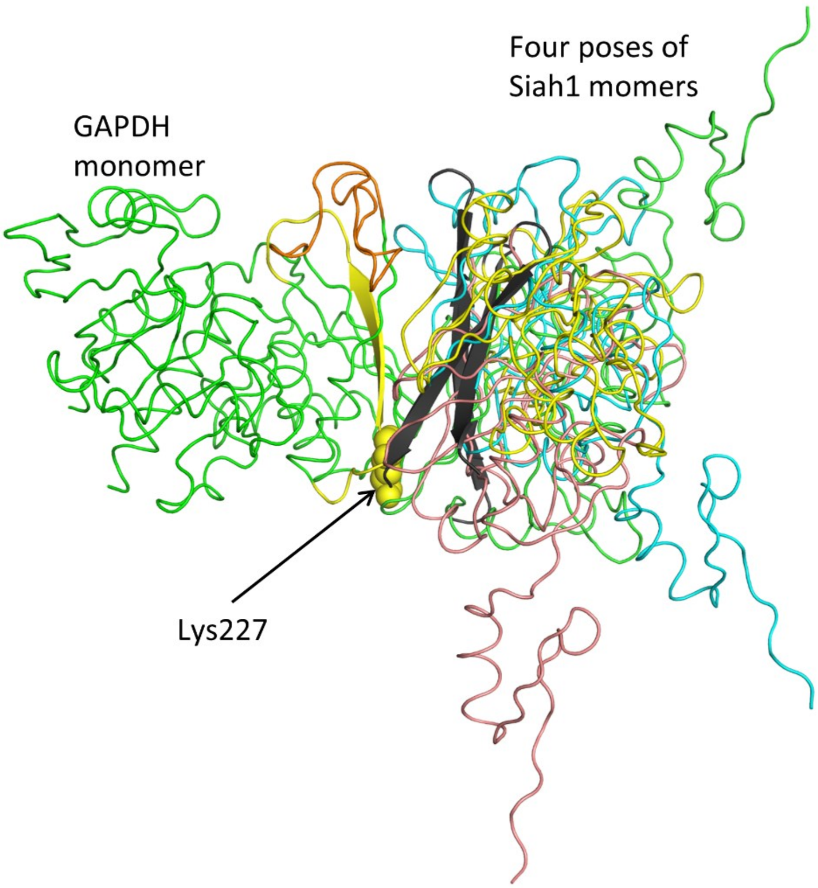

Figure 6.8. Blind docking analysis of the GAPDH monomer (green) and Siah1 monomer. The four poses from the top ten poses show interactions between residues of 222-240 of GAPDH (yellow β-sheet) and 270-282 of Siah1 (black β-sheet). The preferred binding pose for Siah1 monomer - GAPDH monomer complex should be similar to those shown in this image.

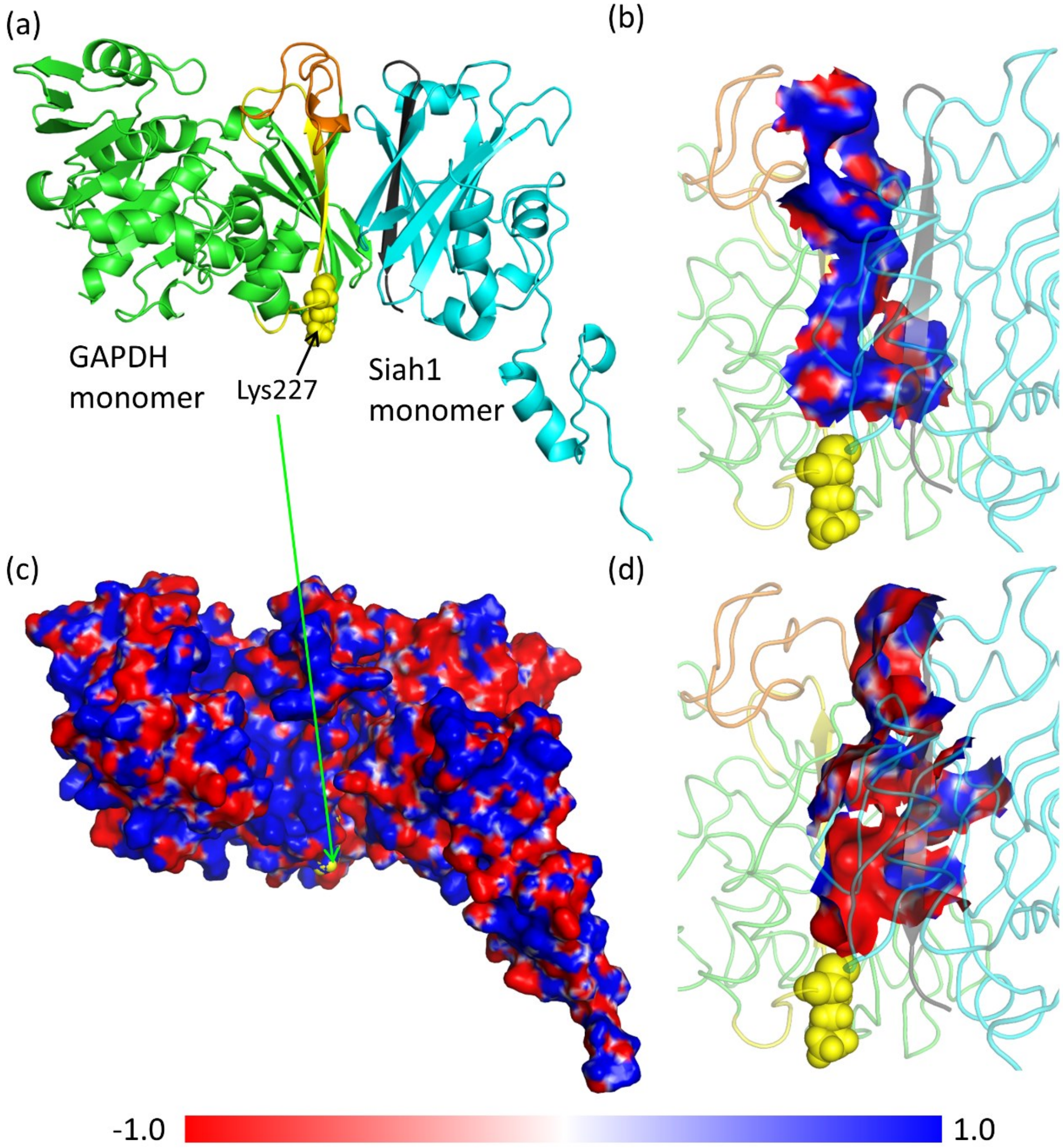

Figure 6.9. Docking analysis of the GAPDH monomer and the Siah1 monomer. (a) The secondary structure of the docking pose of GAPDH monomer (green) interacting with the Siah1 monomer (cyan). Residue 222-240 (yellow β-sheet) and Lys227 (yellow spheres) of GAPDH monomer are in close proximity to residues 270-282 (black β-sheets) of Siah1. (b) Electrostatic surface of the complex in the same docking pose. Note that mostly the SBD (residues 90-282) of Siah1 interacts with GAPDH. The interacting electrostatic surface of the (c) GAPDH monomer and (d) Siah1 monomer. Note, the high complementarity between the interacting residues. Largely positively charged surfaces of GAPDH interacts with the negatively charged surface of Siah1, indicating strong interactions between the GAPDH and Siah1 monomers. Note that the structures in panels (c,d) are rotated to show the interacting regions. See caption to Figure 6.2 for details.

Targeted docking analysis performed by defining the binding site near Lys227 of GAPDH and residues 281-282 of Siah1 showed similar docking poses to those in Figure 6.8. One of the selected docking poses in Figure 6.9 reveals that the positively charged electrostatic surface of GAPDH monomer interacts with the negatively charged electrostatic surface of the Siah1 monomer. Similar complementarity is seen for the interacting surface between GAPDH monomer and Siah1 dimer complex (Figure 6.7) but the GAPDH monomer interface with Siah1 dimer (interface area 1121 Å^2) is larger than with the Siah1 monomer (723 Å^2) as calculated with PDBePISA server.[209]

Similar to the GAPDH monomer and Siah1 dimer complex, the binding pose for the GAPDH monomer - Siah1 monomer complex also shows interactions between the S-loop of GAPDH and the SBD of Siah1. This would stabilize the S-loop of the GAPDH monomer and favor complex formation.

6.5. Conclusions

Analysis of electrostatic surfaces predicts that the GAPDH monomer has a large complementary surface area for Siah1 binding, but not the GAPDH tetramer. The docking analyses further confirm the formation of a stable complex between the GAPDH monomer and the Siah1 dimer or monomer but the GAPDH tetramer does not form a stable Siah1 complex. Complex formation with the GAPDH monomer would stabilize its S-loop, which is disordered and highly dynamic. Also, stabilization of the S-loop in the GAPDH monomer by protein partners other than Siah1 could be favored and contribute to the numerous moonlighting functions of GAPDH. Further experimental analysis could confirm GAPDH monomer interaction with the Siah1 dimer or monomer.

Chapter 7. Quantum Mechanics / Molecular Mechanics Simulations of Thionitrate (E-Cys-NO_2) Decomposition in the Active-site of GAPDH

7.1. Abstract

Thionitrates (E-Cys-NO_2) are active intermediates, which are implicated in the biotransformation of organic nitrates by enzymes containing active thiols (E-Cys). Our study on the decomposition of CH_3SNO_2, a model compound for E-Cys-NO_2, indicate that the activation barriers are small for thionitrate decomposition by hydrolysis and thiolysis and can even involve a barrierless pathway. However, the activation barriers were not evaluated in an enzyme active-site. Thus, we carried out quantum mechanics / molecular mechanics (QM/MM) simulations to investigate E-Cys-NO_2 decomposition in the active-site of glyceraldehyde-3-phosphate dehydrogenase (GAPDH). QM/MM simulations reveal that hydrolysis of E-Cys-NO_2 by OH^- involve proton relay between 3 water molecules and the activation free energy is ~ 50 kcal/mol, which is comparable to the decomposition of CH_3SNO_2 by one water molecule. We do not see the attack of OH^- along S–N bond, thus further QM/MM simulations are required to investigate all the pathways for decomposition of E-Cys-NO_2 in GAPDH active-site.

7.2. Introduction

Thionitrates are active intermediates in organic nitrate decomposition.[54] Many enzymes such as mitochondrial aldehyde dehydrogenase (ALDH2)[52] and glyceraldehyde-3-phosphate dehydrogenase (GAPDH) [48] are implicated in the biotransformation of glyceryl trinitrate (GTN), a prodrug that releases nitrite (NO_2^-) or nitric oxide (NO) upon decomposition. The consensus emerged that the catalytic cysteine residue of these enzymes forms a thionitrate (E-Cys-NO_2) in the enzyme active-site.[54] This was further confirmed by the crystal structure of a triple mutant of ALDH2, which showed for the first time E-Cys-NO_2 formation in the enzyme active-site.[55,58] Various computational and experimental studies of small molecule thionitrates ($RSNO_2$) were carried out to explain the underlying mechanism of E-Cys-NO_2 decomposition.[56,62,64,65,115,117]

In Chapter 2 of this thesis, we use CH_3SNO_2 as a model compound for E-Cys-NO_2 to understand the mechanism of its decomposition using state-of-the-art quantum mechanics (QM) calculations. We calculated activation barriers for all the proposed pathways for decomposition of thionitrate (Figure 2.1) in the gas phase and solvent effects were included using an implicit solvent model. Our study shows that the activation barriers for thionitrate decomposition via homolysis, which releases NO, are prohibitively high (> 40 kcal/mol), whereas hydrolysis and thiolysis, which releases NO_2^-, are substantially smaller (~ 17 kcal/mol). We further showed that linear attack along S–N bond by anionic nucleophiles, such as OH^- and CH_3S^-, are barrierless (~ 0 kcal/mol). The implicit solvent model includes solvation effect using different dielectric constant but the effect of the enzyme active-site was not included in our previous study. However, a computational study treating the whole protein using quantum mechanics is impossible thus, we used a hybrid quantum mechanics / molecular mechanics (QM/MM) approach to include the effect of the enzyme active-site on the decomposition of E-Cys-NO_2. Specifically, QM/MM simulations were carried out to investigate the hydrolysis of E-Cys-NO_2 in the GAPDH active-site. We evaluated hydrolysis by an attack of water and OH^- in the active-site of GAPDH. Hydrolysis by H_2O does not give the expected reaction coordinates so, we show the only hydrolysis by OH^- in the GAPDH active-site.

7.3. Computational Methods

We extracted a subunit-P from the crystal structure of human GAPDH (PDB 1U8F) [105] to generate thionitrate at catalytic Cys152. We used a similar approach to that described in Section 3.3 to prepare the GAPDH-monomer-Cys152-NO_2 (here onwards denoted as GAPDH-NO_2) for molecular dynamics (MD) simulations. We carried out 10 ns MD simulations using the NPT ensemble with CHARMM27 force field [106,174] and NAMD2.9 [99] software. We chose one of the consensus poses as the reactant starting point for the QM/MM calculations.

QM/MM calculations were carried out using the CP2K program [210]. The energy for the QM region was calculated by the Becke−Lee−Yang−Parr (BLYP) density functional method [211] and triple zeta plane wave Gaussian basis sets with Goedecker−Tetter−Hutter pseudopotential (TZVP-GTH).[212,213] The link atoms between the QM and MM region were defined by integrated molecular orbital molecular mechanics (IMOMM) approach. QM/MM simulations were performed at a constant temperature and volume.

We constrained the S(Cys152-NO_2)---O(OH^-) distance and the mean force calculated based on the time average of Lagrange parameter obtained from the simulations with imposed constraint. The potential of mean force is then calculated by numerical integration of the mean force.[214]

7.4. Results and Discussion

In Section 2.1 of this thesis, we proposed that Glu317 in the vicinity of Cys152 in the GAPDH active-site could activate a water molecule, which could attack the sulfur of Cys152-NO_2 to release nitrite. We also showed that reaction of CH_3SNO_2 with OH^- has small activation barrier of ~ 17 kcal/mol for top OH^- attack (Figure 2.6a), whereas the linear attack along the S–N bond by OH^- is barrierless (Figure 2.6c). The first GAPDH-NO_2 MD simulation carried out showed a water molecule close to Cys152-NO_2 and Glu317 (Figure 7.1a). We replaced the water molecule with OH^- and carried out MD simulations to investigate the reaction of OH^- with Cys152-NO_2. We examined two scenarios: one where MD simulations were performed with Glu317 in the glutamate form (deprotonated) and one with Glu317 in the glutamic acid (neutral) form. OH^- moves towards the protonated His179 and forms strong H-bond interactions within a short MD simulation (2 ns), when Glu317 is in the deprotonated form. However, OH^- forms a strong H-bond with the neutral sidechain of Glu317.

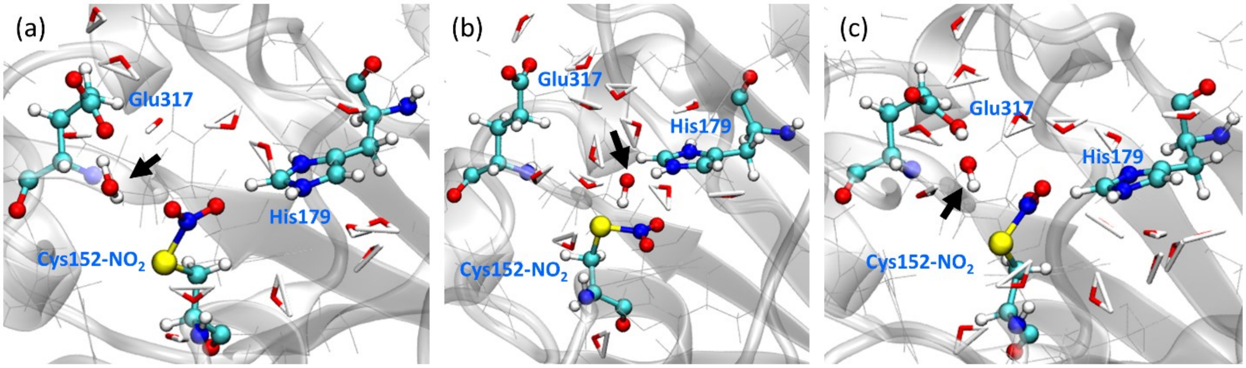

Figure 7.1. Water and OH^- in the vicinity of Cys152-NO_2 in the active-site of GAPDH. (a) MD simulations indicate that a water molecule is present in the vicinity of Cys152-NO_2 and Glu317. (b) MD simulations with OH^- in the active-site and Glu317 in its glutamate form show that OH^- moves towards the protonated His179 to form H-bond interactions. (c) MD simulations with OH^- in the active-site and Glu317 in neutral form show OH^- forms a strong H-bond interaction with Glu317 and remains in a position to attack the sulfur of Cys152-NO_2.

We used one of the consensus snapshots from the MD simulations with OH^- in the active-site and neutral Glu317, where OH^- is in close proximity to Cys152-NO_2. We constrained the O–H distance in sidechain of Glu317 so it does not interact with OH^- to form a water molecule. We selected the sidechains of residues Ile14, Cys152, His179, Asn316, Glu317, Tyr320 (ball-stick model) and five water molecules around Cys152 and Glu317 as the QM region (Figure 7.2a). The rest of the system was treated as the MM region. The S(Cys152)----O(OH^-) distance was scanned at a window of 0.2 Å and a 2-ps QM/MM simulation was carried out, with a total of 24 ps. At the end of each 2-ps QM/MM simulation window, the last geometry was used for the new window.

OH^- forms a H-bond interaction with a water molecule, which is bridged between OH^- and Glu317 (Figure 7.2). OH^- extracts a proton from the water molecule and is converted to a water molecule, which attacks sulfur of Cys152-NO_2. Thus, the reaction coordinates indicate a top attack of a water molecule assisted by 3 water molecules seen in Section 2.4.3.

The potential of mean force for the reaction indicates that the formation of Cys152-OH, where the S–O distance is 1.71 Å, requires ~ 48 kcal/mol activation free energy. Thus, the QM/MM values agree with that calculated for CH_3SNO_2 hydrolysis by one water molecule (Table 7.1). However, the QM/MM reaction involves three water molecules (Figure 7.2) and hence overestimates the activation free energy compared to CH_3SNO_2 hydrolysis by three water molecules in the gas phase (Table 7.1).

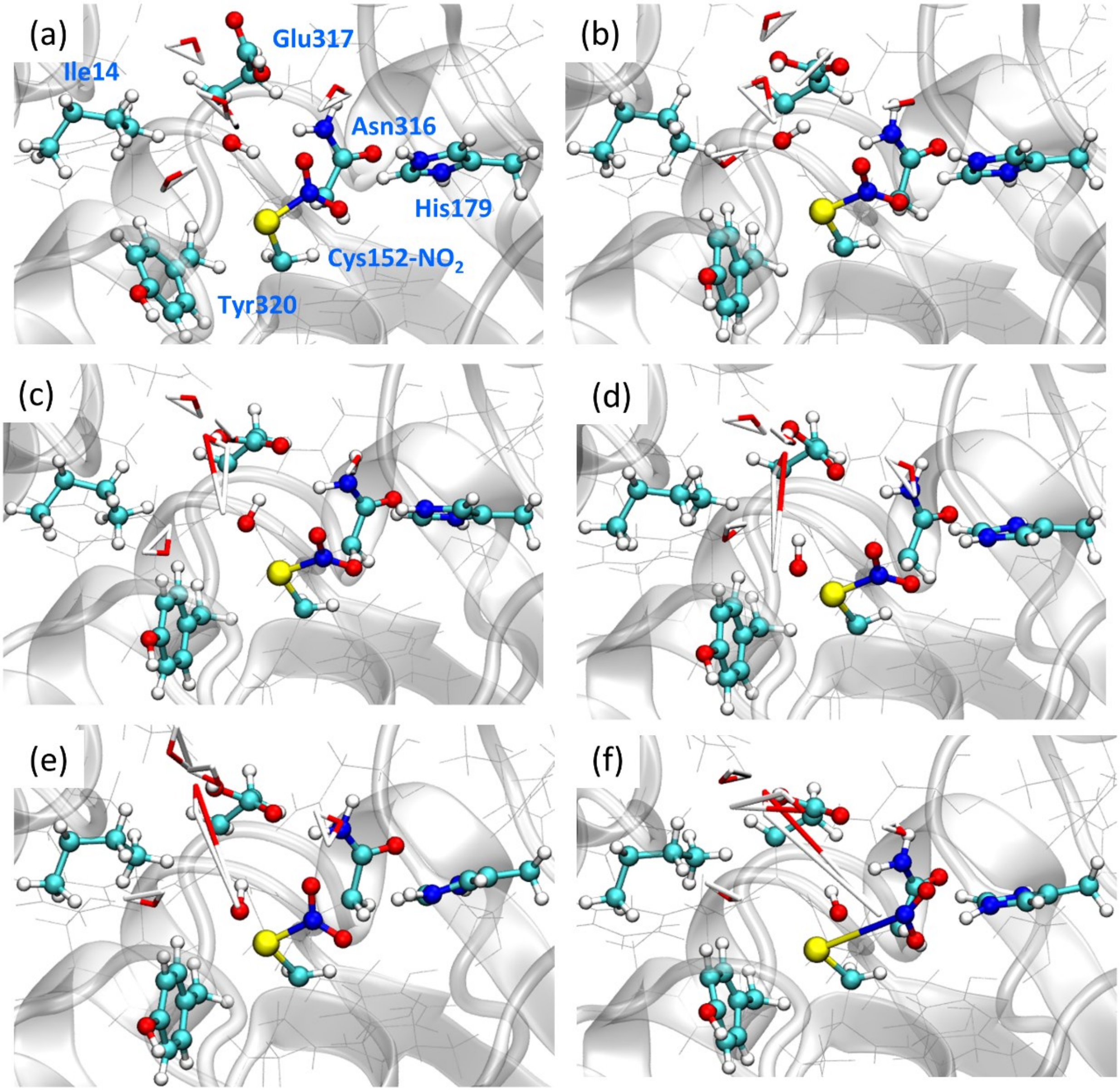

Figure 7.2. Reaction coordinates for OH⁻ attack on Cys152-NO$_2$ calculated with QM/MM. Residues Ile14, Cys152, His179, Asn316, Glu317, Tyr320 (ball-stick model), OH⁻ (ball-stick model) and 5 water molecules (stick model) are included in the QM region, while the rest of the system is considered as the MM region. The snapshots of the reaction are taken at S(Cys152-NO$_2$)–O(OH⁻) distances of (a) 3.3, (b) 2.9, (c) 2.3, (d) 2.1, (e) 1.7 and (f) 1.6 Å. The hydrolysis of Cys152-NO$_2$ involves three water molecules.

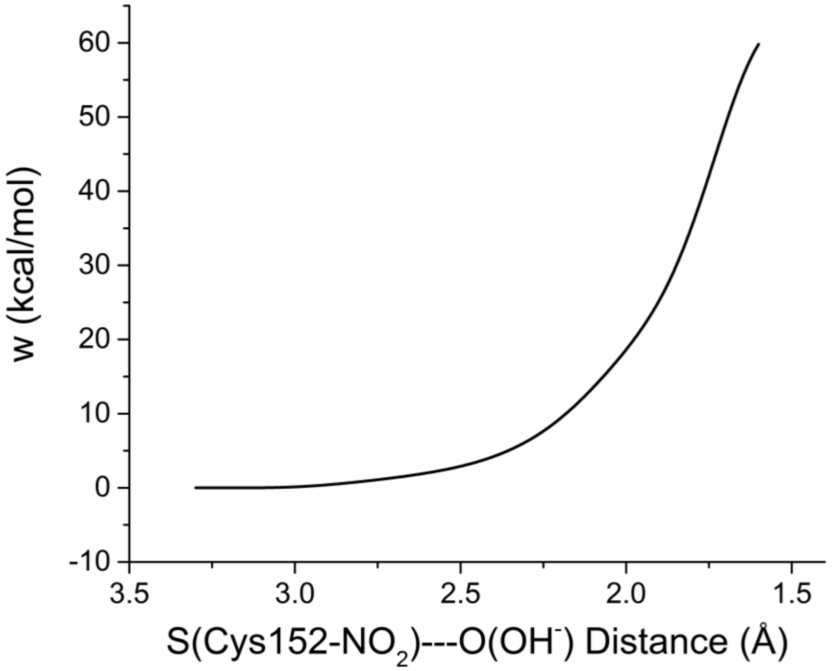

Figure 7.3. The potential mean force of OH^- attack on Cys152-NO_2 calculated with QM/MM. Cys152-OH with S–O distance of 1.7 Å formation requires ~ 48 kcal/mol.

Table 7.1. Activation free energy (kcal/mol) for the hydrolysis of CH_3SNO_2 by one and three H_2O in the gas phase

Model chemistry	Hydrolysis by H_2O (top)	Hydrolysis by 3 H_2O (top)
CCSD(T)//MP2/aug-cc-pVTZ	61.2	35.7
BLYP/6-311G(2df,2pd)	45.8	28.2
BLYP/6-311G+(2df,2pd)	51.1	32.6
BLYP/Def2TZVP	49.8	30.7
BLYP/Def2TZVPP	50.3	31.7

QM/MM simulation showed that H_2O, not OH^-, attacks S atom. Thus, the simulations were carried out with constrained O–H distances of the QM water molecules and the sidechain of Glu317. Other parameters were kept same. OH^- attacks on the S atom along the S–N bond (Figure

7.5) due to favorable electrostatic interactions between anionic nucleophile OH^- and σ-hole on sulfur atom (See section 2.4.5). The attack of OH^- along the S–N bond in the active-site of GAPDH is barrierless (Figure 7.5), as also seen for CH_3SNO_2 (Section 2.4.4).

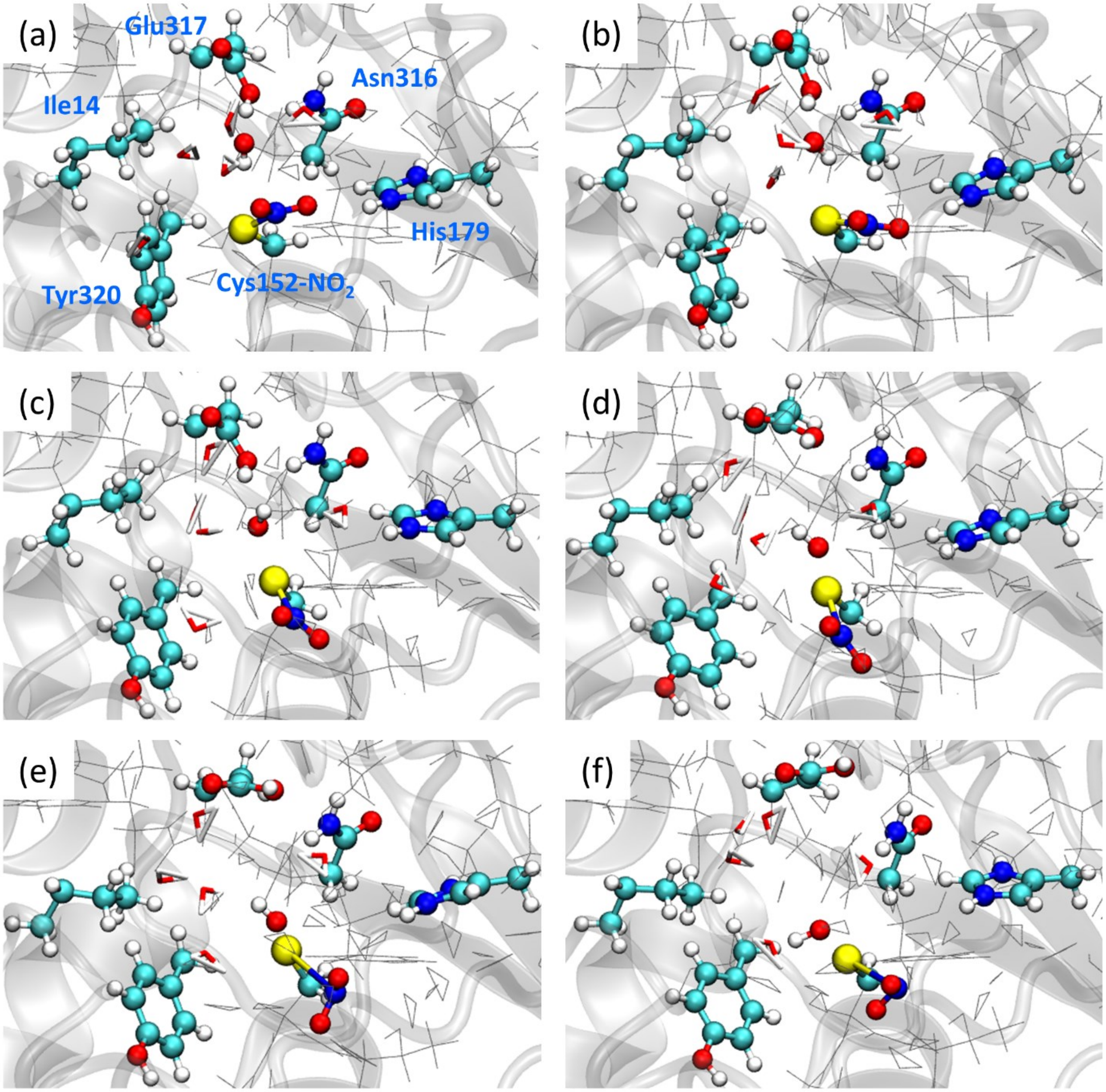

Figure 7.4. Reaction coordinates for OH^- attack on Cys152-NO_2 with constrained O–H distances of QM water molecules and Glu317 sidechain. The snapshots of the reaction are taken at S(Cys152-NO_2)–O(OH^-) distances of (a) 3.3, (b) 2.9, (c) 2.3, (d) 2.1, (e) 1.7 and (f) 1.6 Å. OH^- attacks sulfur linearly along the S–N bond.

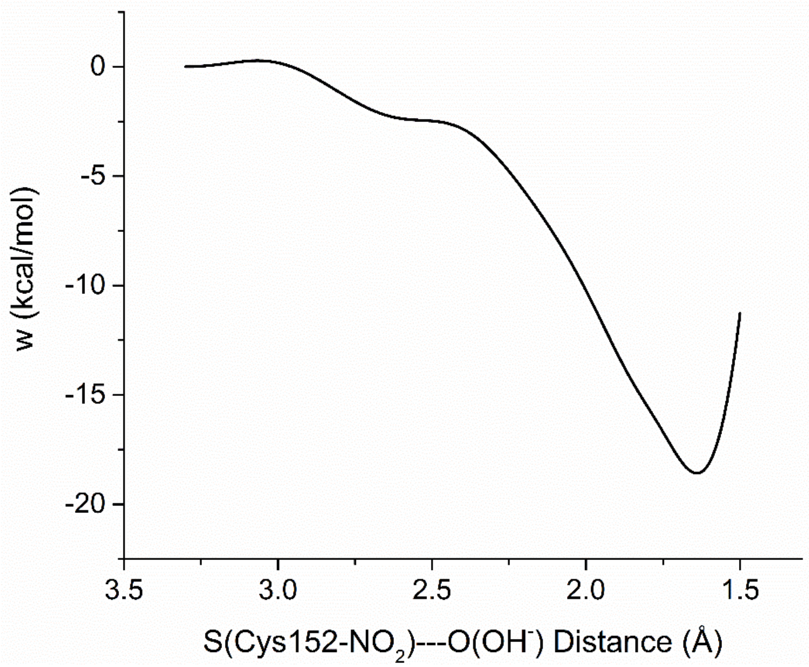

Figure 7.5. The potential mean force of OH$^-$ attack on Cys152-NO$_2$ with constrained O–H distances of QM water molecules and Glu317 sidechain. The OH$^-$ attack along the S–N bond is barrierless in GAPDH active-site.

7.5. Summary

QM/MM simulations for GAPDH-NO$_2$ hydrolysis by OH$^-$, which has reaction coordinates similar to the gas-phase hydrolysis of CH$_3$SNO$_2$ by three water molecules, indicate that the activation free energy for hydrolysis is ~ 50 kcal/mol in the GAPDH active-site. The calculated activation free energy is comparable to CH$_3$SNO$_2$ hydrolysis by one water molecule in the gas phase. Allowing OH$^-$ to attack the S atom linearly along the S–N bond is barrierless. Additional QM/MM simulations with (1) Cys152-NO$_2$ in a conformation with sulfur interaction with protonated His179, and (2) neutral His179 are necessary to better define the mechanism of E-Cys-NO$_2$ decomposition in the active-site of GAPDH.

Chapter 8. Conclusions and Outlook

The goal of my thesis was to investigate the structural and dynamical role of GAPDH in GTN bioactivation and to shed more light on GAPDH's role in NO Biochemistry. We used various computational techniques starting from a QM investigation of the mechanism of decomposition of a small molecule, to QM/MM investigation of the same reaction in an enzyme active-site. The computational modeling approaches, including protein-protein docking and MD simulations, were carried out to understand and predict the reactivity and dynamics of GAPDH.

An investigation of CH_3SNO_2 decomposition using QM as model compound for E-Cys-NO_2 decomposition helped distinguish energetically favorable and unfavorable decomposition pathways. We found that thionitrate can be readily attacked by anionic nucleophiles, which explains their low stability. The QM calculations also provided the starting geometry and reaction coordinates for a decomposition pathway to set up the QM/MM calculations for E-Cys-NO_2 decomposition in the active-site of GAPDH.

To further understand the different functions of GAPDH, we carried out MD simulations of GAPDH-NAD^+, GAPDH-NADH and apo-GAPDH to investigate its cofactor-dependent structural dynamics. We show that cofactor binding results in concerted motions of the NBD in the GAPDH tetramer and stabilizes the active-site. Thus, the cofactor controls the dynamics of the tetramer and hence moderates the functions of GAPDH.

We further investigated the dynamics of the GAPDH tetramer, dimer and monomer to explore how deoligomerization changes dynamics and contributes to controlling GAPDH's different functions. We identify a structurally disordered region, the S-loop, which is highly dynamic in the monomer. This intrinsically disordered region is stabilized by binding with protein partners, which could dictate some functions of GAPDH. One such protein partner is Siah1, which is known to bind S-nitrosated GAPDH (E-Cys-NO). From our docking analysis, we propose that Siah1 likely binds to GAPDH monomer and stabilize the disordered S-loop. This, in turn, stabilizes the complex, which translocated to the nucleus to initiate apoptosis.

In sum, our study reveals important structural and dynamical characteristics of GAPDH, which is well-known for its moonlighting functions. These structural characteristics likely play a role in the diverse functions of GAPDH. Our results provide a basis for GAPDH analysis not only as a tetrameric protein, but also as a structurally dynamic molecule, that can attain multiple oligomeric states.

Outlook

The QM studies on CH_3SNO_2 decomposition indicate that attack of anionic nucleophiles (OH^- or CH_3S^-) along S–N bond is barrierless. Also, hydrolysis with 3-4 water molecules, which represents the linear attack of water along the S–N bond lowers the activation barrier significantly. Thus, QM/MM simulation of 3-4 water molecules attack along the S–N bond of E-Cys-NO_2 should be evaluated to estimate the activation barrier in the active-site.

ALDH2 is also implicated in catalysis of GTN and decomposition is known to E-Cys-NO_2 with it catalytic Cys302.[55] However, ALDH2 turn over GTN 10-fold faster than GAPDH (Section 2.5.3). Thus, comparison of OH^- attack on E-Cys-NO_2 in ALDH2 and GAPDH using QM/MM simulations would provide insight into the variation of GTN turnover by these enzymes. Also, Cys156 present in the active-site of GAPDH in addition to catalytic Cys152, is buried in the protein matrix. Thus, Cys156 is not able to attack Cys152 so it is not possible to examine thiolysis of E-Cys-NO_2 in GAPDH using QM/MM simulations. In contrast, ALDH2 contains Cys301 and Cys303 close to catalytic Cys302 (Figure 2.8) so thiolysis should be evaluated in ALDH2 by

QM/MM to provide insight into the contributions of hydrolysis and thiolysis pathways in E-Cys-NO_2 decomposition in the same enzyme.

MD simulations of GAPDH-NAD^+ and apo-GAPDH compare the effect of all four NAD^+ bound and unbound on GAPDH tetramer dynamics, respectively. Removal of one, two or three cofactors would provide more insight into the cofactor induced dynamic changes in the GAPDH tetramer. Also, pulling one, two or three cofactors out of their binding sites may provide insight into the folding of NAD binding site. ATP also destabilizes the tetramer so its effect on GAPDH dynamics should be investigated. Additionally, the dynamics of GAPDH with Cys152 and His179 in their neutral forms should be compared with the data obtained here.

We analyzed the dynamics of the GAPDH dimer and monomer, which provides insight into how deoligomerization changex the tetramer dynamics. However, a detailed study on how the subunits dissociate to generate the dimer or the monomer has not yet been carried out. Thus, pulling one or two subunits from the tetramer and observing the changes in its dynamic could provide insight into the unfolding mechanism of the tetramer. Coarse-grained or accelerated MD simulation would be suitable techniques to carry out these studies. A further potential of mean force calculation of pulling a subunit from either tetramer or dimer in presence or absence of a cofactor would provide insight into the energy barrier for deoligomerization of the tetramer or the dimer.

The crystal structure predicts the selectivity cleft to be closed in human GAPDH whereas our MD simulations suggest that this cleft is open in human apo-GAPDH. MD simulations of *L. Mexicana* GAPDH in presence and absence of NAD^+ have not been carried out to compare the changes in the size of the selectivity cleft in apo- vs holo-enzyme. This study would help understand the dynamics of selectivity cleft and in turn help design selective inhibitors of protozoan GAPDH.

References

(1) Sirover, M. A. New insights into an old protein: the functional diversity of mammalian glyceraldehyde-3-phosphate dehydrogenase. *Biochim. Biophys. Acta - Protein Struct. Mol. Enzymol.* **1999**, *1432*, 159–184 DOI: 10.1016/S0167-4838(99)00119-3.

(2) Seidler, N. W. *GAPDH: Biological Properties and Diversity*; 2013; Vol. 985.

(3) Sirover, M. A. On the functional diversity of glyceraldehyde-3-phosphate dehydrogenase: biochemical mechanisms and regulatory control. *Biochim. Biophys. Acta* **2011**, *1810*, 741–751 DOI: 10.1016/j.bbagen.2011.05.010.

(4) Allison, W. S.; Connors, M. J. The activation and inactivation of the acyl phosphatase activity of glyceraldehyde-3-phosphate dehydrogenase. *Arch. Biochem. Biophys.* **1970**, *136*, 383–391 DOI: 10.1016/0003-9861(70)90209-2.

(5) Park, J. H.; Meriwether, B. P.; Clodfelder, P.; Cunningham, L. W. The hydrolysis of p-nitrophenyl acetate catalyzed by 3-phosphoglyceraldehyde dehydrogenase. *J. Biol. Chem.* **1961**, *236*, 136–141.

(6) Robbins, A. R.; Ward, R. D.; Oliver, C. A mutation in glyceraldehyde 3-phosphate dehydrogenase alters endocytosis in CHO cells. *J. Cell Biol.* **1995**, *130*, 1093–1104 DOI: 10.1083/jcb.130.5.1093.

(7) Alvarez-Dominguez, C.; Madrazo-Toca, F.; Fernandez-Prieto, L.; Vandekerckhove, J.; Pareja, E.; Tobes, R.; Gomez-Lopez, M. T.; Del Cerro-Vadillo, E.; Fresno, M.; Leyva-Cobián, F.; et al. Characterization of a Listeria monocytogenes Protein Interfering with Rab5a. *Traffic* **2008**, *9*, 325–337 DOI: 10.1111/j.1600-0854.2007.00683.x.

(8) Zang, W. Q.; Fieno, A. M.; Grant, R. A.; Yen, T. S. B. Identification of glyceraldehyde-3-phosphate dehydrogenase as a cellular protein that binds to the hepatitis B virus posttranscriptional regulatory element. *Virology* **1998**, *248*, 46–52 DOI: 10.1006/viro.1998.9255.

(9) Singh, R.; Green, M. R. Sequence-specific binding of transfer RNA by glyceraldehyde-3-phosphate dehydrogenase. *Science* **1993**, *259*, 365–368.

(10) Baxi, M. D.; Vishwanatha, J. K. Uracil DNA-glycosylase/glyceraldehyde-3-phosphate dehydrogenase is an Ap4A binding protein. *Biochemistry* **1995**, *34*, 9700–9707 DOI: 10.1021/bi00030a007.

(11) Cool, B. L.; Sirover, M. a. Immunocytochemical localization of the base excision repair enzyme uracil DNA glycosylase in quiescent and proliferating normal human cells. *Cancer Res.* **1989**, *49*, 3029–3036.

(12) Azam, S.; Jouvet, N.; Jilani, A.; Vongsamphanh, R.; Yang, X.; Yang, S.; Ramotar, D. Human glyceraldehyde-3-phosphate dehydrogenase plays a direct role in reactivating oxidized forms of the DNA repair enzyme APE1. *J. Biol. Chem.* **2008**, *283*, 30632–30641 DOI:

10.1074/jbc.M801401200.

(13) Barbini, L.; Rodríguez, J.; Dominguez, F.; Vega, F. Glyceraldehyde-3-phosphate dehydrogenase exerts different biologic activities in apoptotic and proliferating hepatocytes according to its subcellular localization. *Mol. Cell. Biochem.* **2007**, *300*, 19–28 DOI: 10.1007/s11010-006-9341-1.

(14) Hara, M. R.; Agrawal, N.; Kim, S. F.; Cascio, M. B.; Fujimuro, M.; Ozeki, Y.; Takahashi, M.; Cheah, J. H.; Tankou, S. K.; Hester, L. D.; et al. S-nitrosylated GAPDH initiates apoptotic cell death by nuclear translocation following Siah1 binding. *Nat. Cell Biol.* **2005**, *7*, 665–674 DOI: 10.1038/ncb1268.

(15) Sirover, M. A. New nuclear functions of the glycolytic protein, glyceraldehyde-3-phosphate dehydrogenase, in mammalian cells. *J. Cell. Biochem.* **2005**, *95*, 45–52 DOI: 10.1002/jcb.20399.

(16) Rondinelli, R. H.; Epner, D. E.; Tricoli, J. V. Increased glyceraldehyde-3-phosphate dehydrogenase gene expression in late pathological stage human prostate cancer. *Prostate Cancer Prostatic Dis.* **1997**, *1*, 66–72 DOI: 10.1038/sj.pcan.4500208.

(17) Higashimura, Y.; Nakajima, Y.; Yamaji, R.; Harada, N.; Shibasaki, F.; Nakano, Y.; Inui, H. Up-regulation of glyceraldehyde-3-phosphate dehydrogenase gene expression by HIF-1 activity depending on Sp1 in hypoxic breast cancer cells. *Arch. Biochem. Biophys.* **2011**, *509*, 1–8 DOI: 10.1016/j.abb.2011.02.011.

(18) Sunaga, K.; Takahashi, H.; Chuang, D. M.; Ishitani, R. Glyceraldehyde-3-phosphate dehydrogenase is over-expressed during apoptotic death of neuronal cultures and is recognized by a monoclonal antibody against amyloid plaques from Alzheimer’s brain. *Neurosci. Lett.* **1995**, *200*, 133–136 DOI: 10.1016/0304-3940(95)12098-O.

(19) Butterfield, D. A.; Hardas, S. S.; Lange, M. L. B. Oxidatively modified glyceraldehyde-3-phosphate dehydrogenase (GAPDH) and alzheimer’s disease: Many pathways to neurodegeneration. *J. Alzheimer’s Dis.* **2010**, *20*, 369–393 DOI: 10.3233/JAD-2010-1375.

(20) Kragten, E.; Lalande, I.; Zimmermann, K.; Roggo, S.; Schindler, P.; Müller, D.; Van Oostrum, J.; Waldmeier, P.; Fürst, P. Glyceraldehyde-3-phosphate dehydrogenase, the putative target of the antiapoptotic compounds CGP 3466 and R-(-)-deprenyl. *J. Biol. Chem.* **1998**, *273*, 5821–5828 DOI: 10.1074/jbc.273.10.5821.

(21) Barinova, K.; Khomyakova, E.; Semenyuk, P.; Schmalhausen, E.; Muronetz, V. Binding of alpha-synuclein to partially oxidized glyceraldehyde-3-phosphate dehydrogenase induces subsequent inactivation of the enzyme. *Arch. Biochem. Biophys.* **2018** DOI: 10.1016/j.abb.2018.02.002.

(22) Cooper, A. J.; Sheu, K. F.; Burke, J. R.; Strittmatter, W. J.; Blass, J. P. Glyceraldehyde 3-phosphate dehydrogenase abnormality in metabolically stressed Huntington disease fibroblasts. *Dev. Neurosci.* **1998**, *20*, 462–468 DOI: 10.1159/000017344.

(23) Bae, B.-I.; Hara, M. R.; Cascio, M. B.; Wellington, C. L.; Hayden, M. R.; Ross, C. A.; Ha, H. C.; Li, X.-J.; Snyder, S. H.; Sawa, A. Mutant Huntingtin: Nuclear translocation and cytotoxicity mediated by GAPDH. *Proc. Natl. Acad. Sci.* **2006**, *103*, 3405–3409 DOI: 10.1073/pnas.0511316103.

(24) Chuang, D.-M.; Hough, C.; Senatorov, V. V. Glyceraldehyde-3-Phosphate Dehydrogenase, Apoptosis, and Neurodegenerative Diseases. *Annu. Rev. Pharmacol. Toxicol.* **2005**, *45*, 269–290 DOI: 10.1146/annurev.pharmtox.45.120403.095902.

(25) Burke, J. R.; Enghild, J. J.; Martin, M. E.; Jou, Y. S.; Myers, R. M.; Roses, A. D.; Vance, J. M.; Strittmatter, W. J. Huntingtin and DRPLA proteins selectively interact with the enzyme GAPDH. *Nat. Med.* **1996**, *2*, 347–350.

(26) Koshy, B.; Matilla, T.; Burright, E. N.; Merry, D. E.; Fischbeck, K. H.; Orr, H. T.; Zoghbi, H. Y. Spinocerebellar ataxia type-1 and spinobulbar muscular atrophy gene products interact with glyceraldehyde-3-phosphate dehydrogenase. *Hum. Mol. Genet.* **1996**, *5*, 1311–1318.

(27) Schulze, H.; Schuler, A.; Stüber, D.; Döbeli, H.; Langen, H.; Huber, G. Rat brain glyceraldehyde-3-phosphate dehydrogenase interacts with the recombinant cytoplasmic domain of Alzheimer's beta-amyloid precursor protein. *J. Neurochem.* **1993**, *60*, 1915–1922.

(28) Sen, N.; Hara, M. R.; Ahmad, A. S.; Cascio, M. B.; Kamiya, A.; Ehmsen, J. T.; Agrawal, N.; Hester, L.; Doré, S.; Snyder, S. H.; et al. GOSPEL: A Neuroprotective Protein that Binds to GAPDH upon S-Nitrosylation (DOI:10.1016/j.neuron.2009.05.024). *Neuron* **2009**, *63*, 709 DOI: 10.1016/j.neuron.2009.08.032.

(29) Raje, C. I.; Kumar, S.; Harle, A.; Nanda, J. S.; Raje, M. The macrophage cell surface glyceraldehyde-3-phosphate dehydrogenase is a novel transferrin receptor. *J. Biol. Chem.* **2007**, *282*, 3252–3261 DOI: 10.1074/jbc.M608328200.

(30) Wakasugi, K.; Nakano, T.; Morishima, I. Oxidative stress-responsive intracellular regulation specific for the angiostatic form of human tryptophanyl-tRNA synthetase. *Biochemistry* **2005**, *44*, 225–232 DOI: 10.1021/bi048313k.

(31) White, M. R.; Khan, M. M.; Deredge, D.; Ross, C. R.; Quintyn, R.; Zucconi, B. E.; Wysocki, V. H.; Wintrode, P. L.; Wilson, G. M.; Garcin, E. D. A Dimer Interface Mutation in Glyceraldehyde-3-Phosphate Dehydrogenase Regulates Its Binding to AU-rich RNA. *J. Biol. Chem.* **2015**, *290*, 1770–1785 DOI: 10.1074/jbc.M114.618165.

(32) Perucho, M.; Salas, J.; Salas, M. L. Study of the interaction of glyceraldehyde-3-phosphate dehydrogenase with DNA. *Biochim. Biophys. Acta* **1980**, *606*, 181–195.

(33) Tristan, C.; Shahani, N.; Sedlak, T. W.; Sawa, A. The diverse functions of GAPDH: Views from different subcellular compartments. *Cellular Signalling*, 2011, *23*, 317–323.

(34) Suresh, S.; Bressi, J. C.; Kennedy, K. J.; Verlinde, C. L. M. J.; Gelb, M. H.; Hol, W. G. J. Conformational changes in leishmania mexicana glyceraldehyde-3-phosphate dehydrogenase induced by designed inhibitors. *J. Mol. Biol.* **2001**, *309*, 423–435 DOI: 10.1006/jmbi.2001.4588.

(35) Bressi, J. C.; Verlinde, C. L. M. J.; Aronov, A. M.; Shaw, M. L.; Shin, S. S.; Nguyen, L. N.; Suresh, S.; Buckner, F. S.; van Voorhis, W. C.; Kuntz, I. D.; et al. Adenosine analogues as selective inhibitors of glyceraldehyde-3-phosphate dehydrogenase of trypanosomatidae via structure-based drug design. *J. Med. Chem.* **2001**, *44*, 2080–2093 DOI: 10.1021/jm000472o.

(36) Verlinde, C. L. M. J.; Callens, M.; Van Calenbergh, S.; Van Aerschot, A.; Herdewijn, P.; Hannaert, V.; Michels, P. A. M.; Opperdoes, F. R.; Hol, W. G. J. Selective Inhibition of Trypanosomal Glyceraldehyde-3-phosphate Dehydrogenase by Protein Structure-Based Design: Toward New Drugs for the Treatment of Sleeping Sickness. *J. Med. Chem.* **1994**, *37*, 3605–3613 DOI: 10.1021/jm00047a017.

(37) Aronov, A. M.; Verlinde, C. L. M. J.; Hol, W. G. J.; Gelb, M. H. Selective tight binding inhibitors of trypanosomal glyceraldehyde-3- phosphate dehydrogenase via structure-based drug design. *J. Med. Chem.* **1998**, *41*, 4790–4799 DOI: 10.1021/jm9802620.

(38) Souza, D. H. .; Garratt, R. .; Araújo, A. P. .; Guimarães, B. .; Jesus, W. D. .; Michels, P. A. .; Hannaert, V.; Oliva, G. *Trypanosoma cruzi* glycosomal glyceraldehyde-3-phosphate dehydrogenase: structure, catalytic mechanism and targeted inhibitor design. *FEBS Lett.* **1998**, *424*, 131–135 DOI: 10.1016/S0014-5793(98)00154-9.

(39) Tomazela, D. M.; Pupo, M. T.; Passador, E. A. P.; Da Silva, M. F. D. G. F.; Vieira, P. C.; Fernandes, J. B.; Rodrigues Fo, E.; Oliva, G.; Pirani, J. R. Pyrano chalcones and a flavone from Neoraputia magnifica and their Trypanosoma cruzi glycosomal glyceraldehyde-3-phosphate dehydrogenase-Inhibitory activities. *Phytochemistry* **2000**, *55*, 643–651 DOI: 10.1016/S0031-9422(00)00248-X.

(40) Van Calenbergh, S.; Soenens, J.; Herdewijn, P.; Herdewijn, P.; Rozenski, J.; Veriinde, C. L. M. J.; Hol, W. G. J.; De Bruyn, A.; Callens, M.; Blaton, N. M.; et al. Synthesis and Structure-Activity Relationships of Analogs of 2′-Deoxy-2′-(3-methoxybenzamido)adenosine, a Selective Inhibitor of Trypanosomal Glycosomal Glyceraldehyde-3-phosphate Dehydrogenase. *J. Med. Chem.* **1995**, *38*, 3838–3849 DOI: 10.1021/jm00019a014.

(41) Daubenberger, C. A.; Pöltl-Frank, F.; Jiang, G.; Lipp, J.; Certa, U.; Pluschke, G. Identification and recombinant expression of glyceraldehyde-3-phosphate dehydrogenase of Plasmodium falciparum. *Gene* **2000**, *246*, 255–264 DOI: 10.1016/S0378-1119(00)00069-X.

(42) Cha, S.-J.; Kim, M.-S.; Pandey, A.; Jacobs-Lorena, M. Identification of GAPDH on the surface of *Plasmodium* sporozoites as a new candidate for targeting malaria liver invasion. *J. Exp. Med.*

2016, *213*, 2099–2112 DOI: 10.1084/jem.20160059.

(43) Sirover, M. A. Structural analysis of glyceraldehyde-3-phosphate dehydrogenase functional diversity. *Int. J. Biochem. Cell Biol.* **2014**, *57*, 20–26 DOI: 10.1016/j.biocel.2014.09.026.

(44) Dimmeler, S.; Lottspeich, F.; Brune, B. Nitric oxide causes ADP-ribosylation and inhibition of glyceraldehyde-3- phosphate dehydrogenase. *J. Biol. Chem.* **1992**, *267*, 16771–16774.

(45) Hyslop, P. A.; Hinshaw, D. B.; Halsey, W. A.; Schraufstätter, I. U.; Sauerheber, R. D.; Spragg, R. G.; Jackson, J. H.; Cochrane, C. G. Mechanisms of oxidant-mediated cell injury. The glycolytic and mitochondrial pathways of ADP phosphorylation are major intracellular targets inactivated by hydrogen peroxide. *J. Biol. Chem.* **1988**, *263*, 1665–1675.

(46) Garcia, J. I.; Seabra, A. B.; Kennedy, R.; English, A. M. Nitrite and nitroglycerin induce rapid release of the vasodilator ATP from erythrocytes: Relevance to the chemical physiology of local vasodilation. *J. Inorg. Biochem.* **2010**, *104*, 289–296 DOI: 10.1016/j.jinorgbio.2009.12.009.

(47) Bergfeld, G. R.; Forrester, T. Release of ATP from human erythrocytes in response to a brief period of hypoxia and hypercapnia. *Cardiovasc. Res.* **1992**, *26*, 40–47.

(48) Seabra, A. B.; Ouellet, M.; Antonic, M.; Chrétien, M. N.; English, A. M. Catalysis of nitrite generation from nitroglycerin by glyceraldehyde-3-phosphate dehydrogenase (GAPDH). *Nitric Oxide* **2013**, *35*, 116–122 DOI: 10.1016/j.niox.2013.09.003.

(49) Li, H.; Liu, X.; Cui, H.; Chen, Y. R.; Cardounel, A. J.; Zweier, J. L. Characterization of the mechanism of cytochrome P450 reductase-cytochrome P450-mediated nitric oxide and nitrosothiol generation from organic nitrates. *J. Biol. Chem.* **2006**, *281*, 12546–12554 DOI: 10.1074/jbc.M511803200.

(50) Li, H.; Cui, H.; Liu, X.; Zweier, J. L. Xanthine oxidase catalyzes anaerobic transformation of organic nitrates to nitric oxide and nitrosothiols: Characterization of this mechanism and the link between organic nitrate and guanylyl cyclase activation. *J. Biol. Chem.* **2005**, *280*, 16594–16600 DOI: 10.1074/jbc.M411905200.

(51) Ji, Y.; Anderson, D. J.; Bennett, B. M. Role of microsomal glutathione transferase 1 in the mechanism-based biotransformation of glyceryl trinitrate in LLC-PK1 cells. *Biochem. Pharmacol.* **2009**, *77*, 1702–1708 DOI: 10.1016/j.bcp.2009.02.022.

(52) Chen, Z.; Zhang, J.; Stamler, J. S. Identification of the enzymatic mechanism of nitroglycerin bioactivation. *Proc. Natl. Acad. Sci. U. S. A.* **2002**, *99*, 8306–8311 DOI: 10.1073/pnas.122225199.

(53) Ignarro, L. J. Nitric Oxide Donors and Cardiovascular Agents Modulating the Bioactivity of Nitric Oxide: An Overview. *Circ. Res.* **2002**, *90*, 21–28 DOI: 10.1161/hh0102.102330.

(54) Page, N. A.; Fung, H.-L. Organic nitrate metabolism and action: toward a unifying hypothesis and the future-a dedication to Professor Leslie Z. Benet. *J. Pharm. Sci.* **2013**, *102*, 3070–3081 DOI:

10.1002/jps.23550.

(55) Lang, B. S.; Gorren, A. C. F.; Oberdorfer, G.; Wenzl, M. V.; Furdui, C. M.; Poole, L. B.; Mayer, B.; Gruber, K. Vascular bioactivation of nitroglycerin by aldehyde dehydrogenase-2: reaction intermediates revealed by crystallography and mass spectrometry. *J. Biol. Chem.* **2012**, *287*, 38124–38134 DOI: 10.1074/jbc.M112.371716.

(56) Cameron, D. R.; Borrajo, A. M. P.; Thatcher, G. R. J.; Bennett, B. M. Organic nitrates, thionitrates, peroxynitrites, and nitric oxide: a molecular orbital study of the (X = O, S) rearrangement, a reaction of potential biological significance. *Can. J. Chem.* **1995**, *73*, 1627–1638 DOI: 10.1139/v95-202.

(57) Chen, Z.; Stamler, J. S. Bioactivation of nitroglycerin by the mitochondrial aldehyde dehydrogenase. *Trends Cardiovasc. Med.* **2006**, *16*, 259–265 DOI: 10.1016/j.tcm.2006.05.001.

(58) Wenzl, M. V.; Beretta, M.; Griesberger, M.; Russwurm, M.; Koesling, D.; Schmidt, K.; Mayer, B.; Gorren, A. C. F. Site-directed mutagenesis of aldehyde dehydrogenase-2 suggests three distinct pathways of nitroglycerin biotransformation. *Mol. Pharmacol.* **2011**, *80*, 258–266 DOI: 10.1124/mol.111.071704.

(59) Münzel, T.; Daiber, A.; Mülsch, A. Explaining the phenomenon of nitrate tolerance. *Circ. Res.* **2005**, *97*, 618–628 DOI: 10.1161/01.RES.0000184694.03262.6d.

(60) Bennett, B. M.; McDonald, B. J.; Nigam, R.; Simon, W. C. Biotransformation of organic nitrates and vascular smooth muscle cell function. *Trends Pharmacol. Sci.* **1994**, *15*, 245–249 DOI: 10.1016/0165-6147(94)90319-0.

(61) Oae, S.; Shinhama, K.; Fujimori, K.; Kim, Y. H. Physical properties and various reactions of thionitrites and related substances. *Bull. Chem. Soc. Jpn.* **1980**, *53*, 775–784 DOI: 10.1246/bcsj.53.775.

(62) Oae, S.; Shinhama, K. Organic Thionitrites and Related Substances. A Review. *Org. Prep. Proced. Int.* **1983**, *15*, 165–198 DOI: 10.1080/00304948309355444.

(63) Goto, K.; Hino, Y.; Kawashima, T.; Kaminaga, M.; Yano, E.; Yamamoto, G.; Takagi, N.; Nagase, S. Synthesis and crystal structure of a stable S-nitrosothiol bearing a novel steric protection group and of the corresponding S-nitrothiol. *Tetrahedron Lett.* **2000**, *41*, 8479–8483 DOI: 10.1016/S0040-4039(00)01487-8.

(64) Goto, K.; Shimada, K.; Furukawa, S.; Miyasaka, S.; Takahashi, Y.; Kawashima, T. Formation of a Stable Sulfenic Acid by Hydrolysis of a Thionitrate and a Sulfenyl Bromide. *Chem. Lett.* **2006**, *35*, 862–863 DOI: 10.1246/cl.2006.862.

(65) Artz, J. D.; Yang, K.; Lock, J.; Sanchez, C.; Bennett, B. M.; Thatcher, G. R. J. Reactivity of thionitrate esters: putative intermediates in nitrovasodilator activity. *Chem. Commun.* **1996**, 927

DOI: 10.1039/cc9960000927.

(66) Rossman, M. G.; Liljas, A.; Brändén, C.-I.; Banaszak, L. J. 2 Evolutionary and Structural Relationships among Dehydrogenases. In; Boyer, P. D. B. T.-T. E., Ed.; Academic Press, 1975; Vol. 11, pp. 61–102.

(67) Skarżyński, T.; Wonacott, A. J. Coenzyme-induced conformational changes in glyceraldehyde-3-phosphate dehydrogenase from Bacillus stearothermophilus. *J. Mol. Biol.* **1988**, *203*, 1097–1118 DOI: 10.1016/0022-2836(88)90130-1.

(68) Kuravsky, M. L.; Barinova, K. V.; Asryants, R. a.; Schmalhausen, E. V.; Muronetz, V. I. Structural basis for the NAD binding cooperativity and catalytic characteristics of sperm-specific glyceraldehyde-3-phosphate dehydrogenase. *Biochimie* **2015**, *115*, 28–34 DOI: 10.1016/j.biochi.2015.04.016.

(69) Conway, a; Koshland, D. E. Negative cooperativity in enzyme action. The binding of diphosphopyridine nucleotide to glyceraldehyde 3-phosphate dehydrogenase. *Biochemistry* **1968**, *7*, 4011–4023.

(70) Boers, W.; Oosthuizen, C.; Slater, E. C. Binding of NAD+ and NADH to rabbit-muscle glyceraldehydephosphate dehydrogenase. *Biochim. Biophys. Acta - Enzymol.* **1971**, *250*, 35–46 DOI: https://doi.org/10.1016/0005-2744(71)90117-3.

(71) Hoagland, V. D.; Teller, D. C. Influence of substrates on the dissociation of rabbit muscle D-glyceraldehyde 3-phosphate dehydrogenase. *Biochemistry* **1969**, *8*, 594–602.

(72) Osborne, H. H.; Hollaway, M. R. The investigation of substrate-induced changes in subunit interactions in glyceraldehyde 3-phosphate dehydrogenases by measurement of the kinetics and thermodynamics of subunit exchange. *Biochem. J.* **1975**, *151*, 37–45.

(73) Rudolph, R.; Heider, I.; Jaenicke, R. Mechanism of Reactivation and Refolding of Glyceraldehyde-3-Phosphate Dehydrogenase from Yeast after Denaturation and Dissociation. *Eur. J. Biochem.* **1977**, *81*, 563–570 DOI: 10.1111/j.1432-1033.1977.tb11983.x.

(74) Nagy, E.; Henics, T.; Eckert, M.; Miseta, A.; Lightowlers, R. N.; Kellermayer, M. Identification of the NAD+-binding fold of glyceraldehyde-3-phosphate dehydrogenase as a novel RNA-binding domain. *Biochem. Biophys. Res. Commun.* **2000**, *275*, 253–260 DOI: 10.1006/bbrc.2000.3246.

(75) Colell, A.; Green, D. R.; Ricci, J. E. Novel roles for GAPDH in cell death and carcinogenesis. *Cell Death Differ.* **2009**, *16*, 1573–1581 DOI: 10.1038/cdd.2009.137.

(76) Puder, M.; Soberman, R. J. Glutathione conjugates recognize the Rossmann fold of glyceraldehyde-3- phosphate dehydrogenase. *J. Biol. Chem.* **1997**, *272*, 10936–10940 DOI: 10.1074/jbc.272.16.10936.

(77) Roitel, O.; Sergienko, E.; Branlant, G. Dimers generated from tetrameric phosphorylating

glyceraldehyde-3- phosphate dehydrogenase from Bacillus stearothermophilus are inactive but exhibit cooperativity in NAD binding. *Biochemistry* **1999**, *38*, 16084–16091 DOI: 10.1021/bi9912802.

(78) Roitel, O.; Ivinova, O.; Muronetz, V.; Nagradova, N.; Branlant, G. Thermal unfolding used as a probe to characterize the intra- and intersubunit stabilizing interactions in phosphorylating D-glyceraldehyde-3-phosphate dehydrogenase from Bacillus stearothermophilus. *Biochemistry* **2002**, *41*, 7556–7564 DOI: 10.1021/bi012084+.

(79) Polyakova, O. V; Roitel, O.; Asryants, R. a; Poliakov, A. a; Branlant, G.; Muronetz, V. I. Misfolded forms of glyceraldehyde-3-phosphate dehydrogenase interact with GroEL and inhibit chaperonin-assisted folding of the wild-type enzyme. *Protein Sci.* **2005**, *14*, 921–928 DOI: 10.1110/ps.041211205.

(80) Carlile, G. W.; Chalmers-Redman, R. M.; Tatton, N. A.; Pong, A.; Borden, K. E.; Tatton, W. G. Reduced apoptosis after nerve growth factor and serum withdrawal: conversion of tetrameric glyceraldehyde-3-phosphate dehydrogenase to a dimer. *Mol. Pharmacol.* **2000**, *57*, 2–12.

(81) Mazzola, J. L.; Sirover, M. A. Aging of human glyceraldehyde-3-phosphate dehydrogenase is dependent on its subcellular localization. *Biochim. Biophys. Acta - Gen. Subj.* **2005**, *1722*, 168–174 DOI: 10.1016/j.bbagen.2004.12.010.

(82) Magar, M. E. Optical Rotatory Dispersion of Aldolase and Glyceraldehyde 3-Phosphate Dehydrogenase. *J. Biol. Chem.* **1967**, *242*, 2517–2521.

(83) Ovádi, J.; Telegdi, M.; Batke, J.; Keleti, T. Functional Non-Identity of Subunits and Isolation of Active Dimers of d-Glyceraldehyde-3-phosphate Dehydrogenase. *Eur. J. Biochem.* **1971**, *22*, 430–438 DOI: 10.1111/j.1432-1033.1971.tb01561.x.

(84) ELODI, P.; JECSAI, G. Studies on D-glyceraldehyde-3-phosphate dehydrogenase. XV. The effect of urea. *Acta Physiol. Acad. Sci. Hung.* **1960**, *17*, 175–182.

(85) ELODI, P.; JECSAI, G.; MOZOLOVSZKY, A. Studies on D-glyceraldehyde-3-phosphate dehydrogenase. XIV. The effect of pH on the steric properteis. *Acta Physiol. Acad. Sci. Hung.* **1960**, *17*, 165–173.

(86) Cumming, R. C.; Schubert, D. Amyloid-beta induces disulfide bonding and aggregation of GAPDH in Alzheimer's disease. *FASEB J.* **2005**, *19*, 2060–2062 DOI: 10.1096/fj.05-4195fje.

(87) Meyer-Siegler, K.; Mauro, D. J.; Seal, G.; Wurzer, J.; DeRiel, J. K.; Sirover, M. A. A human nuclear uracil DNA glycosylase is the 37-kDa subunit of glyceraldehyde-3-phosphate dehydrogenase. *Proc. Natl. Acad. Sci. U. S. A.* **1991**, *88*, 8460–8464.

(88) Martyniuk, C. J.; Fang, B.; Koomen, J. M.; Gavin, T.; Zhang, L.; Barber, D. S.; LoPachin, R. M. Molecular Mechanism of Glyceraldehyde-3- Phosphate Dehydrogenase (Gapdh) Inactivation By

A,B-Unsaturated Carbonyl Derivatives. *Chem Res Toxicol. Chem Res Toxicol December* **2011**, *19*, 2302–2311 DOI: 10.1021/tx200437y.

(89) Buehner, M.; Ford, G. C.; Moras, D.; Olsen, K. W.; Rossmann, M. G. Structure determination of crystalline lobster d-glyceraldehyde-3-phosphate dehydrogenase. *J. Mol. Biol.* **1974**, *82*, 563–585 DOI: https://doi.org/10.1016/0022-2836(74)90249-6.

(90) Arutyunova, E. I.; Danshina, P. V.; Domnina, L. V.; Pleten, A. P.; Muronetz, V. I. Oxidation of glyceraldehyde-3-phosphate dehydrogenase enhances its binding to nucleic acids. *Biochem. Biophys. Res. Commun.* **2003**, *307*, 547–552 DOI: 10.1016/S0006-291X(03)01222-1.

(91) Ryzlak, M. T.; Pietruszko, R. Heterogeneity of glyceraldehyde-3-phosphate dehydrogenase from human brain. *Biochim. Biophys. Acta - Protein Struct. Mol. Enzymol.* **1988**, *954*, 309–324 DOI: https://doi.org/10.1016/0167-4838(88)90086-6.

(92) Head-Gordon, M.; Pople, J. A.; Frisch, M. J. MP2 energy evaluation by direct methods. *Chem. Phys. Lett.* **1988**, *153*, 503–506 DOI: 10.1016/0009-2614(88)85250-3.

(93) Frisch, M. J.; Head-Gordon, M.; Pople, J. A. Semi-direct algorithms for the MP2 energy and gradient. *Chem. Phys. Lett.* **1990**, *166*, 281–289 DOI: https://doi.org/10.1016/0009-2614(90)80030-H.

(94) Dunning, T. H. Gaussian basis sets for use in correlated molecular calculations. I. The atoms boron through neon and hydrogen. *J. Chem. Phys.* **1989**, *90*, 1007 DOI: 10.1063/1.456153.

(95) Crawford, T. D.; Schaefer, H. F. *Rev. Comput. Chem.*; Lipkowitz, K. B.; Boyd, D. B., Eds.; Reviews in Computational Chemistry; John Wiley & Sons, Inc.: Hoboken, NJ, USA, 2000; Vol. 14.

(96) Raghavachari, K.; Trucks, G. W.; Pople, J. A.; Head-Gordon, M. A fifth-order perturbation comparison of electron correlation theories. *Chem. Phys. Lett.* **1989**, *157*, 479–483 DOI: 10.1016/S0009-2614(89)87395-6.

(97) Miertuš, S.; Scrocco, E.; Tomasi, J. Electrostatic interaction of a solute with a continuum. A direct utilizaion of AB initio molecular potentials for the prevision of solvent effects. *Chem. Phys.* **1981**, *55*, 117–129 DOI: 10.1016/0301-0104(81)85090-2.

(98) Miertuŝ, S.; Tomasi, J. Approximate evaluations of the electrostatic free energy and internal energy changes in solution processes. *Chem. Phys.* **1982**, *65*, 239–245 DOI: 10.1016/0301-0104(82)85072-6.

(99) Phillips, J. C.; Braun, R.; Wang, W.; Gumbart, J.; Tajkhorshid, E.; Villa, E.; Chipot, C.; Skeel, R. D.; Kalé, L.; Schulten, K. Scalable molecular dynamics with NAMD. *J. Comput. Chem.* **2005**, *26*, 1781–1802 DOI: 10.1002/jcc.20289.

(100) Bakan, A.; Bahar, I. The intrinsic dynamics of enzymes plays a dominant role in determining the

structural changes induced upon inhibitor binding. *Proc. Natl. Acad. Sci.* **2009**, *106*, 14349–14354 DOI: 10.1073/pnas.0904214106.

(101) Gur, M.; Zomot, E.; Bahar, I. Global motions exhibited by proteins in micro- to milliseconds simulations concur with anisotropic network model predictions. *J. Chem. Phys.* **2013**, *139* DOI: 10.1063/1.4816375.

(102) Doruker, P.; Atilgan, a R.; Bahar, I. Dynamics of proteins predicted by molecular dynamics simulations and analytical approaches: application to alpha-amylase inhibitor. *Proteins* **2000**, *40*, 512–524 DOI: 10.1002/1097-0134(20000815)40:3<512::AID-PROT180>3.0.CO;2-M.

(103) Atilgan, A. R.; Durell, S. R.; Jernigan, R. L.; Demirel, M. C.; Keskin, O.; Bahar, I. Anisotropy of Fluctuation Dynamics of Proteins with an Elastic Network Model. *Biophys. J.* **2001**, *80*, 505–515 DOI: 10.1016/S0006-3495(01)76033-X.

(104) Eyal, E.; Yang, L. W.; Bahar, I. Anisotropic network model: Systematic evaluation and a new web interface. *Bioinformatics* **2006**, *22*, 2619–2627 DOI: 10.1093/bioinformatics/btl448.

(105) Jenkins, J. L.; Tanner, J. J. High-resolution structure of human D-glyceraldehyde-3-phosphate dehydrogenase. *Acta Crystallogr. D. Biol. Crystallogr.* **2006**, *62*, 290–301 DOI: 10.1107/S0907444905042289.

(106) MacKerell, A. D.; Bashford, D.; Bellott, M.; Dunbrack, R. L.; Evanseck, J. D.; Field, M. J.; Fischer, S.; Gao, J.; Guo, H.; Ha, S.; et al. All-atom empirical potential for molecular modeling and dynamics studies of proteins. *J. Phys. Chem. B* **1998**, *102*, 3586 DOI: 10.1021/jp973084f.

(107) Laino, T.; Mohamed, F.; Laio, A.; Parrinello, M. An efficient real space multigrid QM/MM electrostatic coupling. *J. Chem. Theory Comput.* **2005**, *1*, 1176–1184 DOI: 10.1021/ct050123f.

(108) Lauretti, G. R.; Perez, M. V; Reis, M. P.; Pereira, N. L. Double-blind evaluation of transdermal nitroglycerine as adjuvant to oral morphine for cancer pain management. *J. Clin. Anesth.* **2002**, *14*, 83–86 DOI: 10.1016/S0952-8180(01)00360-9.

(109) Wimalawansa, S. .; De Marco, G.; Gangula, P.; Yallampalli, C. Nitric oxide donor alleviates ovariectomy-induced bone loss. *Bone* **1996**, *18*, 301–304 DOI: 10.1016/8756-3282(96)00005-1.

(110) Wu, W.-P.; Hao, J.-X.; Ongini, E.; Impagnatiello, F.; Presotto, C.; Wiesenfeld-Hallin, Z.; Xu, X.-J. A nitric oxide (NO)-releasing derivative of gabapentin, NCX 8001, alleviates neuropathic pain-like behavior after spinal cord and peripheral nerve injury. *Br. J. Pharmacol.* **2004**, *141*, 65–74 DOI: 10.1038/sj.bjp.0705596.

(111) del Soldato, P.; Sorrentino, R.; Pinto, A. NO-aspirins: a class of new anti-inflammatory and antithrombotic agents. *Trends Pharmacol. Sci.* **1999**, *20*, 319–323 DOI: 10.1016/S0165-6147(99)01353-X.

(112) Thatcher, G. R. J.; Nicolescu, A. C.; Bennett, B. M.; Toader, V. Nitrates and NO release:

contemporary aspects in biological and medicinal chemistry. *Free Radic. Biol. Med.* **2004**, *37*, 1122–1143 DOI: 10.1016/j.freeradbiomed.2004.06.013.

(113) Yeates, R. A.; Laufen, H.; Leitold, M. The reaction between organic nitrates and sulfhydryl compounds. A possible model system for the activation of organic nitrates. *Mol. Pharmacol.* **1985**, *28*, 555–559.

(114) Krishnatry, A. S.; Kamei, T.; Wang, H.; Qu, J.; Fung, H.-L. Identification of nitroglycerin-induced cysteine modifications of pro-matrix metalloproteinase-9. *Rapid Commun. Mass Spectrom.* **2011**, *25*, 2291–2298 DOI: 10.1002/rcm.5118.

(115) Goto, K.; Yoshikawa, S.; Ideue, T.; Sase, S. Transnitrosation from a stable thionitrate to an amine with concomitant formation of a sulfenic acid. *J. Sulfur Chem.* **2013**, *34*, 705–710 DOI: 10.1080/17415993.2013.794801.

(116) Ignarro, L. J.; Lippton, H.; Edwards, J. C.; Baricos, W. H.; Hyman, A. L.; Kadowitz, P. J.; Gruetter, C. A. Mechanism of vascular smooth muscle relaxation by organic nitrates, nitrites, nitroprusside and nitric oxide: evidence for the involvement of S-nitrosothiols. *J. Pharmacol. Exp. Ther.* **1981**, *218*, 739–749.

(117) Choi, Y. J.; Lee, Y. S. The Rearrangement Reaction of CH3SNO2 to CH3SONO Studied by a Density Functional Theory Method. *Bull. Chem. Soc.* **2004**, *25*, 1657–1658.

(118) Balazy, M.; Kaminski, P. M.; Mao, K.; Tan, J.; Wolin, M. S. S-Nitroglutathione, a Product of the Reaction between Peroxynitrite and Glutathione That Generates Nitric Oxide. *J. Biol. Chem.* **1998**, *273*, 32009–32015 DOI: 10.1074/jbc.273.48.32009.

(119) Frisch, M. J.; Head-Gordon, M.; Pople, J. A. A direct MP2 gradient method. *Chem. Phys. Lett.* **1990**, *166*, 275–280 DOI: 10.1016/0009-2614(90)80029-D.

(120) Jensen, F. *Introduction to Computational Chemistry*; John Wiley & Sons, 2006.

(121) Fukui, K. The path of chemical reactions - the IRC approach. *Acc. Chem. Res.* **1981**, *14*, 363–368 DOI: 10.1021/ar00072a001.

(122) Hratchian, H. P.; Schlegel, H. B. No Title. In *Theory and Applications of Computational Chemistry: The First 40 Years*; Dykstra, C.; Frenking, G.; Kim, K.; Scuseria, G., Eds.; Elsevier Inc.: Amsterdam, 2005; pp. 195–249.

(123) Frisch, M. J.; Trucks, G. W.; Schlegel, H. B.; Scuseria, G. E.; Robb, M. A.; Cheeseman, J. R.; Scalmani, G.; Barone, V.; Mennucci, B.; Petersson, G. A.; et al. Gaussian, Inc., Wallingford CT, 2009.

(124) Sano, T.; Shimada, K.; Aoki, Y.; Kawashima, T.; Sase, S.; Goto, K. Modeling of the Bioactivation of an Organic Nitrate by a Thiol to Form a Thionitrate Intermediate. *Molecules* **2016**, *22*, 19 DOI: 10.3390/molecules22010019.

(125) Koch, D. M.; Toubin, C.; Xu, S.; Peslherbe, G. H.; Hynes, J. T. Concerted proton-transfer mechanism and solvation effects in the HNC/HCN isomerization on the surface of icy grain mantles in the interstellar medium. *J. Phys. Chem. C* **2007**, *111*, 15026–15033 DOI: 10.1021/jp076220h.

(126) Koch, D. M.; Toubin, C.; Peslherbe, G. H.; Hynes, J. T. A theoretical study of the formation of the aminoacetonitrile precursor of glycine on icy grain mantles in the interstellar medium. *J. Phys. Chem. C* **2008**, *112*, 2972–2980 DOI: 10.1021/jp076221+.

(127) Moran, E. E.; Timerghazin, Q. K.; Kwong, E.; English, A. M. Kinetics and mechanism of S-nitrosothiol acid-catalyzed hydrolysis: Sulfur activation promotes facile NO+ release. *J. Phys. Chem. B* **2011**, *115*, 3112–3126 DOI: 10.1021/jp1035597.

(128) Freeman, F.; Adesina, I. T.; La, J. Le; Lee, J. Y.; Poplawski, A. A. Conformers of cysteine and cysteine sulfenic acid and mechanisms of the reaction of cysteine sulfenic acid with 5,5-dimethyl-1,3-cyclohexanedione (dimedone). *J. Phys. Chem. B* **2013**, *117*, 16000–16012 DOI: 10.1021/jp409022m.

(129) Freeman, F. Mechanisms of reactions of sulfur hydride hydroxide: Tautomerism, condensations, and C-sulfenylation and O-sulfenylation of 2,4-pentanedione. *J. Phys. Chem. A* **2015**, *119*, 3500–3517 DOI: 10.1021/acs.jpca.5b00779.

(130) Ivanova, L. V.; Cibich, D.; Deye, G.; Talipov, M. R.; Timerghazin, Q. K. Modeling of S-Nitrosothiol–Thiol Reactions of Biological Significance: HNO Production by S-Thiolation Requires a Proton Shuttle and Stabilization of Polar Intermediates. *ChemBioChem* **2017**, *18*, 726–738 DOI: 10.1002/cbic.201600556.

(131) Reddie, K. G.; Carroll, K. S. Expanding the functional diversity of proteins through cysteine oxidation. *Curr. Opin. Chem. Biol.* **2008**, *12*, 746–754 DOI: 10.1016/j.cbpa.2008.07.028.

(132) Salsbury, F. R.; Poole, L. B.; Fetrow, J. S. Electrostatics of cysteine residues in proteins: Parameterization and validation of a simple model. *Proteins Struct. Funct. Bioinforma.* **2012**, *80*, 2583–2591 DOI: 10.1002/prot.24142.

(133) Marino, S. M.; Gladyshev, V. N. Redox biology: computational approaches to the investigation of functional cysteine residues. *Antioxid. Redox Signal.* **2011**, *15*, 135–146 DOI: 10.1089/ars.2010.3561.

(134) Khomyakov, D. G.; Timerghazin, Q. K. Toward reliable modeling of S-nitrosothiol chemistry: Structure and properties of methyl thionitrite (CH3SNO), an S-nitrosocysteine model. *J. Chem. Phys.* **2017**, *147*, 044305 DOI: 10.1063/1.4995300.

(135) Lu, J. M.; Wittbrodt, J. M.; Wang, K.; Wen, Z.; Schlegel, H. B.; Wang, P. G.; Cheng, J. P. NO affinities of S-nitrosothiols: A direct experimental and computational investigation of RS-NO

bond dissociation energies. *J. Am. Chem. Soc.* **2001**, *123*, 2903–2904 DOI: Doi 10.1021/Ja000384t.

(136) Thatcher, G. R. J.; Weldon, H. NO problem for nitroglycerin: organic nitrate chemistry and therapy. *Chem. Soc. Rev.* **1998**, *27*, 331–337 DOI: 10.1039/a827331z.

(137) Gupta, V.; Carroll, K. S. Sulfenic acid chemistry, detection and cellular lifetime. *Biochim. Biophys. Acta - Gen. Subj.* **2014**, *1840*, 847–875 DOI: 10.1016/j.bbagen.2013.05.040.

(138) Beretta, M.; Sottler, A.; Schmidt, K.; Mayer, B.; Gorren, A. C. F. Partially irreversible inactivation of mitochondrial aldehyde dehydrogenase by nitroglycerin. *J. Biol. Chem.* **2008**, *283*, 30735–30744 DOI: 10.1074/jbc.M804001200.

(139) Labandowskiy, J. K.; Hill, R. A.; Heisterbergy, D. J.; Miller, D. D.; Bender, C. F.; Andzelm, J. W. Proton Affini- ties Calculated by Traditional Ab Initio Approaches and by Density Functional Methods. 1–28.

(140) Moser, A.; Range, K.; York, D. M. Accurate proton affinity and gas-phase basicity values for molecules important in biocatalysis. *J. Phys. Chem. B* **2010**, *114*, 13911–13921 DOI: 10.1021/jp107450n.

(141) Peterson, K. A.; Xantheas, S. S.; Dixon, D. A.; Dunning, T. H. Predicting the proton affinities of H2O and NH3. *J. Phys. Chem. A* **1998**, *102*, 2449–2454 DOI: 10.1021/jp971510r.

(142) Artz, J. D.; Toader, V.; Zavorin, S. I.; Bennett, B. M.; Thatcher, G. R. J. In Vitro Activation of Soluble Guanylyl Cyclase and Nitric Oxide Release: A Comparison of NO Donors and NO Mimetics †. *Biochemistry* **2001**, *40*, 9256–9264 DOI: 10.1021/bi002885x.

(143) Møller, C.; Plesset, M. S. Note on an approximation treatment for many-electron systems. *Phys. Rev.* **1934**, *46*, 618–622 DOI: 10.1103/PhysRev.46.618.

(144) Head-Gordon, M.; Head-Gordon, T. Analytic MP2 frequencies without fifth-order storage. Theory and application to bifurcated hydrogen bonds in the water hexamer. *Chem. Phys. Lett.* **1994**, *220*, 122–128 DOI: https://doi.org/10.1016/0009-2614(94)00116-2.

(145) F. Weinhold; Landis, C. R. *Valency and Bonding: A Natural Bond Orbital Donor-Acceptor Perspective*; Cambridge University Press, 2005.

(146) Glendening, E. D.; Weinhold, F. Natural resonance theory: I. General formalism. *J. Comput. Chem.* **1998**, *19*, 593–609 DOI: 10.1002/(sici)1096-987x(19980430)19:6<610::aid-jcc4>3.0.co;2-u.

(147) Glendening, E. D.; Weinhold, F. Natural Resonance Theory: II. Natural bond order and valency. *J. Comput. Chem.* **1998**, *19*, 610–627 DOI: 10.1002/(sici)1096-987x(19980430)19:6<610::aid-jcc4>3.3.co;2-7.

(148) Glendening, E. D.; Badenhoop, J. K.; Weinhold, F. Natural Resonance Theory : *J. Comput. Chem.*

1998, *19*, 628–646 DOI: 10.1002/(SICI)1096-987X(19980430)19:6<628::AID-JCC5>3.0.CO;2-T.

(149) Glendening, E. D.; Badenhoop, J. K.; Reed, A. E.; Carpenter, J. E.; Bohmann, J. A.; Morales, C. M.; Weinhold, F. *NBO 5.0*; Theoretical Chemistry Institute, University of Wisconsin, Madison, WI, 2001.

(150) Weinhold, F.; Landis, C. R. Natural Bond Orbitals and Extensions of Localized Bonding Concepts. *Chem. Educ. Res. Pr.* **2001**, *2*, 91–104 DOI: 10.1039/B1RP90011K.

(151) Keith, T. A. AIMAll (Version 14.04.17), 2014.

(152) Bader, R. F. W. Atoms in Molecules: a quantum theory , 1990.

(153) Popelier, P. L. A. Atoms in Molecules. An Introduction, 2000.

(154) Denis, P. a; Ventura, O. N.; Mai, H. T.; Nguyen, M. T. Ab Initio and Density Functional Study of Thionitroso XNS and Thiazyl Isomers XSN, X) H, F, Cl, Br, OH, SH, NH 2 , CH 3 , CF 3 , and SiF 3. *Society* **2004**, *108*, 5073–5080 DOI: 10.1021/jp0498466.

(155) Arulsamy, N.; Bohle, D. S.; Butt, J. A.; Irvine, G. J.; Jordan, P. A.; Sagan, E. Interrelationships between conformational dynamics and the redox chemistry of S-nitrosothiols. *J. Am. Chem. Soc.* **1999**, *121*, 7115–7123 DOI: 10.1021/ja9901314.

(156) Timerghazin, Q. K.; Peslherbe, G. H.; English, A. M. Resonance description of S-nitrosothiols: Insights into reactivity. *Org. Lett.* **2007**, *9*, 3049–3052 DOI: 10.1021/ol0711016.

(157) Gibbs, G. V.; Hill, F. C.; Boisen, M. B.; Downs, R. T. Power law relationships between bond length, bond strength and electron density distributions. *Phys. Chem. Miner.* **1998**, *25*, 585–590 DOI: 10.1007/s002690050151.

(158) Alkorta, I.; Rozas, I.; Elguero, J. Bond Length–Electron Density Relationships: From Covalent Bonds to Hydrogen Bond Interactions. *Struct. Chem.* **1998**, *9*, 243–247 DOI: 10.1023/A:1022424228462.

(159) Dinadayalane, T. C.; Sastry, G. N.; Leszczynski, J. Comprehensive theoretical study towards the accurate proton affinity values of naturally occurring amino acids. *Int. J. Quantum Chem.* **2006**, *106*, 2920–2933 DOI: 10.1002/qua.21117.

(160) Mayer, B.; Beretta, M. The enigma of nitroglycerin bioactivation and nitrate tolerance: news, views and troubles. *Br. J. Pharmacol.* **2008**, *155*, 170–184 DOI: 10.1038/bjp.2008.263.

(161) Durchslag, H.; Puchwein, G.; Kratky, O.; Schuster, I.; Kirschner, K. X-ray small-angle scattering of yeast glyceraldehyde-3-phosphate dehydrogenase as a function of saturation with nicotinamide-adenine-dinucleotide. *FEBS Lett.* **1969**, *4*, 75–78 DOI: https://doi.org/10.1016/0014-5793(69)80200-0.

(162) Cook, W. J.; Senkovich, O.; Chattopadhyay, D. An unexpected phosphate binding site in glyceraldehyde 3-phosphate dehydrogenase: crystal structures of apo, holo and ternary complex of

Cryptosporidium parvum enzyme. *BMC Struct. Biol.* **2009**, *9*, 9 DOI: 10.1186/1472-6807-9-9.

(163) Schormann, N.; Ayres, C. A.; Fry, A.; Green, T. J.; Banerjee, S.; Ulett, G. C.; Chattopadhyay, D. Crystal Structures of Group B Streptococcus Glyceraldehyde-3-Phosphate Dehydrogenase: Apo-Form, Binary and Ternary Complexes. *PLoS One* **2016**, *11*, e0165917 DOI: 10.1371/journal.pone.0165917.

(164) Shen, Y. Q.; Li, J.; Song, S. Y.; Lin, Z. J. Structure of apo-glyceraldehyde-3-phosphate dehydrogenase from Palinurus versicolor. *J. Struct. Biol.* **2000**, *130*, 1–9 DOI: 10.1006/jsbi.2000.4220.

(165) Ferreira-da-Silva, F.; Pereira, P. J. B.; Gales, L.; Roessle, M.; Svergun, D. I.; Moradas-Ferreira, P.; Damas, A. M. The crystal and solution structures of glyceraldehyde-3-phosphate dehydrogenase reveal different quaternary structures. *J. Biol. Chem.* **2006**, *281*, 33433–33440 DOI: 10.1074/jbc.M605267200.

(166) de Oliveira, O. V.; dos Santos, J. D.; Freitas, L. C. G. Molecular dynamics simulation of the gGAPDH–NAD + complex from Trypanosoma cruzi. *Mol. Simul.* **2012**, *38*, 1124–1131 DOI: 10.1080/08927022.2012.696112.

(167) Peralta, D.; Bronowska, A. K.; Morgan, B.; Dóka, É.; Van Laer, K.; Nagy, P.; Gräter, F.; Dick, T. P. A proton relay enhances H2O2 sensitivity of GAPDH to facilitate metabolic adaptation. *Nat. Chem. Biol.* **2015**, 1–20 DOI: 10.1038/nchembio.1720.

(168) Aronov, a M.; Suresh, S.; Buckner, F. S.; Van Voorhis, W. C.; Verlinde, C. L.; Opperdoes, F. R.; Hol, W. G.; Gelb, M. H. Structure-based design of submicromolar, biologically active inhibitors of trypanosomatid glyceraldehyde-3-phosphate dehydrogenase. *Proc. Natl. Acad. Sci. U. S. A.* **1999**, *96*, 4273–4278 DOI: 10.1073/pnas.96.8.4273.

(169) Ma, J. Usefulness and limitations of normal mode analysis in modeling dynamics of biomolecular complexes. *Structure* **2005**, *13*, 373–380 DOI: 10.1016/j.str.2005.02.002.

(170) Avesani, P.; King, I. *Computational Methods to Study the Structure and Dynamics of Biomolecules and Biomolecular Processes*; Liwo, A., Ed.; Springer Series in Bio-/Neuroinformatics; Springer Berlin Heidelberg: Berlin, Heidelberg, 2014; Vol. 1.

(171) Bakan, A.; Meireles, L. M.; Bahar, I. ProDy: Protein dynamics inferred from theory and experiments. *Bioinformatics* **2011**, *27*, 1575–1577 DOI: 10.1093/bioinformatics/btr168.

(172) Hayward, S.; De Groot, B. L. Normal modes and essential dynamics. In *Methods in Molecular Biology*; 2008; Vol. 443, pp. 89–106.

(173) Olsson, M. H. M.; Søndergaard, C. R.; Rostkowski, M.; Jensen, J. H. PROPKA3: Consistent Treatment of Internal and Surface Residues in Empirical pKa Predictions. *J. Chem. Theory Comput.* **2011**, *7*, 525–537 DOI: 10.1021/ct100578z.

(174) Mackerell, A. D.; Feig, M.; Brooks, C. L. Extending the treatment of backbone energetics in protein force fields: Limitations of gas-phase quantum mechanics in reproducing protein conformational distributions in molecular dynamics simulation. *J. Comput. Chem.* **2004**, *25*, 1400–1415 DOI: 10.1002/jcc.20065.

(175) Humphrey, W.; Dalke, A.; Schulten, K. VMD: Visual molecular dynamics. *J. Mol. Graph.* **1996**, *14*, 33–38 DOI: 10.1016/0263-7855(96)00018-5.

(176) Koukos, P. I.; Glykos, N. M. On the application of good-turing statistics to quantify convergence of biomolecular simulations. *J. Chem. Inf. Model.* **2014**, *54*, 209–217 DOI: 10.1021/ci4005817.

(177) David, C. C.; Jacobs, D. J. Principal component analysis: a method for determining the essential dynamics of proteins. *Methods Mol. Biol.* **2014**, *1084*, 193–226 DOI: 10.1007/978-1-62703-658-0_11.

(178) Amadei, A.; Linssen, A. B. M.; Berendsen, H. J. C. Essential dynamics of proteins. *Proteins Struct. Funct. Bioinforma.* **1993**, *17*, 412–425 DOI: 10.1002/prot.340170408.

(179) Bosnjak, I.; Bojovic, V.; Segvic-Bubic, T.; Bielen, A. Occurrence of protein disulfide bonds in different domains of life: a comparison of proteins from the Protein Data Bank. *Protein Eng. Des. Sel.* **2014**, *27*, 65–72 DOI: 10.1093/protein/gzt063.

(180) Itoga, M.; Tsuchiya, M.; Ishino, H.; Shimoyama, M. Nitric oxide-induced modification of glyceraldehyde-3-phosphate dehydrogenase with NAD+ is not ADP-ribosylation. *J. Biochem.* **1997**, *121*, 1041–1046.

(181) Hara, M. R.; Cascio, M. B.; Sawa, A. GAPDH as a sensor of NO stress. *Biochim. Biophys. Acta - Mol. Basis Dis.* **2006**, *1762*, 502–509 DOI: 10.1016/j.bbadis.2006.01.012.

(182) Constantinides, S. M.; Deal, W. C. Reversible dissociation of tetrameric rabbit muscle glyceraldehyde 3-phosphate dehydrogenase into dimers or monomers by adenosine triphosphate. *J. Biol. Chem.* **1969**, *244*, 5695–5702.

(183) Durrieu, C.; Bernier-Valentin, F.; Rousset, B. Microtubules bind glyceraldehyde 3-phosphate dehydrogenase and modulate its enzyme activity and quaternary structure. *Arch. Biochem. Biophys.* **1987**, *252*, 32–40 DOI: 10.1016/0003-9861(87)90005-1.

(184) Arutyunova, E. I.; Domnina, L. V.; Chudinova, A. A.; Makshakova, O. N.; Arutyunov, D. Y.; Muronetz, V. I. Localization of non-native D-glyceraldehyde-3-phosphate dehydrogenase in growing and apoptotic HeLa cells. *Biochem.* **2013**, *78*, 91–95 DOI: 10.1134/S0006297913010112.

(185) Roitel, O.; Vachette, P.; Azza, S.; Branlant, G. P but not R-axis interface is involved in cooperative binding of NAD on tetrameric phosphorylating glyceraldehyde-3-phosphate dehydrogenase from Bacillus stearothermophilus. *J. Mol. Biol.* **2003**, *326*, 1513–1522 DOI: 10.1016/S0022-2836(03)00049-4.

(186) Park, J.; Han, D.; Kim, K.; Kang, Y.; Kim, Y. O-GlcNAcylation disrupts glyceraldehyde-3-phosphate dehydrogenase homo-tetramer formation and mediates its nuclear translocation. *Biochim. Biophys. Acta* **2009**, *1794*, 254–262 DOI: 10.1016/j.bbapap.2008.10.003.

(187) Markossian, K. a; Khanova, H. a; Kleimenov, S. Y.; Levitsky, D. I.; Chebotareva, N. a; Asryants, R. a; Muronetz, V. I.; Saso, L.; Yudin, I. K.; Kurganov, B. I. Mechanism of thermal aggregation of rabbit muscle glyceraldehyde-3-phosphate dehydrogenase. *Biochemistry* **2006**, *45*, 13375–13384 DOI: 10.1021/bi0610707.

(188) Jarosz, A. P.; Wei, W.; Gauld, J. W.; Auld, J.; Özcan, F.; Aslan, M.; Mutus, B. Glyceraldehyde 3-phosphate dehydrogenase (GAPDH) is inactivated by S-sulfuration in vitro. *Free Radic. Biol. Med.* **2015**, *89*, 512–521 DOI: 10.1016/j.freeradbiomed.2015.09.007.

(189) Samson, A. L.; Knaupp, A. S.; Kass, I.; Kleifeld, O.; Marijanovic, E. M.; Hughes, V. a; Lupton, C. J.; Buckle, A. M.; Bottomley, S. P.; Medcalf, R. L. Oxidation of an Exposed Methionine Instigates the Aggregation of Glyceraldehyde-3-phosphate Dehydrogenase. *J. Biol. Chem.* **2014**, *289*, 26922–26936 DOI: 10.1074/jbc.M114.570275.

(190) Cowan-Jacob, S. W.; Kaufmann, M.; Anselmo, A. N.; Stark, W.; Grütter, M. G. Structure of rabbit-muscle glyceraldehyde-3-phosphate dehydrogenase. *Acta Crystallogr. - Sect. D Biol. Crystallogr.* **2003**, *59*, 2218–2227 DOI: 10.1107/S0907444903020493.

(191) Castilho, M. S.; Pavão, F.; Oliva, G.; Ladame, S.; Willson, M.; Périé, J. Evidence for the two phosphate binding sites of an analogue of the thioacyl intermediate for the trypanosoma cruzi glyceraldehyde-3-phosphate dehydrogenase-catalyzed reaction, from its crystal structure. *Biochemistry* **2003**, *42*, 7143–7151 DOI: 10.1021/bi0206107.

(192) Moras, D.; Olsen, K. W.; Sabesan, M. N.; Buehner, M.; Ford, G. C.; Rossmann, M. G. Studies of asymmetry in the three-dimensional structure of lobster D-glyceraldehyde-3-phosphate dehydrogenase. *J. Biol. Chem.* **1975**, *250*, 9137–9162.

(193) Nakajima, H.; Amano, W.; Fujita, A.; Fukuhara, A.; Azuma, Y.-T.; Hata, F.; Inui, T.; Takeuchi, T. The active site cysteine of the proapoptotic protein glyceraldehyde-3-phosphate dehydrogenase is essential in oxidative stress-induced aggregation and cell death. *J. Biol. Chem.* **2007**, *282*, 26562–26574 DOI: 10.1074/jbc.M704199200.

(194) Sawa, A.; Khan, A. A.; Hester, L. D.; Snyder, S. H. Glyceraldehyde-3-phosphate dehydrogenase: nuclear translocation participates in neuronal and nonneuronal cell death. *Proc. Natl. Acad. Sci. U. S. A.* **1997**, *94*, 11669–11674 DOI: 10.1073/pnas.94.21.11669.

(195) Dastoor, Z.; Dreyer, J. L. Potential role of nuclear translocation of glyceraldehyde-3- phosphate dehydrogenase in apoptosis and oxidative stress. *J. Cell Sci.* **2001**, *114*, 1643–1653.

(196) Sen, N.; Hara, M. R.; Kornberg, M. D.; Cascio, M. B.; Bae, B.-I.; Shahani, N.; Thomas, B.;

Dawson, T. M.; Dawson, V. L.; Snyder, S. H.; et al. Nitric oxide-induced nuclear GAPDH activates p300/CBP and mediates apoptosis. *Nat. Cell Biol.* **2008**, *10*, 866–873 DOI: 10.1038/ncb1747.

(197) Molina Y Vedia, L.; McDonald, B.; Reep, B.; Brüne, B.; Di Silvio, M.; Billiar, T. R.; Lapetina, E. G. Nitric oxide-induced S-nitrosylation of glyceraldehyde-3-phosphate dehydrogenase inhibits enzymatic activity and increases endogenous ADP-ribosylation. *J. Biol. Chem.* **1992**, *267*, 24929–24932.

(198) Polekhina, G.; House, C. M.; Traficante, N.; Mackay, J. P.; Relaix, F.; Sassoon, D. A.; Parker, M. W.; Bowtell, D. D. L. Siah ubiquitin ligase is structurally related to TRAF and modulates TNF-alpha signaling. *Nat. Struct. Biol.* **2002**, *9*, 68–75 DOI: 10.1038/nsb743.

(199) Rimsa, V.; Eadsforth, T. C.; Hunter, W. N. Two high-resolution structures of the human E3 ubiquitin ligase Siah1. *Acta Crystallogr. Sect. F Struct. Biol. Cryst. Commun.* **2013**, *69*, 1339–1343 DOI: 10.1107/S1744309113031448.

(200) Mattaj, I. W.; Englmeier, L. NUCLEOCYTOPLASMIC TRANSPORT: The Soluble Phase. *Annu. Rev. Biochem.* **1998**, *67*, 265–306 DOI: 10.1146/annurev.biochem.67.1.265.

(201) Görlich, D.; Kutay, U. Transport between the cell nucleus and the cytoplasm. *Annu. Rev. Cell Dev. Biol.* **1999**, *15*, 607–660 DOI: 10.1146/annurev.cellbio.15.1.607.

(202) Dolinsky, T. J.; Nielsen, J. E.; McCammon, J. A.; Baker, N. A. PDB2PQR: An automated pipeline for the setup of Poisson-Boltzmann electrostatics calculations. *Nucleic Acids Res.* **2004**, *32*, 665–667 DOI: 10.1093/nar/gkh381.

(203) Baker, N. A.; Sept, D.; Joseph, S.; Holst, M. J.; McCammon, J. A. Electrostatics of nanosystems: Application to microtubules and the ribosome. *Proc. Natl. Acad. Sci.* **2001**, *98*, 10037–10041 DOI: 10.1073/pnas.181342398.

(204) The PyMOL Molecular Graphics System, Version 1.5.0.3 Schrödinger, LLC.

(205) Duhovny, D.; Nussinov, R.; Wolfson, H. J. Efficient Unbound Docking of Rigid Molecules. **2002**, 185–200 DOI: 10.1007/3-540-45784-4_14.

(206) Schneidman-Duhovny, D.; Inbar, Y.; Nussinov, R.; Wolfson, H. J. PatchDock and SymmDock: Servers for rigid and symmetric docking. *Nucleic Acids Res.* **2005**, *33*, 363–367 DOI: 10.1093/nar/gki481.

(207) Andrusier, N.; Nussinov, R.; Wolfson, H. J. FireDock: fast interaction refinement in molecular docking. *Proteins* **2007**, *69*, 139–159 DOI: 10.1002/prot.21495.

(208) Mashiach, E.; Schneidman-Duhovny, D.; Andrusier, N.; Nussinov, R.; Wolfson, H. J. FireDock: a web server for fast interaction refinement in molecular docking. *Nucleic Acids Res.* **2008**, *36*, W229-32 DOI: 10.1093/nar/gkn186.

(209) Krissinel, E.; Henrick, K. Inference of Macromolecular Assemblies from Crystalline State. *J. Mol. Biol.* **2007**, *372*, 774–797 DOI: 10.1016/j.jmb.2007.05.022.

(210) The CP2K Developers Group. Available at: http://www.cp2k.org (Accessed Jan 31, 2018).

(211) Becke, A. D. Density-functional thermochemistry. III. The role of exact exchange. *J. Chem. Phys.* **1993**, *98*, 5648–5652 DOI: 10.1063/1.464913.

(212) VandeVondele, J.; Hutter, J. Gaussian basis sets for accurate calculations on molecular systems in gas and condensed phases. *J. Chem. Phys.* **2007**, *127* DOI: 10.1063/1.2770708.

(213) Goedecker, S.; Teter, M. Separable dual-space Gaussian pseudopotentials. *Phys. Rev. B - Condens. Matter Mater. Phys.* **1996**, *54*, 1703–1710 DOI: 10.1103/PhysRevB.54.1703.

(214) Bernasconi, L.; Baerends, E. J.; Sprik, M. Long-range solvent effects on the orbital interaction mechanism of water acidity enhancement in metal ion solutions: A comparative study of the electronic structure of aqueous Mg and Zn dications. *J. Phys. Chem. B* **2006**, *110*, 11444–11453 DOI: 10.1021/jp0609941.